PHD

Nondestructive Testing / Structural Health Monitoring of Gas Turbine Components (Alternative Format Thesis)

Mevissen, Frank

Award date:
2023

Awarding institution:
University of Bath

Nondestructive Testing / Structural Health Monitoring of Gas Turbine Components

Frank Mevissen

A thesis submitted for the degree of

Doctor of Philosophy

University of Bath
Department of Mechanical Engineering

October 2022

COPYRIGHT

[redacted]

Frank Mevissen

ACKNOWLEDGEMENTS

First, I would like to thank and express my profound gratitude and appreciation to my research supervisor, Professor Michele Meo, whose support and discussions contributed significantly to the success of this work. Professor Meo helped me advance my work, especially during the difficult phases, and he also gave me the opportunity to present my research results at Stanford University, which was rather a valuable experience for me while preparing this thesis.

I would also like to thank Dr Gian Piero Malfense Fierro, Marco Boccaccio and all other postgraduate research students at the Department of Mechanical Engineering, University of Bath. During my first time in Bath in particular, I received much valuable support while planning and performing experiments in the laboratory.

I am truly thankful to Dr Sven-Hendrik Wiers, Dirk Sauer, Reiner Brinkmann, Dr Ulrich Orth and Dr Alexander Wiedermann from MAN Energy Solutions for their support and for promoting this research project. Thanks are also due to many of my colleagues in the gas turbine division who have offered me advice and help. I would also like to thank Wolfgang Bernauer, Dirk Formella, Udo Kosters, Hermann Huebner, Joey Stimke and Anders Such for the acquisition and production of samples and their discussions of the experimental results. Finally, I would like to thank Peter Szymansky and *PSL Technik* for manufacturing the samples using the soft melt laser welding process.

On a personal note, I would like to express my very profound gratitude to my parents, Gerda and Peter Mevissen, for their unwavering support and continuous encouragement to achieve my goals, no matter how far away they are.

My sincerest thanks are due to my beloved wife, Yvonne, and my children, Ena-Maria, Joshua, Jonathan and Konstantin, who I am greatly proud of and thankful to. Their encouragement and support are always the most important factor in my life, especially during the last few years.

Abstract

Modern gas turbines offer high potential for future energy generation using alternative fuels. Therefore, these machines need to be further developed to increase the service life of their built-in components and simultaneously increase their performance and efficiency. This can be achieved mainly through a higher compressor outlet pressure and a higher turbine inlet temperature, which lead to high stresses on the hot-gas-leading components in particular. These loads and environmental influences can lead to certain failures in gas turbines, including ruptures, creep deflections, high- and low-cycle fatigues, oxidation, corrosion, erosion, rubbing or wear, foreign object damage, thermal mechanical failures and combinations thereof. Since these factors can lead to cracks and component failure, reliable testing techniques are important for early maintenance. However, because of the complexity and costs associated with these techniques, it is desirable to use these components for as long as possible.

The first research focus is on studying creep damage and early detection of cracks in turbine blades with modulated nonlinear ultrasonic methods. In general, nonlinear techniques have significant advantages over linear ones and enable earlier detection of failures. In a further development of the nonlinear method, ultrasonic waves were emitted with multiple frequencies, which generate harmonic and modulated response frequencies when the waves pass through failures in materials. This offers further possibilities for failure detection and classification. Therefore, the wave equation was solved analytically with multiple excitation frequencies to derive novel nonlinearity parameters. These parameters are the ratios of the measured amplitudes of the harmonic/modulated response frequencies and the fundamental frequencies, and thus they form the basis for failure evaluation. Their existence was verified numerically and experimentally, allowing cracks to be identified and their sizes estimated.

Plastic deformation forms during creep, which is one of the most common failure modes in gas turbines. In this type of failure, the components deform under a constant load depending on the time and temperature. Therefore, creep samples made of the Hastelloy X material were examined to obtain a better understanding of the damage process. The results showed that pores and microcracks propagate from the outside inwards. At the core of the samples, molybdenum was found to be primarily precipitated, while chromium was the main precipitation element in the edge area, leading to the formation of a chromium oxide layer. Moreover, modulated ultrasonic tests showed that the harmonic nonlinearity parameters in particular react very sensitively to the damage sizes of the pores and microcracks.

If the cracks are closed, the ultrasonic waves can pass through the flaws unhindered, without the generation of harmonic or modulated response frequencies. Therefore, the second research focus, ultrasonically stimulated thermography, is on the detection of such cracks. With this technique, turbine blades with trailing edge cracks were vibrated to detect the increase in temperature as a result of frictional heat in the crack area with a thermal imaging camera. When a piezo actuator was used for excitation, the increase in temperature was determined as a function of the excitation frequency, which localised a hidden crack under the ceramic thermal barrier coating. In addition, with a constant excitation frequency and increasing energy input into the actuator, the temperature behaviour revealed whether the crack was constrained or preloaded. This was simulated with a developed finite element model to verify the experimental results.

In conclusion, the proposed techniques allow the sensitive and early detection of different types of cracks and creep damage with a high accuracy, which in turn allows a stable and safe use of the gas turbine components during operation.

CONTENTS

List of Figures

Chapter 6. Creep Detection and Metallurgical Evaluation

Chapter 7. Thermosonic Techniques for Crack Detection

List of Tables

LIST OF ABBREVIATIONS AND ACRONYMS

ACT	Air-Coupled Transducer
AE	Acoustic Emission
AMR	Anisotropic Magnetoresistive
APDL	Ansys Parametric Design Language
AWG	Acoustic Waveguide
CAN	Contact Acoustic Nonlinearity
CMR	Colossal Magnetoresistance
DWTS	Direct-Write Thermal Spray
EC	Eddy Current
EDX	Energy Dispersive X-Ray
EMAT	Electromagnetic Acoustic Transducer
FDTD	Finite Difference Time Domain
FEM	Finite Element Method
FFT	Fourier Transformation
FOD	Foreign Object Damage
GMR	Giant Magnetoresistance
HCF	High-Cycle Fatigue
HPT	High Pressure Turbine
IR	Infrared
LC	Capacitor-Inductor Circuit
LCF	Low-Cycle Fatigue
LDR	Local Defect Resonance
LDV	Laser Doppler Vibrometer
LZT	Lead Zirconate Titanate
NACT	Nonlinear Air-Coupled Thermosonics
NDT	Nondestructive Testing
NDT&E	Nondestructive Testing and Evaluation
NETD	Noise Equivalent Differential Temperature
NEWMS	Nonlinear Elastic Wave Modulation Spectroscopy
PE	Pulse-Echo Method
PSD	Power Spectral Density
PZT	Piezoelectric Transducer
RLM	Reflected Light Microscope

SAW	Surface Acoustic Waves
SEM	Scanning Electron Microscope
SH	Shear Horizontal
SHM	Structural Health Monitoring
SLDV	Scanning Laser Doppler Vibrometer
SLM	Selective Laser Melting
SNR	Signal-to-Noise Ratio
TBC	Thermal Barrier Coating
TGO	Thermally Grown Oxide
TMF	Thermal Mechanical Failure
TMR	Tunnel Magnetoresistance
ToF	Time-of-Flight
TTU	Thru-Transmission Ultrasonic
UCTS	Uniform Crystal Temperature Sensor

1 INTRODUCTION

1.1 Motivation

In general, the components inside a gas turbine are exposed to high loads. This particularly includes the turbine blades, which need to withstand extreme conditions. Therefore, monitoring the condition of turbine blades is very important, as incipient damage, such as cracks, must be detected early before any catastrophic events occur. This ideology forms the basis of condition-based maintenance, which increases the operational reliability of a machine and reduces the maintenance costs. Figure 1 shows the typical design of a gas turbine. In this machine, the air that is sucked in is compressed and forwarded to the combustion chambers, where it is heated up and passed through the turbine for expansion. Part of the energy is used to drive the compressor rotor.

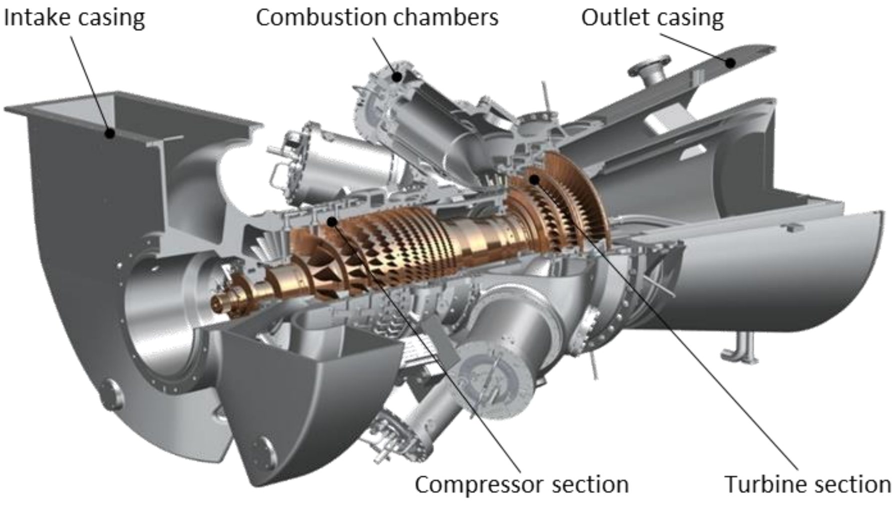

Figure 1. Gas turbine design.

Depending on the operating mode of a gas turbine, a distinction is made between continuous-duty machines and cyclic-duty machines. Continuous-duty machines are normally used to generate electricity. In this mode of operation, an electric generator is driven with a relatively constant speed. In cyclic-duty machines, on the other hand, gas turbines are used for mechanical drive applications, in which another turbo machines are driven. Since the speed of the gas turbine rotor is adapted to the requirements of the driven machine, the rotor speed can vary widely. However, because of these operating modes, different failure modes can damage the gas turbine components [1–3]. Moreover, along with the varying speed of peaking machines and high temperature, thermal mechanical failure (TMF) reduces the service life of the components [2]. In addition, along with the constantly high temperature and mechanical load, creep, oxidation and corrosion lead to the most important life limiters in peaking machines [2]. Low-cycle fatigue (LCF) and high-cycle fatigue (HCF) can be influenced by the design of the components, whereas foreign object damage (FOD) and corrosion depend on the load and the environmental conditions [4]. Both static and rotating parts are exposed to high temperature loads and are typically provided with a ceramic thermal barrier coating (TBC). The degradation of this TBC leads to overheating and, thus, to one of the failure modes mentioned above, which may result in component failure. Table 1 summarises the most important failure modes depending on the operating mode of gas turbines [1–3].

Table 1. Failure modes of gas turbine components.

Continuous duty	Cyclic duty
Creep deflection	TMF
Oxidation	LCF/HCF
Corrosion	Rubbing/wear
Erosion	FOD
LCF/HCF	Combined failure mechanism (creep/fatigue, corrosion/fatigue or oxidation/erosion)
Rupture	
Rubbing/wear	
FOD	
Combined failure mechanism (creep/fatigue, corrosion/fatigue or oxidation/erosion)	

Various techniques are available to detect the above-mentioned failure modes in turbine blades. For example, with the tip timing method, the dynamic behaviour of a turbine blade can be evaluated during operation [5]. The radial clearance between the sensor and the blade tip and the lateral movement of the blade tip can be measured. By measuring the time of one revolution of the blade, information regarding the blade vibrations can be obtained, whereby different sensor technologies are available. Many failure modes can be identified by monitoring the temperature of critical components. Given the change in temperature observed, degradation of the TBC in particular can be detected [6–9]. However, this technology is difficult to implement in-situ because of the extreme conditions inside gas turbines. Other technologies are already used successfully for structural health monitoring (SHM) and nondestructive testing and evaluation (NDT&E) in gas turbines. All of these techniques are shown in Table 2 and discussed in detail in Chapter 3.

Table 2. Failure modes of gas turbines.

	Sensing technology	**Failure modes**
Tip timing method	Microwave probes Optical sensors Inductive sensors Eddy current sensors Magnetoresistive sensors Capacitance sensors	Creep Cracks Rubbing Wear
Temperature measurements	Pyrometry	—
	Infrared thermography	Creep LCF Corrosion Erosion Oxidation
	Phosphor thermometry	—
	Induction thermography	Cracks
Ultrasound	Waveguides Thermosonic Laser ultrasonic High-temperature transducers Electromagnetic acoustic transducers	Creep Cracks Wear
	Acoustic emission	Creep Cracks
	Vibrational monitoring	Rubbing FOD Cracks
	Millimetre waves	Cracks Wear
	Pressure measurements	Cracks Creep Rubbing
	Direct-write thermal spray	Cracks
	Uniform crystal temperature sensor	—
	Performance monitoring	Cracks Wear

Modern ultrasound techniques, which are the focus of this work, are successfully used to detect cracks, as discussed in Chapter 2.2. Various possibilities exist for generating ultrasonic waves and sending them to the components to be tested. In general, the piezo components of typical ultrasound sensors have a very simple design and are very robust. Because of their high sensitivity, favourable signal-to-noise ratio (SNR), high strength, chemical inertness, heat resistance, low weight and low cost, piezoelectric ceramic sensors made of lead zirconate titanate (LZT) are mostly used [10]. More recent research has also focussed on new materials for piezo elements, which can allow their use in-situ in the hot-gas area of gas turbines [11–13].

Early detection of cracks is certainly an important goal in NDT&E and SHM. However, before a crack forms in a component, certain indicators can signal a material failure in advance. Thus, early detection can help better estimate the service life of a component. Modern ultrasound technologies, such as nonlinear techniques, offer the potential to make a valuable contribution through a combination of sensors and the corresponding evaluation technique. Among these techniques, frequency modulation, in which several fundamental frequencies interact with each other at the material failure, has not been fully analysed and has only been partially investigated experimentally. These investigations of the different failure modes represent the main part of this research.

Nonlinear ultrasound NDT&E technologies are only successful if the signal is disturbed in the material and harmonic frequencies are generated. If a crack is closed, the ultrasonic waves can pass through the flaws unhindered and remain undetected. Thermosonic techniques are used to counteract this disadvantage. In these techniques, the component is vibrated, causing the cracked surfaces to rub against each other. The generated frictional heat is then detected using a thermal imaging camera. In general, various excitation techniques are available, some of which excite the test components so strongly that the components or the TBC becomes damaged [14–17]. However, in contactless excitation techniques, the energy input into the component may be insufficient [18]. Currently, a large body research is concerned with the detection of cracks and the distribution of heat in components. However, up till now, the given parameters, such as the temperature increase as a function of the frequency and the energy supply of excitation, have not been considered. Therefore, these investigations represent the second pillar of this research work.

1.2 Research Aim and Objectives

The aim of this research work is to propose novel improved NDT&E and SHM methods based on modulated nonlinear ultrasonic wave propagation techniques and ultrasonically stimulated thermography for the structural integrity assessment of gas turbines. To improve the sensitivity and accuracy of the detection and localisation of structural damage on turbine blades, the nonlinear ultrasound techniques were further developed. To this end, the objectives are defined in relation to the research background discussed in the previous chapter. The main objectives of this work are summarised below:

- **Nonlinear ultrasound:**
  - To identify novel nonlinearity parameters in multi-frequency excitation and evaluate the levels of accuracy and reliability compared to single-frequency excitation
  - To conduct a combined numerical and experimental campaign to detect failures in materials on the basis of the developed analytical concepts
  - To perform a metallurgical analysis of the Hastelloy X material with creep damage and failure detection using ultrasonic modulation techniques
- **Ultrasonically stimulated thermography:**
  - To design an experimental setup for the detection of cracks in turbine blades without damaging the turbine blades or the TBC
  - To examine turbine blades with cracks using vibrothermography by measuring the frequency-dependent temperature increase
  - To design an experimental setup for examining preloads in the crack area
  - To perform various numerical simulations to reproduce the experimental part and understand the behaviour of cracks during excitation in order to optimise the experimental setup and accuracy

1.3 Thesis Outline

This thesis follows an alternative thesis format (by publications). Accordingly, peer-reviewed journal papers are integrated as chapters and listed in Table 3, and the conference attended is highlighted in Table 4 (for reference only).

Chapter 2 provides an overview of the literature and the theoretical background in relation to this research work. Ultrasonic and vibrothermography testing methods are presented in detail for the detection of failures. In addition, an overview of the current state of the literature is provided to highlight the current limitations and challenges in relation to the detection and localisation of material changes, such as creep and crack formation. The accepted manuscripts are presented in Chapters 3–7. Each chapter begins with a summary of the scope, methodology and results of the publication presented.

Chapter 3 provides an overview, in the form of a review, of the various failure modes in gas turbine components. It also presents and assesses the possible techniques for detecting these failures.

Chapter 4 describes the analytical derivation of two superimposed frequencies up to the third order of nonlinearity. It also offers a numerical and experimental proof of the newly derived nonlinearity parameters for crack detection.

In Chapter 5, the previously determined analytical model is extended to four fundamental frequencies. The newly developed grouping concept combines several harmonic frequencies and sidebands at certain frequencies. Therefore, higher signal energies are provided at these specific frequencies, thus offering a higher possibility of crack detection and crack size estimation. In this study, excitation with one frequency, excitation with two frequencies and excitation with four frequencies were all compared.

Chapter 6 describes the evaluation of creep samples, wherein metallurgical results were evaluated with reflected light and scanning electron microscopy. Nonlinear ultrasonic modulation was also used to evaluate the determined nonlinearity parameters and compare them to the metallurgical results.

Chapter 7 discusses the second research focus, ultrasonically stimulated thermography. Turbine blades with cracks at different positions on the trailing edges were examined using a new test setup concept. A piezo actuator was used to excite the blades up to 100 kHz. Then, the increase observed in temperature was evaluated as a function of the excitation frequency and the voltage supplied to the actuator in order to investigate the preloads in the crack area. Finally, a developed finite element model was used to simulate the dynamic behaviour of cracks and the increase in temperature.

Finally, Chapter 8 outlines the conclusions of this study and the recommendations for future work.

Table 3. Peer-reviewed journal papers.

Chapter	Publication Details (Reference)
3	Mevissen, F., & Meo, M. (2019). A review of NDT/structural health monitoring techniques for hot gas components in gas turbines. *Sensors*, *19*(3), 711. https://doi.org/10.3390/s19030711
4	Mevissen, F., & Meo, M. (2020). A nonlinear ultrasonic modulation method for crack detection in turbine blades. *Aerospace*, *7*(6), 72. https://doi.org/10.3390/aerospace7060072
5	Mevissen, F., & Meo, M. (2021). Nonlinear ultrasound crack detection with multi-frequency excitation—a comparison. *Sensors*, *21*(16), 5368. https://doi.org/10.3390/s21165368
6	Mevissen, F., & Meo, M. (2022). Creep detection of Hastelloy X material for gas turbine components with nonlinear ultrasonic frequency modulation. *Materials Characterization*, *191*, 112099. https://doi.org/10.1016/j.matchar.2022.112099
7	Mevissen, F., & Meo, M. (2022). Ultrasonically stimulated thermography for crack detection of turbine blades. *Infrared Physics & Technology*, *122*, 104061. https://doi.org/10.1016/j.infrared.2022.104061

Table 4. Conference paper.

	Publication Details (Reference)
	Mevissen, F., & Meo, M. (2019, September 10–12). *Detection of cracks in turbine blades with nonlinear ultrasonic frequency modulation* [Paper presentation]. IWSHM 2019, Stanford, CA, United States. https://doi.org/10.12783/shm2019/32192

2 LITERATURE REVIEW

This chapter provides an overview of the current state of research in relation to this study. It focusses on the use of nonlinear ultrasound techniques and ultrasonically stimulated thermography in evaluating failures in hot-gas-leading components in gas turbines. Notably, the overview offered in this chapter can be combined with the introductory chapters of the published works (Chapters 3–7) to obtain a broader and more detailed idea of the academic arguments. This can help bridge the gaps identified and make an original contribution to knowledge.

Chapter 2.1 provides an overview of the use of linear ultrasonic techniques in component testing. Then, Chapter 2.2 describes the nonlinear ultrasonic testing techniques related to this work. It also outlines how the nonlinear properties of ultrasonic waves are used efficiently for component testing and highlights the advantages of nonlinear over linear technologies. Chapter 2.2.1 describes the detection of cracks with a particular focus on the opening and closing of cracks with the corresponding nonlinear response. Since this study mainly focusses on frequency modulation techniques, Section 2.2.2 outlines how failures are detected in components with superimposed waves. In general, the initiation of plastic deformation is considered an important indicator of the service life of gas turbine components. An overview of the current state of research is provided in Chapter 2.2.3. Creep is one of the main problems for the high loaded gas turbine components, and it can ultimately lead to component failure. An overview of the recent literature on nonlinear ultrasonic technologies, primarily in the context of gas turbine components, is provided in Chapter 2.2.4. Overall, ultrasonically stimulated thermography is intended to overcome the disadvantages of nonlinear ultrasound technologies in the case of closed cracks. Chapter 2.3 highlights the current state of research in which cracks are vibrated to detect the resulting frictional heat with a thermal imaging camera.

2.1 Linear Ultrasound

For many years, linear ultrasonic techniques have been used to detect material failures, with the speed of sound, attenuation, transmission and reflection coefficient used as failure indicators [19–22]. Generally, the phase and amplitude of the received signal change when the signal passes through failures in the material, whereas the frequency of the transmitted signal remains the same compared to the received signal [23].

To inspect a material, it is important to distinguish between the pulse-echo (PE) method and the through-transmission ultrasonic (TTU) technique. In the PE method, one sensor is used to send and receive ultrasonic waves. When the wave passes a crack or an imperfection in the material, part of it is reflected back, and the signal generated can be evaluated [24]. In the TTU technique, on the other hand, two sensors are used instead of one, which is particularly suitable for inspecting materials with several layers [25, 26].

Linear techniques exhibit equivalent behaviour on the stress–strain diagram through the relationship $\sigma_{us} = E\frac{\partial u_x}{\partial x}$, where σ_{us} is the applied stress due to the periodic ultrasonic pulse, E is Young's modulus, u_x is the displacement and x is the wave propagation distance for the one-dimensional case.

Generally, various wave types are used to detect cracks and estimate their sizes. Besides longitudinal waves, the most relevant wave types used for gas turbine applications are Rayleigh waves and Lamb waves [27–33]. In Rayleigh waves, which are also often called surface acoustic waves (SAWs), longitudinal and shear components propagate at the same speed near the surface of the material. The disadvantage of Rayleigh waves is that waves with high frequencies do not penetrate as deeply into the material as low-frequency waves, where the penetration depth is approximately equal to one wavelength [34]. In contrast, waves with high frequencies are useful in detecting microcracks [35]. This wave type is very useful for NDT&E in gas turbines, since cracks in these components mainly occur on the surface as a result of the high temperature gradients [36]. Because the phase velocity of SAWs depends on the elasticity tensor of the material, this wave type is used to determine the elastic properties of the components and the coatings itself. Even small changes in the phase velocity allow conclusions regarding the density, Young's modulus or Poisson's ratio [37].

Lamb waves are elastic waves in which displacement occurs both in the direction of wave propagation (longitudinal) and perpendicular (transverse) to it. Lamb waves are dispersive, meaning that the wave propagation velocity *c* depends on the frequency and on the elastic constants and density of the material, resulting in mixed pressure and shear waves [38]. Lamb waves are particularly interesting for the detection of damage, because they can propagate over long distances [27, 39]. Since these waves have different wavelengths and propagation speeds, they interact differently in response to small disturbances due to damage [40]. In general, Lamb waves propagate with the symmetric mode S_0 and the fundamental antisymmetric mode A_0, with other vibration modes occurring as well (symmetric Lamb waves [S_0, S_1, S_2, …] and antisymmetric Lamb waves [A_0, A_1, A_2, …]). Therefore, dispersion curves are used to map the relationship between wave speed and frequency. Exemplary dispersion diagrams for the phase velocity and group velocity are shown in Figures 1a and 1b for the Inconel 718 material, which is often used in the hot-gas area of gas turbines.

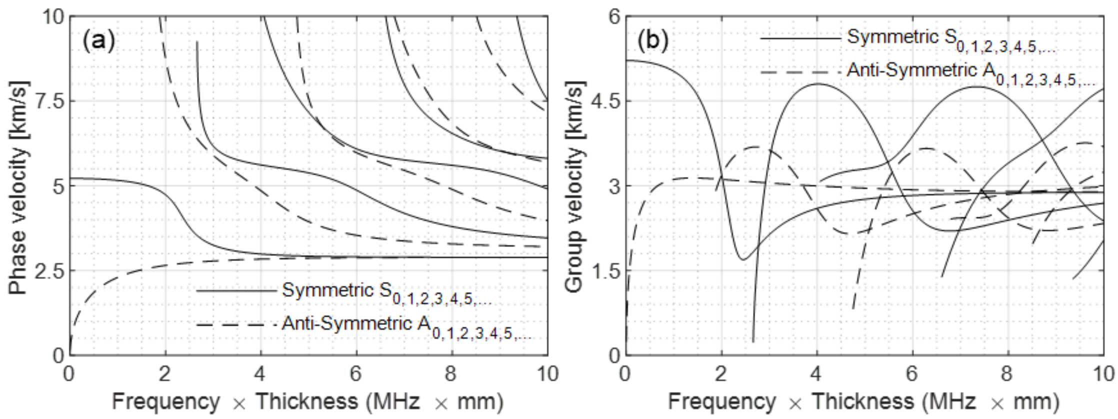

Figure 1. Dispersion Curve Inconel 718: (a) phase velocity; (b) group velocity.

With SHM in the turbine area of gas turbines, the challenge is to develop sensors that can handle high temperatures and the coupling of the test object to them. Therefore, studies were performed on sensor materials such as $La_2Ti_2O_7$ (lanthanum titanate) and La_2Ti_2O (lanthanum niobate), which can be used at high temperatures reaching up to 1000 °C [11–13]. Notably, the influence of temperature on the physical properties and ultimately on the measurement results was examined in [41].

Ceramic insulation layers are often applied to the components in the hot-gas area to lower the material's temperature. In this context, a TBC is usually used, which consists of four layers (Figure 2). Starting from the bottom, these layers are the metal substrate, a metallic bond coat, a thermally grown oxide (TGO) and a ceramic topcoat [42–47]. Particularly, the erosion wear of this coating was evaluated using linear ultrasound techniques in [48–56].

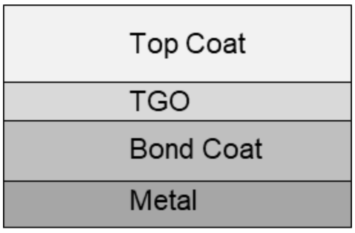

Figure 2. Layers TBC.

To overcome the temperature problem, acoustic waveguides (AWGs) are used to monitor the condition of coated gas turbine vanes, which transmit acoustic waves into the components [57]. One indicator that signals the need for maintenance of the turbine blade is a change in the amplitude and speed of the sound wave, which changes as the coating wears down. For instance, the wave speed is approximately 2500 m/s in the case of an intact coating and approximately 5000 m/s in the case of a completely worn coating [57]. When the waves enter the AWGs, they are converted into longitudinal waves. These AWGs are only 1 mm in diameter and need to withstand the extreme conditions encountered when the gas turbine is operating [58]. This technology was also used in gas turbines for testing purposes [59]. In their study, Atkinson and Hayward described the transition from AWGs to guide vanes and investigated whether it is possible to examine the acoustic entry signal generated by the rotating blades [60]. Therefore, the acoustic signals caused by the pulsating gas pressure were evaluated using AWGs [61], and condition monitoring was also performed successfully with AWGs for other hot-gas applications [62–65].

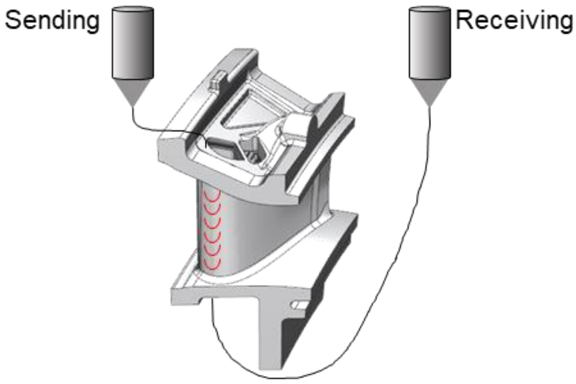

Figure 3. Scheme of acoustic waveguides.

Another possibility is the generation of ultrasonic waves with laser ultrasound. In this method, an ultrasonic wave is transmitted with light. When pulsed light from a laser hits the surface of a material, it becomes absorbed on the surface, generates heat and thermal strain and ultimately emits ultrasonic waves. These waves are independent of the angle of the laser and propagate perpendicularly to the sample surface [66]. The acoustic waves can then be received with piezoelectric transducers (PZTs), electromagnetic acoustic transducers (EMATs) or laser interferometers. In this context, the decisive advantage is the contactless excitation, which works with complex-shaped components, such as turbine blades, because the surfaces of the sensitive components are protected. The disadvantage is, however, the low SNR [67, 68], although in [36, 69, 70] cracks were successfully detected using this technique.

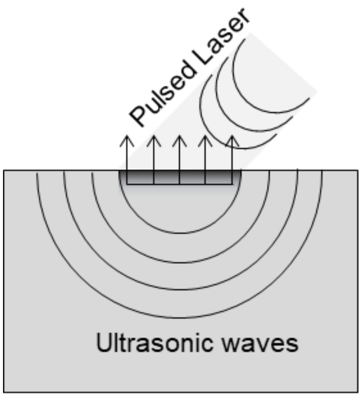

Figure 4. Scheme of laser ultrasound.

Notably, the EMAT technology also works with no contact with the samples. In this technology, an alternating current is fed into the induction coil of a sensor, generating electromagnetic oscillations, which in turn induce eddy currents on the surface of the test object. As a result of the interaction of eddy currents and the permanent magnetic field of the sensor, the Lorentz force generates ultrasonic waves directly on the surface of the test object. Indeed, when Rayleigh waves were used to detect cracks, different wave types were generated [71–74]. Therefore, the basic requirement for a successful measurement is that the sample is either electrically conductive or has favourable magnetic properties [74].

2.2 Nonlinear Ultrasound

If an emitted sinusoidal ultrasonic wave hits a flaw in an isotropic material, the initial wave is disturbed and harmonic waveforms are generated [75–77]. These harmonic frequencies are generated as a result of the lattice anharmonicity (intrinsic nonlinearity), dislocations (microstructural changes) and cracks [78].

After the amplitudes of these frequencies are measured and compared to the fundamental frequencies, these values are used as an indicator for the detection of material changes [77]. In this context, the one-dimensional nonlinear Hooke's law can be described as a power series as follows:

$$\sigma_{us} = E\frac{\partial u_x}{\partial x} + \beta\frac{E}{2}\left(\frac{\partial u_x}{\partial x}\right)^2 + \gamma\frac{E}{6}\left(\frac{\partial u_x}{\partial x}\right)^3 + \cdots, \qquad (1)$$

where β and γ are the nonlinearity parameters of the second and third order, respectively [79, 80]. However, it is worth noting that linear ultrasound techniques are usually limited in terms of failure detection, whereas nonlinear ultrasound techniques have higher detection rates for early-stage material defects [77, 81].

2.2.1 Crack Detection

In general, nonlinear ultrasound techniques are useful in the detection of cracks in materials [82–84]. To obtain a successful measurement, it is important to know whether the crack is open or closed. In the case of open cracks, the depth of the crack can be estimated using nonlinear ultrasound techniques, wherein the ultrasonic waves become strongly scattered when they come into contact with the crack. However, because of the residual compressive stresses in closed cracks or because of the oxide layers produced on the crack surfaces, it may be difficult to identify failures, as the ultrasonic waves simply penetrate through closed cracks [85]. Figure 5a shows a schematic of how harmonic frequencies are formed at the contact points of the crack asperities of open cracks and how these waves are not influenced by closed cracks, as in Figure 5b.

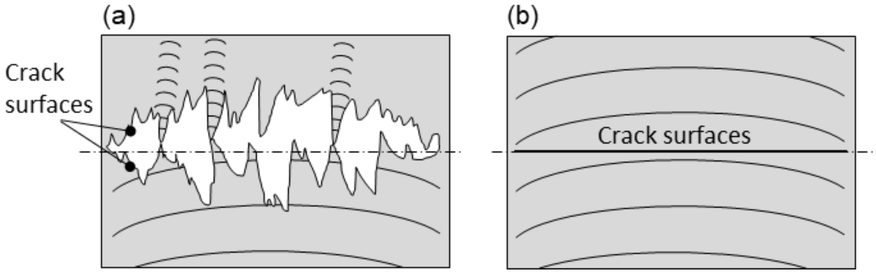

Figure 5. Crack: (a) open; (b) closed.

Contact acoustic nonlinearity (CAN) is a research area that focusses on the excitation of cracks, the interaction of crack surfaces and the evaluation of acoustic signals [82]. Solodov et al. showed that, with CAN, subharmonics and higher harmonics show a dynamic threshold behaviour, as well as hysteresis and instability effects [86]. Moreover, the lengths of closed cracks were detected using subharmonic frequencies [87–89]. Notably, the presented techniques are only successful if the crack dynamics of closed cracks are changed by the excitation of the ultrasonic waves or by a change in temperature [85].

Yamanaka et al. used the equation of motion with linearly damped vibrations as the basis for the analytical modelling of open and closed cracks. In their study, the subharmonics generated by ultrasound excitation at partially closed cracks exhibited a high potential for crack detection compared to superharmonic frequencies [90–92]. The second-harmonic frequency was also used to estimate the lengths of closed cracks [93]. Moreover, the acoustic effect was examined in [94–98], mainly with the second-harmonic frequency between the contact surfaces of a crack. Furthermore, an analysis of the interface between rough surfaces in elastoplastic contact was presented with ultrasonic wave interactions at closed cracks [99, 100], and new elastic constants were introduced to describe the nonlinear behaviour of the cracks [101].

Moreover, a model was developed to analyse vertical closed cracks with the finite difference time domain (FDTD) technique [102–105]. Viscous damping parameters were used to simulate residual compressive stresses on closed crack surfaces. Generally, the FDTD is a grid-based differential, numerical modelling concept that uses the time domain method. This allows a wide frequency band to be evaluated, in which nonlinear material properties are considered. With FDTD, longitudinal and shear waves associated with the detection of closed cracks were examined in numerical simulations [106].

2.2.2 Frequency Modulation

This section illustrates the literature overview and advantages of frequency modulation. In general, different fundamental frequencies interact with each other when passing failures, and they generate harmonic frequencies and mutually dependent sidebands, with certain nonlinearity parameters used for evaluation. The following shows how these parameters have evolved.

To assess materials with nonlinearity parameters, a method that compares the amplitudes of the harmonic frequency to the fundamental frequency of a received signal was developed [107–111]. In this context, the value obtained from considering the second-harmonic frequency in relation to the fundamental frequency is referred to as the second-harmonic nonlinearity parameter (β). The basis for this derivation is provided by the following one-dimensional wave equation:

$$\rho \frac{\partial^2 u(x,t)}{\partial t^2} = \frac{\partial \sigma_{us}}{\partial x}, \tag{2}$$

where ρ is the mass density and $u(x,t)$ represents the displacement, which is solved with the nonlinear stress definition in Equation (1) and sine wave excitation. The following equation shows the solution with the mutual amplitude dependence [112]:

$$\beta = \frac{8A_2}{A_1^2 k_{f1}^2 x}, \tag{3}$$

where A_2 is the amplitude of the second-harmonic frequency, A_1 is the amplitude of the fundamental frequency, k_{f1} is the wavenumber of the fundamental frequency and x is the wave propagation distance. With an assumed constant wavenumber and wave propagation distance, the relationship $\beta \propto \frac{A_2}{A_1^2}$ can be used for evaluation. Figure 6 shows an example of a frequency spectrum used for evaluation.

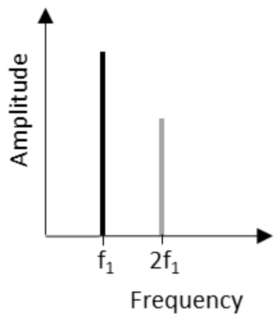

Figure 6. Frequency spectrum of a second-harmonic frequency.

This technique was also used to evaluate geomaterials [113] and further developed for third-order nonlinearity [80]. With one fundamental frequency, the third-harmonic frequency, along with its nonlinearity parameter (γ), is used for evaluation besides the second-harmonic frequency:

$$\gamma = \frac{48A_3}{A_1^3 k_{f1}^3 x}, \tag{4}$$

where A_3 is the amplitude of the third-harmonic frequency. Therefore, the ratio $\gamma \propto \frac{A_3}{A_1^3}$ can also be used to evaluate the experimental results (Figure 7).

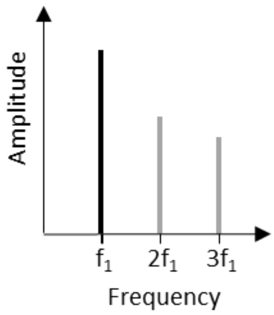

Figure 7. Frequency spectrum of a third-harmonic frequency.

Because of the low received signal energy at higher-harmonic orders, these were not considered further for the evaluation of the nonlinearity parameters [82, 114, 115]. To analytically describe frequency modulation with two frequencies, second-order nonlinearity parameters were derived for two superimposed fundamental frequencies so as to determine the residual fatigue life of the components [79, 116, 117]:

$$\begin{aligned} \beta_{f_2+f_1} &= \frac{4A_{f_2+f_1}}{A_1 A_2 k_{f1} k_{f2} x}, \\ \beta_{f_2-f_1} &= \frac{4A_{f_2-f_1}}{A_1 A_2 k_{f1} k_{f2} x}, \end{aligned} \tag{5}$$

where $\beta_{f_2+f_1}$ is a nonlinearity parameter, $A_{f_2+f_1}$ is the amplitude of the summing sideband (f_2 + f_1), $\beta_{f_2-f_1}$ is a nonlinearity parameter and $A_{f_2-f_1}$ is the amplitude of the difference sideband (f_2 − f_1). Here, $A_{1,2}$ represents the amplitudes and $k_{f1,2}$ represents the wavenumbers of the fundamental frequencies. Figure 8 shows a frequency spectrum with derived harmonic and sideband frequencies, in which the nonlinearity of the third order was not considered [79, 117].

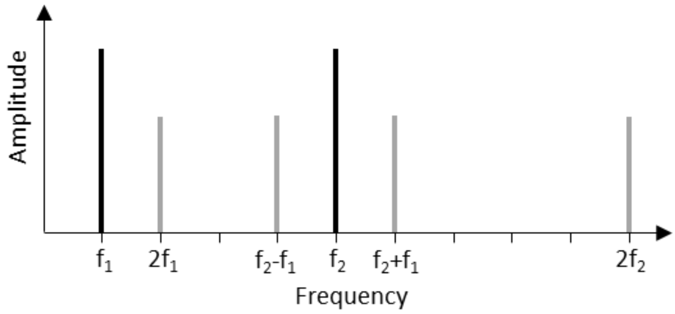

Figure 8. Frequency spectrum of modulation.

It can be clearly observed that the two fundamental frequencies depend on the nonlinearity parameters, which provides additional information for determining cracks and the residual fatigue life of the components [118, 119]. An evaluation was performed by measuring the amplitude of the sideband frequencies and the two fundamental frequencies ($\beta_{f_2+f_1} \propto \frac{A_{f_2+f_1}}{A_1 A_2}$ and $\beta_{f_2-f_1} \propto \frac{A_{f_2-f_1}}{A_1 A_2}$).

Van den Abeele et al. studied the behaviour of the harmonic and modulated response frequencies of two superimposed fundamental frequencies to detect cracks [120]. They also investigated the influence of the amplitude-dependent resonance frequency [121]. High- and low-frequency waves were superimposed to determine damage in materials. This method is called nonlinear elastic wave modulation spectroscopy (NEWMS), and it describes the superposition of these waves [122, 123]. In another study, Pfeiderer et al. investigated the nonlinear dynamic behaviour of cracks with subharmonics, ultra-subharmonics and ultra-frequency pairs [124]. Multi-frequency excitation was successfully used to determine grain size fluctuations and distributions in metal samples [125] and to detect corrosion on aircraft components [126]. A three-frequency phased array technique was used to identify cracks, while a start signal was sent to dynamically stimulate cracks. The sent pump signals of the dual-frequency excitation generated nonlinear frequency modulation, which was used for further evaluations [127].

2.2.3 Material Dislocation

Generally, plastic deformation may result in nonlinearities in materials because of microstructural changes and nonlinear properties, which can provide information regarding the fatigue life of the components [107, 128–131]. During the process of plastic deformation, the superposition of a static load with ultrasonic excitation reduces the flow stress in the component, a phenomenon that was studied in [132–134]. The second-harmonic frequency was also found to exhibit clear strengths in detecting dislocations in materials [135–137], which even made microdamage visible [138–141].

Overall, Lamb waves have been found to yield favourable results when used to detect dislocations in materials. It has also been proven that the nonlinearity parameters of metal plates increase with Lamb waves and that the parameter values propagate linearly with the distance of propagation [142, 143]. Pruell et al. used Lamb waves to classify plasticity [144] and showed that these waves yield favourable outcomes in the detection of thermal ageing [145]. During the process of detecting dislocations in materials, the harmonics of different wave types demonstrated a positive behaviour. Therefore, SAWs were used to detect not only the level of plasticity in aluminium samples [135], but also dislocations due to LCF [146, 147]. In another study, Dutta et al. investigated the acoustoplastic effect through additional stresses in a component or through heating when ultrasonic waves are used for excitation [148].

The first attempt to physically describe the dislocation behaviour of a lattice structure was made by Frank and Reed in 1950, who developed dislocation multiplication to describe sliding within an isotropic material [149]. Hikata et al. expanded the physical dislocation model with constant line tension and combined it with the wave equation to draw conclusions on dislocation with a transmitted ultrasonic signal. The following equation shows the derived dislocation nonlinearity parameter (β_d) as a function of the dislocation parameters and the applied load (σ) in the one-dimensional case [77, 150]:

$$\beta_d \propto \frac{A_2}{A_1^2} \propto \frac{\left(\frac{E_2}{E_1^3}+\frac{12}{5}\frac{\Omega\Lambda L^4 R^3}{\mu^3 b^2}\sigma\right)k^2 x}{\left(\frac{1}{E_1}+\frac{2}{3}\frac{\Omega\Lambda L^2 R}{\mu}\right)^2}, \tag{6}$$

where Ω is the conversion factor from shear to longitudinal strain, Λ is the dislocation density, L is the length of the dislocation segment, R is the Schmid factor, μ is the shear modulus, b is the Burgers vector, k is the wavenumber, x is the wave propagation distance and E_1 and E_2 are the elastic moduli.

Overall, measuring the amplitudes of the fundamental frequency (A_1) and second-harmonic frequency (A_2) helped experimentally prove the corresponding second-order nonlinearity parameter for the identification of dislocations [77, 150]. In their study, Cantrell [76] and Apple et al. [151] extended the dislocation model to consider the effects of lattice resistance on the dislocations [76, 151]. Moreover, an analytically alternative derivation concept was provided in [152], which energetically considers line stress. In addition, in the case of propagating ultrasound, the behaviour of microstructure defects was examined for acoustic nonlinearities in [153]. In another study, Zhang et al. investigated dislocation lines with various orientations, since the changing acoustic nonlinearities depend on the dislocation line [154, 155]. This was further experimentally proven on stainless-steel samples and martensitic stainless steel [156]. It is also worth noting that if a load acts in different directions, this leads to mixed dislocations due to the local stresses. This in turn leads to a back stress in the tension field [137, 152]. So far, physical dislocation models have been derived with constant line tension. Therefore, the variation of this value has been demonstrated in [157, 158], in which Poisson's ratio was introduced for the first time.

2.2.4 Creep

Creep damage begins when a mechanical load and a temperature load are present at the same time. During this process, an elastic strain first occurs, followed by a primary strain stage. Then, the strain rate increases to a constant creep rate. The secondary stage of creep is characterised by a slow but constant plastic flow of material. In the tertiary stage, more pores are formed and the level of strain increases further until the component fails [159] (Figure 9).

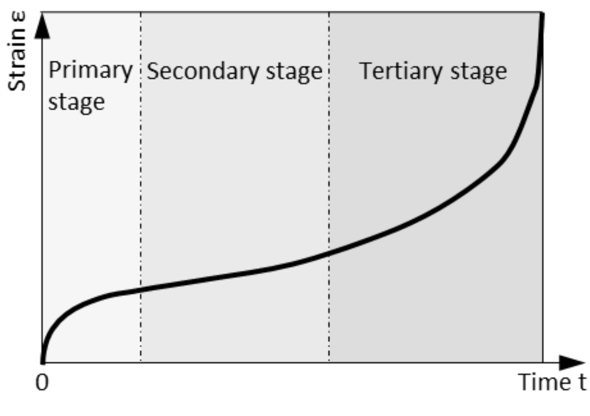

Figure 9. Creep stages.

From a safety viewpoint, predicting the service life of highly stressed components is important not only for gas turbines in general, but also for defining the exact component maintenance required. This is why various physical models have been developed to estimate the service life under creep load [160–164]. For example, the crack growth kinetics of creep damage were examined in [165], and different research efforts were made with numerical methods, allowing precise statements regarding creep behaviour. The Larson–Miller parameter was also used to numerically determine the service life of turbine blades under creep load [166] and to determine the influence of explicitly high temperatures on hot-gas-leading components [162]. Since the blade root is also exposed to extreme loads, as with the blade airfoil [167], finite element simulations were used to simulate the creep behaviour in the fir-tree area of the turbine disc [168].

In general, nonlinear ultrasonic measurement technology showed promising results for the detection of creep damage. For example, Baby et al. used second-harmonic nonlinearity parameters for creep characterisation, as this parameter increases up to a creep fraction life of ~0.6 and then decreases until it breaks [169]. In another study, Balasubramaniam et al. described a new nonlinear ultrasound technique for characterising creep damage [170]. They assessed the nonlinear response of samples at much lower amplitudes than in earlier studies on nonlinear material behaviour. The second-harmonic nonlinearity parameter was also used to detect creep damage on welded steel pipes [171], in which the weld seam does not have higher creep rates than the surrounding material and no increase in the nonlinearity parameters is ascertained. In a further study, the nonlinearity parameter was used to determine creep [172], and this was described as the most sensitive nonlinearity parameter for this application [173].

Creep damage was also detected using Lamb waves. Given the dispersive behaviour of this wave type, Xiang et al. proposed phase synchronisation [174] to make the fundamental frequency and harmonic frequency move with the same phase velocity. The results showed that, with this method, the nonlinearity parameter increased as the creep damage started with the dislocations. Then, more voids were generated and the nonlinearity values decreased as a result of the higher creep load [78, 174]. Combining the excitation of nonlinear Lamb waves with the dislocation model showed that the precipitation–dislocation interaction strongly influences the nonlinearity parameter of the second order [78, 175].

Because of the aggressive atmosphere in the flow channels of gas turbines, together with the creep damage, oxidation usually occurs on the components, which may also lead to component failure [176–178].

2.3 Ultrasonically Stimulated Thermography

Overall, nonlinear ultrasound technology has been found to successfully detect defects in materials, especially cracks. However, if the cracks are closed, then the ultrasonic waves may pass unhindered and, hence, no harmonic frequencies are generated. To solve this issue, besides the CAN technique, an ultrasonically stimulated thermography method was used. With this technique, the components were set to vibrate so that the cracked surfaces rub against each other. Then, the resulting frictional heat was detected using a thermal imaging camera. An overview of the currently used thermographic techniques for NDT&E is provided in [179]. Delamination is a common problem in composites. In laminated composites, the adhesion between the layers often fails first. With vibrothermographic techniques, these internal defects can be made visible [180, 181].

Overall, the statistical methods used to detect cracks in turbine blades have recently gained attention [182], and other postprocessing techniques for thermographic images have also been found to improve crack detection [183–186]. Filter techniques were also used, in which the first image without excitation is used to subtract the following images to visualise the damage more clearly.

Vibrothermographic techniques have been found to be useful in the detection of closed cracks. In this context, the temperature effect of a closed crack was investigated in [187], in addition to the combined dynamic behaviour of open and closed cracks [188]. Moreover, the dissipated frictional energy (P) was set to be proportional to the kinetic energy ($P \propto v^2$), where v is the particle velocity of the crack under all vibration modes. Depending on the excitation frequencies and relevant natural frequencies at the crack area, different vibration modes are obtained (Figure 10). For example, if the crack is open to the outside, then the crack surfaces will rub against each other either by oscillating (Figure 10a) or in a plane in opposite directions (Figure 10b). If both crack surfaces vibrate, then clapping may occur (Figure 10c).

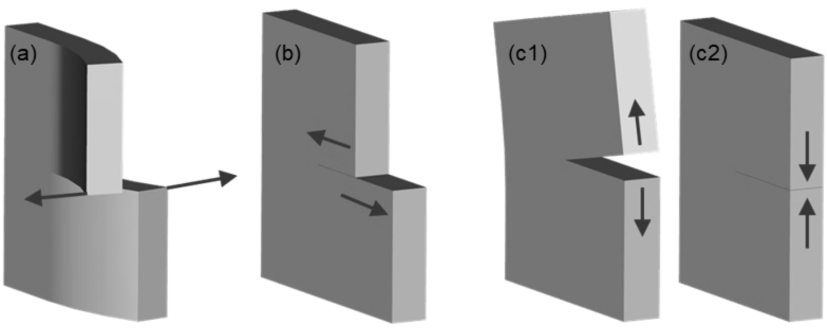

Figure 10. Crack modes: (a) rubbing mode, swing; (b) rubbing mode, in plane; (c) clapping mode.

Analytical procedures consider the dissipated energy of cracks during excitation. For example, the so-called energy and heat index was used to classify cracks using thermosonic infrared [189–191]. In addition, the power loss at the cracks was determined by measuring vibration damping and crack elongation during the process of ultrasonic excitation. Cracks were detected using ultrasound excitation directly on a sample component [192]. The gas turbine parts that are in contact with hot gas are equipped with a TBC, which may result in two problems. First, cracks may form under the TBC without being detected, resulting in an increased risk while the gas turbine is operating. Therefore, Hyde et al. developed and experimentally proved a thermographic detection technique for this purpose [163]. The results showed that the heat increase moved to the crack tips when the cracks opened, and the cracks were detected as completely enclosed by the TBC. Second, parts of the four-layered TBC may come off, which might damage other components while passing through the flow channel. However, the service life of faulty components is reduced because of the higher temperature load on the defective areas. Holland demonstrated the delamination of a TBC with vibrothermal methods [193]. Because of the heat generated at the crack locations, a frequency dependency was demonstrated. In another study, Zang et al. developed a vibrothermographic technique that involves the emission of multiple frequencies to detect cracks on turbine blades [194, 195]. The vibration amplitude was also used as a parameter, combined with alternative attachment of the sample and vibration generator [196]. The best results were achieved with the transmission of different frequencies.

In ultrasonically stimulated thermography, thermal imaging cameras are used on the receiver side. To stimulate the components, various possibilities are provided with corresponding advantages and disadvantages, which are presented below. One of the most popular excitation techniques is the use of sonotrodes, which are also known as ultrasonic horns [169–185]. These horns consist of stacked PZTs, which come into direct contact with the test components when they are excited. Typically, frequencies of 20–40 kHz are transmitted to the components with high energy, creating a quasi-chaotic frequency spectrum [14, 192, 197–203]. This occurs because only single impulses and not periodic signals are transmitted to the components. One disadvantage of this technique, however, is that the high energy input can damage the contact surfaces between the sonotrode and the sample [14–17]. In another study, piezoelectric sensors were also used with component contact for excitation if the signal was amplified accordingly [204–206]. To avoid the disadvantages of sonotrodes, contactless component excitation was studied. Turbine blades were excited with air-coupled transducers (ACTs), and cracks were detected using a thermal imaging camera [18]. Generally, ACTs focus the energy input in the test component at one point. If the sensor position deviates only slightly from the focus on the specimen, then insufficient energy will be conducted into the component and the cracked surfaces will not be excited either [18]. High-frequency loudspeakers were also used without contact to excite components [207, 208].

A very new area of research is the investigation of local defect resonance (LDR). In this area, cracks change the local stiffness, hence changing the resonance behaviour, which is used as a crack indicator [209–218].

3 Failure Modes and Detection Techniques in Gas Turbines

The aim of this study is to develop sensitive and accurate methods for identifying and classifying failures in gas turbine components. To obtain a holistic overview of the failure modes and the currently used and researched detection techniques, a review paper is presented in this chapter, which pursues the following objectives:

- Description of the possible failure modes in gas turbines
- Identification and evaluation of failure detection techniques

This chapter is an extension of the topics presented in Chapter 1.1. Overall, the importance of detecting failures in gas turbine components at an early stage is highlighted, as failures can destroy the entire machine. Even in this extreme case, it is important to ensure that no gas turbine fragments leave the outer casing of the gas turbine, to avoid endangering human life. In addition to this safety aspect, an economic aspect has also been discussed, highlighting how to use such expensive and sensitive components for as long as possible through appropriate component monitoring.

This study also described which failure modes occur in gas turbines, whereby a distinction was made between the different operating modes of gas turbines. If a gas turbine is operated continuously to generate electricity, then the loads on the turbine components are different than if the gas turbine was used as a driving machine, in which the speed varies continuously.

Furthermore, possible techniques for detecting the described failure modes were discussed. Techniques for gap measurement between the rotating blade and the casing, ultrasound techniques and temperature monitoring techniques of components were presented. Traditional measurement techniques, such as vibration measurements and performance monitoring of gas turbines, were also considered. Finally, these techniques are assessed according to the following criteria:

- Applicability to NDT or SHM
- Temperature limit
- Bandwidth, accuracy and sensitivity
- Costs

The form ‘Statement of Authorship’ and the paper are provided on the following pages.

This declaration concerns the article entitled:			
A review of NDT/structural health monitoring techniques for hot gas components in gas turbines			
Publication status			
Draft manuscript ☐ Submitted ☐ Accepted ☐ Published ☒			
Publication details (reference)			
Mevissen, F., & Meo, M. (2019). A review of NDT/structural health monitoring techniques for hot gas components in gas turbines. *Sensors*, *19*(3), 711. https://doi.org/10.3390/s19030711			
Candidate's contribution to the paper (detailed, and also given as a percentage)			
Formulation of ideas: 50% The idea of publishing a review paper was my supervisor's, Professor Michele Meo, and the idea of classifying failure modes and evaluating them was mine.			
Design of methodology: 90% I carried out the literature research and differentiated between the different failure modes and detection techniques and evaluated them. I then discussed the results with my supervisor.			
Experimental work: — Not applicable.			
Presentation of data in journal format: 90% I wrote down the evaluations, defined the structure of the manuscript and created all the figures. Professor Michele Meo provided feedback on the draft and helped with the paper submission and review processes.			
Statement from candidate			
This paper contains original research that I have conducted during the period of my higher degree of research candidature.			
Signed	[redacted]	**Date**	20/10/2022

A review of NDT/structural health monitoring techniques for hot gas components in gas turbines

Frank Mevissen and Michele Meo

Department of Mechanical Engineering, University of Bath, Bath, BA2 7AY, UK

Abstract

The need for non-destructive testing/structural health monitoring (SHM) is becoming increasingly important for gas turbine manufacturers. Incipient cracks have to be detected before catastrophic events occur. With respect to condition-based maintenance, the complex and expensive parts should be used as long as their performance or integrity is not compromised. In this study, the main failure modes of turbines are reported. In particular, we focus on the turbine blades, turbine vanes and the transition ducts of the combustion chambers. The existing monitoring techniques for these components, with their own particular advantages and disadvantages, are summarised in this review. In addition to the vibrational approach, tip timing technology is the most used technique for blade monitoring. Several sensor types are appropriate for the extreme conditions in a gas turbine, but besides tip timing, other technologies are also very promising for future NDT/SHM applications. For static parts, like turbine vanes and the transition ducts of the combustion chambers, different monitoring possibilities are identified and discussed.

1. Introduction

The components of a gas turbine, in direct contact with hot gas, are subject to high loads. These include turbine blades that have to withstand extreme conditions. Monitoring the health of these components is important for two reasons. First, it is important to detect incipient cracks before catastrophic events occur, and second, it is the basis for condition-based maintenance.

Structural health monitoring (SHM) is a further development of non-destructive testing and evaluation (NDT&E). Years ago, it seemed to be sufficient to test components before use or again in a disassembled machine. The vision is moving in the direction of realizing component damage detection in real time. Once the damage occurs, a warning is issued and information about the remaining life of the affected component is displayed. This leads to increased operating safety of the machine and at the same time reduces maintenance costs and time. Therefore, an optimal utilisation of these parts from the customer point of view is highly desirable.

An exemplary SHM system consists of many components. Transducers are needed for actuation and sensing. A signal generator supplies the actuator with diagnostic input while the sensor carries the measured data to the data acquisition system. A NDT/SHM system requires appropriate transducers, its signal processing system to reduce noise, consider environmental conditions and write down the damage signature. In order to implement this practically, knowledge of typical damage experienced by the structures are required. This can be a physical model of the structure, a statistical model or machine learning schemes [1]. Proulx published a book on SHM of rotating machines focused on vibration methods [2]. In [3–5] new sensor technologies and trends in SHM are reported.

This review summarises the different failure modes, which are relevant for NDT/SHM in industrial gas turbines and currently used monitoring technologies. In particular, critical defects are discussed and how to determine the remaining useful life of the turbine components. For the component load it makes a big difference whether the machine is started up once and stays in this state for a long time or whether permanent load changes take place. Depending on these operating modes, the life limiting factors for the highly loaded turbine components are shown.

Furthermore it is indicated, which consequences small cracks on turbine blades can have. The subsequent turbine stages up to the entire machine can be severely damaged. A challenge is certainly the massive, forged turbine discs where the blades are mounted. For example, at overspeed, it must be ensured that the centrifugal force always bursts the blades first before the discs do. Only in this way can it be ensured that no rotor components break through the outer casing of the gas turbine.

We also review the different monitoring techniques for gas turbine blades, vanes and combustion chamber transition ducts (Figure 1). For the static parts (vanes and transition ducts), the same monitoring techniques could be used.

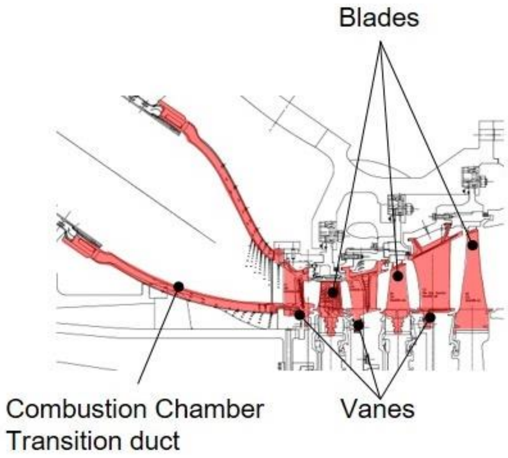

Figure 1. Gas turbine–Combustion chamber transition duct, turbine vanes and blades.

Strain gauges were used to obtain information about the components during machine operation. However, these have some significant disadvantages. With the tip timing method, sensors are placed opposite the rotating blades in the casing. These can usually determine both the important gap between blade and casing and the dynamic behaviour of the blades in-situ. To implement this technically, there are a number of sensor technologies, which are presented in more detail. This principle is already well established in turbomachinery, but there are some promising alternatives that are based on very different concepts. These monitoring techniques can set the course for a shift away from scheduled-based maintenance.

The physics of the different techniques are described in this review. Also the accuracy, the sensitivity and the bandwidth of the sensors are explained. Due to the limited installation space in the turbine area, the sizes of the sensors are also important and are evaluated. A particular challenge is the high ambient temperature, in which the sensors must work. The limits are shown below. Qualitatively the sensor costs are also evaluated. The hot gas components, in particular, have complex designs and are expensive. The great competition and price pressure in this business segment makes it necessary to offer cost-optimized series machines and signal processing units. Relevant research examples with the general areas of application are shown.

2. Failure modes

Continuous duty machines are typically applied in power generation. Therefore, an electric generator will be driven at a relatively constant speed.

Cyclic duty means mechanical drive applications where a gas turbine drives another turbomachine (e.g., a compressor). The speed of the gas turbine is adjusted to requirements of the driven unit. Due to this different operating behaviour, different failure modes can occur. The typical failure modes for hot gas parts in a gas turbine in continuous duty and cyclic duty machines are listed in Table 1 [6–8].

Table 1. Typical failure modes for hot gas components inside a gas turbine.

Continuous Duty	Cyclic Duty
Rupture	TMF
Creep deflection	Low- and High-cycle fatigue
Low- and High-cycle fatigue	Rubbing/wear
Oxidation	Foreign object damage
Erosion	Combined failure mechanism (creep/fatigue, corrosion/fatigue, oxidation/erosion and so on)
Corrosion	
Rubbing/wear	
Foreign object damage	
Combined failure mechanism (creep/fatigue, corrosion/fatigue, oxidation/erosion and so on)	

For peaking machines, thermal mechanical fatigue (TMF) is the main life limiting failure mode. For continuous duty machines, creep, oxidation and corrosion are the main life limiters [7].

Low-cycle and high-cycle fatigue are primary influenced by design issues, while foreign object damage and corrosion are load and environment dependent [9].

One typical failure mode for the transition ducts of combustion chambers is wear at the mating surfaces. High temperature gradients, especially at transient operating conditions, allow the parts to rub against each other. Another failure mode is the degradation of the thermal barrier coating (TBC) in the combustion chambers [7]. A missing or degraded coating will lead to overheating of the combustion chamber components. In Figure 2 the typical construction of a single-shaft gas turbine is shown. The air is led via the inlet housing in the compressor section and compressed. In the combustion chambers, the air is heated to 1200 °C. In the turbine section, the hot gas expands and leads to highly loaded hot gas components. Part of the energy is needed to drive the compressor; the other part is fed into the electric generator for power generation.

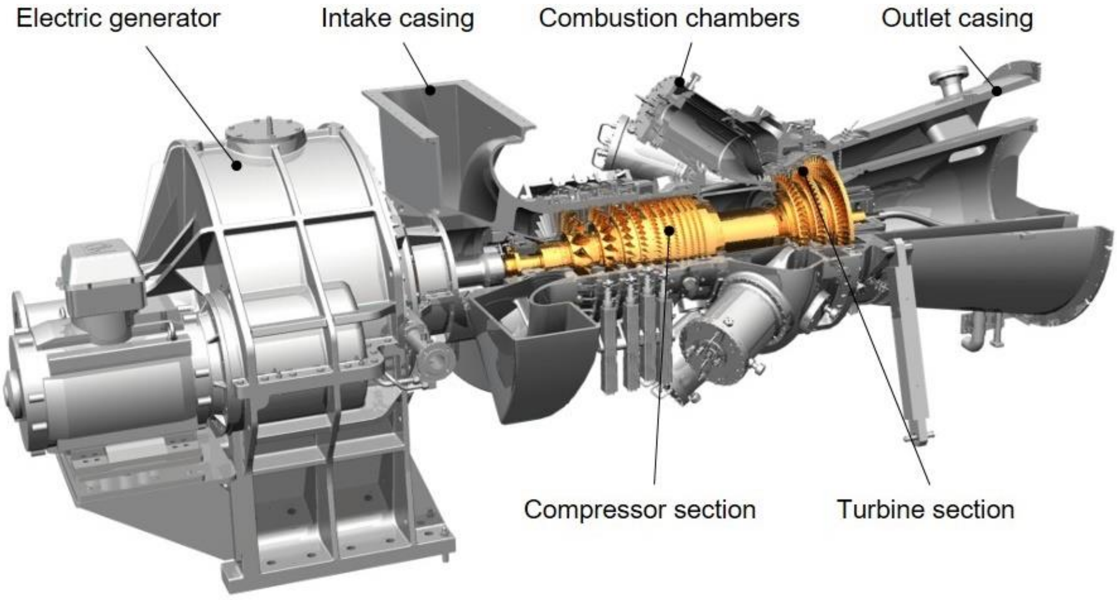

Figure 2. Typical gas turbine construction.

The overheated turbine vanes are shown in Figure 3 and Figure 4. In Figure 5, an incipient tear in a turbine blade is illustrated, while in Figure 6, cracked turbine blades are displayed.

Figure 3. Overheated turbine vane.

Figure 4. Overheated turbine vane inside machine.

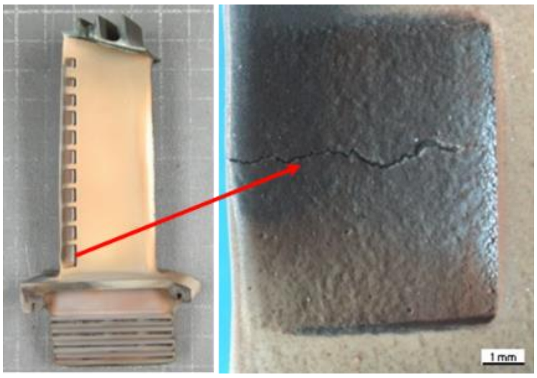

Figure 5. Tear in turbine blade.

Figure 6. Cracked turbine blades.

Examples of failures in turbine blades in military jet engines with the failures analysis are reported in [10–12].

3. Hot gas component monitoring

Historically, a common principle to detect vibration and frequencies in rotating blades is with the use of strain gauges. The application of strain gauges is very complex and not every blade can be equipped with these sensors. Furthermore, they are not suitable for long-term operation. Nowadays, several technical alternatives exist with different advantages and disadvantages.

In [13] a historical summary of the use of strain gauges is reported. Kestner et al. studied the correlations between different installed sensor types on blade vibrations. The authors used acoustic pressure, bearing vibration, tip timing and gas path measurement from an operating machine [14].

Guo et al. developed a new method to identify engine order, amplitude, natural frequency and damping coefficients of the blades using three casing mounted sensors [15].

3.1. Tip timing method

The tip timing method allows for the possibility of measuring, in-situ, the dynamic behaviour of a turbine blade. The radial clearance between the sensor and blade tip can be measured and also the lateral movement of the blade tip. Additional information like time of arrival can be evaluated (Equation (1)), which gives information about blade vibrations:

$$d_i = \frac{2\pi r}{T} \cdot \Delta t_i, \tag{1}$$

where d_i is the deflection of blade i, r is the turbine radius, T is the period for one revolution and Δt_i is the difference between theoretical and practical time of arrival for blade i. In Figure 7 the design of a typical tip timing system is outlined.

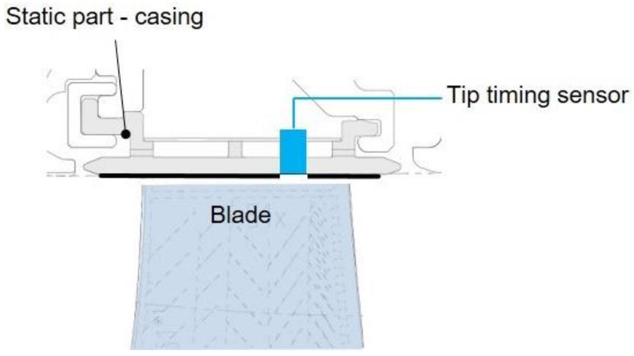

Figure 7. Design of a tip timing system.

One general problem is that the circumference clearances could differ because of the ovalisation of the casing [16].

A significant challenge is the small changes in position of the blades during an engine starting and stopping. This is because a small clearance exists between the fir-tree of the turbine blade and the turbine disc. Therefore, the mechanical repeatability is not high [16]. The blade tips of gas turbine blades, often have a complex geometry, which could be problematic for failure detection with some tip timing sensors [17, 18]. Figure 8 shows the tip geometry of a typical turbine blade.

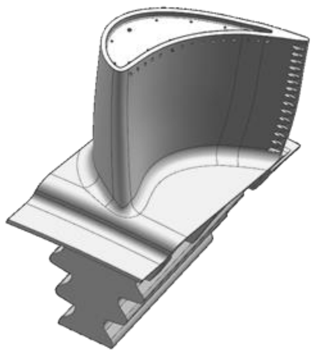

Figure 8. Turbine blade.

With the tip timing monitoring technologies, the following failure modes could be detected:

- Crack detection
- Creep deflection
- Rubbing/wear

Witos et al. showed a theoretical approach for health monitoring of compressor blades. With the tip timing method they tried to answer why a blade cracked and with the metal magnetic memory method the localisation of the crack position was determined

[19, 20]. Rokicki et al. analysed bearing failures of a jet engine with tip timing. Experiments with damaged and working bearings were compared [21]. Tamura et al. focused on non-contact vibration measurement in gas turbines and different sensor technologies were used [22]. Dimitriadis et al. developed a mathematical model to simulate blade tip timing tests [23]. Gallego-Garrido et al. compared different analysis methods for tip timing data [24, 25]. The uncertainties of blade tip timing were studied by Russhard [26] and Satish et al. [27].

3.1.1. Microwave probes

Microwaves can be used to measure tip clearance. Microwaves are electromagnetic waves that propagate in the GHz range. A typical microwave tip clearance probe includes the transmittance and a receiving antenna. The microwave sensor sends a continuous microwave signal to the target and measures the reflected signal. This signal is then compared with an existing reference signal and the phase difference with the distance to the blade. The phase differences of the reflected signal are directly proportional to the distance between the sensor and the target [28]. The whole system is shown in Figure 9.

A typical transmitted signal is:

$$X_0 = A_s \cos(\omega_s t + \varphi_0). \tag{2}$$

The received signal is:

$$Y = A(t)\cos\big(\omega_s t + \varphi_0 + \varphi_l + \varphi(t)\big) + A_r \cos(\omega_s t + \varphi_l), \tag{3}$$

where φ_l is the summed phase in the transmission path and $\varphi(t)$ is the phase difference caused by the change in the tip clearance. The term $A_r \cos(\omega_s t + \varphi_l)$ is the reflected signal from the sensor itself. This should be removed later in the signal processing [29]. Temperature factors of phase φ_l can be obtained by setting the frequency outside the sensor bandwidth. Thus the tip clearance can be determined from $\varphi(t)$ after the calibration.

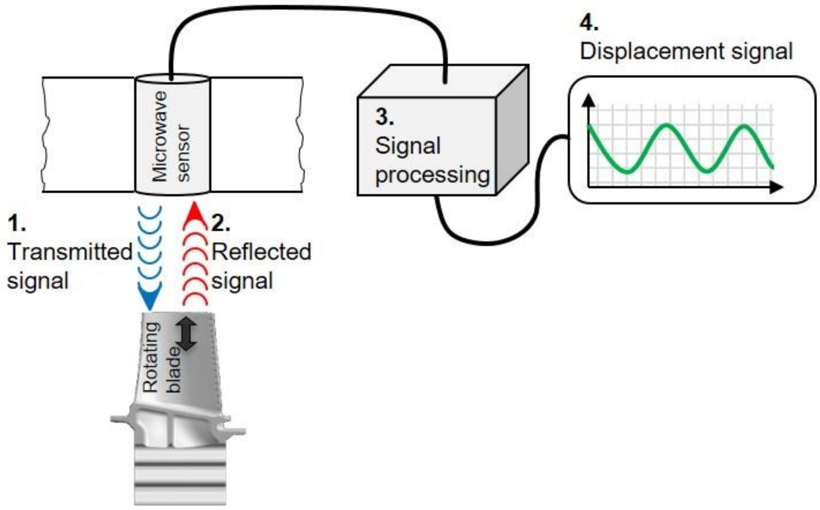

Figure 9. Microwave tip timing system.

The blade damage will be detected by measuring dimensional changes reflected in the blade tip clearance [16]. These sensors have a large bandwidth and are able to operate at high temperatures [29, 30]. Practically, it was shown that a temperature of 900 °C is feasible [31, 32]. Furthermore, the temperature influence was tested, and high temperature measurements are possible [30]. One challenge is the change of phase with temperature, which can be correlated [16]. A validation with optic tip timing systems showed that microwave tip timing systems achieve good accuracy [16, 29]. Some failure can develop over a long period of time [29], so accurate sensors are essential. Repeatability errors are caused by [16]:

- Drifts in electronic component
- Sensor material (change due to temperature effect)
- Contamination of the probe

Compared to eddy current (EC) probes, microwave sensors have a superior resolution and measurement range [30]. Typically the sensors have an outer diameter between 8.5 and 10 mm [17, 31]. Many types of damage show just a small change in tip clearance, for example, blade root cracking is around 0.025–0.1 mm (small crack). A sensor for this application needs a sensitivity of at least 0.05 mm, and test conducted showed sensor sensitivities of 0.025 mm [16]. Violetti et al. showed that these sensors are suitable for long-term use [30].

Microwave sensors are a technology that requires further investigation. In particular, the calibration techniques are not fully developed [33]. The distortion of asymmetric turbine casing can be caught with more probes. Typical 4–8 sensors are used [16].

The first application in a gas turbine was reported by Wagner et al. in 1998. For pilot tests a 65 MW gas turbine were used [34]. Zhang et al. proved experimentally the general feasibility of blade tip timing with microwave sensors [29]. Woike et al. especially focused on the turbine blades. 5.8 GHz and 24 GHz sensors were used, to measure successfully the blade tip clearance [33]. Hafner et al. investigated the possibility for online tip clearance measurement with microwave sensors and the immediate visualisation of the results [35]. In field machines no applications of microwave sensors were found. For SHM, this monitoring technology is very promising.

3.1.2. Optical sensors

A laser Doppler vibrometer (LDV) is a measuring device to determine the vibration frequency and vibration amplitude where, the laser is focused on the surface to be measured. Due to the doppler effect, the frequency of the backscattered laser light shifts as the surface to be measured moves.

If the wavelength of the light is superimposed on that of the vibrating object, the following result is obtained for a 180° scattering angle:

$$\Delta f_D = f_L - f_O, \tag{4}$$

$$\Delta f_D = \frac{2V}{\lambda}, \tag{5}$$

where Δf_D is the resulting frequency, f_L is the frequency of the light, f_0 is the frequency and V is the velocity of the vibrating object.

In Figure 10, the basic structure of an LDV system is outlined. The reference beam does not leave the LDV. It is directed via a bragg cell onto the photodetector, where it interferes with the reflected measuring beam. The bragg cell is an acousto-optic modulator and shifts the frequency of the reference beam. The result is a frequency-modulated voltage, which is directly proportional to the speed of the measured object. Using fast Fourier transform (FFT), the measurement results can be further analysed.

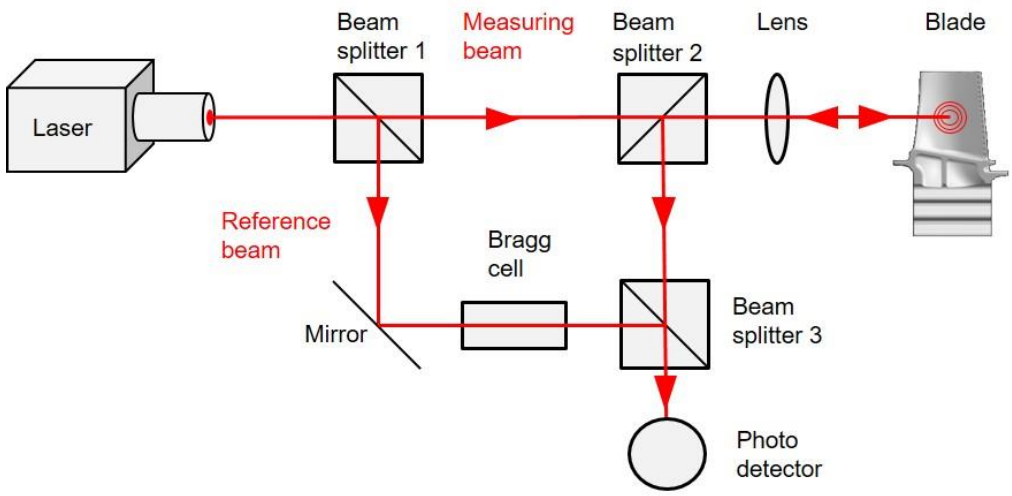

Figure 10. Principle sketch of a laser doppler vibrometer system.

Laser Doppler vibrometers (LDVs) are non-contact vibration measurement instruments. They can also be used for tip timing.

A scanning LDV (SLDV) allows for scanning of whole surfaces. This technology has high sensitivity, even when the sensor is not placed directly on the blade [36]. Optical sensors have good time accuracy and are small sized with a large bandwidth [29, 37]. They have an excellent lateral and spatial resolution, a fast response and are often used because of their reliability and repeatability [38]. SLDVs are a good solution to detecting the dynamic shapes of a structure [39].

Recent studies have shown that optical fibre probes are suitable for development testing [40]. However, outside the laboratory, debris and low tolerances make their application difficult [17, 38, 41]. The reported shading problems are disadvantageous [42], as are the optical waveguides with limited operating temperatures and the required inspection window to the blade tip that may be polluted within a short period of time. Therefore, optical sensors are not optimal for long-term instrumentation [37]. To counteract these disadvantages, the use of purge air for cooling was proposed. However, this means additional systems with additional weight. Optical techniques are dominant in the available literature [41]. To monitor the dynamic behaviour of blades in development machines, this is an important technical solution, but for long-term use, it is considered challenging for SHM applications.

Reinhardt et al. made experiments to determine vibration frequencies and amplitudes of turbine blades with a laser vibrometer [43]. Lezhin et al. compared different vibration measurement systems with numerical calculations [44]. The investigation of bladed disks with optical laser probes were publicised by several authors [45–49]. In-situ tip clearance measurements with laser doppler method were presented by Büttner et al. [50, 51]. Gil-García et al. [52] and Zielinski et al. [53] focused their work on time of arrival measurements on compressor and turbine blades, to determine blade vibration. Overton developed an LDV system to measure tip clearance more accurately, compared to the capacitive method [54]. Sharma et al. [55] and García et al. [56] used laser vibrometry for SHM aspects. To measure the whole rotor deformation during rotation, Günther et al. made experiments with optical sensors [57]. Oberholster et al. explored a new approach to detect blade damage with Eulerian LDV [58]. Pfister et al. investigated the application to measure simultaneously position and velocity on moving rough surfaces with only one sensor [59].

3.1.3. Inductive sensors

Inductive sensors consist of multiple mini-sized planar spiral coils. The sensor measures the tip clearance by measuring the inductance change of planar spiral coils by the passage of the rotor blades. The smaller the tip clearance, the higher the inductance drops, due to the larger EC induced in the blade tip [17]. As the turbine blades passes the magnetic field of the sensor, an eddy current flows because of the electromagnetic induction. This increases the induction current flow, whereby the load of the oscillation circuit increases and the vibration is damped or stopped. The sensor measures this change (Figure 11). According to Faraday’s law, Equation (6) is given:

$$U_I = \oint_c (\vec{v} \times \vec{B}) d\vec{l}, \tag{6}$$

where U_I is the magnitude of the induced voltage, B the course of the magnetic induction, l the function of coil length and v the resulting speed.

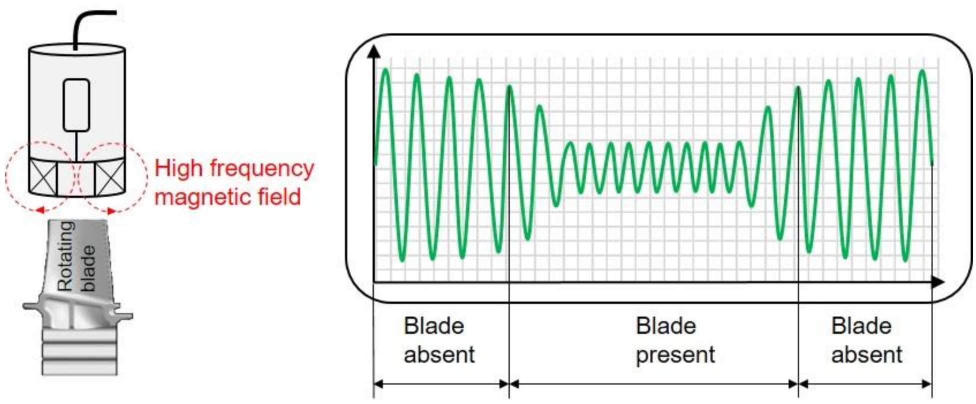

Figure 11. Principle inductive sensor.

These sensors typically operate at temperatures below 60 °C. Higher temperatures decrease the magnetisation of the permanent magnet and increase the impedance of the winding. They are characterised by long life, high reliability and resistance to contamination [40]. Another advantage is their simple construction. Clearances are tested from 0 to 5 mm with a resolution of 10 μm at a rotation speed of up to 80,000 rpm. Inductive sensors are of simple design, low in cost and easy to install. They have high resolution, high sensitivity and the capability of monitoring a large number of tip clearances simultaneously. These sensors do not need a penetrating hole through the casing. Therefore, the device is more sensitive to the relative vibration between the casing and the sensor. However, this only works if the casing does not contain ferrous material, because the magnetic field, and thus the output signal amplitude is reduced significantly. The sensors cannot detect variation in tip clearances of less than 50 μm. The main disadvantages are the calibration effort and the limited lateral resolution. These sensors can only detect one tip clearance at a specific location at the blade tip. Therefore, for advanced health monitoring techniques, multiple sensors are needed. The low temperature resistance of the sensors does not allow to be used in the turbine part of a gas turbine. However, for the first compressor stages of a gas turbine, their use is still conceivable.

Przysowa et al. developed a new inductive sensor for blade health monitoring systems for military turbofans. Also the resistance to high temperature and contamination were verified [40, 60]. Du et al. developed multiplexed inductive sensors for detection of blade tip clearances [17].

3.1.4. Eddy current sensors

EC sensors emit a high frequency electromagnetic field. The passing blade in this field induces ECs in the blade tip, acting against the existing high frequency field. The following change in coil impedance can be measured [61]. The general expression is shown in Equation (7):

$$V(t) = n \cdot \frac{d\Phi}{dt}, \tag{7}$$

where V is the sensor voltage, Φ the magnetic flux passing through the coil and n is the number of turns on the coil.

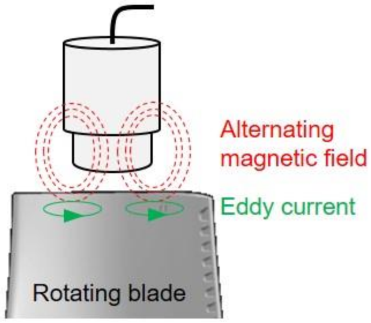

Figure 12. Principle of an EC sensor.

This principle is shown in Figure 12. The determination of the change of this phase position is the main difference compared to the inductive sensors.

Parts of the sensor start to melt at 93 °C [62]. It was reported that some companies have developed EC sensors that are able to operate at high temperatures up to 1000 °C if an air-cooling system is used [63]. EC sensors have good accuracy [29] and are typically embedded in the casing and the arrival time of the blades will be measured. From this basis, blade deformation can be calculated. They do not work well with non-conductive materials (composites). Furthermore, it is difficult to measure high vibration frequencies without a priori knowledge [64].

Cardwell et al. developed a new EC sensor for blade tip timing of engine fans [65]. Lui et al. proposed a new method to improve the measuring accuracy of EC sensors by considering torsional vibration [66]. Ghana et al. showed new tip timing algorithm for EC sensors which was verified in laboratory and real engines [67]. Tsutomu et al. published their work on the usage of EC sensors for displacement measurements successfully [68]. Przysowa et al. studied health monitoring techniques with EC sensors for military aircrafts [69].

3.1.5. Magnetoresistive sensors

Magnetoresistivity is the effect that describes the change in the electrical resistance of a material by applying an external magnetic field. These include, in particular, the anisotropic magnetoresistive effect (AMR effect), the giant magnetoresistance effect (GMR effect), the colossal magnetoresistance effect (CMR effect), the tunnel magnetoresistance effect (TMR effect) and the planar Hall effect. The use depends on whether the component to be examined is magnetic.

To describe the strength of the respective magnetoresistive effect, the quotient of resistance change and resistance without external field is used:

$$\frac{\Delta R}{R[\%]} = \frac{R(H)-R(0)}{R(0)} \cdot 100, \tag{8}$$

where $R(H)$ is the resistance in dependence of the magnetic field, $R(0)$ is the resistance without external magnetic field, $\frac{\Delta R}{R}$ is the characteristic of the magnetoresistive effect. When the blade passes the sensor, the magnetic field will be distorted. This variation can be measured (Figure 13).

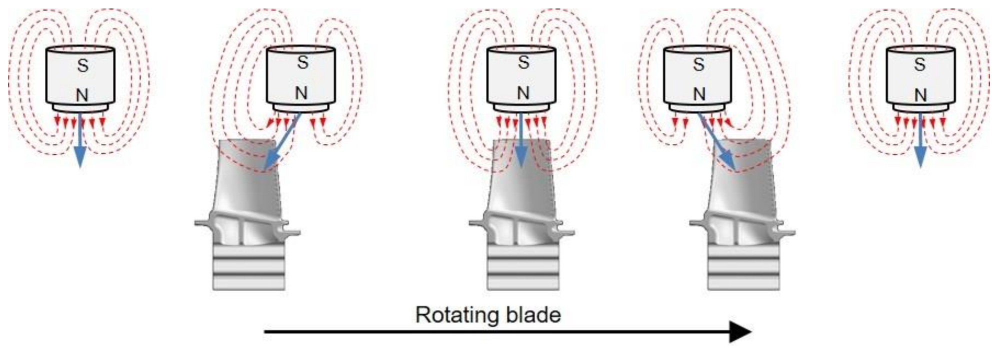

Figure 13. Function of a magnetoresistive sensor.

The main advantage of this technology is the relatively small sensor size. Typically, the sensor has a maximum outer diameter of 8 mm. In addition, the simple design lowers the sensor costs [38, 42]. They have good tolerances to debris, which is an important for the accuracy and long-term operation. The fast rise time (~20 ns) is also advantageous and their high signal repeatability and time accuracy is comparable to the optical systems and the clearance measurements are in line with capacitive sensors [42].

A new development shows that these sensors have the potential to survive up to 700–800 °C. However, the robustness, durability and accuracy has to be tested [63].

Procházka et al. made fundamental research on this sensor technology in turbomachinery. An online system was developed to monitor the vibrational amplitudes and frequencies of all blades. Possible blade damage could be notified and also blade elongation and blade twisting was shown [70, 71]. Brouckaert et al. developed a new magnetoresistive sensor for non-contact blade vibration measurements [72]. Tomassini et al. presented a new sensor design as well [73, 74]. The new sensor was successful verified in test benches and in a jet-engine.

3.1.6. Capacitance sensors

The electrical capacitance, between two electrically conductive materials insulated from one another, is equal to the ratio of the charge quantity Q and the electrical voltage U ($C = \frac{Q}{U}$). The change in electrical capacitance can be used inter alia to determine distances. In our case capacitance sensors measure the capacitance change between the probe and the blade tip. When the capacitor plate generates an electrostatic field and a turbine blade is present, the capacitance changes so that the oscillator begins to oscillate (Figure 14). Equation (9) shows the relationship of capacitance, sensor geometry and rotor to stator gap:

$$C_x = \frac{\varepsilon_r \varepsilon_0 S}{d}, \tag{9}$$

where C_x is the capacitance from sensor to blade, ε_r and ε_0 are the permittivity of the medium and the vacuum, S is the area between two sensor plates and d is the distance from blade to sensor.

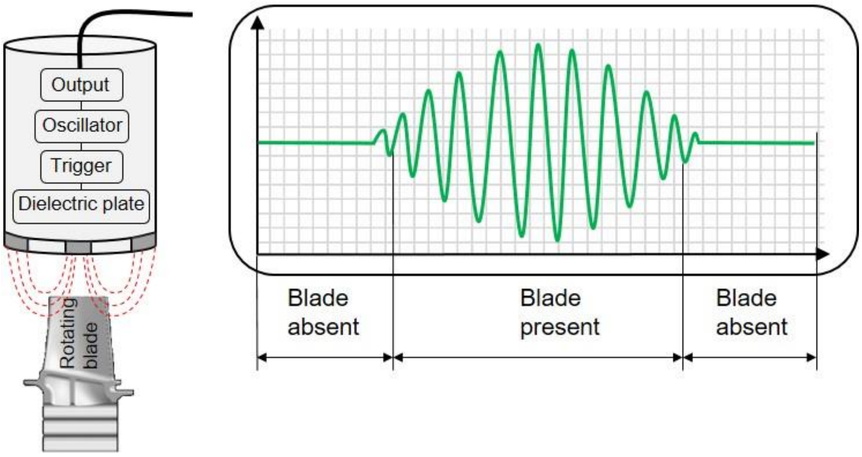

Figure 14. Principle capacitance sensor.

The use of plastics limits the operating temperature of some sensors to 200 °C [75]. Capacitive sensors are predominant due to the improved temperature robustness [37] compared to the other sensor technologies. However, in a gas turbine, the thermal load of the sensors is much higher, therefore, cooling is required. The sensor diameter is relatively small [78] allowing for easier implementation in the engine.

The main disadvantages are the calibration effort and the limited lateral resolution. Some sensors have limitations in bandwidth [29]. The electronic circuits of these systems have to be placed only a few centimetres away from the probe head. The distance from the probe head to the first amplifier has to be at a maximum of 1 m. The output of the probe is nonlinear. For a high precision, the blade tip geometry must be considered. Therefore a ‘calibration wheel’ can be used. With increasing distance between the probe head and blade tip, the signal-to-noise ratio (SNR) decreases. Also, a minimal clearance exists. These sensor types have low costs and are of a simple design [76]. However, the measured capacitance often not only gives the correct clearance because the dielectric property of air could change, due to variations in pressure and humidity [17].

Capacitance probes have a greater potential than optical probes because it is difficult to measure tip clearance with them [41].

Sarma et al. [77] and later Drumm et al. [78] designed a dual-amplifier circuit configuration for tip clearance measurements. Mönch et al. [79] and Müller et al. [80] developed a tip clearance system for compressor and turbine blades. For the usage in micro gas turbines, Fabian et al. described the special requirement of a capacitive tip clearance measurements system in this application [81]. Lavagnoli et al. studied the implementation of a high frequency capacitive sensor on a large transonic turbine stage [82]. These works show that these sensors can be used in hot gas sections for industrial gas turbines for health monitoring of turbine blades.

3.2. Vibrational monitoring

Vibration sensors, like accelerometers, displacement sensors and velocity sensors, are the widest used techniques for blade fault diagnosis in field conditions.

In industrial gas turbines eddy current proximity transducers are usually used on the bearings to measure the rotor vibrations. The same sensors are also used in the keyphasor to determine the phase angle and the axial position of the rotor [83]. The functional principle is identical to that described in Section 3.1.4. For measuring the casing vibration mostly accelerometers are used. A piezoceramic sensor plate converts dynamic pressure fluctuations into electrical signals. The pressure fluctuation is generated by a seismic mass attached to the piezoceramic and acts on the piezoceramic when the overall system is accelerated (Figure 15).

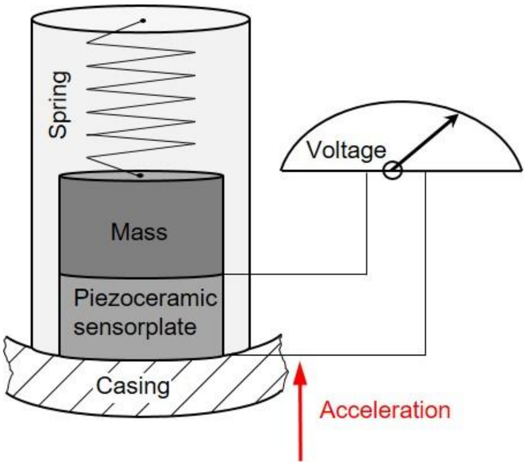

Figure 15. Principle accelerometer.

These signatures combined can be taken for health prognosis of the blades. For the frequency analysis, the most common technique is the frequency spectrum analysis technique. This means the conversion of the vibration signals from time domain into the frequency domain [84]. By analysing these frequencies, the location and failure types can be detected. These sensors work with a frequency of 10 kHz [85]. This method is effective in detecting severe blade faults (e.g., terminal rubbing), while minor faults (e.g., impending rubbing) are mostly not detectable. Therefore, vibrational analysis is not a reliable tool for SHM in field engines [86–88].

Südmersen et al. showed a combination of pressure measurements, casing vibration measurements and shaft displacement [89]. Lebold et al. presented a work to demonstrate the feasibility of torsional vibration measurements for shaft crack detection. It was mentioned that the same technique may be used for crack detection in turbine blades [90]. In a case study, it was shown that when blade faults are the only failure in the gas turbine, they will often not readily be detected with conventional vibration measurements. The reason is that these failures do not generate enough excitation compared to the other vibration amplitudes in the machine [91]. Alternatively, it was demonstrated that blade related failures could be detected before catastrophic events occur [84]. Ghouti et al. used the shaft torsional vibration signals to extract blade vibration signatures [92].

Zielinski et al. descripted the configuration of different measurement systems with two different probe types [53]. Zhang et al. studied the start-up vibration signatures of an industrial gas turbine for condition monitoring [93]. Sinha et al. presented a study to reduce the number of vibrational probes by improving the signal processing [83]. Loutas et al. tried the combination of vibration, acoustic emission and oil debris for condition monitoring [94]. Schlagwein et al. focused on mistuning effects on blades [95]. In [96–100] it was shown, how condition based maintenance with machine-learning approaches were realised. To detect blade damage with vibrational analysis following papers were published [23, 92, 101–116]. Several books were written with focus on vibration of rotating machines [2, 117–120].

Despite some disadvantages of this technology, this is a long-proven and cost-effective monitoring technique in gas turbines. This also plays an important role in the performance monitoring (Section 3.11.).

3.3. Ultrasound

Ultrasound is a common non-destructive testing method for detection of crack or material changes [121–123]. Ultrasonic waves usually propagate in a band from 20 kHz to about 1 GHz [124]. The ultrasonic harmonic waves presented can be described with the general wave equation:

$$\psi = Asin(kx - \omega t + \phi), \tag{10}$$

where ϕ is the initial phase angle, k the wavenumber with the wavelength $\lambda = 2\pi/k$, the period $T = 1/f$ and the frequency $f = \omega/2\pi$. Typically an ultrasonic wave is sent and the reflected signal from the crack can be used for failure prediction. The most commonly used piezoelectric transducers for SHM in gas turbine applications are limited in operating temperature.

The most relevant guided waves for gas turbine are Rayleigh waves and Lamb waves. Many authors are researching these waves for early crack detection and determination of crack sizes [1, 125–130].

Rayleigh waves are the simplest forms. The longitudinal and shear motions are linked and propagate at a common velocity. The terms ‘surface acoustic waves (SAW)’ and ‘Rayleigh waves’ are usually used as equivalents.

In addition to the possibilities presented below, surface waves with angled sensors are generated on the component. The disadvantage is that a coupling fluid is needed. Furthermore it should be noted, however, that higher-frequency waves penetrate less in the material than low-frequency waves. For Rayleigh waves, the penetration depth is about one wavelength [131]. These waves are very promising for NDT&E. Especially in high-temperature components, cracks will develop near the surface. Therefore Rayleigh waves are a good tool for inspection [132]. They can be used to evaluate the elastic properties of samples and coatings. The phase velocity of the SAW depends on elastic tensor of the material. This means that SAW information can determine the mechanical properties of components. The phase velocity is sensitive to see small changes in material density, Young's modulus and Poisson's ratio [133].

In a far-field characterization, the spatial resolution is half a wavelength ($\lambda/2$). Therefore, it is important to use very high frequencies to detect micro-cracks. The disadvantage is that at very high frequencies SNR problems occur. Far-field methods are unsuitable for the detection of micro-cracks. In contrast, in the near-field the spatial resolution is much better [134].

Lamb waves are elastic waves that propagate in solid plates whose particle motion lies in the plane that contains the direction of wave propagation and the plate normal (the direction perpendicular to the plate). Basically deflections occur both in the propagation direction (longitudinal) and vertically (transversal). Lamb waves are dispersive in nature. The speed of propagation c depends on the frequency (or wavelength), and elastic constants and density of the material. Therefore, Lamb waves are mixed pressure and shear waves [124]. To determine the relationship between wave velocity and frequency of a sample, dispersion curves can be used. Lamb waves for damage detection are important because they can propagate over long distances and they can show complex phenomena [123, 125].

Lamb waves consist of the fundamental symmetric mode S_0 and the fundamental antisymmetric mode A_0. These modes occur for each excitation frequency. For Lamb waves of short wavelength, several modes of oscillation occur for one wavelength. These are used for symmetrical and antisymmetric Lamb waves (S_0, S_1, S_2 and so on, respectively A_0, A_1, A_2 and so on). These modes have different wavelengths and propagation speeds. They interact differently with small disturbances and mode conversion could occur in presence of damage or other changes [135].

Linear ultrasonic technology focuses on the measurement of the velocity of sound, attenuation, transmission coefficients and reflection coefficients for crack detection [1, 136–138].

Nonlinear ultrasound techniques provide the ability to detect creep and thermal aging. Generation of the second harmonic or higher-order harmonics can be used for accurate flaw detection. The relationship between the amplitude of the second harmonic wave and the fundamental wave is a proven approach [1, 139–146].

Berwig et al. focused on examining the blade root of a turbine blade with Rayleigh waves for surface cracks. These blades are made of γ-titanium aluminide and are brittle. After manufacturing the blade root, this investigation serves the final quality control [147–149].

Lane developed an ultrasonic array system to inspect single-crystal turbine blades in-situ [150]. Ultrasonic phased arrays consist of several ultrasound transducers, where the excitation time and amplitude is controlled individually by computer. This gives the possibility, to focus the ultrasonic waves. This leads to a more accurate statement about the crack position and size. In addition, the SNR is improved [151, 152]. Chatillon et al. has dealt with complex geometries to detect errors with the phased array transducer [153].

The next subsections show special applications that are already used for the SHM of gas turbine components or that offer promising solutions for future research.

3.3.1. Waveguides

Harold et al. have filed a patent dealing with the condition monitoring of gas turbine components by means of acoustic waveguides (AWG) [154]. The general idea is to send an acoustic wave through waveguides to each vane. The sound waves pass through the vanes and are received by a second acoustic waveguide. A filter removes the lower frequencies below 30 kHz. As the coating on the blade deteriorates the size and/or velocity of the resulting acoustic wave changes. This is an indication that a blade must be serviced. The wave velocity for an intact coating is about 2500 m/s and for a completely deteriorated coating almost 5000 m/s. The principle of this idea is shown in Figure 16.

The patent also describes the possibility of performing measurements without an acoustic input signal. As the rotating blades spin past the vanes, the blade produces a pulsating gas pressure, causing acoustic waves in the vane. This signal can be measured via an acoustical waveguide.

The inventors gave a good description of how the acoustic waveguides can be designed and fastened with the sensors and vanes. The AWGs are connected to the vanes by either a point or a few inches long. When entering the AWG, the waves are converted into longitudinal waves. They must be a good transmitter for high-frequency acoustic signals (20 to 500 kHz) and be weldable. A variety of metals and composites are also possible. For the investigations of this patent, a wire with a diameter of 1 mm of platinum and platinum/13% rhodium was chosen. They must survive in the environment of hot oxidative gases and high dynamic loads. Typically AWGs use small wires or rods with a diameter of 0.25 to 6.4 mm [155].

Willsch et al. have implemented this concept practically in an industrial gas turbine [156]. Atkinson et al. have studied how the acoustic waves from the transducer are directed into the AWG via a conical transformer [157]. This is an elegant solution to the temperature issue but it is not feasible for industrial applications.

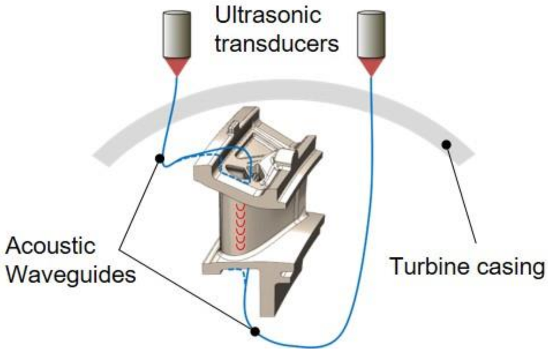

Figure 16. Schematic setup of an acoustic waveguide sensor.

Waveguides are also used for temperature measurement with ultrasound (ultrasound thermometry). The basic idea is to run ultrasonic waves through the waveguide. By increasing the temperature, the waveguide expands. This can be measured in the delayed ultrasonic signal and give conclusions about the temperature to be measured [158–162].

3.3.2. Thermosonic or ultrasonic stimulated thermography

This is a NDT&E method to detect micro-cracks on the surface and sub-surface of test parts. The test object is vibrated ultrasonically with or without contact or air-coupled transducers. As a result, the contact surfaces of the crack rub against each other and generate heat. With an infrared camera, the crack can then be detected (Figure 17).

Dyrwal et al. have demonstrated that with this technique micro-cracks can be detected on the outer shroud of a turbine blade. In this work different techniques were compared. The non-contact nonlinear air-coupled thermosonics (NACT) technique was the most promising [163]. Zhang investigated the physical process of the chaotic excitation of a turbine blade to improve the fault detection capability of thermosonic technology [164].

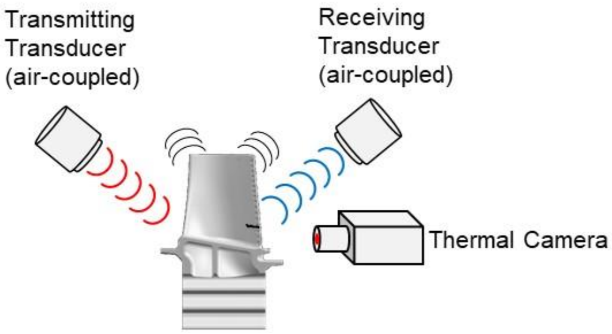

Figure 17. Thermosonic measurements with air-coupled transducer on a turbine blade.

Further literature is available for the air-coupled transducers [165–167].

3.3.3. Laser ultrasonic

In laser ultrasound, the ultrasonic wave is transmitted with light. The light of a laser hits a material surface where it is absorbed in a layer near the surface, resulting in heating, thermal expansion and finally emission of an ultrasonic wave (Figure 18). The generated ultrasonic waves propagate perpendicular to the sample surface and are independent of the angle of the laser [168].

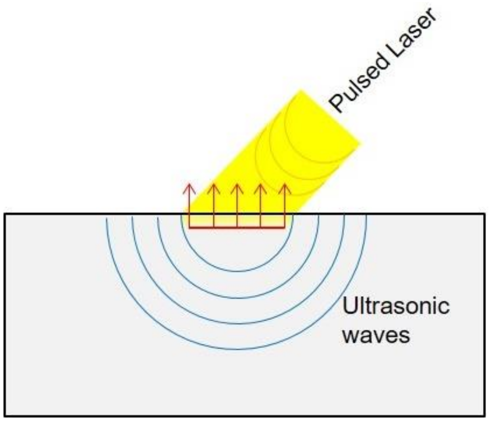

Figure 18. Principle laser ultrasonic.

Compared to conventional piezoelectric transducers (PZT), ultrasound generation by laser irradiation offers several advantages. No sensor contact is required; they have high spatial resolution and can work on complex designed surfaces. The acoustic waves can be received with PZT or electromagnetic acoustic transducers (EMAT). Laser interferometers on the receiving side are also possible.

The surface of the component to be examined is not damaged. One disadvantage is the poor SNR with laser ultrasound [169, 170]. Masserey et al. and An et al. worked on crack detection using laser ultrasound with focus on complex designed geometries [132, 171]. Pei et al. studied the inspection of inner cracks [172]. Dhital et al. investigated a similar topic, but used air-coupled transducers for damage detection [173].

Direct applications of this technology in the turbomachinery sector have not been identified, but this is a promising NDT&E approach. An SHM application is difficult here because laser ultrasonic has the same disadvantages as the optical technique shown above.

3.3.4. High temperature transducers

To solve the problem of extremely high temperatures in gas turbines, there are also promising approaches to use high-temperature ultrasonic sensors. On the one hand, it is important to solve the problem that the sensors themselves survive the high temperature, but on the other hand, there must also be a functioning acoustic coupling between the sensor and the test object. $La_2Ti_2O_7$ (lanthanum titanate) or $LiNbO_3$ (lithium niobate) enables operation at higher temperatures (Curie temperature higher than 1000 °C) [63]. Other promising materials are also possible. Many of these ideas are still in developmental status and commercially difficult to make available, but as an SHM approach, shows potential good performance [174–176].

3.3.5. EMAT

Alternating current is conducted into the induction coil of the sensor. This generates electromagnetic oscillations, which in turn induce eddy currents on the surface of the test object. The eddy current interacts with the permanent magnetic field of the sensor and generates ultrasonic waves through the Lorentz force directly on the surface of the test object (Figure 19).

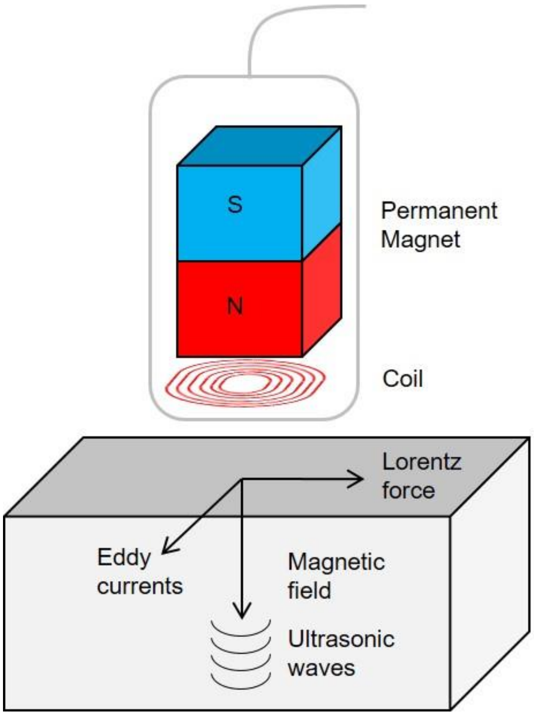

Figure 19. Working principle EMAT.

The main advantage is certainly that EMATs works contactless and the sensor is located a few millimetres from the test object. That means that no coupling is needed. In addition, a wide variety of ultrasonic wave types can be generated that would not be possible with PZTs. For example, transverse shear waves (SH) can be transmitted and received. They can also be used at significantly higher temperatures. The disadvantage is that metal particles can be attracted by the magnet. In addition, there is the danger of magnetization of the test object. These sensors are typically quite bulky and are not commonly used in aerospace applications [177].

Edwards et al. and Jian et al. researched Rayleigh waves generated by EMAT for crack detection [178–180]. Dixon et al. studied a hybrid method in order to bring the ultrasonic waves into the component by means of a laser and to detect them using EMAT [181].

3.4. Temperature measurements

Pyrometry and infrared thermography are good methods to detect creep, low-cycle fatigue, corrosion, erosion and oxidation [87, 182]. Phosphor thermometry is able to identify failures such as cracks, erosion, corrosion and wear [183]. These techniques will be presented in detail in the next chapters.

3.4.1. Pyrometry

With this technique, thermal radiation at the target point of the turbine blades can be measured. They are used for non-contact temperature measurement. The emitted thermal radiation of a body can be measured with the help of a pyrometer (Figure 20).

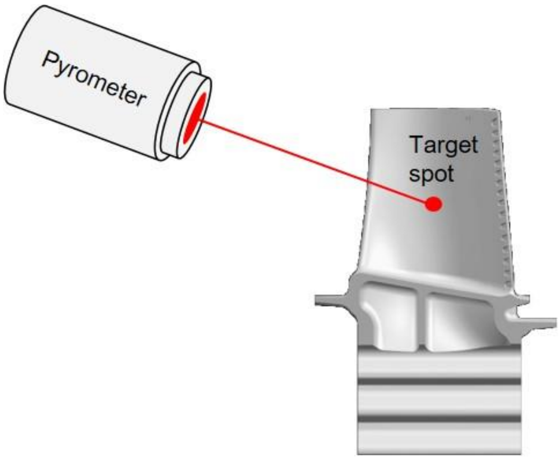

Figure 20. Principle pyrometry.

The relationship between the surface temperature and the emitted radiant energy is defined by Planck's law (Equation (11)):

$$E_b(\lambda, T) = \frac{c_1\lambda^{-5}}{\exp\left(\frac{c_2}{\lambda T}\right)-1}, \tag{11}$$

where E_b is the monochromatic radiation, T the temperature, λ the wavelength, c_1 and c_2 the radiation constants.

Pyrometers have the capability to measure ~40 points per blade [184]. To make these sensors work, no upper temperature limit exists. However, a minimum temperature limit of ~500 °C is required. They have a fast response and no physical contact with the turbine blades. Pyrometry is also immune to electromagnetic interference. However, finding a position to install the probe where it can view the blade surfaces is problematic and the optic has to be protected from deposits. The instrumentation is vulnerable to extreme temperatures, vibrations and high pressures. The combustion gases are turbulent with variable densities and high velocities. The sensors in the flow channel have to operate at an oxidising atmosphere. Corrosion is also a failure mode. It could be difficult to gain enough radiation of the small target area of the blades. In addition, records for representative temperature measurements are needed. Difficulties are reported in specifying the emission accurately [182].

The development of a blade temperature management system with pyrometers was reported by different authors [185–189]. Alaruri et al. [190] and Gao et al. [191] analysed the emissivity of different superalloys with TBC and verified the theoretical approach experimentally. Kerr et al. [192] and Daniel et al. [193] presented an overview of measurement and reflection errors associated with pyrometers.

3.4.2. Infrared thermography

This is an imaging process for displaying the surface temperature of objects. Every body with a temperature above the absolute zero emits heat radiation. An infrared camera converts the infrared radiation, which is invisible to the human eye, into electrical signals. From this, the camera creates a picture. Infrared cameras are used to take infrared pictures of the whole aerofoil that has to be evaluated (Figure 21).

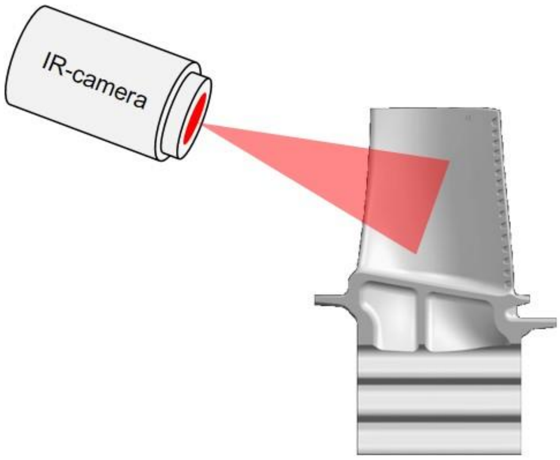

Figure 21. Principle infrared thermography.

Lemieux from Siemens Westinghouse Power Corporation showed a conceptual design of this technology in gas turbines where two IR cameras were used. These cameras also have a blade positioning sensor allowing tracking of all blades [194]. The automatic comparison of the IR pictures showed temperature increases at specific points of the blade. This could also be used to monitor degradation of the TBC or cracks.

Bison et al. evaluated especially this topic. They compared pulsed thermography and thermal wave interferometry to estimate ageing effects of the TBC [195, 196]. Sun et al. showed a multilayer analysis method to detect change in TBC properties as well [197]. Meola et al. developed a non-destructive testing method to detect small remaining ceramic fragments in the casted core [198].

3.4.3. Phosphor thermometry

The basis of this technique is a thermal history coating. Active rare earth ions are introduced. This could be integrated in the TBC, which is what the hot gas parts in a gas turbine are mostly coated with. By illuminating with an excitation light after a machine run, phosphorescence gives information about the temperature that the coatings experience. Figure 22 shows a combustion chamber outlet liner, with thermal paints, after service.

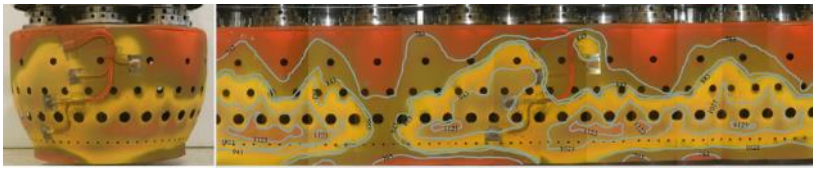

Figure 22. Thermal paint gradients of the combustor outer liner [206], with permission from Begell House, Inc.

A temperature capability of –5 to 1550 °C is given and a precision of ±5 °C was proved. The disadvantage of pyrometry and infrared thermography is the lower susceptibility to background radiation. Feist et al. showed in different publications the industrial application of phosphor thermometry. To develop these special paintings a Rolls-Royce jet engine was used for verification [183, 200–204]. The application in an industrial gas turbine was proven as well. The surface temperature of combustion chamber transition ducts, turbine blades and sideplates were measured and used for validation for the CFD calculations [205, 206].

3.5. Induction thermography

In inductively excited thermography, an electrically conductive component is inductively impressed by a near-surface eddy current. The resulting heating of the component can be visualized with an infrared camera (Figure 23). Cracks disturb the current flow and thus also influence the temperature development in the test part. This technique is similar (Section 3.3.2.) to thermosonic technique, where the excitation is achieved using ultrasound excitation. The penetration depth of the electromagnetic field is described by the skin effect:

$$\delta = \sqrt{\frac{2\rho}{\omega\mu}}, \tag{12}$$

where δ describes the skin depth, ρ is the conductor resistivity, ω the angular frequency and μ the absolute permittivity. The choice of the excitation frequency determines, inter alia, the depth to be examined into the component. In addition, coil geometry and power are also important test parameters [207].

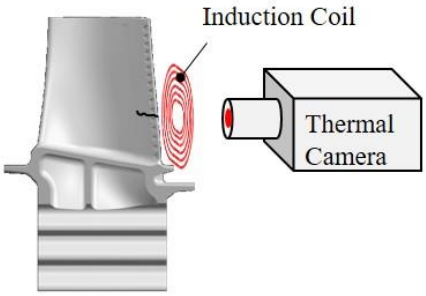

Figure 23. Principle inductive thermography.

The method is of particular interest where the crack detection with conventional methods is difficult or impossible. Compared to other excitation techniques, inductive excitation offers the advantage of being less sensitive to radiation or emission differences on a test surface, as the heat is generated directly in the test part [207].

Sensitivity to crack detection on components can be compared to magnetic particle inspection [208]. The advantage of induction thermography compared to magnetic particle testing is that it is non-contact. In addition, the use of chemicals is avoided. Accuracy is limited when components with highly reflective surfaces are tested, which have a low emissivity [208].

Carl et al. developed a system for automatic crack detection of turbine blades. A robotic arm puts the blades in test position. After the measurement was carried out, the automatic evaluation of the blades takes place [207]. Šrajbr et al. used induction thermography for automated crack inspection of aircraft structures [209, 210]. Bamberg et al. also introduces a system for inspecting turbomachinery components for cracks using induction thermography [211]. Vrana dealt with active thermography and examined cracks in the foot area of gas turbine blades [212].

Spießberger et al. compared inductive thermography with ultrasonically excited thermography [213]. The detectability of cracks in induction thermography depends on their orientation in the component and in ultrasound-excited thermography, this is largely independent. With ultrasonic excitation, the detection of defects is possible at a greater depth than in the inductively excited thermography, since the heat of fracture generated by ultrasound diffuses from greater depths to the surface. With complex geometries, it is difficult to excite the component surface evenly with induction. It is then often only possible to examine individual component areas. If the entire component is to be tested, the use of ultrasound-excited thermography appears to be more sensitive. For materials with low thermal conductivity, ultrasound-excited thermography is more suitable as a test method [213].

3.6. Acoustic emission (AE)

The basis of AE are transient elastic waves. They are generated due to the release of energy in a material when a crack occurs. The frequency range is between 100 KHz and 1 MHz.

Defects in a machine generate an individual type of crack growth. This phenomenon results in elastic waves, which can be detected with AE sensors (Figure 24) [85].

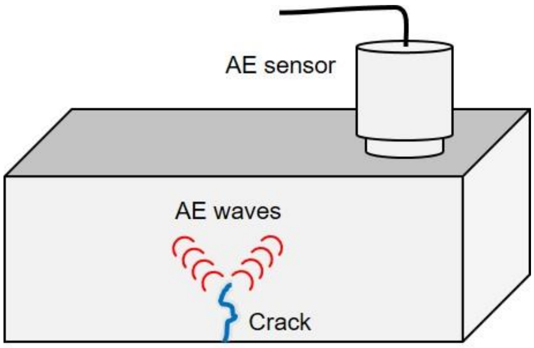

Figure 24. Principle AE measurement.

Al-Obaidi et al. provided a good explanation on how AE works: 'Instead of supplying energy to the object under examination, AE simply listens for the energy released by the object' [214, p.4].

AE is sensitive enough to monitor minor changes in the gas turbine parts. It has the potential to detect failures at an early stage. Furthermore, the crack position can be detected without intrusion. AE sensors were used to observe roller bearings in gas turbines [215]. It was found that AE is a proper tool to detect rubbing from rotor to stator.

Mba et al. showed promising experiments for early rub detection in turbine rotors [216]. AE is very sensitive to incipient cracks compared to vibrational measurements. It was shown that the AE technique is able to detect cracks in blades earlier than vibrational analysis [87]. One drawback is the attenuation of the signal. Therefore, the sensor has to be placed close to the signal source [217]. The accuracy of AE is limited because the propagation of the velocity of the acoustic wave depends on temperature, pressure and the relative speed of the medium [37].

Mba et al. developed an AE technique for monitoring rotating machines as well [217]. The focus was on bearings, pumps, gearboxes, engines and rotating structures. Leahy et al. investigated experimentally rubbing detection between rotor and stator of a steam turbine [218, 219]. Nashed et al. explored the sources of fluid generated AE in a running turbine [215]. These findings can be used for blade faults predictions.

AE is a relatively simple and cost effective monitoring technique for health monitoring of hot gas components. These sensors are limited by the high temperatures in the gas turbine, so that use in the hot gas without active cooling is not possible.

3.7. Mm-waves

Mm-waves are microwaves with wavelengths in the millimetre range between 1 and 10 mm. This corresponds to a frequency band from 30 to 300 GHz. The physical principle is the same as described for tip-timing measurement in Section 3.1.1.

The mm-wave technique is commonly used in motion detection and special radar systems. It can be used to measure movements of turbine blades, rotor-stator clearances and the degradation of TBCs. TBCs typically consist of four layers. Starting from the bottom the metal substrate, the metallic bond coat, the thermally grown oxide (TGO) and the ceramic topcoat. Mm-waves are nearly totally reflected by metal surfaces. TBCs have a high dielectric constant of typically 25. The waves will be partly absorbed and differently reflected. These differently reflected waves could be used to detect the degradation of the coating (Figure 25). An antenna sends the waves to the moving blades and the reflected waves will be evaluated. Tests were done with 2.45 and 10 GHz sensors. Further investigations concerning the electromagnetic losses of TBCs are necessary. Willsch et al. have shown this SHM application in a running gas turbine [156].

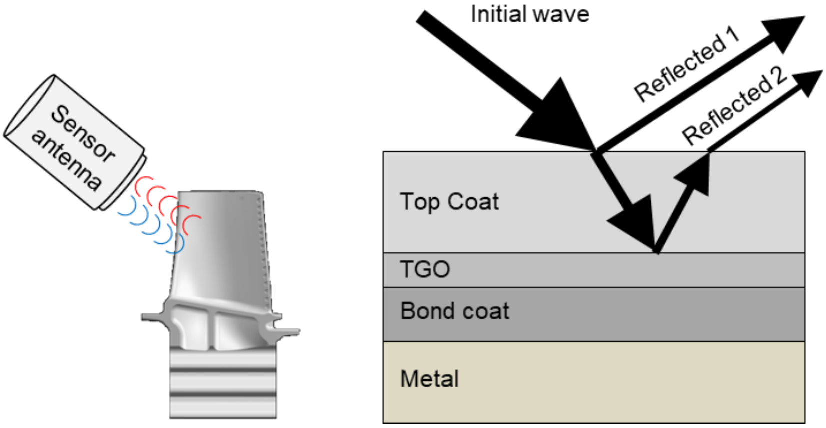

Figure 25. Principle of mm-wave propagation in TBC coating.

The degradation of a TBC is a relevant indicator for health monitoring of the hot gas parts. However, an active cooling strategy for the antenna is needed.

3.8. Pressure measurements

In gas turbine casings are placed several pressure sensors. The distortion of the pressure fields around the blades can be used for fault detection [220]. An experimental study was completed to find a correlation between compressor casing vibrations and the pressure field around the compressor blades [87]. The pressure field around the compressor blades gives a clearer picture about the blade fault compared to vibrational analysis [88]. It was shown that pressure measurements deliver better results than common vibrational probes [87]. Mathioudakis et al. found different signatures corresponding to the different blade faults [220, 221]. Failure modes, such as blade creep, rotor eccentricity and rubbing, were experimentally detected [88]. Forbes et al. presented a concept to combine internal casing pressure measurements with casing vibration measurements. It was proven that blade defects can be detected [222–226].

3.9. Direct-write thermal spray (DWTS) sensors

DWTS is a spray process that accelerates material to high speeds and hits a substrate. This creates a dense and strongly adherent deposit. Typically, the material is injected in the form of a powder, wire or rod into a high velocity combustion or thermal plasma flame. As a result, thermal and kinetic energy is supplied to the particles (Figure 26). This is a similar process to apply TBC to a component [227]. The DWTS process allows the additive generation of sensor circuits on complex shaped components without pre-masking.

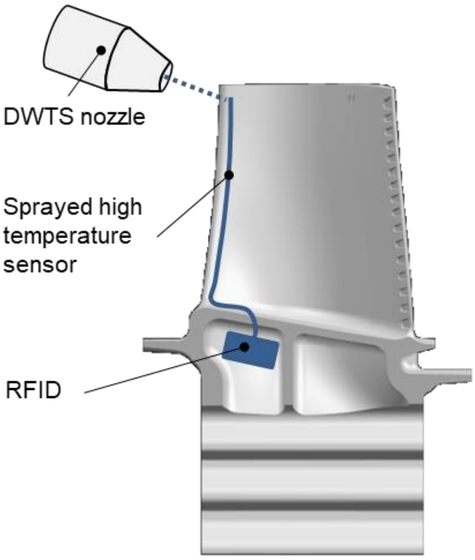

Figure 26. Principle DWTS on a turbine blade.

Longtin et al. have studied the use of temperature sensors and strain gauges manufactured by DWTS. K-type thermocouples can measure high operating temperatures. Industry standard K-type thermocouples are made of Chromel (90Ni/10Cr) and Alumel (95Ni/3Mn/2Al/1Si) [227]. A K-type thermocouple consists of a pair of metallic conductors made of these different metals. These are connected at one end and are suitable for temperature measurement due to the thermoelectric effect. In principle, the thermocouple provides electrical energy from heat at a temperature difference along the electrical conductor (Figure 27).

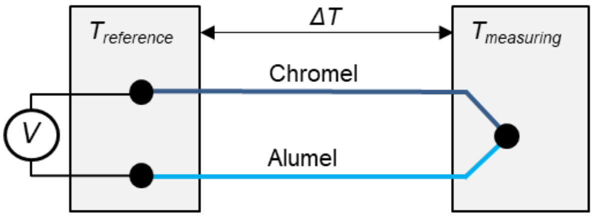

Figure 27. K-type thermocouple.

Schönberg et al. has also applied K-type thermocouples with DWTS direct to the surface of a test component. In this way, in-situ temperature measurement data of the turbine blades can be determined [228]. Zhang et al. has developed a system to weld K-type thermocouples directly onto the TBC, which then embeds the sensor through a second ceramic layer [229].

Capacitive strain gauges are well suited for determining the mechanical stress of a component in extreme environmental conditions. Compared to resistive stain gauges, they have a better SNR and are not so sensitive to high temperature and temperature fluctuations. If the fingers of the sensor are displaced relative to each other by the component load, this results in a capacitive change ΔC. This is approximately proportional to the strain ε [230] (Figure 28).

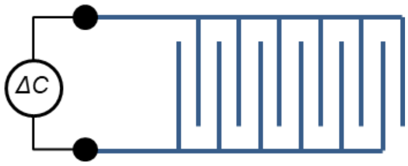

Figure 28. Capacitive strain gauge.

Li et al. used DWTS and ultrafast laser micromachining to produce the sensor. After spraying a layer, the laser worked out the exact sensor contour [230].

It is advantageous that thermal spray is already used as a standard method for applying a protective layer in gas turbine components. As a result, the sprayed-on layer adheres directly to the component. No adhesive or mechanical connection is necessary. It is also possible to form a capacitor-inductor circuit (LC). This would provide the opportunity to transmit the measurement data passively and wirelessly [230–232].

Chen et al. dealt with micromachining strain gauges using DWTS and precision laser [233]. Hon et al. have published an overview of the various direct write technologies and their state of development [234]. Pique reports different areas of application in his book on direct-writing technologies [235].

This technique is a promising way to determine the condition of the turbine blades in-situ and may be considered in future research. It will certainly be difficult, due to the high temperature, to use the electronic components for data transmission as shown in Figure 26. Passive data transmission systems would be a good solution.

3.10. Uniform crystal temperature sensor (UCTS)

These sensors are particularly suitable for prototype machines to determine the temperature at certain points of the test subject. The crystal sensor is inserted into the test object and a pocket with a diameter of 0.75 mm and 0.75 mm deep must be removed. After inserting the crystal, it is closed again. When the test run is finished, the sensor must be removed for evaluation [236]. The temperature changes the lattice structure of the crystal, allowing an accuracy of ±3.3 °C [237]. The application temperature is 150 to 1430 °C [237]. DeVoe et al. have studied their use in gas turbine blades [238, 239].

3.11. Performance monitoring

Performance monitoring processes different input data. The temperature, pressure and speed of the gas turbine are used to calculate the performance of the machine. This method is also able to detect blade faults. This fault changes the aerodynamic behaviour of the blades, and ultimately, the performance of the whole machine. A combination of performance and vibration monitoring is known as a hybrid method. It was shown that blade deformation, blade wearing and blade fouling could be detected [240].

Lattime et al. discussed the degradation of the high pressure turbine (HPT) performance. Especially, wear on blade tip and sealing can account for losses in the HPT performance of 1% and more [241]. Salar et al. developed a method to detect faulty components inside a gas turbine. Therefore, a gas path analysis and extended Kalman filters were used. The main parameters to detect the degradation are efficiency and flow capacity of the compressor and the turbine [242]. Diallo et al. established a new statistical signal processing technique for performance monitoring [243]. A physics-based modelling approach for performance deterioration were shown by Hanachi et al. [244]. Heat loss index and power deficit index were used as indicators. Different methodologies to improve the robustness of performance monitoring against sensor faults were developed [245, 246]. Tahan et al. reviewed current gas path performance monitoring techniques. The different failure modes in a gas turbine and the possibilities to detect them with performance monitoring were listed [247].

This technique is very promising for future condition based maintenance concepts. Many sensor technologies are already available as standard monitoring in series machines that can be used for the evaluation. A research focus should be on the further development of modern signal processing techniques.

4. Conclusions

The most relevant failure modes for gas turbine hot gas components have been described. For blade health monitoring, TMF, creep, oxidation and corrosion are the main life limiters depending on the turbine configuration. For the transition ducts of the combustion chambers, wear of the mating surfaces and degradation of TBCs and cracks are problematic.

A review of most relevant NDT/SHM techniques for gas turbine was reported. Tip timing technology allows for measurement of the tip clearance of the blades, time of arrival and also axial deflection. This is a very powerful method for which several sensor technologies could be used. Optical measurements are the best choice for prototype machines because of their accuracy and resolution, but the sensitive optics could be problematic for long-term operation in field machines. Inductive and magnetoresistive sensors are not able to work in the first turbine stage because of their limited temperature. Microwave, EC and capacitive sensors seem to be a good choice for turbine tip timing.

The pyrometry enables the measurement of heat radiation at different points of the blades. IR cameras take infrared pictures of every blade during every rotation. Both monitoring techniques compare previous measurements and pictures. Phosphor thermometry is a new innovative method for temperature detection. However, all of them are rather complex solutions for health monitoring in field machines.

AE is a powerful diagnosis technique. The sensor has to be placed close to the signal source. This is a promising method to detect rubbing; however, limited accuracy and signal attenuation of this technique needs can be a limiting factor.

Millimetre waves are a possibility to detect degradation of TBCs. However, a sensor antenna directly placed in the hot gas disturbs the flow and the sensor has to be actively cooled.

The detection of pressure differences in the flow channel could also be a good indicator for health monitoring of gas turbine components, especially in combination with other technologies.

The vibrational approach is the classical technique, where for example accelerometers on the bearings and on the casings provide important information on the machine behaviour; however, it is known that blade failures could not be detected readily with conventional vibration measurements.

The ultrasound methods presented offer promising possibilities in the field of NDT&E and SHM.

The current review reports some current NDT/SHM solutions, able to mostly monitor the components contactless and the results shows that a combination of monitoring technology would provide valuable information about the performance and integrity of gas turbine components.

A summary of the different techniques with the corresponding properties is shown qualitatively in Table 2. Here it is presented which failure modes can be detected with the individual techniques and whether they are primarily suitable for NDT or SHM. In addition, important properties and also the costs are summarised.

Table 2. Summary–Properties of sensor technologies.

	Sensing Technology	**Failure Modes**	**NDT**	**SHM**	**Temp. limit**	**Band-width**	**Accuracy**	**Sensitivity**	**Costs**
Tip timing method	Microwave probes	Creep Crack Rubbing Wear		X	+	+	+	0	0
	Optical sensors			X	−	+	+	+	−
	Inductive sensors			X	−	+	+	+	+
	EC sensors			X	−	0	+	0	0
	Magnetoresistive sensors			X	+	+	+	+	+
	Capacitance sensors			X	+	0	0	0	+
	Vibrational monitoring	Rubbing FOD Crack		X	0	+	-	-	+
Ultrasound	Waveguides	Creep Crack Wear		X	+	0	+	+	+
	Thermosonic		X		−	0	+	+	0
	Laser Ultrasonic		X		−	0	+	+	−
	High temperature transducers			X	+	0	+	+	−
	EMAT		X		−	0	+	+	0
Temperature measurements	Pyrometry	−		X	−	+	+	+	−
	Infrared thermography	Creep LCF Corrosion Erosion Oxidation	X	X	−	+	+	+	−
	Phosphor thermometry	−		X	+	−	0	0	−
	Induction thermography	Crack	X		−	+	+	+	−
	AE	Crack		X	−	0	0	-	+
	Mm-waves	Crack Wear	X	X	−	0	+	+	−
	Pressure measurements	Crack Creep Rubbing		X	+	+	+	+	+
	DWTS	Crack		X	+	+	0	+	−
	UCTS	−		X	+	+	0	+	−
	Performance monitoring	Crack Wear		X	+	0	−	−	+

'+' means positive and '−' means negative in this context. '0' means neutral.

Acknowledgement

Thanks to the MAN Energy Solutions SE for their support.

References

1. Mitra, M., & Gopalakrishnan, S. (2016). Guided wave based structural health monitoring: A review. *Smart Mater. Struct., 25*(5), 53001.
2. Proulx, T. (2011). *Rotating machinery, Structural Health Monitoring, shock and vibration, Volume 5, Proceedings of the 29th IMAC, A Conference on Structural Dynamics 2011*. New York, NY, USA: Springer.
3. Mukhopadhyay, S. C. (2011). *New developments in sensing technology for structural health monitoring.* Berlin/Heidelberg, Germany: Springer.
4. Niezrecki, C. (2017). *Structural Health Monitoring & Damage Detection, Volume 7: Proceedings of the 35th IMAC, A Conference and Exposition on Structural Dynamics 2017.* Cham, Switzerland: Springer.
5. Ostachowicz, W. (2013). *New trends in structural health monitoring.* London, Uk: Springer.
6. Jansohn, P. (2013). *Modern gas turbine systems: High efficiency, low emission, fuel flexible power generation*. (Woodhead Publishing series in energy, no. 20). Cambridge, UK: Woodhead Publishing.
7. Pallos, K. J. (2001). *GER-3957B - Gas Turbine Repair Technology.* Atlanta, GA, USA: GE Energy Services Technology.
8. Meher-Homji, C. B. (1995). Blading Vibration and Failures in Gas Turbines: Part A — Blading Dynamics and the Operating Environment. In *ASME 1995 International Gas Turbine and Aeroengine Congress and Exposition: Volume 4: Heat Transfer; Electric Power; Industrial and Cogeneration*, *ASME 1995 International Gas Turbine 1995, Houston, TX, USA, 5 June 1995*. (Vol. 4, p. V004T11A014). New York, NY, USA: American Society of Mechanical Engineers.
9. Jaw, L. C., Wu, D. N., & Bryg, D. J. (2001). Tracking and Control of Gas Turbine Engine Component Damage/Life. In *RTO AVT Symposium*, *RTO AVT Symposium, Manchester, UK, 8-11 October 2001*. (RTO-MP-079(I)).
10. Mishra, R. K., & Srinivasan, K. (2016). Failure of Low-Pressure Turbine Blades in Military Turbofan Engines: Causes and Remedies. *J. Fail. Anal. Prev., 16*(4), 622–628.
11. Mishra, R. K., Thomas, J., Srinivasan, K., Nandi, V., & Raghavendra Bhatt, R. (2017). Failure analysis of an un-cooled turbine blade in an aero gas turbine engine. *Eng. Fail. Anal., 79*, 836–844.
12. Park, M., Hwang, Y.-H., Choi, Y.-S., & Kim, T.-G. (2002). Analysis of a J69-T-25 engine turbine blade fracture. *Eng. Fail. Anal., 9*(5), 593–601.
13. Russhard, P. (2015). The rise and fall of the rotor blade strain gauge. *Mech. Mach. Sci., 23, 27-37.*
14. Kestner, B., Lieuwen, T., Hill, C., Angello, L., Barron, J., & Perullo, C. A. (2015). Correlation analysis of multiple sensors for industrial gas turbine compressor blade health monitoring. *J. Eng. Gas Turb. Power*, *137*(11), 112605.
15. Guo, H., Duan, F., & Zhang, J. (2016). Blade resonance parameter identification based on tip-timing method without the once-per revolution sensor. *Mech. Syst. Signal Process., 66-67*, 625–639.
16. Geisheimer, J. L., Kwapisz, D., Holst, T., & Hafner, M. (2013). Blade Tip Clearance Sensors for Use in Engine Health Monitoring Applications. *SAE Int. J. Aerosp., 6*(2), 417–423.
17. Du, L., Zhu, X., & Zhe, J. (2014). A high sensitivity inductive sensor for blade tip clearance measurement. *Smart Mater. Struct., 23*(6), 65018.
18. Kwapisz, D., Hafner, M., & Queloz, S. (2010). Calibration and characterization of a CW radar for blade tip clearance measurement. In *Proceedings of the 7th European Radar Conference, Paris, France, 30 September–1 October 2010.*
19. Witos, M., & Wisnioch, M. (2009). Compressor Blade Health Monitoring with Use of Tip Timing and Modal Analysis Method. *PAMM, 9*(1), 209–212.
20. Witos, M., & Wachlaczenko M. (2016). Structural Health Monitoring of Compressor and Turbine Blades with the Use of Variable Reluctance Sensor and Tip Timing Method. In *Proceedings of the 19th World Conference on Non-Destructive Testing, Munich, Germany, 13–17 June 2016.*

21. Rokicki, E., Majewski, P., Rzadkowski, R., Szczepanik, R., Spychała, J., & Drewczyński, M. (2014). Analysis of Middle Bearing Failure in Rotor Jet Engine Using Tip-Timing and Tip-Clearance Technique. In *Proceedings of the ASME Turbo Expo: Turbine Technical Conference and Exposition, Düsseldorf, Germany, 16–20 June 2014*. (p. V07AT31A014). Düsseldorf, Germany: American Society of Mechanical Engineers.

22. Tamura, K., Ono, M., Torii, S., & Morimoto, K. (2014). Non-contact Vibration Measurement of the Rotor Blades that Play a Pivotal Role in the Reliability of Gas Turbines. *Mitsubishi Heavy Ind. Tech. Rev.*, 51, 10.

23. Dimitriadis, G., Carrington, I. B., Wright, J. R., & Cooper, J. E. (2002). Blade-tip timing measurement of synchronous vibrations of rotating bladed assemblies. *Mech. Syst. Signal Process., 16*(4), 599–622.

24. Gallego-Garrido, J., Dimitriadis, G., & Wright, J. R. (2007). A Class of Methods for the Analysis of Blade Tip Timing Data from Bladed Assemblies Undergoing Simultaneous Resonances—Part I: Theoretical Development. *Int. J. Rotating Mach., 2007*(591), 1–11.

25. Gallego-Garrido, J., Dimitriadis, G., Carrington, I. B., & Wright, J. R. (2007). A Class of Methods for the Analysis of Blade Tip Timing Data from Bladed Assemblies Undergoing Simultaneous Resonances—Part II: Experimental Validation. *Int. J. Rotating Mach., 2007*(4), 1–10.

26. Russhard, P. (2016). Blade tip timing (BTT) uncertainties. In *AIP Conference Proceedings*. (Volume 1740). Melville, NY, USA: AIP Publishing.

27. Satish, T. N., Murthy, R., & Singh, A. K. (2014). Analysis of uncertainties in measurement of rotor blade tip clearance in gas turbine engine under dynamic condition. *Proc. Inst. Mech. Eng. Part G J. Aerosp. Eng., 228*(5), 652–670.

28. Roeder, J. W., Bencic, T. J., Hughes, C. E., & Woike, M. R. (2009). Testing of a Microwave Blade Tip Clearance Sensor at the NASA Glenn Research Center - NASA/TM-2009-215589. In *47th Aerospace Sciences Meeting.* Cleveland, OH, USA: NASA Glenn Research Center.

29. Zhang, J., Duan, F., Niu, G., Jiang, J., & Li, J. (2017). A Blade Tip Timing Method Based on a Microwave Sensor. *Sensors, 17*(5), 1097.

30. Violetti, M., Qin Xu, O., Hochreutiner, A. K., & Skrivervik, A. K. (2012). New microwave sensor for on-line Blade Tip Timing in gas and steam turbines. In *Proceedings of the 2012 Asia-Pacific Microwave Conference Proceedings (APMC), Kaohsiung, Taiwan, 4–7 December 2012.*

31. Violetti, M., Skrivervik, A. K., Qin Xu, M., & Hafner, M. (2012). New microwave sensing system for blade tip clearance measurement in gas turbines. In *Proceedings of the 2012 IEEE Sensors, Taipei, Taiwan, 28–31 October 2012.*

32. Woike, M., Abdul-Aziz, A., Oza, N., & Matthews, B. (2013). New sensors and techniques for the structural health monitoring of propulsion systems. *Sci. World J., 2013*, 596506.

33. Abdul-Aziz, A., Woike, M. R., & Bencic, T. J. (2010). A Microwave Blade Tip Clearance Sensor for Propulsion Health Monitoring - NASA/TM-2010-216736. In *Infotech@Aerospace 2010 Conference; Sponsoring Organization.* Cleveland, OH, USA: NASA Glenn Research Center.

34. Wagner, M., Schulze, A., Vossiek, M., Stephelbauer, C., Weigel, R., Vortmeyer, N., et al. (1998). Novel microwave vibration monitoring system for industrial power generating turbines. In *Proceedings of the IEEE MTT-S International Microwave Symposium Digest, Baltimore, MD, USA, 7–12 June 1998*. (Volume 3).

35. Hafner, M. A., Holst, T. A., & Billington, S. A. (2011). Blade tip measurement advanced visualization using a three dimensional representation. In *Proceedings of the ASME Turbo Expo 2011, Vancouver, BC, Canada, 6–10 June 2011*. (Volume 3). Vancouver, BC, Canada: American Society of Mechanical Engineers.

36. Neri, P., & Peeters, B. (2015). Non-Harmonic Fourier Analysis for bladed wheels damage detection. *J. Sound Vib., 356*, 181–194.

37. Schicht, A., Schwarzer, S., & Schmidt, L.-P. (2012). Tip Clearance Measurement Technique for Stationary Gas Turbines Using an Autofocusing Millimeter-Wave Synthetic Aperture Radar. *IEEE Trans. Instrum. Meas., 61*(6), 1778–1785.

38. Tomassini, R., Rossi, G., & Brouckaert, J.-F. (2016). On the development of a magnetoresistive sensor for blade tip timing and blade tip clearance measurement systems. *Rev. Sci. Instrum., 87*(10), 102505.

39. Gopalakrishnan, S. (2011). *Computational techniques for structural health monitoring.* London, UK: Springer.

40. Przysowa, R., & Rokicki, E. (2015). Inductive sensors for blade tip-timing in gas turbines. *J. KONBIN, 36*(1), 147-164.

41. Lawson, C. P., & Ivey, P. C. (2005). Tubomachinery blade vibration amplitude measurement through tip timing with capacitance tip clearance probes. *Sens. Actuators A Phys., 118*(1), 14–24.

42. Tomassini, R., Rossi, G., & Brouckaert, J.-F. On the development of a magnetoresistive sensor for blade tip timing and blade tip clearance measurement systems. In *AIP Conference Proceeding*. (Volume 1600). Melville, NY, USA: AIP Publishing.

43. Reinhardt, A. K., Kadambi, J. R., & Quinn, R. D. (1995). Laser vibrometry measurements of rotating blade vibrations. *J. Eng. Gas Turb. Power, 117*(3), 484–488.

44. Lezhin, D. S., Falaleev, S. V., Safin, A. I., Ulanov, A. M., & Vergnano, D. (2017). Comparison of Different Methods of Non-contact Vibration Measurement. *Procedia Eng., 176*, 175–183.

45. Heath, S., & Imregun, M. (1996). An improved single-parameter tip-timing method for turbomachinery blade vibration measurements using optical laser probes. *Int. J. Mech. Sci., 38*(10), 1047–1058.

46. Battiato, G., Firrone, C. M., & Berruti, T. M. (2017). Forced response of rotating bladed disks: Blade Tip-Timing measurements. *Mech. Syst. Signal Process., 85*, 912–926.

47. Di Maio, D., & Ewins, D. J. (2012). Experimental measurements of out-of-plane vibrations of a simple blisk design using Blade Tip Timing and Scanning LDV measurement methods. *Mech. Syst. Signal Process., 28*, 517–527.

48. Chen, Z., Yang, Y., Xie, Y., Guo, B., & Hu, Z. (2013). Non-contact crack detection of high-speed blades based on principal component analysis and Euclidian angles using optical-fiber sensors. *Sens. Actuators A Phys., 201*, 66–72.

49. Gwashavanhu, B., Oberholster, A. J., & Heyns, P. S. (2016). Rotating blade vibration analysis using photogrammetry and tracking laser Doppler vibrometry. *Mech. Syst. Signal Process., 76-77*, 174–186.

50. Büttner, L., Pfister, T., & Czarske, J. (2006). Fiber-optic laser Doppler turbine tip clearance probe. *Opt. Lett., 31*(9), 1217–1219.

51. Pfister, T., Büttner, L., Czarske, J., Krain, H., & Schodl, R. (2006). Turbo machine tip clearance and vibration measurements using a fibre optic laser doppler position sensor. *Meas. Sci. Technol., 17*(7), 1693–1705.

52. Gil-Garcia, J. M., Garcia, I., Zubia, J., & Aranguren, G. (2015). Measurement of blade tip clearance and time of arrival in turbines using an optic sensor. In *Proceedings of the 2015 International Conference on Applied Electronics (AE), Pilsen, Czech Republic, 8–9 September 2015.*

53. Zielinski, M., & Ziller, G. (2000). Noncontact vibration measurements on compressor rotor blades. *Measurement Science And Technology, 11*(7), 847–856.

54. Overton, G. (2006). Fiberoptic probe measures turbine tip clearance. *Laser Focus World, 42*(6), 20–23.

55. Sharma, V. K., Hanagud, S., & Ruzzene, M. (2006). Damage Index Estimation in Beams and Plates Using Laser Vibrometry. *Aiaa J., 44*(4), 919–923.

56. García, I., Zubia, J., Beloki, Ayesta, et al. (Eds.) (2016) *8th European Workshop On Structural Health Monitoring (EWSHM 2016), Bilbao, Spain, 5-8 July 2016.*

57. Günther, P., Dreier, F., Pfister, T., Czarske, J., Haupt, T., & Hufenbach, W. (2011). Measurement of radial expansion and tumbling motion of a high-speed rotor using an optical sensor system. *Mech. Syst. Signal Process., 25*(1), 319–330.

58. Oberholster, A. J., & Heyns, P. S. (2011). Eulerian laser Doppler vibrometry: Online blade damage identification on a multi-blade test rotor. *Mech. Syst. Signal Process., 25*(1), 344–359.

59. Pfister, T., Büttner, L., & Czarske, J. (2005). Laser doppler profile sensor with sub-micrometre position resolution for velocity and absolute radius measurements of rotating objects. *Meas. Sci. Technol., 16*(3), 627–641.

60. Przysowa, R., Majewski, P., & Rokicki, E. (2014). Optimized magnetic sensors to measure speed and position in adverse environments. In *Proceedings of the IET & ISA 60th International Instrumentation Symposium 2014, Cavendish Square, London, UK, 24–26 June 2014.*

61. Procházka, P. (2016). Sensors for noncontact vibration diagnostics in rotating machinery. In *AIP Conference Proceedings*. (Volume 1740). Melville, NY, USA: AIP Publishing.

62. Roeseler, C., Flotow, A. von, & Tappert, P. (2002). Monitoring blade passage in turbomachinery through the engine case (no holes). In *Proceedings of the IEEE Aerospace Conference Proceedings, Big Sky, MT, USA, 9–16 March 2002.*

63. Ghoshal, A., Le, D., & Kim, H. (2012). Technological assessment of high temperature sensing systems under extreme environment. *Sens. Rev., 32*(1), 66–71.

64. Neumann, M., Dreier, F., Günther, P., Wilke, U., Fischer, A., Büttner, L., et al. (2015). A laser-optical sensor system for blade vibration detection of high-speed compressors. *Mech. Syst. Signal Process., 64-65*, 337–346.

65. Cardwell, D. N., Chana, K. S., & Russhard, P. (2008). The use of eddy current sensors for the measurement of rotor blade tip timing-sensor development and engine testing. In *Proceedings of the ASME Turbo Expo 2008, Power for Land, Sea and Air, Berlin, Germany, 9–13 June 2008*. (Volume 2). Berlin, Germany: American Society of Mechanical Engineers.

66. Liu, C., & Jiang, D. (2012). Improved Blade Tip Timing in Blade Vibration Monitoring with Torsional Vibration of the Rotor. *J. Phys. Conf. Ser., 364*, 12136.

67. Chana, K. S., Sridhar, V., & Singh, D. (2016). The use of eddy current sensors for the measurement of rotor blade tip timing: Development of a new method based on integration. In *Proceedings of the ASME Turbo Expo 2016, Turbomachinery Technical Conference and Exposition, Seoul, South Korea, 13–17 June 2016*. (Volume 6). Seoul, South Korea: American Society of Mechanical Engineers.

68. Tsutomu, M., Sho, G., Kenta, D., Yoshinori, K., Yuichi, A., Shigemi, E., et al. (2011). Method for Identifying Type of Eddy-Current Displacement Sensor. *IEEE Trans. Magn., 47*(10), 3554–3557.

69. Przysowa, R., & Spychała, J. (2008). Health Monitoring of Turbomachinery Based on Blade Tip-Timing and Tip-Clearance: RTO-MP-AVT-157. https://www.researchgate.net/profile/Radoslaw_Przysowa/publication/273137276_Health_Monitoring_of_Turbomachinery_Based_on_Blade_Tip-Timing_and_Tip-Clearance/links/54f97cfa0cf28d6deca4a6d9/Health-Monitoring-of-Turbomachinery-Based-on-Blade-Tip-Timing-and-Tip-Clearance.pdf. Accessed 10 October 2018.

70. Procházka, P., & Vanek, F. (2013). New methods of non-contact sensing of blade vibrations and deflections in turbomachinery. In *Proceedings of the 2013 IEEE International Instrumentation and Measurement Technology Conference (I2MTC), Minneapolis, MN, USA, 6–9 May 2013.*

71. Procházka, P., & Vank, F. (2011). Contactless diagnostics of turbine blade vibration and damage. *J. Phys. Conf. Ser., 305*(1), 12116.

72. Brouckaert, J.-F., Marsili, R., Rossi, G., & Tomassini, R. (2012). Development and experimental characterization of a new non contact sensor for blade tip timing. In *AIP Conference Proceedings, AIP Conference Proceedings*. (Volume 1457). Melville, NY, USA: AIP Publishing.

73. Tomassini, R., & Rossi, G. (2016). Noncontact vibration measurements using magnetoresistive sensing elements. In *AIP Conference Proceedings*, *AIP Conference Proceedings*. (Volume 1740). Melville, NY, USA: AIP Publishing.

74. Tomassini, R. (2016). *Blade Tip Timing and Blade Tip Clearance Measurement System Based on Magnetoresistive Sensors*. Ph.D. Thesis. University of Padua, Padua, Italy.

75. Lawson, C. P. (2003). *Capacitance Tip Timing Techniques in Gas Turbines*. Ph.D. Thesis. Cranfield University, Silsoe, UK.

76. Steiner, A. (2000). Techniques for blade tip clearance measurements with capacitive probes. *Meas. Sci. Technol., 11*(7), 865–869.

77. Sarma, G. R., & Barranger, J. P. (1992). Capacitance-type blade-tip clearance measurement system using a dual amplifier with ramp/DC inputs and integration. *IEEE Trans. Instrum. Meas., 41*(5), 674–678.

78. Drumm, M., & Hause, W. C. (2000). High performance rotor monitoring. In *roceedings of the 19th 2000 Digital Avionics Systems Conference (DASC), Philadelphia, PA, USA, 7–13 October 2000*. (Vol. 2).

79. Mönich, M., & Bailleul, G. (1993). Capacitive Measurement System for Blade Clearances. *Sens. Rev., 13*(4), 23–26.

80. Mueller, D., Mozumdar, S., & Johann, E. (1997). Capacitive measurement of compressor and turbine blade tip to casing running clearance. *J. Eng. Gas Turbines Power, 119*(4), 877–884.

81. Fabian, T., Sangkyun Kang, F., & Prinz, F. (2002). Capacitive blade tip clearance measurements for a micro gas turbine. In *Proceedings of the 19th IEEE IMTC/2002 Instrumentation and Measurement Technology Conference, Anchorage, AK, USA, 21–23 May 2002*. (Volume 2).

82. Lavagnoli, S., Paniagua, G., Tulkens, M., & Steiner, A. (2012). High-fidelity rotor gap measurements in a short-duration turbine rig. *Mech. Syst. Signal Process., 27*, 590–603.

83. Sinha, J. K., & Elbhbah, K. (2013). A future possibility of vibration based condition monitoring of rotating machines. *Mech. Syst. Signal Process., 34*(1-2), 231–240.

84. Abdelrhman, A. M., Leong, M. S., Saeed, S. A. M., & Al Obiadi, S. M. A. A.-O. (2012). A Review of Vibration Monitoring as a Diagnostic Tool for Turbine Blade Faults. *Appl. Mech. Mater., 229-231*, 1459–1463.

85. Elmaleeh, M., & Saad, N. (2008). Development of acoustic emission diagnostic system for condition monitoring of rotating machines. In *Proceedings of the IEEE 2nd International Power and Energy Conference (PECon), Johor Bahru, Malaysia, 1–3 December 2008.*

86. Lim, M. H., & Leong, M. S. (2010). Improved Blade Fault Diagnosis Using Discrete Blade Passing Energy Packet and Rotor Dynamics Wavelet Analysis. In *Proceedings of the ASME Turbo Expo 2010, ASME Turbo Expo 2010: Power for Land, Sea, and Air, Glasgow, UK, June 14–18, 2010*. (pp. 31–37). New York, NY, USA: ASME.

87. Abdelrhman, A. M., Hee, L. M., Leong, M. S., & Al-Obaidi, S. (2015). Condition Monitoring of Blade in Turbomachinery: A Review. *Adv. Mech. Eng., 6*(4), 210717.

88. Hee, L. M., & Leong, M. S. (2010). Improved blade fault diagnosis using discrete Blade Passing Energy Packet and rotor dynamics wavelet analysis. In *Proceedings of the ASME Turbo Expo 2010: Power for Land, Sea and Air, Glasgow, UK, 17–18 June 2010*: American Society of Mechanical Engineers. (Vol. 3).

89. Südmersen, Ü., Pietsch, O., Scheer, C., Reimche, W., & Bach, F.-W. (2002). Condition Monitoring of Steam Turbines by combined vibration and process parameter analysis. In *Proceedings of the Conferência Technologia de Equipamentos, Salvador, Brazil, 9–12 September 2002.*

90. Lebold, M. S., Maynard, K., Reichard, K., Trethewey, M., Bieryla, D., Lissenden, C., et al. (2004). Using torsional vibration analysis as a synergistic method for crack detection in rotating equipment. In *Proceedings of the 2004 IEEE Aerospace Conference, Big Sky, MT, USA, 6–13 March 2004*. (Vol. 6).

91. Leong, M. S. (2008). Field Experiences of Gas Turbines Vibrations -A Review and Case Studies. *J. Syst. Des. Dyn., 2*(1), 24–35.

92. Al-Bedoor, B. O., Ghouti, L., Adewusi, S. A., Al-Nassar, Y., & Abdlsamad, M. (2003). Experiments on the extraction of blade vibration signature from the shaft torsional vibration signals. *J. Qual. Maint. Eng., 9*(2), 144–159.

93. Yu Zhang, S. Cruz-Manzo, & A. Latimer (2016). Start-up Vibration Analysis for Novelty Detection on Industrial Gas Turbines. In *Proceedings of the 2016 International Symposium on Industrial Electronics (INDEL), Banja Luka, Bosnia Herzegovina, 3–5 November 2016.*

94. Loutas, T. H., Roulias, D., Pauly, E., & Kostopoulos, V. (2011). The combined use of vibration, acoustic emission and oil debris on-line monitoring towards a more effective condition monitoring of rotating machinery. *Mech. Syst. Signal Process.*, *25*(4), 1339–1352.

95. Schlagwein, G., & Schaber, U. (2006). Non-contact blade vibration measurement analysis using a multi-degree-of-freedom model. *Proc. Inst. Mech. Eng. Part A: J. Power Energy*, *220*(6), 611–618.

96. Sendhil, K. S., & Senthil, K., M. (2014). Condition monitoring of rotating machinery through vibration analysis. *J. Sci. Ind. Res.*, *73*(4), 258–261.

97. Yunusa-kaltungo, A., & Sinha, J. K. (2017). Effective vibration-based condition monitoring (eVCM) of rotating machines. *J. Qual. Maint. Eng.*, *23*(3), 279–296.

98. Matthaiou, I., Khandelwal, B., & Antoniadou, I. (2017). Vibration Monitoring of Gas Turbine Engines: Machine-Learning Approaches and Their Challenges. *Front. Built Environ.*, *3*, 54.

99. Lifson, A., Quentin, G. H., Smalley, A. J., & Knauf, C. L. (1989). Assessment of gas turbine vibration monitoring. *J. Eng. Gas Turbines Power*, *111*(2), 257–263.

100. Fábry, S., & Češkovič, M. (2017). Aircraft gas turbine engine vibration diagnostics. *Mag. Aviat. Dev.*, *5*(4), 24–28.

101. Madhavan, S., Jain, R., Sujatha, C., & Sekhar, A. S. (2014). Vibration based damage detection of rotor blades in a gas turbine engine. *Eng. Fail. Anal.*, *46*, 26–39.

102. Djaidir, B., Hafaifa, A., & Kouzou, A. (2017). Faults detection in gas turbine rotor using vibration analysis under varying conditions. *J. Theory Appl. Mech.*, *55*(2), 393–406.

103. Gubran, A. A., & Sinha, J. K. (2014). Shaft instantaneous angular speed for blade vibration in rotating machine. *Mech. Syst. Signal Process.*, *44*(1-2), 47–59.

104. Kumar, S., Roy, N., & Ganguli, R. (2007). Monitoring low cycle fatigue damage in turbine blade using vibration characteristics. *Mech. Syst. Signal Process.*, *21*(1), 480–501.

105. Rajagopalan, V., Behera, A., Bhattacharya, A., Prabhu, R., & Badami, V. (2012). Estimation of static deflection under operational conditions for blade health monitoring. In *Proceedings of the 2012 IEEE Conference on Prognostics and System Health Management (PHM), Beijing, China, 23–25 May 2012*.

106. Heath, S., & Imregun, M. (1998). A survey of blade tip-timing measurement techniques for turbomachinery vibration. *J. Eng. Gas Turbines Power*, *120*(4), 784–791.

107. Hu, Z., Lin, J., Chen, Z.-S., Yang, Y.-M., & Li, X.-J. (2015). A Non-Uniformly Under-Sampled Blade Tip-Timing Signal Reconstruction Method for Blade Vibration Monitoring. *Sensors*, *15*(2), 2419–2437.

108. Guru, S. S., Shylaja, S., Kumar, S., & Murthy, R. (2014). Pre-emptive Rotor Blade Damage Identification by Blade Tip Timing Method. *J. Eng. Gas Turb. Power*, *136*(7), 72503.

109. Heath, S. (2000). A new technique for identifying synchronous resonances using tip-timing. *J. Eng. Gas Turb. Power*, *122*(2), 219–225.

110. Pan, M., Yang, Y., Guan, F., Hu, H., & Xu, H. (2017). Sparse Representation Based Frequency Detection and Uncertainty Reduction in Blade Tip Timing Measurement for Multi-Mode Blade Vibration Monitoring. *Sensors*, *17*(8), 1745.

111. Wu, F., Liang, L., Xing, J., Wang, L., & Jia, L. (2014). Blade tip timing vibration monitoring method based on fiber Bragg grating. *Photonic Sens.*, *4*(2), 188–192.

112. Rao, R. A., & Dutta, B. K. (2012). Vibration analysis for detecting failure of compressor blade. *Eng. Fail. Anal.*, *25*, 211–218.

113. Jones, H. (1996). Shedding light on vibration. *Mech. Eng.*, *118*(11), 94–98.

114. Kadoya, Y., Mase, M., Kaneko, Y., Umemura, S., Oda, T., & Johnson, C. M. (1995). Noncontact Vibrational Measurement Technology of Steam Turbine Blade. *JSME Int. J. Ser. C Dyn. Control Robot. Des. Manuf.*, *38*(3), 486–493.

115. Satyam, M., Rao, V., & Devy, C. G. (1994). Cepstrum Analysis -An Advanced Technique in Vibration Analysis of Defects in Rotating Machinery. *Def. Sci. J.*, *44*(1), 53–60.

116. Sinha, J. K., Hahn, W., Elbhbah, K., Tasker, G., & Ullah, I. (2012). Vibration investigation for low pressure turbine last stage blade failure in steam turbines of a power plant. In *In Proceedings of the ASME Turbo Expo 2012, Copenhagen, Denmark, 11–15 June 2012*. (Volume 7). Copenhagen, Denmark: American Society of Mechanical Engineers.

117. Sinha, J. K. (2015). *Vibration engineering and technology of machinery: Proceedings of VETOMAC X 2014, held at the University of Manchester, UK, 9-11 September 2014.* Cham, Switzerland: Springer.

118. Warren, C., Niezrecki, C., & Avitabile, P. (2011). Optical non-contacting vibration measurement of rotating turbine blades II. In *Conference Proceedings of the Society for Experimental Mechanics Series*. (Volume 1). New York, NY, USA: Springer.

119. Di Maio, D., & Castellini, P. (2017). *Rotating Machinery, Hybrid Test Methods, Vibro-Acoustics & Laser Vibrometry, Volume 8: Proceedings of the 35th IMAC, A Conference and Exposition on Structural Dynamics 2017.* Cham, Switzerland: Springer.

120. Deraemaeker, A. (2010). *New trends in vibration based structural health monitoring.* Vienna, Austria: Springer.

121. Tagashira, T., Sugiyama, N., Matsuda, Y., & Matsuki, M. (1997). *Measurement of blade tip clearance using an ultrasonic sensor.* Reston, VA, USA: American Institute of Aeronautics and Astronautics.

122. Tagashira, T., Sugiyama, N., Matsuda, Y., & Matsuki, M. (1998). *An experimental study of ultrasonic tip clearance sensor.* Reston, VA, USA: American Institute of Aeronautics and Astronautics.

123. Giurgiutiu, V. (2014). *Structural health monitoring with piezoelectric wafer active sensors.* Oxford, UK: Elsevier Academic Press.

124. Cheeke, J. D. N. (2002). *Fundamentals and applications of ultrasonic waves*. (CRC series in pure and applied physics). Boca Raton, FL, USA: CRC Press.

125. Cho, H., & Lissenden, C. J. (2012). Structural health monitoring of fatigue crack growth in plate structures with ultrasonic guided waves. *Struct. Health Monit.*, *11*(4), 393–404.

126. Chan, H., Masserey, B., & Fromme, P. (2015). High frequency guided ultrasonic waves for hidden fatigue crack growth monitoring in multi-layer model aerospace structures. *Smart Mater. Struct.*, *24*(2), 25037.

127. Masserey, B., & Fromme, P. (2017). Analysis of high frequency guided wave scattering at a fastener hole with a view to fatigue crack detection. *Ultrasonics*, *76*, 78–86.

128. Masserey, B., & Fromme, P. (2015). In-situ monitoring of fatigue crack growth using high frequency guided waves. *NDT E Int.*, *71*, 1–7.

129. Masserey, B., & Fromme, P. Noncontact monitoring of fatigue crack growth using high frequency guided waves. In *SPIE 9061, Sensors and Smart Structures Technologies for Civil, Mechanical, and Aerospace Systems 2014*, *SPIE 9061, Sensors and Smart Structures Technologies for Civil, Mechanical, and Aerospace Systems 2014.* San Diego, California, USA.

130. Masserey, B., & Fromme, P. (2013). Fatigue crack growth monitoring using high-frequency guided waves. *Struct. Health Monit.*, *12*(5-6), 484–493.

131. Vanlanduit, S., Guillaume, P., & van der Linden, G. (2003). On-line monitoring of fatigue cracks using ultrasonic surface waves. *NDT E Int.*, *36*(8), 601–607.

132. Masserey, B., Aebi, L., & Mazza, E. (2006). Ultrasonic surface crack characterization on complex geometries using surface waves. *Ultrasonics*, *44 (Suppl. 1)*, e957–e961.

133. Lin, B., Zhang, L., Dorantes, D., Li, Y., Fu, X., & Hu, X. (2011). Numerical simulation of surface acoustic wave and detection of surface crack in steel. *Trans. Tianjin Univ.*, *17*(4), 254–258.

134. Mukhopadhyay, S. C. (2011). *New Developments and Applications in Sensing Technology*. (1st edn, Vol. 83). Berlin / Heidelberg, Germany: Springer.

135. Willberg, C., Duczek, S., Vivar-Perez, J. M., & Ahmad, Z. A. B. (2015). Simulation Methods for Guided Wave-Based Structural Health Monitoring: A Review. *Appl. Mech. Rev.*, *67*(1), 10803.

136. Rose, J. L., & Soley, L. E. (2000). Ultrasonic guided waves for anomaly detection in aircraft components. *Mater. Eval.*, *58*, 1080-1086.

137. Achenbach, J. D., Lin, W., & Keer, L. M. (1986). Mathematical modelling of ultrasonic wave scattering by sub-surface cracks. *Ultrasonics*, *24*(4), 207–215.

138. Rose, J. L., Pelts, S. P., & Quarry, M. J. (1998). A comb transducer model for guided wave NDE. *Ultrasonics*, *36*(1), 163–169.

139. Malfense Fierro, G. P. (2014). *Development of Nonlinear Ultrasound Techniques for Multidisciplinary Engineering Applications*. Ph.D. Thesis. University of Bath, Bath, UK.

140. Dutta, D., Sohn, H., Harries, K. A., & Rizzo, P. (2009). A Nonlinear Acoustic Technique for Crack Detection in Metallic Structures. *Struct. Health Monit.*, *8*(3), 251–262.

141. Friswell, M. I., & Penny, J. E. T. (2002). Crack Modeling for Structural Health Monitoring. *Struct. Health Monit.*, *1*(2), 139–148.

142. Kawashima, K., Omote, R., Ito, T., Fujita, H., & Shima, T. (2002). Nonlinear acoustic response through minute surface cracks: FEM simulation and experimentation. *Ultrasonics*, *40*(1), 611–615.

143. Morris, W. L., Buck, O., & Inman, R. V. (1979). Acoustic harmonic generation due to fatigue damage in high-strength aluminum. *J. Appl. Phys.*, *50*(11), 6737–6741.

144. Nazarov, V. E., & Sutin, A. M. (1997). Nonlinear elastic constants of solids with cracks. *Acoust. Soc. Am.*, *102*(6), 3349–3354.

145. Ostrovsky, L. A. (1991). Wave processes in media with strong acoustic nonlinearity. *Acoust. Soc. Am.*, *90*(6), 3332–3337.

146. Barnard, D. J. (2002). Monitoring Fatigue Damage Accumulation with Rayleigh Wave Harmonic Generation Measurements. In *Proceedings of the AIP Conference, Bellingham, WA, USA, 14–19 July 2002*. (pp. 1393–1400).

147. Berwig, P. (2014). *Anwendung von Ultraschall-Rayleigh-Wellen zur Rissdetektion an Turbinenschaufeln aus Titanaluminid*. Bachelor Thesis. Hochschule für Angewandte Wissenschaften München, Munich, Germany. (In German)

148. Rau, E., Bamberg, J., Burchards, J., Berwig, & P., Voelkl, W. High resolution crack detection on turbine blade roots by the use of eddy current and ultrasonic Rayleigh waves. http://www.ndt.net/article/wcndt2016/papers/we3a2.pdf. Accessed 1 March 2018.

149. Rau, E., Bamberg J., & Berwig, P. (2015). Ultraschallprüfung an Turbinenschaufeln mittels Oberflächenwellen. https://www.dgzfp.de/Portals/ ultraschall2015/BB/8.pdf. Accessed 24 February 2018. (In German)

150. Lane, C. (2014). *The Development of a 2D Ultrasonic Array Inspection for Single Crystal Turbine Blades.* Cham, Switzerland: Springer.

151. Olympus (2004). *Introduction to Phased Array Ultrasonic Technology Applications: Olympus guideline.* Waltham, MA, USA: Olympus.

152. Drinkwater, B. W., & Wilcox, P. D. (2006). Ultrasonic arrays for non-destructive evaluation: A review. *NDT E Int.*, *39*(7), 525–541.

153. Chatillon, S., Cattiaux, G., Serre, M., & Roy, O. (2000). Ultrasonic non-destructive testing of pieces of complex geometry with a flexible phased array transducer. *Ultrasonics*, *38*(1-8), 131–134.

154. Harrold, R. T., & Sanjana, Z. N. (2002). *Acoustic waveguide sensing the condition of components within gas turbines*. (U.S. Patent 6487909B2).

155. Harrold, R. T., & Sanjana, Z. N. (2006). *Monitoring thermal barrier coating deterioration via acoustic response to gas flow, pressure and impact*. (U.S. Patent 7062971B2).

156. Willsch, M., Bosselmann, T., & Theune, N. M. (2004). New approaches for the monitoring of gas turbine blades and vanes. In *Proceedings of the Sensors 2004 IEEE, Vienna, Austria, 24–27 October 2004.*

157. Atkinson, D., & Hayward, G. (2001). The generation and detection of longitudinal guided waves in thin fibers using a conical transformer. *IEEE Trans. Ultrason. Ferroelectr. Freq. Control, 48*(4), 1046–1053.

158. Wai, Y., Gao, Y., Xiao, Z., Wang, G., Tian, M., & Liang, H. (2016). Ultrasonic Al_2O_3 Ceramic Thermometry in High-Temperature Oxidation Environment. *Sensors, 16*(11), 1905.

159. Carlson, N. M., Musick, C. A., Watkins, A. D., Tillotson, R. D., & Mullenix, P. D. (1999). Evaluation of a novel temperature sensing probe for monitoring and controlling glass temperature in a joule-heated glass melter. In *Proceedings of the Waste management Science Technology in the Ceramic and Nuclear industries (Symbosium I), Indianapolis, IN, USA, 25–28 April 1999.* Austin, TX, USA: American Ceramic Society.

160. Periyannan, S., Rajagopal, P., & Balasubramaniam, K. (2017). Ultrasonic bent waveguides approach for distributed temperature measurement. *Ultrasonics, 74*, 211–220.

161. Huang, K. N., Huang, C. F., Li, Y. C., & Young, M. S. (2003). Temperature measurement system based on ultrasonic phase-shift method. In *Proceedings of the 2003 IEEE EMBS Asian-Pacific Conference on Biomedical Engineering, Kyoto, Japan, 20–22 October 2003.*

162. Tsai, W.-Y., Chen, H.-C., & Liao, T.-L. (2005). An ultrasonic air temperature measurement system with self-correction function for humidity. *Meas. Sci. Technol., 16*(2), 548–555.

163. Dyrwal, A., Meo, M., & Ciampa, F. (2018). Nonlinear air-coupled thermosonics for fatigue micro-damage detection and localisation. *NDT E Int., 97*(3), 59–67.

164. Zhang, D. (2014). *Study of Chaotic Ultrasound and Frequency Sweep Excitations in Sonic IR NDE Technology*. Ph.D. Thesis. Wayne State University, Detroit, MI, USA.

165. Chimenti, D. E. (2014). Review of air-coupled ultrasonic materials characterization. *Ultrasonics, 54*(7), 1804–1816.

166. Lim, H. J., Song, B., Park, B., & Sohn, H. (2015). Noncontact fatigue crack visualization using nonlinear ultrasonic modulation. *NDT E Int., 73*, 8–14.

167. Thiele, S., Kim, J.-Y., Qu, J., & Jacobs, L. J. (2014). Air-coupled detection of nonlinear Rayleigh surface waves to assess material nonlinearity. *Ultrasonics, 54*(6), 1470–1475.

168. Zhou, Z., Zhang, K., Zhou, J., Sun, G., & Wang, J. (2015). Application of laser ultrasonic technique for non-contact detection of structural surface-breaking cracks. *Opt. Laser Technol., 73*, 173–178.

169. Arias, I. (2003). *Modeling of the Detection of Surface-Breaking Cracks by Laser Ultrasonics*. Ph.D. Thesis, Northwestern University, Evanston, IL, USA.

170. Liu, P., Nazirah, A. W., & Sohn, H. (2016). Numerical simulation of damage detection using laser-generated ultrasound. *Ultrasonics, 69*, 248–258.

171. An, Y.-K., Kwon, Y., & Sohn, H. (2013). Noncontact laser ultrasonic crack detection for plates with additional structural complexities. *Struct. Health Monit., 12*(5-6), 522–538.

172. Pei, C., Demachi, K., Fukuchi, T., Koyama, K., & Uesaka, M. (2013). Cracks measurement using fiber-phased array laser ultrasound generation. *J. Appl. Phys., 113*(16), 163101.

173. Dhital, D., & Lee, J. (2012). A Fully Non-Contact Ultrasonic Propagation Imaging System for Closed Surface Crack Evaluation. *Exp. Mech., 52*(8), 1111–1122.

174. Amini, M. H., Sinclair, A. N., & Coyle, T. W. (2015). High Temperature Ultrasonic Transducer for Real-time Inspection. *Phys. Procedia, 70*, 343–347.

175. Kažys, R., Voleišis, A., & Voleišienė, B. (2008). High temperature ultrasonic transducers. *Ultragarsas, 63*(2), 7–17.

176. Searfass, C. T., & Tittmann, B. R. (2010). High temperature ultrasonic transducer up to 1000 °C using lithium niobate single crystal. *Appl. Phys. Lett., 97*(23), 232901.

177. Salas, K. I., & Cesnik, C. E. S. (2009). Guided wave excitation by a CLoVER transducer for structural health monitoring: theory and experiments. *Smart Mater. Struct., 18*(7), 75005.

178. Edwards, R. S., Dixon, S., & Jian, X. (2006). Depth gauging of defects using low frequency wideband Rayleigh waves. *Ultrasonics, 44*(1), 93–98.

179. Jian, X., Dixon, S., Guo, N., & Edwards, R. (2007). Rayleigh wave interaction with surface-breaking cracks. *J. Appl. Phys., 101*(6), 64906.

180. Jian, X., Dixon, S., Guo, N., Edwards, R. S., & Potter, M. (2006). Pulsed Rayleigh wave scattered at a surface crack. *Ultrasonics, 44 (Suppl. 1)*, e1131-e1344.

181. Dixon, S., Burrows, S. E., Dutton, B., & Fan, Y. (2011). Detection of cracks in metal sheets using pulsed laser generated ultrasound and EMAT detection. *Ultrasonics, 51*(1), 7–16.

182. Kerr, C., & Ivey, P. (2004). Optical pyrometry for gas turbine aeroengines. *Sens. Rev., 24*(4), 378–386.

183. Feist, J. P., Sollazzo, P. Y., Berthier, S., Charnley, B., & Wells, J. (2012). Precision Temperature Detection Using a Phosphorescence Sensor Coating System on a Rolls-Royce Viper Engine. In *Proceedings of the ASME Turbo Expo 2012, Copenhagen, Denmark, 11 June 2012*. (pp. 917–926). New York, NY, USA: American Society of Mechanical Engineers.

184. Meher-Homji, C. B. (1995). Blading Vibration and Failures in Gas Turbines: Part C — Detection and Troubleshooting. In *ASME 1995 International Gas Turbine and Aeroengine Congress and Exposition, ASME 1995 International Gas Turbine and Aeroengine Congress and Exposition, Houston, TX, USA, 5 June 1995*. (p. V004T11A016). New York, NY, USA: American Society of Mechanical Engineers.

185. Rohy, D. A., & Compton, W. A. (1972). Radiation Pyrometer for Gas Turbine Bades. *SAE Trans., 81*, 720001–720196.

186. Becker, W. J., Roby, R. J., O'Brien, W. F., & Bensing, G. K. (1994). Dynamic turbine blade temperature measurements. *J. Propul. Power, 10*(1), 69–78.

187. Beynon, T. G. R. (1981). *Turbine Pyrometry - An Equipment Manufacturer's View.* New York, NY, USA: ASME.

188. Lucia, M., & Lanfranchi, C. (1994). An infrared pyrometry system for monitoring gas turbine blades: Development of a computer model and experimental results. *J. Eng. Gas Turb. Power, 116*(1), 172–177.

189. Douglas, J., Smith, C. A., & Taylor, S. (1999). An integrated approach to the application of high bandwidth optical pyrometry to turbine blade surface temperature mapping. In *Proceedings of the 18th International Congress on Instrumentation in Aerospace Simulation Facilities, Toulouse, France, 14–17 June 1999.*

190. Alaruri, S., Bianchini, L., & Brewington, A. (1998). Effective spectral emissivity measurements of superalloys and YSZ thermal barrier coating at high temperatures using a 1.6µm single wavelength pyrometer. *Opt. Lasers Eng., 30*(1), 77–91.

191. Gao, S., Feng, C., Wang, L., & Li, D. (2016). Multi-spectral temperature measurement method for gas turbine blade. *Opt. Rev., 23*(1), 17–25.

192. Kerr, C. (2002). An overview of the measurement errors associated with gas turbine aeroengine pyrometer systems. *Meas. Sci. Technol., 13*(6), 873–881.

193. Ketui, D., Chi, F., & Shan, G. (2016). Single wavelength and ratio pyrometry reflection errors in temperature measurement of gas turbine blade. *Measurement, 86*, 133–140.

194. Lemieux, D. H. (2003). On-Line Thermal Barrier Coating Monitoring for Real-Time Failure Protection and Life Maximization. Orlando, FL, USA: Siemens Westinghouse Power Corporation.

195. Bison, P. G., Cernuschi, F., & Grinzato, E. (2006). Ageing evaluation of thermal barrier coating: Comparison between pulsed thermography and thermal wave interferometry. *Quant. Infrared Thermogr. J., 3*(2), 169–181.

196. Bison, P., Cernuschi, F., & Grinzato, E. (2008). In-depth and In-plane Thermal Diffusivity Measurements of Thermal Barrier Coatings by IR Camera: Evaluation of Ageing. *Int. J. Thermophys., 29*(6), 2149–2161.

197. Sun, J. G., & Tao, N. (2016). Thermal property measurement for thermal barrier coatings using pulsed thermal imaging – multilayer analysis method, *1706*, 100004.

198. Meola, C., Carlomagno, G. M., Di Foggia, M., & Natale, O. (2008). Infrared thermography to detect residual ceramic in gas turbine blades. *Appl. Phys. A, 91*(4), 685–691.

199. Topal, A., Catori, C., Cagan, L., Uslu, S., Turan, O., & Piskin, A. (2014). One-Dimensional Heat Transfer Analysis and Experimental Investigation of a Gas Turbine Combustor. In *Proceedings of the CONV-14: International Symposium on Convective Heat and Mass Transfer, Kusadasi, Turkey, 8–13 June 2014*. (p. 15). Antalya, Turkey: Begell House.

200. Feist, J. P., Sollazzo, P. Y., Berthier, S., Charnley, B., & Wells, J. (2012). Application of an Industrial Sensor Coating System on a Rolls-Royce Jet Engine for Temperature Detection. In *Proceedings of the ASME Turbo Expo 2012, Copenhagen, Denmark, 11–15 June 2012*. (p. 191).

201. Heyes, A. L., Rabhiou, A., Feist, J. P., & Kempf, A. M. (2012). Phosphor Based Temperature Indicating Paints. In *Proceedings of the ASME Turbo Expo 2012, Copenhagen, Denmark, 11 June 2012*. (p. 927). New York, NY, USA: American Society of Mechanical Engineers.

202. Pilgrim, C. C., Sollazzo, P. Y., Feist, J. P., Beyrau, F., Heyes, A. L., Yañez Gonzalez, A., et al. (2014). Temperature Sensing inside Thermal Barrier Coatings using Phosphor Thermometry. In *Proceedings of the IET & ISA 60th International Instrumentation Symposium, London, UK, 24-26 June 2014*. (p. 3.1.2).

203. Yañez, G. A., Pilgrim, C. C., Feist, J. P., Sollazzo, P. Y., Beyrau, F., & Heyes, A. L. (2015). On-Line Temperature Measurement Inside a Thermal Barrier Sensor Coating During Engine Operation. *J. Turbomach., 137*(10), 101004.

204. Khalid, A. H., Kontis, K., & Behtash, H.-Z. (2010). Phosphor thermometry in gas turbines: Consideration factors. *Proc. Inst. Mech. Eng. Part G J. Aerosp. Eng., 224*(7), 745–755.

205. Pilgrim, C. C., González, A. Y., Saggese, R., Krewinkel, R., Blaswich, M., Feist, J. P., et al. (2017). Surface temperature measurement in an industrial gas turbine using thermal history paints. In *Proceedings of 12th European Conference on Turbomachinery Fluid dynamics & Thermodynamics, Stockholm, Sweden, 3–7 April 2017*. (ETC2017-303).

206. Krewinkel, R., Färber, J., Lauer, M., Frank, D., Orth, U., Gonzalez, A. Y., et al. (2016). Validation of Surface Temperature Measurements on a Combustor Liner Under Full-Load Conditions Using a Novel Thermal History Paint. In *Proceedings of ASME Turbo Expo 2016: Turbomachinery Technical Conference and Exposition, Seoul, South Korea, 13-17 June 2016.* New York, NY, USA: The American Society of Mechanical Engineers.

207. Carl, V., & Zenzinger, G. (2005). Automatische Rissprüfung mit induktiv angeregter Thermografie. https://www.ndt.net/article/dgzfp05/v58.pdf. Accessed 13 July 2018. (In German)

208. Netzelmann, U., Walle, G., Lugin, S., Ehlen, A., Bessert, S., & Valeske, B. (2015). Induction thermography: principle, applications and first steps towards standardization. In *Proceedings of the 2015 Asia International Conference on Quantitative InfraRed Thermography, Quantitative InfraRed Thermography Asia 2015, Mahabalipuram, Indian, 6-10 July 2015.*

209. Šrajbr, C., & Mehler, S. (2013). Induktionsthermografie zur automatisierten Rissprüfung von Flugzeugstrukturen aus Aluminium. http://www.dgzfp.de/Portals/thermo2013/BB/vortrag%12.pdf. Accessed 13 July 2018. (In German)

210. Šrajbr, C. (2015). Anwendung der Induktionsthermografie im industriellen Umfeld. https://www.dgzfp.de/Portals/thermo2015/BB/13.pdf. Accessed 13 July 2018. (In German)

211. Bamberg, J., Erbeck, G., & Zenzinger, G. (1999). EddyTherm: Ein Verfahren zur bildgebenden Rißprüfung metallischer Bauteile. https://www.ndt.net/article/dgzfp/pdf/zfp68-bamberg.pdf. Accessed 15 July 2018. (In German)

212. Vrana, J. (2008). *Grundlagen und Anwendungen der aktiven Thermographie mit elektromagnetischer Anregung: Induktions- und Konduktionsthermographie*. Ph.D. Thesis. Universität des Saarlandes, Saarbrücken, Germany. (In German)

213. Spießberger, C., Dillenz, A., & Zweschper, T. (2011). Rissprüfung mittels aktiver Thermografieverfahren: Induktions- und Ultraschallanregung im Vergleich. http://www.dgzfp.de/Portals/thermo2011/BB/v07.pdf. Accessed 13 July 2018. (In German)

214. Al-Obaidi, S. M. A., Leong, M. S., Hamzah, R. R., & Abdelrhman, A. M. (2012). A Review of Acoustic Emission Technique for Machinery Condition Monitoring: Defects Detection & Diagnostic. *Appl. Mech. Mater., 229-231*, 1476–1480.

215. Nashed, M. S., Steel, J. A., & Reuben, R. L. (2014). The use of acoustic emission for the condition assessment of gas turbines: Acoustic emission generation from normal running. *Proc. Inst. Mech. Eng. Part E J. Process Mech. Eng., 228*(4), 286–308.

216. Mba, D., & Hall, L. (2002). The transmission of acoustic emission across large-scale turbine rotors. *NDT E Int., 35*(8), 529–539.

217. Mba, D. (2006). Development of Acoustic Emission Technology for Condition Monitoring and Diagnosis of Rotating Machines: Bearings, Pumps, Gearboxes, Engines, and Rotating Structures. *Shock Vib. Dig., 38*(1), 3–16.

218. Leahy, M., Mba, D., Cooper, P., Montgomery, A., & Owen, D. (2006). Experimental investigation into the capabilities of acoustic emission for the detection of shaft-to-seal rubbing in large power generation turbines: A case study. *Proc. Inst. Mech. Eng. Part J J. Eng. Tribol., 220*(7), 607–615.

219. Mba, D., Cooke, A., Roby, D., & Hewitt, G. (2004). Detection of shaft-seal rubbing in large-scale power generation turbines with acoustic emissions. Case study. *Proc. Inst. Mech. Eng. Part A J. Power Energy, 218*(2), 71–81.

220. Mathioudakis, K., Papathanasiou, A., Loukis, E., & Papailiou, K. (1991). Fast response wall pressure measurement as a means of gas turbine blade fault identification. *J. Eng. Gas Turb. Power, 113*(2), 269–275.

221. Mathioudakis, K., Loukis, E., & Papailiou, K. (1990). Casing Vibration and Gas Turbine Operating Conditions. *J. Eng. Gas Turb. Power, 112*(4), 478–485.

222. Forbes, G. L., & Randall, R. B. (2013). Estimation of turbine blade natural frequencies from casing pressure and vibration measurements. *Mech. Syst. Signal Process., 36*(2), 549–561.

223. Forbes, G. L. (2010). *Non-contact gas turbine blade vibration monitoring using internal pressure and casing response measurements*. Ph.D. Thesis. The University of New South Wales, Sydney, Australia.

224. Forbes, G. L., & Randall, R. B. (2009). *Simulation of gas turbine blade vibration measurement from unsteady casing wall pressure.* Adelaide, Australia: Australian Acoustical Society.

225. Forbes, G. L., & Randall, R. B. (2007). *Simulated Gas Turbine Casing Response to Rotor Blade Pressure Excitation.* Adelaide, Australia: Australian Acoustical Society.

226. Forbes, G. L., & Randall, R. B. (2008). *Detection of a Blade Fault from Simulated Gas Turbine Casing Response Measurements.* Lancaster, PA, USA: DEStech Publications.

227. Longtin, J., Sampath, S., Tankiewicz, S., Gambino, R. J., & Greenlaw, R. J. (2004). Sensors for harsh environments by direct-write thermal spray. *IEEE Sens. J., 4*(1), 118–121.

228. Schonberg, T., Ruusuvuori, K., Christensen, B. H., Boivie, K., Berild, J. P., Ronkainen, H., et al. (2013). Surface embedded temperature sensor on tool part for real time injection moulding process monitoring. In *Proceedings of the 2013 Transducers & Eurosensors XXVII: The 17th International Conference on Solid-State Sensors, Actuators and Microsystems (TRANSDUCERS & EUROSENSORS XXVII), Barcelona, Spain, 16–20 June 2013*. (pp. 116–119).

229. Zhang, Y., Mack, D., Mauer, G., & Vaßen, R. (2018). Laser Cladding of Embedded Sensors for Thermal Barrier Coating Applications. *Coatings, 8*(5), 176.

230. Li, J., Longtin, J. P., Tankiewicz, S., Gouldstone, A., & Sampath, S. (2007). Interdigital capacitive strain gauges fabricated by direct-write thermal spray and ultrafast laser micromachining. *Sens. Actuators A Phys., 133*(1), 1–8.

231. Li, P., Wen, Y., Zheng, M., & Zhou, Z. (2004). Self-powered Piezoelectric Wireless Micro-sensors by Absorbing Electromagnetic Energy. In *Proceedings of the 2004 IEEE Sensors, Vienna, Austria, 24–27 October 2004.* Vienna, Austria: Vienna University of Technology.

232. Xia, R., Farm, C., Choi, W., & Kim, S.-G. (2006). Self-Powered Wireless Sensor System using MEMS Piezoelectric Micro Power Generator. In *Proceedings of the 2006 IEEE Sensors, Daegu, Korea, 22–25 October 2006.*

233. Chen, Q., Tong, T., Longtin, J. P., Tankiewicz, S., Sampath, S., & Gambino, R. J. (2004). Novel Sensor Fabrication Using Direct-Write Thermal Spray and Precision Laser Micromachining. *J. Manuf. Sci. Eng., 126*(4), 830.

234. Hon, K., Li, L., & Hutchings, I. M. (2008). Direct writing technology—Advances and developments. *CIRP Ann., 57*(2), 601–620.

235. Pique, A. (2002). *Direct-write technologies for rapid prototyping applications: sensors, electronics, and integrated power sources.* San Diego, CA, USA: San Diego Academic Press.

236. LG Tech-Link Global. Uniform Crystal Temperature Sensor Technology and Support Services. http://www.lgtechlink.com. Accessed 15 July 2018.

237. Sheth, A., & Thomas, A. (2015). *Uniform crystal temperature sensor (UCTS) application to validation, verification and technical comparison processes.* Lynn, MA, USA: UC DRC.

238. DeVoe, J., Thomas, A., DeVoe, R., & Ginzbursky, E. (2018). Gas temperature measurement in engine conditions using uniform crystal temperature sensors (UCTS): GT2018-76890. In *ASME Turbo Expo 2018: Turbomachinery Technical Conference and Exposition, Olso, Norway, 11-15 June 2018*. (p. V05BT13A016). New York, NY, USA: American Society of Mechanical Engineers.

239. DeVoe, J., Odom, S., & Ginzbursky, L. (2012). Uniform Crystal Temperature Sensor Accuracy Under Transient Conditions: GT2012-68197. In *ASME Turbo Expo 2012, Copenhagen, Denmark, 11-15 June 2012*. (pp. 79–87). New York, NY, USA: American Society of Mechanical Engineers.

240. Kubiak, J. A., Franco, J. M., Carnero, A., Rothhirsch L, A., & Aguirre R., J. (1987). A Diagnosis of Failure of a Compressor Blade. In *Volume 5: Manufacturing Materials and Metallurgy; Ceramics; Structures and Dynamics; Controls, Diagnostics and Instrumentation; Process Industries, Anaheim, CA, USA, 31 May 1987*. (p. V005T13A003). New York, NY, USA: American Society of Mechanical Engineers.

241. Lattime, S. B., & Steinetz, B. M. (2002). Turbine Engine Clearance Control Systems: Current Practices and Future Directions. In *Proceedings of the 38th AIAA/ASME/SAE/ASEE Joint Propulsion Conference & Exhibit, Indianapolis, IN, USA, 7–10 July 2002.*

242. Salar, A., Hosseini, S. M., Zangmolk, B. R., & Sedigh, A. K. (2010). Improving Model-Based Gas Turbine Fault Diagnosis Using Multi-Operating Point Method. In *Proceedings of the 2010 Fourth UKSim European Symposium on Computer Modeling and Simulation (EMS), Pisa, Italy, 17–19 November 2010.*

243. Diallo, O., & Mavris, D. (2011). A data analytics approach to failure precursor detection of gas turbine. In *ASME 2011 Turbo Expo: Turbine Technical Conference and Exposition, Vancouver, British Columbia, Canada, 6-10 June 2011*. (Volume 3). New York, NY, USA: American Society of Mechanical Engineers.

244. Hanachi, H., Liu, J., Banerjee, A., Chen, Y., & Koul, A. (2015). A Physics-Based Modeling Approach for Performance Monitoring in Gas Turbine Engines. *IEEE Trans. Reliab., 64*(1), 197–205.

245. Dewallef, P., & Borguet, S. (2013). A Methodology to Improve the Robustness of Gas Turbine Engine Performance Monitoring Against Sensor Faults. *J. Eng. Gas Turb. Power, 135*(5), 51601.

246. Borguet, S., & Léonard, O. (2010). Comparison of adaptive filters for gas turbine performance monitoring. *J. Comput. Appl. Math., 234*(7), 2202–2212.

247. Tahan, M., Tsoutsanis, E., Muhammad, M., & Abdul K. Z. A. (2017). Performance-based health monitoring, diagnostics and prognostics for condition-based maintenance of gas turbines: A review. *Appl. Energy*, *198*, 122–144.

4 DUAL-FREQUENCY MODULATION

Overall, Chapter 3 presented the failure modes that can occur during the operation of a gas turbine and revealed possible failure detection techniques. In this regard, ultrasonic techniques demonstrated promising potential to efficiently detect material failures. Given their advantages over the linear method, nonlinear ultrasound techniques were further developed to detect initial failures in materials [77, 81]. When an ultrasonic wave passes a flaw, the wave disturbance generates harmonic frequencies. The measured amplitudes of these frequencies are used as a failure indicator, by comparing them to the amplitude of the fundamental frequencies.

In this study, a frequency modulation technique was developed, in which two fundamental frequencies interact with each other at the material failure. Hence, this chapter fills in the current research gap, which is the analytical description of dual-frequency excitation up to the third order of nonlinearity. Therefore, it was possible to derive new nonlinearity parameters for failure identification. These derived harmonic and modulated response frequencies were proven both experimentally and by numerical simulations. To detect cracks, sheet metal samples with artificially generated cracks were used, including turbine guide vanes with failures manufactured by electrical discharge machining processes and turbine blades with real cracks. It was also possible to estimate the nonlinearity parameters depending on the crack length. An amplitude summing concept was proposed to evaluate a total of 12 nonlinearity parameters.

With the new nonlinearity parameters derived in this chapter, defects were detected with a high degree of accuracy and reliability.

The form 'Statement of Authorship' and the paper are provided on the following pages.

<table>
<tr><td colspan="4">This declaration concerns the article entitled:</td></tr>
<tr><td colspan="4">A nonlinear ultrasonic modulation method for crack detection in turbine blades</td></tr>
<tr><td colspan="4">Publication status</td></tr>
<tr><td colspan="4">Draft manuscript ☐ Submitted ☐ Accepted ☐ Published ☒</td></tr>
<tr><td colspan="4">Publication details (reference)</td></tr>
<tr><td colspan="4">Mevissen, F., & Meo, M. (2020). A nonlinear ultrasonic modulation method for crack detection in turbine blades. Aerospace, 7(6), 72.
https://doi.org/10.3390/aerospace706 0072</td></tr>
<tr><td colspan="4">Candidate's contribution to the paper (detailed, and also given as a percentage)</td></tr>
<tr><td colspan="4"><u>Formulation of ideas:</u> 80%
The idea of multiple frequency excitation was my supervisor's, Professor Michele Meo. I identified the research gap and the possibilities of the analytical work.</td></tr>
<tr><td colspan="4"><u>Design of methodology:</u> 90%
All the analytical work and numerical simulations were performed by me and checked by Professor Michele Meo. The sheet metal samples were designed by me.</td></tr>
<tr><td colspan="4"><u>Experimental work:</u> 95%
I obtained the samples and performed all the experiments. Professor Michele Meo made suggestions to improve the conduction of the experiments.</td></tr>
<tr><td colspan="4"><u>Presentation of data in journal format:</u> 90%
I analysed and processed all the collected data, and I created all the images and determined the layout of the manuscript. My co-author, Professor Michele Meo, provided feedback on the draft and helped with the submission, review and publication processes.</td></tr>
<tr><td colspan="4">Statement from candidate</td></tr>
<tr><td colspan="4">This paper contains original research that I have conducted during the period of my higher degree of research candidature.</td></tr>
<tr><td>Signed</td><td>[redacted]</td><td>Date</td><td>20/10/2022</td></tr>
</table>

A nonlinear ultrasonic modulation method for crack detection in turbine blades

Frank Mevissen and Michele Meo

Department of Mechanical Engineering, University of Bath, Bath, BA2 7AY, UK

Abstract

In modern gas turbines, efforts are being made to improve efficiency even further. This is achieved primarily by increasing the generated pressure ratio in the compressor and by increasing the turbine inlet temperature. This leads to enormous loads on the components in the hot gas region in the turbine. As a result, non-destructive testing and structural health monitoring (SHM) processes are becoming increasingly important to gas turbine manufacturers. Initial cracks in the turbine blades must be identified before catastrophic events occur. A proven method is the linear ultrasound method. By monitoring the amplitude and phase fluctuations of the input signal, structural integrity of the components can be detected. However, closed cracks or small cracks cannot be easily detected due to a low impedance mismatch with the surrounding materials. By contrast, nonlinear ultrasound methods have shown that damage can be identified at an early stage by monitoring new signal components such as sub- and higher harmonics of the fundamental frequency in the frequency spectrum. These are generated by distortion of the elastic waveform due to damage/nonlinearity of the material. In this paper, new global nonlinear parameters were derived that result from the dual excitation of two different ultrasound frequencies. These nonlinear features were used to assess the presence of cracks as well as their qualitative sizes. The proposed approach was tested on several samples and turbine blades with artificial and real defects. The results were compared to samples without failure. Numerical simulations were conducted to investigate nonlinear elastic interaction of the stress waves with the damage regions. The results show a clear trend of nonlinear parameters changing as a function of the crack size, demonstrating the capability of the proposed approach to detect in-service cracks.

1. Introduction

Linear ultrasound techniques are a proven method in modern component inspection. Failure detection is carried out here by changes in the elastic properties such as sound velocity, damping, transmission coefficients, and reflection coefficients [1–3].

Hikata et. al. brought a significant development of this technique in 1965. They found that a sinusoidal ultrasonic wave distorts the fundamental frequency as it propagates in the presence of nonlinearities [4]. An ultrasonic wave propagates into a solid with the fundamental frequency. If this is disturbed during propagation in the body, harmonics are generated. If the amplitudes of these harmonic frequencies are now measured and compared with the fundamental frequencies, these comparative values are a good indicator for detecting changes in the material [4].

Where linear ultrasound failure detection techniques reach their limits, nonlinear ultrasound techniques show higher detection rates [4, 5]. This technique offers the possibility to easily assess the remaining life of a component [6–11]. Different nonlinear models are compared in the review paper [12]. The second-order nonlinearity parameter with two fundamental frequencies was used to detect microcracks [13]. Lim et al. developed a technique with the frequency modulation of high-frequency and low-frequency waves [14]. Subharmonic frequencies were used to detect closed cracks [15]. Moll et al. examined the temperature effect on the propagation of guided waves in composites [16]. Using nonlinear ultrasound, various possibilities were shown to determine mechanical stresses in screw connections [17].

In this study, new global nonlinearity parameters are proposed and derived analytically when a material is excited with two different input frequencies. The numerical simulations were done using the commercially available finite element software LS-DYNA to support and validate the proposed approach where the presence of higher harmonic frequencies was modelled. This method was demonstrated in a quasi-one-dimensional calculation model that was expanded to a dual-frequency excitation model. Nonlinear ultrasound investigations were carried out on metal plate samples where the derived parameter values were used for the damage assessment. Welded plates and selective laser melting (SLM) manufactured plates were also investigated. The sums of the amplitude values of all fundamental and harmonic frequencies and the calculated parameter values were evaluated. Subsequently, a damaged turbine vane and blade were examined. The derived nonlinear parameters were calculated and used for crack detection. The failure in the vane was artificially eroded. The crack in the turbine blade, however, was formed during operation in a gas turbine. Especially for the complex shaped turbine blades, the proposed method of crack detection is very promising. The investigation is very efficient with a high level of response and offers customers and suppliers of gas turbines a quick way to inspect components.

2. Global nonlinearity parameter

Jhang et al. investigated the second harmonic parameter β and its dependence on the wave shift. This allowed to understand the properties of a material [18]. This was extended by Frouin et al. [19], Rothenfusser et al. [20], and Yost et al. [21]. Thus, the direct dependence of the amplitudes on the fundamental frequency and the second harmonic frequency became apparent [19]. Boccardi et al. used this procedure for damage localization in composite materials [22]. The derivation of the second harmonic parameter is also shown by Jeong et al. [23]. Ostrovky et al. studied the nonlinearity parameters for geomaterials [24]. They described the proportionality to the amplitude of the third harmonic frequency. Straka et al. worked on a nonlinear elastic wave modulation spectroscopy (NEWMS), where the effect of two superimposed waves was investigated. Low-frequency and high-frequency waves were combined to detect damage [25].

Malfense Fierro and Meo developed a nonlinearity parameter for dual-frequency waves [26–28] for the determination of the residual fatigue life of a component. This technique was further developed by Jinpin et al. [29]. Amura and Meo developed the third-order nonlinearity parameter with one driving frequency [30].

The wave equation should now be solved analytically up to the third-order degree of nonlinearity. The excitation takes place over two different frequencies. In the presence of nonlinearity, Hooke’s law is:

$$\sigma = E\varepsilon + \frac{E\beta}{2}\varepsilon^2 + \frac{E\gamma}{6}\varepsilon^3, \tag{1}$$

where σ is the stress, E is Young’s modulus, ε is the strain, β is the second-order nonlinearity parameter, and γ is the third-order nonlinearity parameter. Due to the weakening signal, higher nonlinearity grades are difficult to detect.

Equation (2) is the nonlinear wave equation with the following assumptions:

- A longitudinal plane wave propagates in a thin circular rod
- Attenuation is neglected

$$\rho \frac{\partial^2 u}{\partial t^2} = \frac{\partial \sigma}{\partial x}, \tag{2}$$

where ρ is the mass density, and u represents the displacement. The wave speed is defined as $c = \sqrt{\frac{E}{\rho}}$ (long rod d ≪ λ), and the strain is defined as $\varepsilon = \frac{\partial u}{\partial x}$. This is now substituted into Equations (1) and (2) and leads to the formulation of:

$$\underbrace{\frac{\partial^2 u}{\partial t^2} - c^2 \frac{\partial^2 u}{\partial x^2}}_{Linear\,part} = \underbrace{\underbrace{c^2 \beta \frac{\partial u}{\partial x}\frac{\partial^2 u}{\partial x^2}}_{2^{nd}\ order} + \underbrace{\frac{c^2 \gamma}{2}\left(\frac{\partial u}{\partial x}\right)^2 \frac{\partial^2 u}{\partial x^2}}_{3^{rd}\ order}}_{Nonlinear\,part}, \tag{3}$$

Equation (3) is solved in two steps. The perturbation method (Equation (4)) is used to find solutions for $u^{(2)}$ with the second-order parameter, β, and $u^{(3)}$ with the third-order parameter, γ.

$$u = u^{(1)} + u^{(2)} + u^{(3)} + \cdots. \tag{4}$$

The assumption for $u^{(1)}$ for dual frequencies is:

$$u^{(1)} = A_1 sin\left[k_{f1}(x - ct)\right] + A_2 cos\left[k_{f2}(x - ct)\right], \tag{5}$$

where A_1 and A_2 are the amplitudes and k_{f1} and k_{f2} are the wavenumbers of the frequencies f_1 and f_2 ($f_1 < f_2$), respectively.

Substituting Equation (5) in the right side of Equation (3), with the second-order nonlinearity parameter, β, and making further transformations with trigonometric formulas leads to:

$$\frac{\partial^2 u}{\partial t^2} - c^2 \frac{\partial^2 u}{\partial x^2} = \frac{c^2\beta}{2}\begin{pmatrix} -2A_1^2 k_{f1}^3 \cos\left[k_{f1}(x-ct)\right] \sin\left[k_{f1}(x-ct)\right] \\ +2A_2^2 k_{f2}^3 \sin\left[k_{f2}(x-ct)\right] \cos\left[k_{f2}(x-ct)\right] \\ +A_1 A_2 {k_{f1}}^2 k_{f2}\left(cos\left[\left(k_{f2}-k_{f1}\right)(x-ct)\right] - cos\left[\left(k_{f2}+k_{f1}\right)(x-ct)\right]\right) \\ -A_1 A_2 k_{f1} {k_{f2}}^2\left(cos\left[\left(k_{f2}-k_{f1}\right)(x-ct)\right] - cos\left[\left(k_{f2}+k_{f1}\right)(x-ct)\right]\right) \end{pmatrix}. \tag{6}$$

Based on this expression, the following assumption is made for $u^{(2)}$:

$$\begin{aligned} u^{(2)} &= g_1(x) \sin\left[2k_{f1}(x-ct)\right] + g_2(x) \cos\left[2k_{f1}(x-ct)\right] \\ &+ g_3(x) \sin\left[2k_{f2}(x-ct)\right] + g_4(x) \cos\left[2k_{f2}(x-ct)\right] \\ &+ g_5(x) \sin\left[\left(k_{f2}+k_{f1}\right)(x-ct)\right] + g_6(x) \cos\left[\left(k_{f2}+k_{f1}\right)(x-ct)\right] \\ &+ g_7(x) \sin\left[\left(k_{f2}-k_{f1}\right)(x-ct)\right] + g_8(x) \cos\left[\left(k_{f2}-k_{f1}\right)(x-ct)\right]. \end{aligned} \tag{7}$$

Substituting Equation (7) in the left side of Equation (3) (linear part) gives:

$$
\begin{aligned}
&-c^2\Big(\frac{d^2g_1}{dx^2}sin\big[2k_{f1}(x-ct)\big]+\frac{dg_1}{dx}4k_{f1}\,cos\big[2k_{f1}(x-ct)\big]\\
&+\frac{d^2g_2}{dx^2}cos\big[2k_{f1}(x-ct)\big]-\frac{dg_2}{dx}4k_{f1}\,sin\big[2k_{f1}(x-ct)\big]\\
&+\frac{d^2g_3}{dx^2}sin\big[2k_{f2}(x-ct)\big]+\frac{dg_3}{dx}4k_{f2}\,cos\big[2k_{f2}(x-ct)\big]\\
&+\frac{d^2g_4}{dx^2}cos\big[2k_{f2}(x-ct)\big]-\frac{dg_4}{dx}4k_{f2}\,sin\big[2k_{f2}(x-ct)\big]\\
&+\frac{d^2g_5}{dx^2}sin\big[\big(k_{f2}+k_{f1}\big)(x-ct)\big]+\frac{dg_5}{dx}2\big(k_{f2}+k_{f1}\big)\,cos\big[\big(k_{f2}+k_{f1}\big)(x-ct)\big]\\
&+\frac{d^2g_6}{dx^2}cos\big[\big(k_{f2}+k_{f1}\big)(x-ct)\big]-\frac{dg_6}{dx}2\big(k_{f2}+k_{f1}\big)\,sin\big[\big(k_{f2}+k_{f1}\big)(x-ct)\big]\\
&+\frac{d^2g_7}{dx^2}sin\big[\big(k_{f2}-k_{f1}\big)(x-\mathrm{c}t)\big]+\frac{dg_7}{dx}2\big(k_{f2}-k_{f1}\big)\,cos\big[\big(k_{f2}-k_{f1}\big)(x-ct)\big]\\
&+\frac{d^2g_8}{dx^2}cos\big[\big(k_{f2}-k_{f1}\big)(x-ct)\big]-\frac{dg_8}{dx}2\big(k_{f2}-k_{f1}\big)\,sin\big[\big(k_{f2}-k_{f1}\big)(x-ct)\big]\Big)\\
&=c^2\beta\frac{\partial u}{\partial x}\frac{\partial^2 u}{\partial x^2}.
\end{aligned}
\tag{8}
$$

Solving the equations by substituting (8) in the right side of Equation (6) with the assumptions $\frac{dg_1}{dx},\frac{d^2g_2}{dx^2},\frac{dg_3}{dx},\frac{d^2g_4}{dx^2},\frac{d^2g_5}{dx^2},\frac{d^2g_6}{dx^2},\frac{dg_6}{dx},\frac{d^2g_8}{dx^2}=0$ yields:

$$
\begin{aligned}
u^{(2)}=&-\frac{\beta A_1^2k_{f1}^2}{8}cos\big[2k_{f1}(x-ct)\big]\,x+\frac{\beta A_2^2k_{f2}^2}{8}cos\big[2k_{f2}(x-ct)\big]x\\
&-\frac{\beta A_1A_2k_{f1}k_{f2}}{4}sin\big[\big(k_{f2}-k_{f1}\big)(x-ct)\big]\,x\\
&+\frac{\beta A_1A_2k_{f1}k_{f2}}{4}sin\big[\big(k_{f2}+k_{f1}\big)(x-ct)\big]\,x.
\end{aligned}
\tag{9}
$$

The solution of Equation (3) should now be extended by the cubic nonlinearity parameter, γ, to obtain a global description of the nonlinearity parameters. Substituting Equation (5) into the right side of Equation (3) in the third-order nonlinearity parameter, γ, gives:

$$
\begin{aligned}
&\frac{\partial^2 u}{\partial t^2}-c^2\frac{\partial^2 u}{\partial x^2}=\\
&\frac{c^2\gamma}{2}\Big[\big(A_1k_{f1}\,cos\big[k_{f1}(x-ct)\big]-A_2k_{f2}\,sin[k_2(x-ct)]\big)^2\\
&\big(-A_1{k_{f1}}^2\,sin\big[k_{f1}(x-ct)\big]-A_2{k_{f2}}^2\,cos[k_2(x-ct)]\big)\Big].
\end{aligned}
\tag{10}
$$

Transformation with binominal and trigonometric formulas leads to:

$$\frac{\partial^2 u}{\partial t^2} - c^2 \frac{\partial^2 u}{\partial x^2} =$$

$$\frac{c^2\gamma}{2}\begin{pmatrix} \left(-\frac{1}{4}{A_1}^3{k_{f1}}^4 - \frac{1}{2}A_1{A_2}^2{k_{f1}}^2{k_{f2}}^2\right) sin\left[k_{f1}(x-ct)\right] \\ + \left(-\frac{1}{2}{A_1}^2A_2{k_{f1}}^2{k_{f2}}^2 - \frac{1}{4}{A_2}^3{k_{f2}}^4\right) cos\left[k_{f2}(x-ct)\right] \\ -\frac{1}{4}{A_1}^3{k_{f1}}^4 sin\left[3k_{f1}(x-ct)\right] \\ +\frac{1}{4}{A_2}^3{k_{f2}}^4 cos[3k_2(x-ct)] \\ + \left(-\frac{1}{4}{A_1}^2A_2{k_{f1}}^2{k_{f2}}^2 - \frac{1}{2}{A_1}^2A_2{k_{f1}}^3k_{f2}\right) cos\left[\left(2k_{f1}+k_{f2}\right)(x-ct)\right] \\ + \left(-\frac{1}{4}{A_1}^2A_2{k_{f1}}^2{k_{f2}}^2 + \frac{1}{2}{A_1}^2A_2{k_{f1}}^3k_{f2}\right) cos\left[\left(2k_{f1}-k_{f2}\right)(x-ct)\right] \\ + \left(\frac{1}{4}A_1{A_2}^2{k_{f1}}^2{k_{f2}}^2 + \frac{1}{2}A_1{A_2}^2k_{f1}{k_{f2}}^3\right) sin\left[\left(2k_{f2}+k_{f1}\right)(x-ct)\right] \\ + \left(-\frac{1}{4}A_1{A_2}^2{k_{f1}}^2{k_{f2}}^2 + \frac{1}{2}A_1{A_2}^2k_{f1}{k_{f2}}^3\right) sin\left[\left(2k_{f2}-k_{f1}\right)(x-ct)\right] \end{pmatrix}. \tag{11}$$

Based on this expression, the solution approach for $u^{(3)}$ is made:

$$\begin{gathered} u^{(3)} = h_1(x)\, sin\left[k_{f1}(x-ct)\right] + h_2(x)\, cos\left[k_{f1}(x-ct)\right] \\ +h_3(x)\, sin\left[k_{f2}(x-ct)\right] + h_4(x)\, cos\left[k_{f2}(x-ct)\right] \\ +h_5(x)\, sin\left[3k_{f1}(x-ct)\right] + h_6(x)\, cos\left[3k_{f1}(x-ct)\right] \\ +h_7(x)\, sin\left[3k_{f2}(x-ct)\right] + h_8(x)\, cos\left[3k_{f2}(x-ct)\right] \\ +h_9(x)\, sin\left[\left(2k_{f1}-k_{f2}\right)(x-ct)\right] + h_{10}(x)\, cos\left[\left(2k_{f1}-k_{f2}\right)(x-ct)\right] \\ +h_{11}(x)\, sin\left[\left(2k_{f1}+k_{f2}\right)(x-ct)\right] + h_{12}(x)\, cos\left[\left(2k_{f1}+k_{f2}\right)(x-ct)\right] \\ +h_{13}(x)\, sin\left[\left(2k_{f2}+k_{f1}\right)(x-ct)\right] + h_{14}(x)\, cos\left[\left(2k_{f2}+k_{f1}\right)(x-ct)\right] \\ +h_{15}(x)\, sin\left[\left(2k_{f2}-k_{f1}\right)(x-ct)\right] + h_{16}(x)\, cos\left[\left(2k_{f2}-k_{f1}\right)(x-ct)\right]. \end{gathered} \tag{12}$$

Substituting Equation (12) in the left side of Equation (11) yields:

$$\begin{gathered} -c^2\left(\frac{d^2h_1}{dx^2} sin\left[k_{f1}(x-ct)\right] + \frac{dh_1}{dx} 2k_{f1}\, cos\left[k_{f1}(x-ct)\right]\right. \\ + \frac{d^2h_2}{dx^2} cos\left[k_{f1}(x-ct)\right] - \frac{dh_2}{dx} 2k_{f1}\, sin\left[k_{f1}(x-ct)\right] \\ + \frac{d^2h_3}{dx^2} sin\left[k_{f2}(x-ct)\right] + \frac{dh_3}{dx} 2k_{f2}\, cos\left[k_{f2}(x-ct)\right] \\ + \frac{d^2h_4}{dx^2} cos\left[k_{f2}(x-ct)\right] - \frac{dh_4}{dx} 2k_{f2}\, sin\left[k_{f2}(x-ct)\right] \\ + \frac{d^2h_5}{dx^2} sin\left[3k_{f1}(x-ct)\right] + \frac{dh_5}{dx} 6k_{f1}\, cos\left[3k_{f1}(x-ct)\right] \\ + \frac{d^2h_6}{dx^2} cos\left[3k_{f1}(x-ct)\right] - \frac{dh_6}{dx} 6k_{f1}\, sin\left[3k_{f1}(x-ct)\right] \\ + \frac{d^2h_7}{dx^2} sin\left[3k_{f2}(x-ct)\right] + \frac{dh_7}{dx} 6k_{f2}\, cos\left[3k_{f2}(x-ct)\right] \end{gathered} \tag{13}$$

$$
\begin{aligned}
&+\frac{d^2h_8}{dx^2}cos\big[3k_{f2}(x-ct)\big]-\frac{dh_8}{dx}6k_{f2}\,sin\big[3k_{f2}(x-ct)\big]\\
&+\frac{d^2h_9}{dx^2}sin\big[\big(2k_{f1}-k_{f2}\big)(x-ct)\big]+\frac{dh_9}{dx}2\big(2k_{f1}-k_{f2}\big)\,cos\big[\big(2k_{f1}-k_{f2}\big)(x-ct)\big]\\
&+\frac{d^2h_{10}}{dx^2}sin\big[\big(2k_{f1}-k_{f2}\big)(x-ct)\big]-\frac{dh_{10}}{dx}2\big(2k_{f1}-k_{f2}\big)\,cos\big[\big(2k_{f1}-k_{f2}\big)(x-ct)\big]\\
&+\frac{d^2h_{11}}{dx^2}sin\big[\big(2k_{f1}+k_{f2}\big)(x-ct)\big]+\frac{dh_{11}}{dx}2\big(2k_{f1}+k_{f2}\big)\,cos\big[\big(2k_{f1}+k_{f2}\big)(x-ct)\big]\\
&+\frac{d^2h_{12}}{dx^2}cos\big[\big(2k_{f1}+k_{f2}\big)(x-ct)\big]-\frac{dh_{12}}{dx}2\big(2k_{f1}+k_{f2}\big)\,sin\big[\big(2k_{f1}+k_{f2}\big)(x-ct)\big]\\
&+\frac{d^2h_{13}}{dx^2}sin\big[\big(2k_{f2}+k_{f1}\big)(x-ct)\big]+\frac{dh_{13}}{dx}2\big(2k_{f2}+k_{f1}\big)\,cos\big[\big(2k_{f2}+k_{f1}\big)(x-ct)\big]\\
&+\frac{d^2h_{14}}{dx^2}cos\big[\big(2k_{f2}+k_{f1}\big)(x-ct)\big]-\frac{dh_{14}}{dx}2\big(2k_{f2}+k_{f1}\big)\,sin\big[\big(2k_{f2}+k_{f1}\big)(x-ct)\big]\\
&+\frac{d^2h_{15}}{dx^2}sin\big[\big(2k_{f2}-k_{f1}\big)(x-ct)\big]+\frac{dh_{15}}{dx}2\big(2k_{f2}-k_{f1}\big)\,cos\big[\big(2k_{f2}-k_{f1}\big)(x-ct)\big]\\
&+\frac{d^2h_{16}}{dx^2}cos\big[\big(2k_{f2}-k_{f1}\big)(x-ct)\big]-\frac{dh_{16}}{dx}2\big(2k_{f2}-k_{f1}\big)sin\big[\big(2k_{f2}-k_{f1}\big)(x-ct)\big]\big).
\end{aligned}
\tag{13 Cont.}
$$

Further assumptions:

$$
\frac{dh_1}{dx},\frac{d^2h_1}{dx^2},\frac{d^2h_2}{dx^2},\frac{d^2h_3}{dx^2},\frac{dh_4}{dx},\frac{d^2h_4}{dx^2},\frac{dh_5}{dx},\frac{d^2h_5}{dx^2},\frac{d^2h_6}{dx^2},\frac{d^2h_7}{dx^2},\frac{dh_8}{dx},\frac{d^2h_8}{dx^2},\frac{d^2h_9}{dx^2},\frac{dh_{10}}{dx},\frac{d^2h_{10}}{dx^2},
$$
$$
\frac{d^2h_{11}}{dx^2},\frac{d^2h_{12}}{dx^2},\frac{dh_{12}}{dx},\frac{d^2h_{13}}{dx^2},\frac{dh_{13}}{dx},\frac{d^2h_{14}}{dx^2},\frac{d^2h_{15}}{dx^2},\frac{dh_{15}}{dx},\frac{d^2h_{16}}{dx^2}=0.
$$

This results in the following solution:

$$
\begin{aligned}
u^{(3)}=&-\frac{\gamma}{8}\left(\frac{{A_1}^3{k_{f1}}^3}{2}+A_1{A_2}^2k_{f1}{k_{f2}}^2\right)cos\big[k_{f1}(x-ct)\big]x\\
&+\frac{\gamma}{8}\left(\frac{{A_2}^3{k_{f2}}^3}{2}+{A_1}^2A_2{k_{f1}}^2k_{f2}\right)sin\big[k_{f2}(x-ct)\big]x\\
&-\frac{\gamma}{48}{A_1}^3{k_{f1}}^3cos\big[3k_{f1}(x-ct)\big]x-\frac{\gamma}{48}{A_2}^3{k_{f2}}^3sin\big[3k_{f2}(x-ct)\big]x\\
&+\frac{\gamma{A_1}^2A_2}{8}\left(\frac{{k_{f1}}^2{k_{f2}}^2}{2\big(2k_{f1}+k_{f2}\big)}+\frac{{k_{f1}}^3k_{f2}}{2k_{f1}+k_{f2}}\right)sin\big[\big(2k_{f1}+k_{f2}\big)(x-ct)\big]x\\
&+\frac{\gamma{A_1}^2A_2}{8}\left(\frac{{k_{f1}}^2{k_{f2}}^2}{2\big(2k_{f1}-k_{f2}\big)}-\frac{{k_{f1}}^3k_{f2}}{2k_{f1}-k_{f2}}\right)sin\big[\big(2k_{f1}-k_{f2}\big)(x-ct)\big]x\\
&+\frac{\gamma A_1{A_2}^2}{8}\left(\frac{{k_{f1}}^2{k_{f2}}^2}{2\big(2k_{f2}+k_{f1}\big)}+\frac{k_{f1}{k_{f2}}^3}{2k_{f2}+k_{f1}}\right)cos\big[\big(2k_{f2}+k_{f1}\big)(x-ct)\big]x\\
&+\frac{\gamma A_1{A_2}^2}{8}\left(-\frac{{k_{f1}}^2{k_{f2}}^2}{2\big(2k_{f2}-k_{f1}\big)}+\frac{k_{f1}{k_{f2}}^3}{2k_{f2}-k_{f1}}\right)sin\big[\big(2k_{f2}-k_{f1}\big)(x-ct)\big]x.
\end{aligned}
\tag{14}
$$

The accumulated solution of Equations (5), (9) and (14) ($u=u^{(1)}+u^{(2)}+u^{(3)}$) is:

$$
\begin{aligned}
u=&A_1sin\big[k_{f1}(x-ct)\big]+A_2cos\big[k_{f2}(x-ct)\big]-\frac{\beta A_1^2k_{f1}^2}{8}cos\big[2k_{f1}(x-ct)\big]\,x\\
&+\frac{\beta A_2^2k_{f2}^2}{8}cos\big[2k_{f2}(x-ct)\big]x-\frac{\beta A_1A_2k_{f1}k_{f2}}{4}sin\big[\big(k_{f2}-k_{f1}\big)(x-ct)\big]\,x
\end{aligned}
\tag{15}
$$

$$+\frac{\beta A_1 A_2 k_{f1} k_{f2}}{4} sin\left[\left(k_{f2}+k_{f1}\right)(x-ct)\right] x$$
$$-\frac{\gamma}{8}\left(\frac{{A_1}^3 {k_{f1}}^3}{2}+A_1 {A_2}^2 k_{f1} {k_{f2}}^2\right) cos\left[k_{f1}(x-ct)\right] x$$
$$+\frac{\gamma}{8}\left(\frac{{A_2}^3 {k_{f2}}^3}{2}+{A_1}^2 A_2 {k_{f1}}^2 k_{f2}\right) sin\left[k_{f2}(x-ct)\right] x$$
$$-\frac{\gamma}{48} {A_1}^3 {k_{f1}}^2 cos\left[3k_{f1}(x-ct)\right] x-\frac{\gamma}{48} {A_2}^3 {k_{f2}}^3 sin\left[3k_{f2}(x-ct)\right] x$$
$$+\frac{\gamma {A_1}^2 A_2}{8}\left(\frac{{k_{f1}}^2 {k_{f2}}^2}{2\left(2k_{f1}+k_{f2}\right)}+\frac{{k_{f1}}^3 k_{f2}}{2k_{f1}+k_{f2}}\right) sin\left[\left(2k_{f1}+k_{f2}\right)(x-ct)\right] x \qquad \text{(15) Cont.}$$
$$+\frac{\gamma {A_1}^2 A_2}{8}\left(\frac{{k_{f1}}^2 {k_{f2}}^2}{2\left(2k_{f1}-k_{f2}\right)}-\frac{{k_{f1}}^3 k_{f2}}{2k_{f1}-k_{f2}}\right) sin\left[\left(2k_{f1}-k_{f2}\right)(x-ct)\right] x$$
$$+\frac{\gamma A_1 {A_2}^2}{8}\left(\frac{{k_{f1}}^2 {k_{f2}}^2}{2\left(2k_{f2}+k_{f1}\right)}+\frac{k_{f1} {k_{f2}}^3}{2k_{f2}+k_{f1}}\right) cos\left[\left(2k_{f2}+k_{f1}\right)(x-ct)\right] x$$
$$+\frac{\gamma A_1 {A_2}^2}{8}\left(-\frac{{k_{f1}}^2 {k_{f2}}^2}{2\left(2k_{f2}-k_{f1}\right)}+\frac{k_{f1} {k_{f2}}^3}{2k_{f2}-k_{f1}}\right) sin\left[\left(2k_{f2}-k_{f1}\right)(x-ct)\right] x.$$

When analysing Equation (15) it becomes clear that the harmonic displacement components depend linearly on the propagation distance, *x*. Exactly this behaviour was verified experimentally [31–33].

With an assumed constant propagation distance and wavenumber, the expressions of Equation (16) can be derived. The displacement, *u*, is interpreted as the accumulated amplitude of the harmonic frequency: $u(x) = A_{f1+f2}$,

$$\begin{aligned}
f_1 &\rightarrow \gamma_{f1} \propto \frac{A_{f1+f2}}{{A_1}^3+A_1 {A_2}^2}, \\
f_2 &\rightarrow \gamma_{f2} \propto \frac{A_{f1+f2}}{{A_2}^3+{A_1}^2 A_2}, \\
2f_1 &\rightarrow \beta_{2f1} \propto \frac{A_{f1+f2}}{{A_1}^2}, \\
2f_2 &\rightarrow \beta_{2f2} \propto \frac{A_{f1+f2}}{{A_2}^2}, \\
3f_1 &\rightarrow \gamma_{3f1} \propto \frac{A_{f1+f2}}{{A_1}^3}, \\
3f_2 &\rightarrow \gamma_{3f2} \propto \frac{A_{f1+f2}}{{A_2}^3}, \\
f_2 \pm f_1 &\rightarrow \beta_{f2\pm f1} \propto \frac{A_{f1+f2}}{A_1 A_2}, \\
2f_1 \pm f_2 &\rightarrow \gamma_{2f1\pm f2} \propto \frac{A_{f1+f2}}{{A_1}^2 A_2}, \\
2f_2 \pm f_1 &\rightarrow \gamma_{2f2\pm f1} \propto \frac{A_{f1+f2}}{A_1 {A_2}^2}.
\end{aligned} \qquad (16)$$

These derived nonlinearity parameters in Equation (16) offer the possibility to evaluate the different variations of higher harmonic or subharmonic frequencies. The derived parameters γ_{f1} and γ_{f2} only combine the fundamental frequencies and thus deliver a purely linear result.

2.1. Validation of the use of the wave equation

The nonlinearity parameters derived in the previous section are valid for one-dimensional wave propagation. Beam samples with artificial and real cracks were tested, and the derived nonlinear parameters were measured.

The derived parameters are used in principle to compare the amplitudes of the higher harmonic frequencies with the fundamental frequencies. SLM samples made of Inconel 718 with the dimensions 6.4 mm × 70 mm × 2 mm were used. The reference sample (SLM–X1–C) was compared with samples with defects (SLM–1R–C, SLM–2R–C, and SLM–5R–C). An overview is shown in (Figure 1a). These samples had artificial cracks with lengths of 1, 2, and 5 mm. For nonlinear frequency modulation, the 5 MHz sensor at the top and the 3/4 MHz sensor at the bottom were placed at a distance of 30 mm from the receiving sensor (Figure 1b).

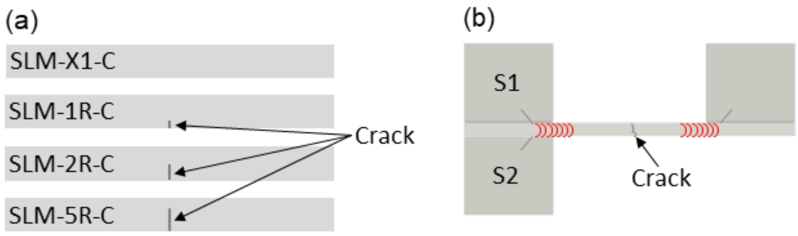

Figure 1. Experiments (a) specimen—overview; (b) experimental setup—principle.

A 5 MHz signal is transmitted with a voltage of 20 V via sensor S1 (Olympus A5014) and a 3-MHz or 4-MHz signal with S2 (Olympus A5014). The ultrasonic waves are sent synchronized over two output channels of the pulse generator AIM-TTI 5011. The signal is captured with the sensor R1 (Olympus A5013), and amplified with a Phoenix ISL 40 dB amplifier. Figure 2 shows the results for the frequency combinations 3/5 MHz (Figure 2a) and 4/5 MHz (Figure 2b).

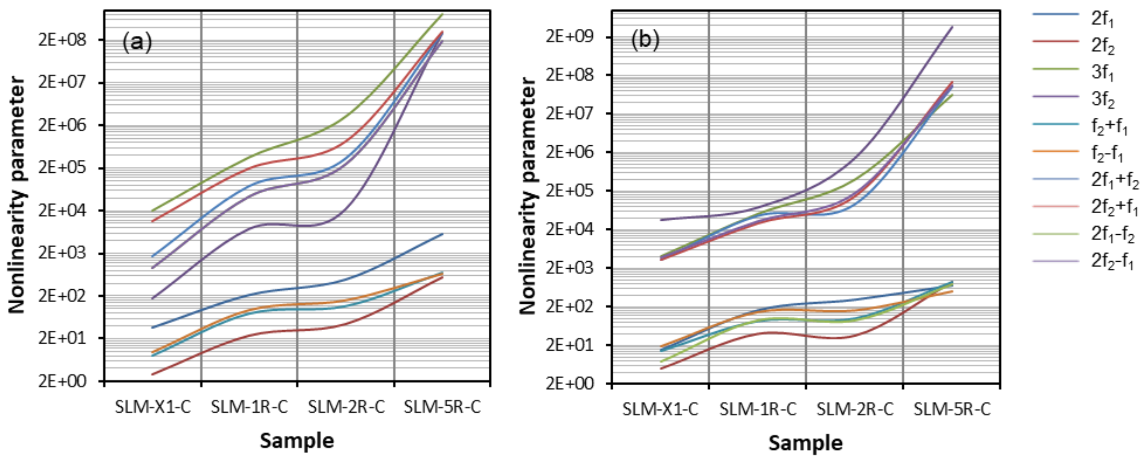

Figure 2. Nonlinearity parameter: (a) f_1 = 3 MHz, f_2 = 5 MHz; (b) f_1 = 4 MHz, f_2 = 5 MHz.

It can be seen that the parameter values measured increase with increasing defect sizes in the samples.

2.2. Amplitude summing method

The total sums of the amplitudes of the fundamental frequencies and the harmonic frequencies were compared. It is expected that the amplitudes of the harmonic frequencies will increase due to nonlinear effects and the amplitudes of the fundamental frequencies will decrease due to energy conservation. This is a quick and effective comparison of the measurements. This approximation can be proven by the energy spectral density approach (Equation (17)):

$$E_S = \int_{-\infty}^{\infty} |\hat{x}(f_n)|^2 df_n \propto \sum_{n=1}^{2} |A_{F,n}| + \sum_{n=3}^{12} |A_{H,n}|, \tag{17}$$

where E_S is the energy, $\hat{x}$ is the signal, $A_{F,n}$ are the fundamental amplitudes, and $A_{H,n}$ are the harmonic amplitudes.

In the following, Σ_{AF} is designated as the summation of the fundamental amplitudes and Σ_{AH} as the summation of the harmonic amplitudes. Table 1 summarises the different fundamental frequencies and the higher and subharmonic frequencies.

Table 1. Summary modes.

Mode	Frequency
n_1	f_1
n_2	f_2
n_3	$2f_1$
n_4	$2f_2$
n_5	$3f_1$
n_6	$3f_2$
n_7	f_2+f_1
n_8	f_2-f_1
n_9	$2f_1+f_2$
n_{10}	$2f_1-f_2$
n_{11}	$2f_2+f_1$
n_{12}	$2f_2-f_1$

It is also shown that the different harmonic frequencies behave contrarily [29]. While individual harmonic frequencies increase with damaged samples, others can certainly decrease.

3. Numerical simulation

3.1. Modelling

The nonlinear interaction of elastic waves with a damage was modelled to support the experimental campaign, and it was critical to understand how higher harmonics and subharmonic frequencies could be generated. For this, the program LS-DYNA was used.

First, the simulation is to be demonstrated in a quasi-one-dimensional case and then in two dimensions [34]. For this purpose, two 2D elements with a ratio of length/width = 10 were modelled [35] (Figure 3). The material 001-ELASTIC with the material properties from Table 2 was selected (based at 20 °C ambient temperature).

Table 2. Material properties Inconel 718.

Material	Inconel 718
Density, ρ	8.2 kg/dm^3
Speed of sound, c	5820 m/s
Young's modulus, E	205000 MPa
Poisson's ratio, υ	0.292

The elements are 0.1 mm apart. In order to simulate the nonlinearities, the 2D elements were connected to nonlinear spring elements (S04_NONLINEAR_ELASTIC_SPRING). The longitudinal waves are generated by the application of a periodic force. For this, a 5 MHz sine wave is introduced into the model (node S). The element size is λ/6, where λ is the wavelength. For frequency domain acoustics, the keyword *FREQUENCY_DOMAIN_ACOUSTIC_BEM was used to compute the acoustic pressure due to vibration of the structure [36].

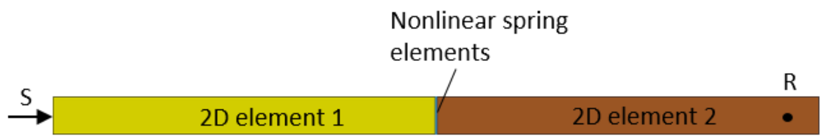

Figure 3. Quasi-one-dimensional LS-DYNA model.

In postprocessing, the acoustic pressure in node R was read out. The frequency spectrum is shown in Figure 4. Here it can be seen that in addition to the basic frequency, *f*, the harmonic frequencies, 2*f* and 3*f*, are also measured. This is now the proof of the generation of nonlinearities in the numerical simulation.

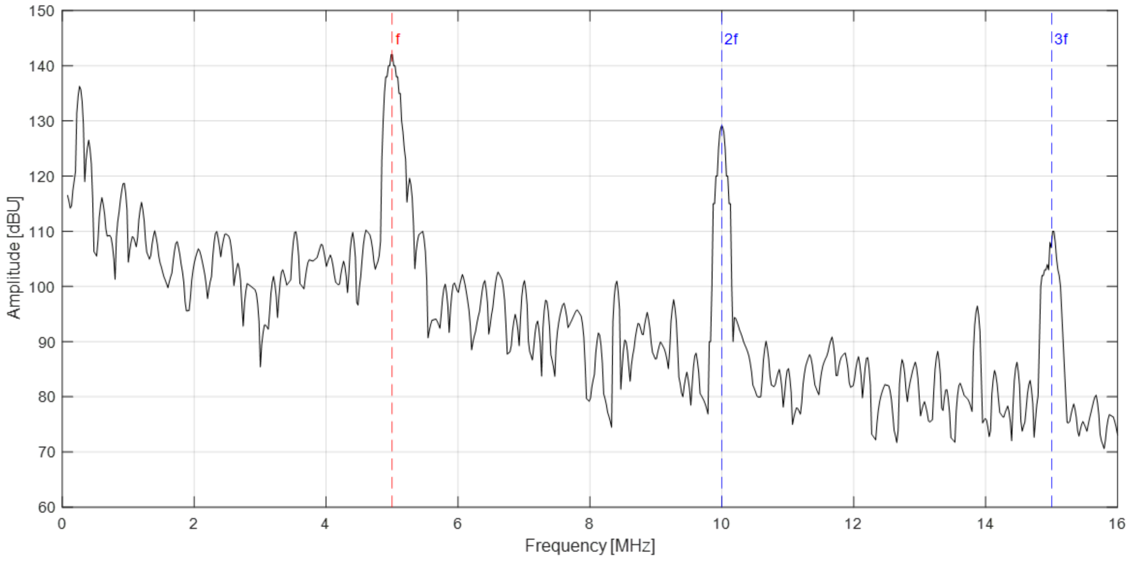

Figure 4. Quasi-one-dimensional frequency spectrum, LS-DYNA simulation with excitation frequency $f = 5$ MHz.

For the two-dimensional case, two different frequency excitations were applied to demonstrate the generation of complex subharmonic and higher harmonic frequencies.

A plate with the dimensions 2 mm × 50 mm × 70 mm modelled with a defect of 5 mm length in the middle part of the plate was introduced. Nonlinear elastic spring elements were used to generate nonlinearities in the defect area. The same material parameters as the 1D case were used.

The excitations are introduced in the plate by two periodic forces. These are set at an angle of 50° (Figure 5). These, in turn, are directed into the component at an angle of 60°, as in the experiments shown in Section 4.2.2.

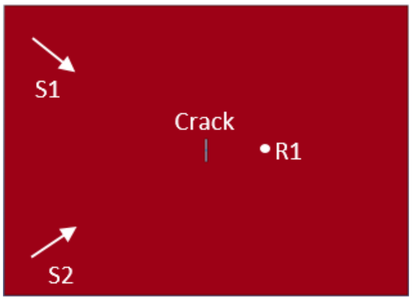

Figure 5. LS-DYNA model.

3.2. Results and discussion

Figure 6 shows the wave propagation with the frequency combination 4/5 MHz. In Figure 6c, the generated disturbance at the defect becomes visible. In the further course, the wave propagation patterns will be more complex, but this is a good basis for further evaluation.

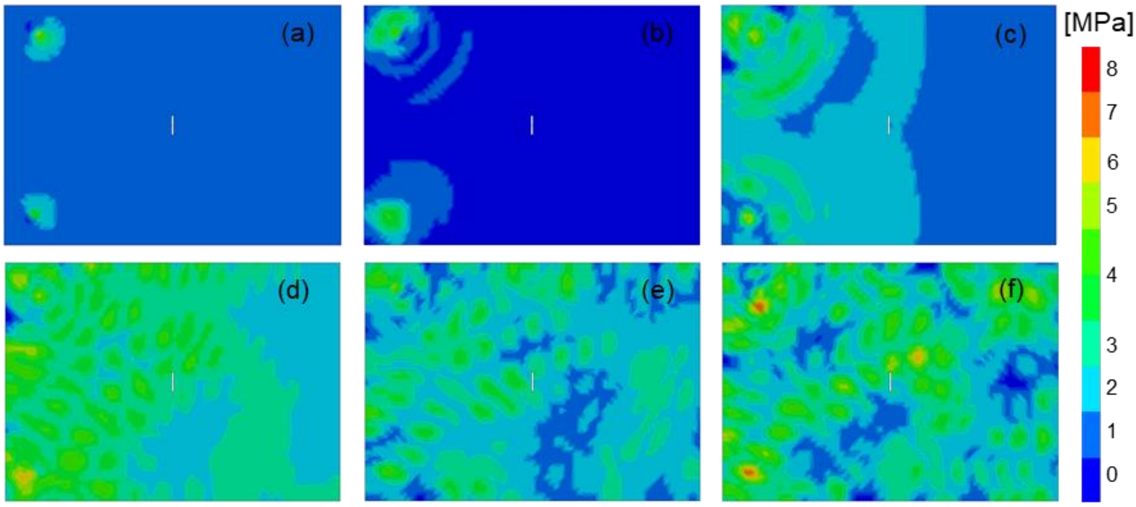

Figure 6. Wave propagation: (a) t = 2,4e–09 s; (b) t = 6,8e–09 s; (c) t = 1,2e–08 s; (d) t = 3,6e–08 s; (e) t = 5,3e–08 s; (f) t = 1,1e–07 s.

The results at node R1 were evaluated. After implementing a fast Fourier transformation (FFT) in the LS-DYNA postprocessing, a frequency spectrum is shown in Figure 7. The frequencies marked in red are the fundamental frequencies, and the blue ones show the higher and subharmonic frequencies. The frequencies predicted in Section 2 are clearly shown here.

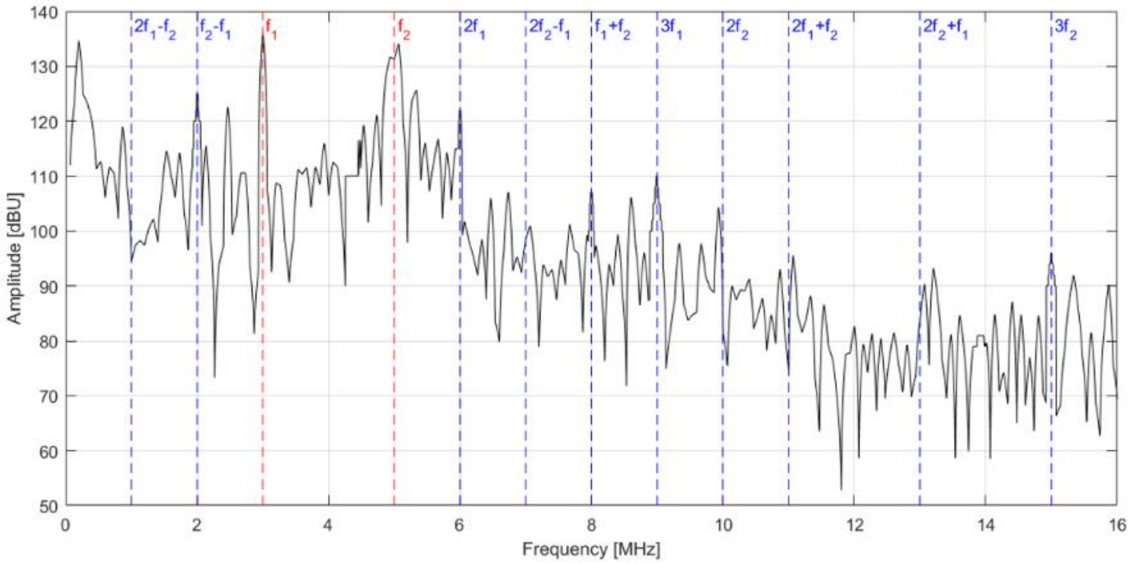

Figure 7. Frequency spectrum, LS-DYNA simulation with excitation frequencies f_1 = 3 MHz and f_2 = 5 MHz.

Figure 8 shows the FFT with the excitation frequencies f_1 = 4 MHz and f_2 = 5 MHz. The analytically predicted complex harmonic frequencies could be clearly demonstrated.

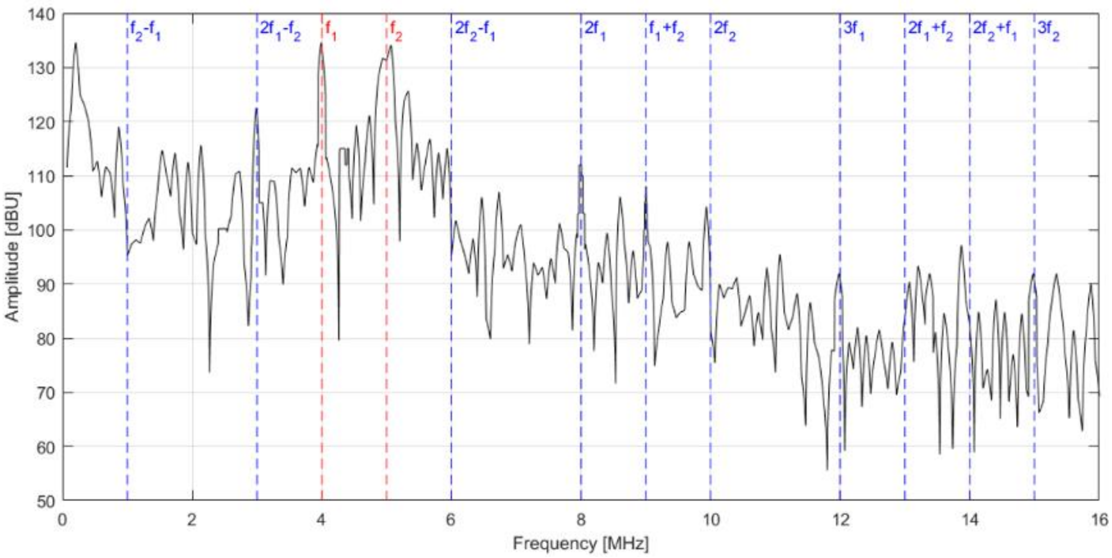

Figure 8. Frequency spectrum, LS-DYNA simulation with excitation frequencies f_1 = 4 MHz and f_2 = 5 MHz.

4. Experimental validation

The proposed nonlinear parameters were used to investigate damage in plates and turbine blades. Transmission experiments were carried out where two Olympus 60°/5 MHz A5014 transducers were selected. The signals were received with an Olympus 70°/5 MHz A5013 transducer and amplified with a Phoenix ISL 40 dB preamplifier. The signal was generated with an AIM-TTI 5011 pulse generator with two output channels and an output voltage of 20 V each. All measurement data were sent to an oscilloscope for further processing. The ambient temperature has an influence on the wave propagation in a component. Since this also has an impact on the formation of the harmonic frequencies [37], the experiments were carried out at constant temperature. The experimental setup is shown in Figure 9. With this basic configuration, all experiments in this paper were made.

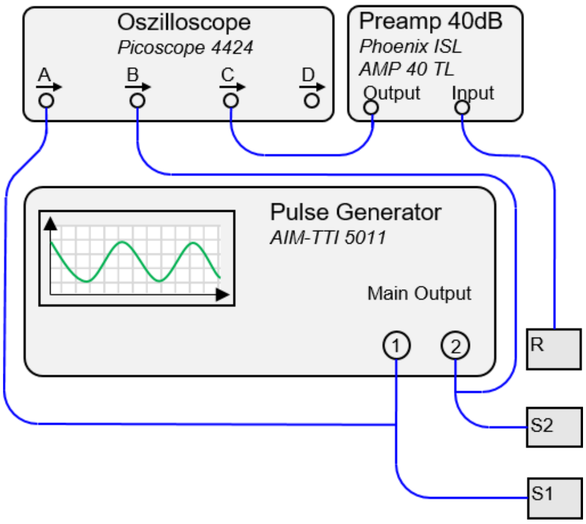

Figure 9. Experimental setup.

4.1. Damage detection methodology

Figure 10 shows a possible methodology for flaw detection in a flowchart. The process begins with the measurement of a reference model for comparison and the sample to be examined. Then, the global nonlinearity parameters, $\delta_{\beta/\gamma}$, the sum values, Σ_{AF} and Σ_{AH}, and the linear fundamental parameters, γ_{f1} and γ_{f2}, are evaluated and calculated after the measurements. The index '*i*' represents the reference model, and '*j*' represents the component to be tested. The presence of nonlinearities in the component is a first indication of a defect. The comparison of the behaviour of the amplitudes of the fundamental and harmonic frequencies gives a clear indication of material defects. Crack size estimation is done via the parameter values as a function of the size of the defect.

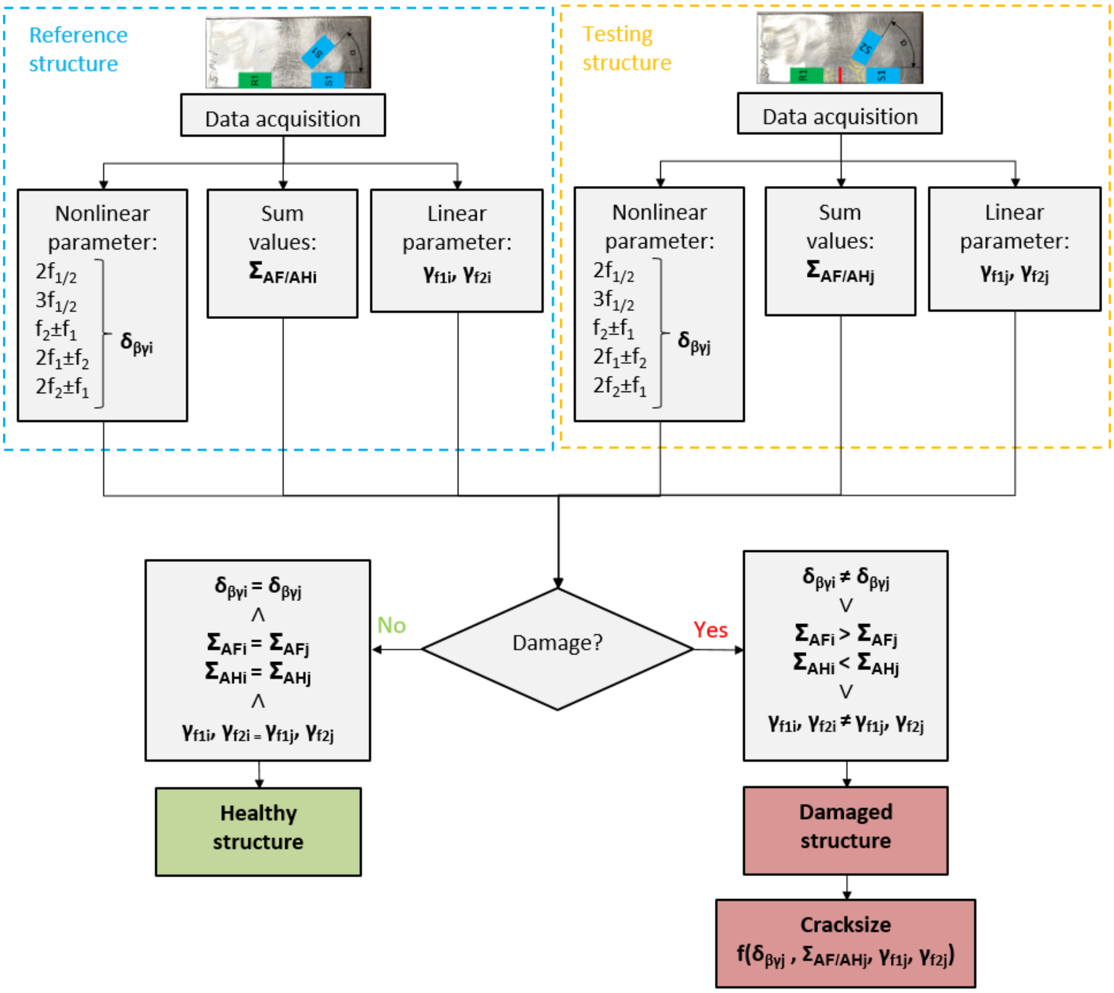

Figure 10. Damage detection methodology.

4.2. Plate samples—welded

The samples used were Inconel 718 plates measuring 2 mm × 70 mm × 35 mm. These consist of two plates and were joined by micro laser welding. Samples were available with 5, 2, and 1 mm defect widths, which were placed both centrally and laterally on the samples. After welding, the samples were machined, so that the weld seam was no longer visible and the same wall thickness was given at each position. For comparison, samples without defect were also analysed. Five variants of each sample were examined, and the arithmetic mean values were further processed. Table 3 summarises the used specimens. Crack generation through a fatigue test would also be possible but would have some disadvantages. The exact crack size and the crack course are hardly controllable here.

Table 3. Welded plate specimens.

Specimen	Crack length	Crack position
X1	—	—
1M	1 mm	Centre
1R	1 mm	Lateral
2M	2 mm	Centre
2R	2 mm	Lateral
5M	5 mm	Centre
5R	5 mm	Lateral

The positioning angle of the sensors was chosen so that the ultrasonic waves can overlap before reaching the crack region.

4.2.1. Evidence higher harmonic frequencies

The higher harmonic nonlinearity parameters, derived in the previous section, were also measured experimentally. Figure 11 shows the superimposed frequency spectrum with the input frequencies of 3 MHz and 5 MHz with a sensor angle of $\alpha = 60°$. Here, the undamaged sample (X1) is compared with the samples with defects (1M, 2M, 5M). The same sensor positioning was used as in Section 4.2.2. The different combinations of higher harmonic and subharmonic frequencies can be seen clearly.

It becomes apparent that the amplitudes of the higher harmonic frequencies $3f_2$, f_2-f_1, $2f_1+f_2$, and $2f_2+f_1$ increase significantly. In contrast, the nonlinearity decreases at $2f_1$ for the damaged samples.

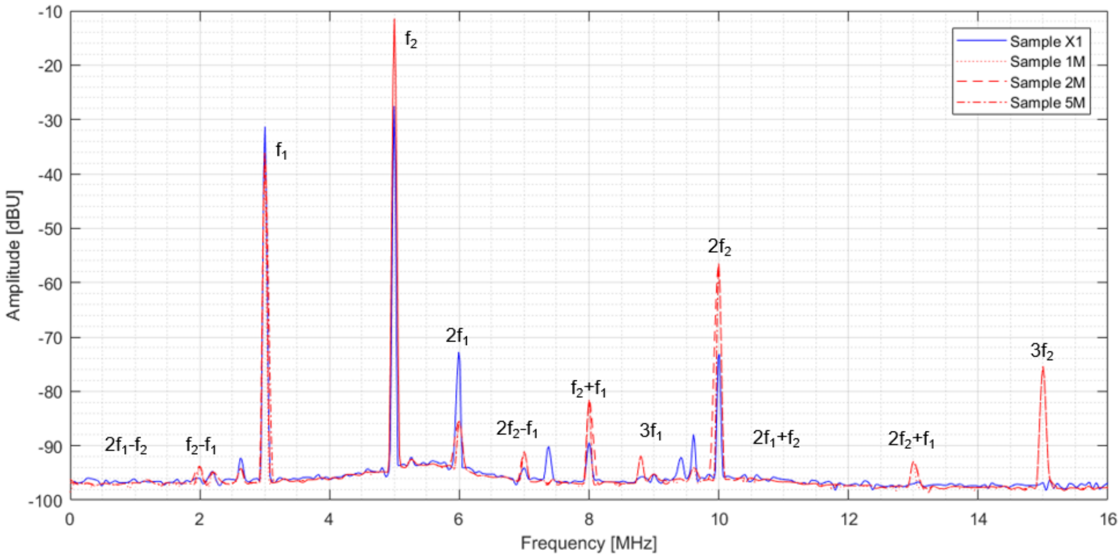

Figure 11. Comparison of frequency spectrum: $f_1 = 3$ MHz, $f_2 = 5$ MHz, $\alpha = 60°$.

Figure 12 shows a similar picture. Here, the fundamental frequencies 4/5 MHz were investigated. The frequencies $2f_1$, f_2+f_1, $2f_1-f_2$, and $2f_2-f_1$ increase strongly compared to the reference measurement, and $3f_2$, however, drops.

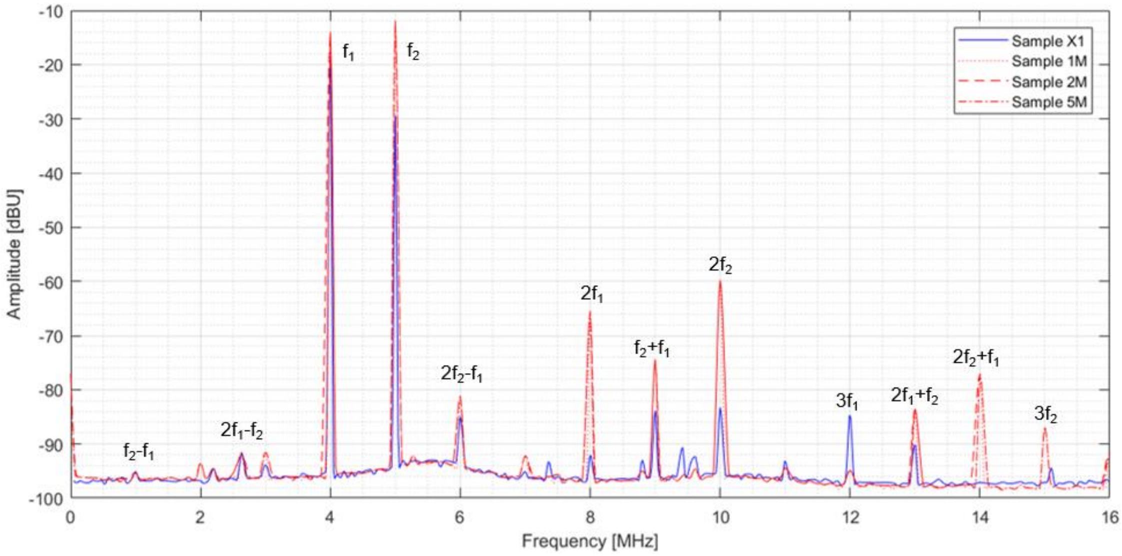

Figure 12. Comparison of frequency spectrum: f_1 = 4 MHz, f_2 = 5 MHz, α = 60°.

The assumption postulated in the previous section could hereby be confirmed. The nonlinearity parameters, determined in Equation (16), were used to calculate and compare the corresponding values from the experiments.

4.2.2. Results and discussion—central defect

Samples 5M, 2M, and 1M were compared to the sample without damage X1. The frequency combinations 3/5 MHz and 4/5 MHz and the angles α = 50°, 60°, and 90° were examined (Figure 13).

Figure 13. Measuring principle—sample with central defect.

At an angle of 50°, the distance to the flaw is shortest compared to the other angle combinations (Figure 14). For the frequency combination 3/5 MHz, all parameter values increase significantly in comparison to those of the initial sample. Interestingly, the peak values are measured at the 1M and the 2M samples. These points represent the maximum of the generated nonlinearities and do not increase with a larger crack. The Σ_{AF} and Σ_{AH} values also show this behaviour. At 4/5 MHz (Figure 14b), the highest parameter values were determined for the 5M sample, with the largest defect. A rise with positive gradients is shown by nearly all parameters. Figure 14b shows a continuous increase in the Σ_{AH} values.

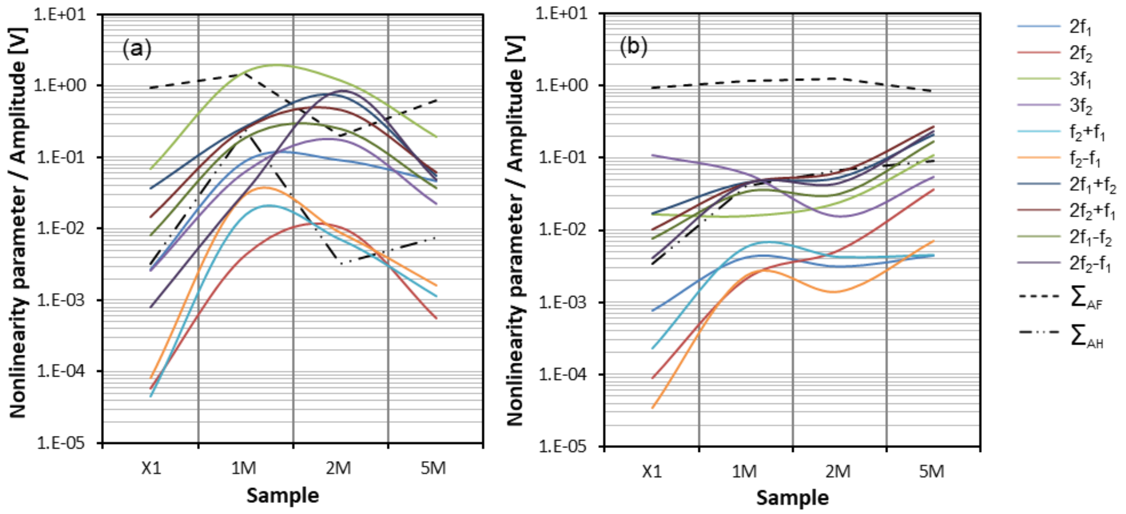

Figure 14. Nonlinearity parameter: (a) f_1 = 3 MHz, f_2 = 5 MHz, α = 50°; (b) f_1 = 4 MHz, f_2 = 5 MHz, α = 50°.

Figure 15a shows the measurement result with the input frequencies 3 MHz and 5 MHz with a sensor angle of α = 60°. In particular, the parameters of the frequencies $2f_1$, $3f_1$, $2f_1+f_2$, and f_2+f_1 show a good curve trend depending on the failure size.

With the input frequencies 4 MHz and 5 MHz and with a sensor angle of α = 60°, the results are presented in Figure 15b. Here, only the nonlinearity parameters of the frequencies $2f_1$ and $3f_2$ show a good trend depending on the size of the failure.

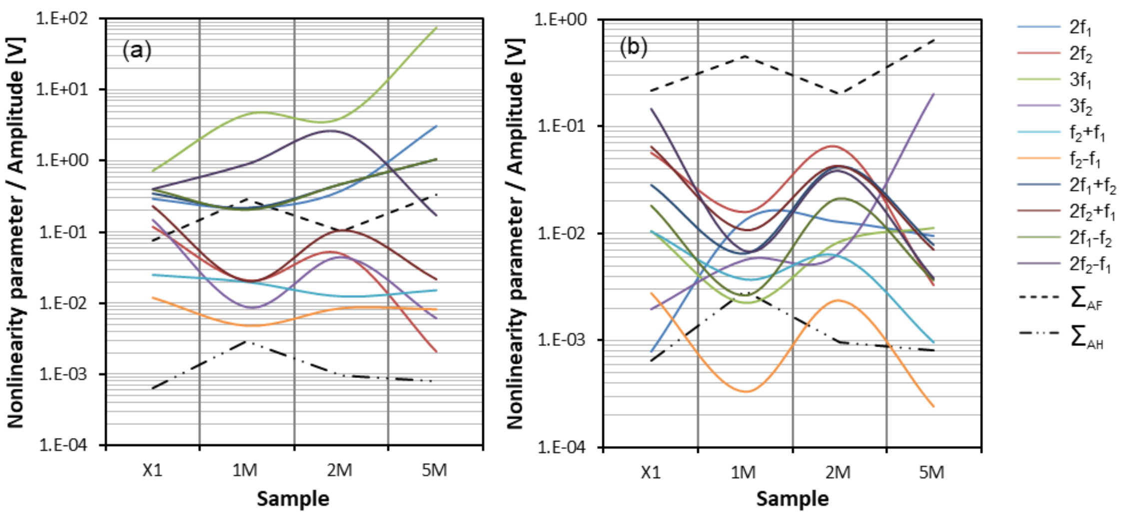

Figure 15. Nonlinearity parameter: (a) f_1 = 3 MHz, f_2 = 5 MHz, α = 60°; (b) f_1 = 4 MHz, f_2 = 5 MHz, α = 60°.

If the angle is changed to α = 90°, the result shows a different view (Figure 16). In this configuration, the collision of the ultrasonic waves is furthest from the crack at this sensor angle. At 3/5 MHz, the parameter values increase and remain relatively constant for the 1M sample. Σ_{AH} also reflects this behaviour.

At 4/5 MHz, it can be clearly seen that the sample 2M in particular shows the highest parameter values. The parameters $2f_1$ and $3f_2$ start with positive gradients and are strong indicators for the presence of damage.

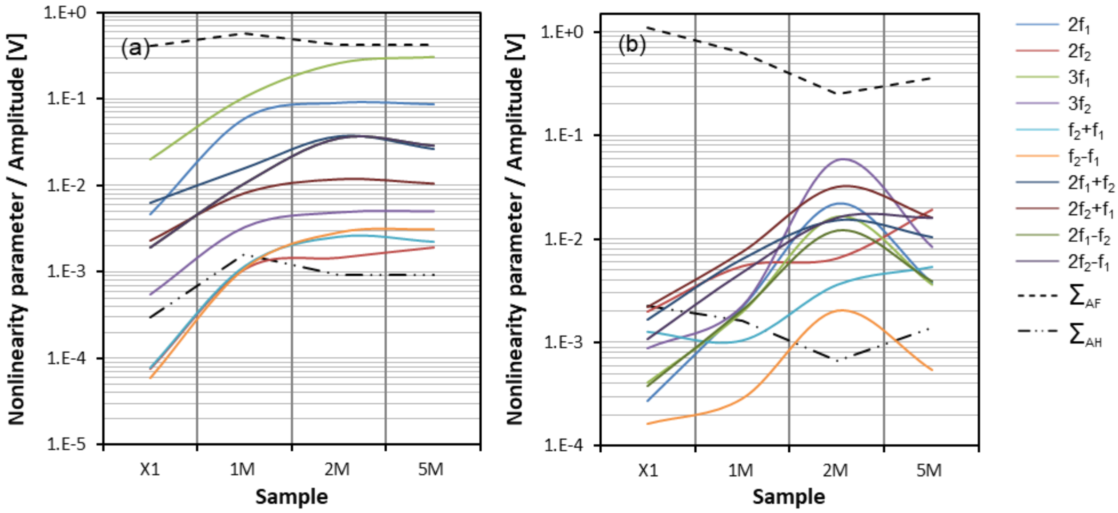

Figure 16. Nonlinearity parameter: (a) f_1 = 3 MHz, f_2 = 5 MHz, α = 90°; (b) f_1 = 4 MHz, f_2 = 5 MHz, α = 90°.

In the previous section, the parameters γ_{f1} and γ_{f2} were derived analytically. This linear definition should also be used to classify cracks (Figure 17). The behaviour of the two fundamental frequencies is reflected in this parameter because it only contains the amplitudes of these frequencies. Especially when measuring at α = 50° and α = 90°, the behaviour is shown as a function of the crack size. The development of the defect can be observed from the undamaged sample.

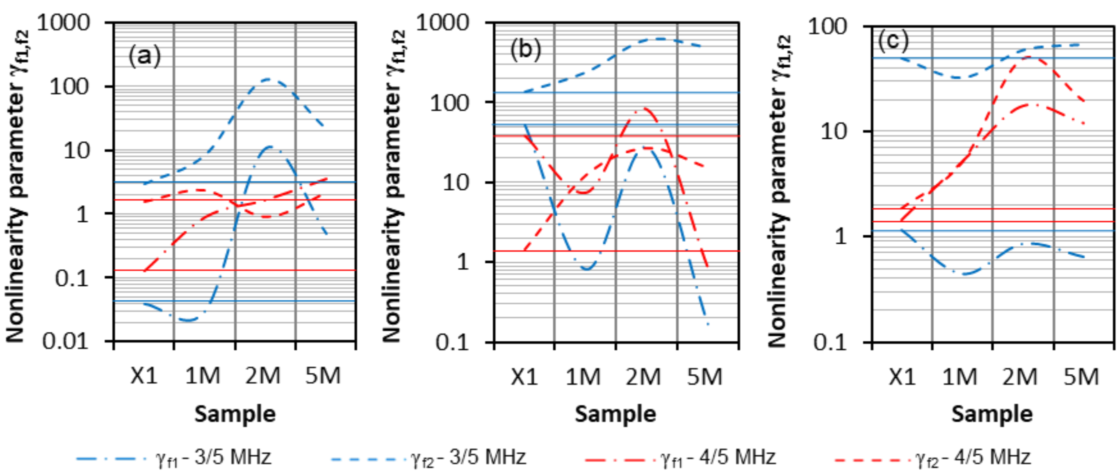

Figure 17. Comparison γ_{f1} and γ_{f2} parameters: (a) α = 50°; (b) α = 60°; (c) α = 90°.

4.2.3. Results and discussion—lateral defect

Figure 18 represents the measurement setup with lateral defects. This matches better to the typical damage pattern on turbine blades where the thin trailing edge is cracked. Samples 5R, 2R and 1R were used for the comparison with X1. The frequency combinations 3/5 MHz and 4/5 MHz with angles of 45°, 60°, and 90° were investigated.

Figure 18. Measuring principle—sample with lateral defect.

Figure 19a shows a clear trend with peak values for the sample 1R. Σ_{AF} have their minimal value here, and Σ_{AH} have the maximum value. At 4/5 MHz, Figure 19b shows a comparable but more moderate behaviour.

The sum of amplitudes of the fundamental frequencies Σ_{AF} decreases in both series of measurements, and the sum of the harmonic amplitudes Σ_{AH} increases due to the generated nonlinearities.

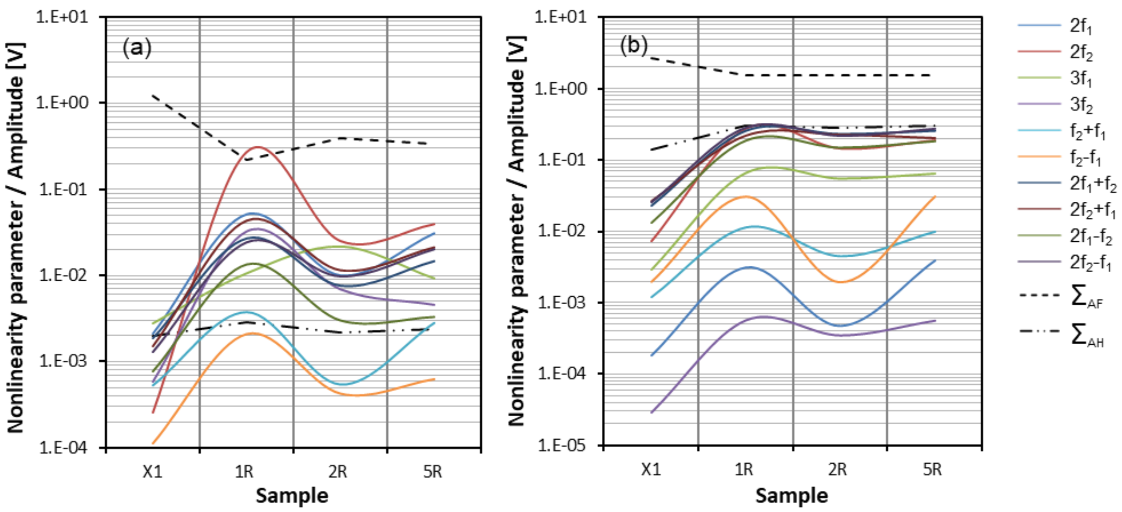

Figure 19. Nonlinearity parameter: (a) f_1 = 3 MHz, f_2 = 5 MHz, α = 45°; (b) f_1 = 4 MHz, f_2 = 5 MHz, α = 45°.

In Figure 20a, the higher harmonic f_2+f_1 and $2f_2+f_1$ start with a positive gradient from the undamaged sample. At 4/5 MHz, only small variations are shown. The Σ_{AH} indicator shows a continuous increase with increased damage size.

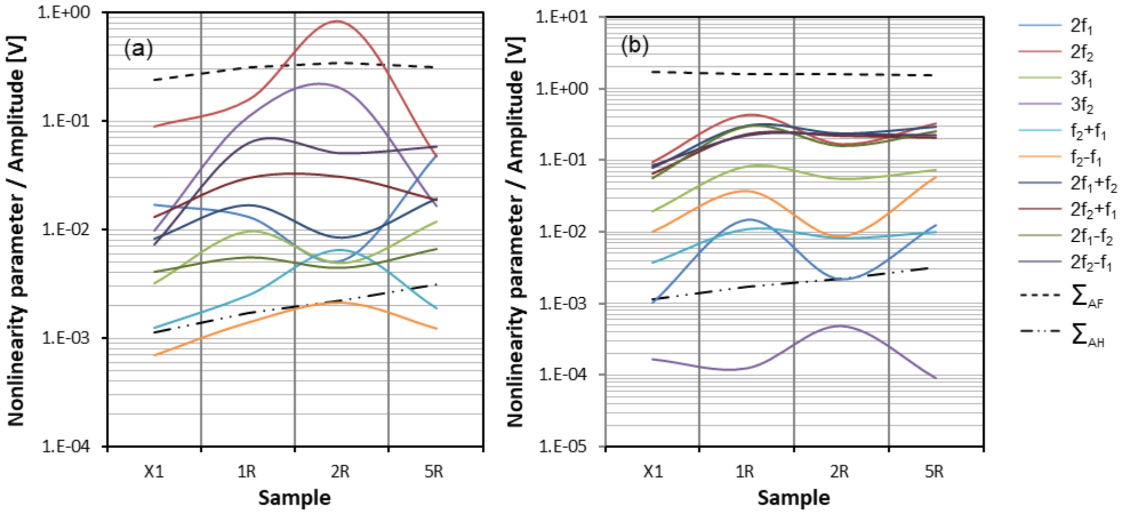

Figure 20. Nonlinearity parameter: (a) f_1 = 3 MHz, f_2 = 5 MHz, α = 60°; (b) f_1 = 4 MHz, f_2 = 5 MHz, α = 60°.

At an angle of α = 90°, a sensor is positioned in the direction of the crack. This is also reflected in the measurement results. Figure 21b shows that the nonlinearities increase and then reach a plateau.

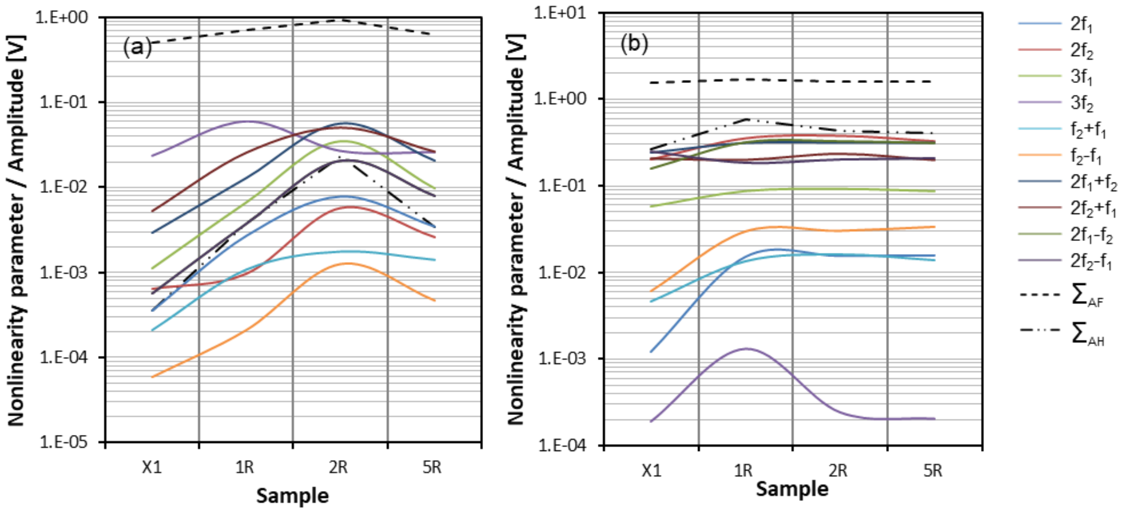

Figure 21. Nonlinearity parameter: (a) f_1 = 3 MHz, f_2 = 5 MHz, α = 90°; (b) f_1 = 4 MHz, f_2 = 5 MHz, α = 90°.

The calculated γ_{f1} and γ_{f2} parameters are shown in Figure 22. The frequency combination 4/5 MHz in particular shows a crack size representing parameter course.

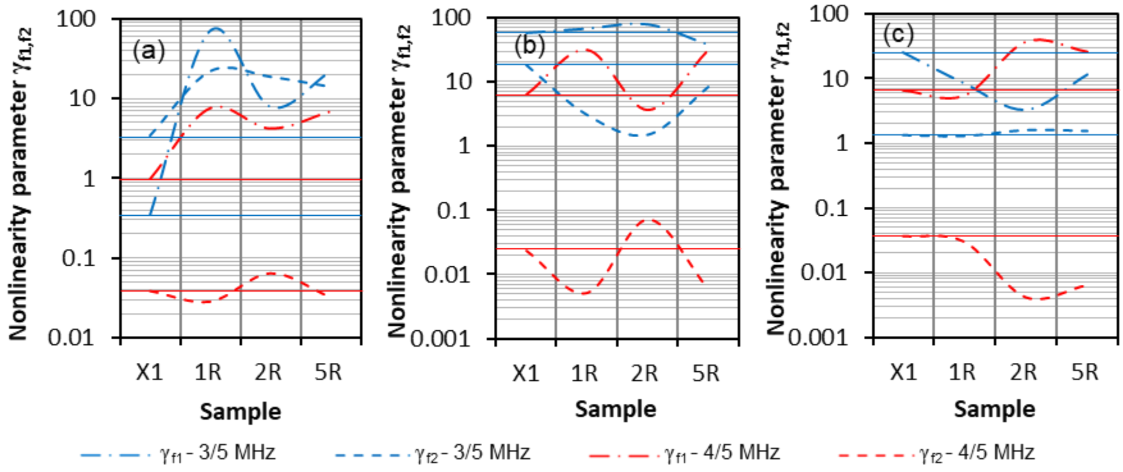

Figure 22. Comparison of γ_{f1} and γ_{f2} parameters: (a) α = 45°; (b) α = 60°; (c) α = 90°.

If a comparison sample without defect is available, a defect can be detected with an estimate of the failure size.

4.3. Plate samples—SLM manufactured

The samples shown in Figure 23 were produced with the material Inconel 718 by SLM. The dimensions of the component and the defect were comparable with the samples in Section 4.2. This method has the advantage that the samples can be produced with the artificial defect in one operation. Compared to forged components, the SLM parts yielded high tensile strength, low ductility, and strong anisotropy associated with building direction. The static properties of the SLM fabricated parts are comparable with those of the wrought parts [38].

The same tests as in Section 4.2.3 were performed on this sample and compared with an undamaged sample. Five variants of each sample were examined, and the arithmetic mean values were used for the evaluations.

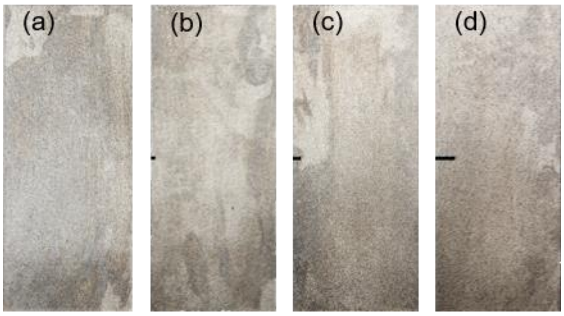

Figure 23. SLM samples: (a) reference sample SLM–X1; (b) sample SLM–1R; (c) sample SLM–2R; (d) sample SLM–5R.

Table 4 summarises the samples used in this section.

Table 4. SLM manufactured metal specimens.

Specimen	Crack Length	Crack Position
SLM–X1	—	—
SLM–1R	1 mm	Lateral
SLM–2R	2 mm	Lateral
SLM–5R	5 mm	Lateral

4.3.1. Results and discussion

At a sensor angle of 45°, there is a constant increase in the excitation combination of 3/5 MHz of all parameter values with a peak in the SLM–2R and the SLM–5R samples (Figure 24a). The Σ_{AF} and Σ_{AH} again behave in opposite directions. With excitation frequencies of f_1 = 4 MHz and f_2 = 5 MHz (Figure 24b), only the parameter $2f_2{-}f_1$ shows the expected trend. It is expected that failures in the material will result in nonlinearities and consequently harmonic frequencies. As a result of the energy conservation of a signal shown, a decrease in the amplitudes of the fundamental frequencies is expected with increasing harmonic frequencies. As can be seen here, this is not always the case. The largest point of error does not necessarily lead to the greatest nonlinearities. Saturation is often observed, which does not allow a further increase.

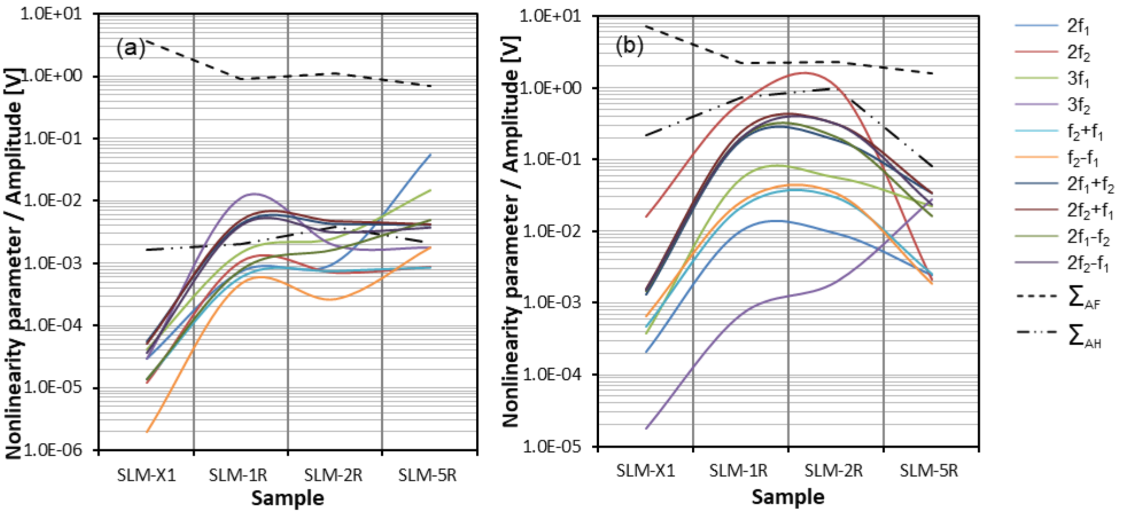

Figure 24. Nonlinearity parameter: (a) f_1 = 3 MHz, f_2 = 5 MHz, α = 45°; (b) f_1 = 4 MHz, f_2 = 5 MHz, α = 45°.

At a sensor angle of 60°, both frequency response variants show the maximum values at the SLM–1R sample (Figures 25a, b).

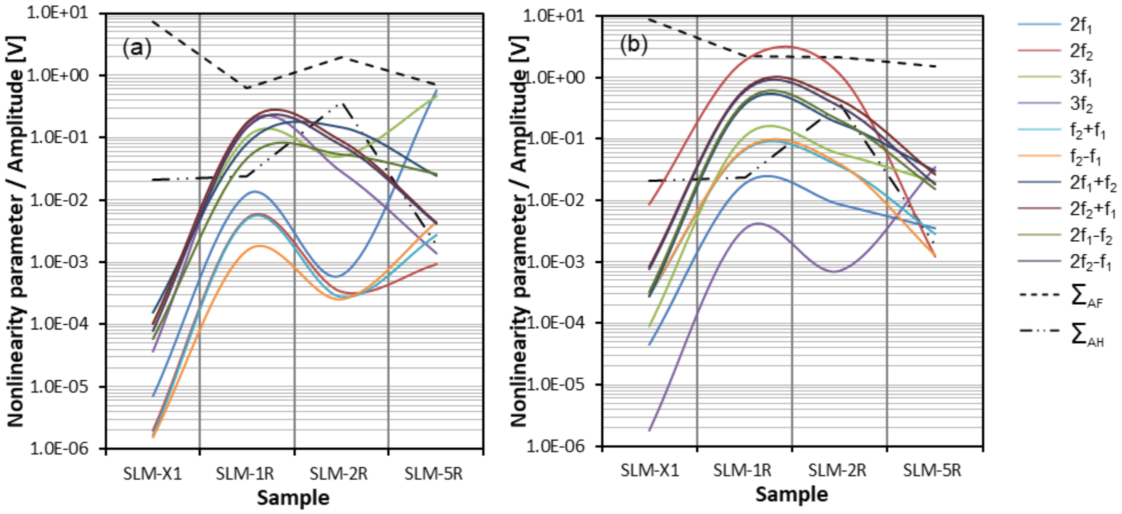

Figure 25. Nonlinearity parameter: (a) f_1 = 3 MHz, f_2 = 5 MHz, α = 60°; (b) f_1 = 4 MHz, f_2 = 5 MHz, α = 60°.

With a sensor orientation of 90°, the behaviour is comparable to the 1R, 2R, and 5R samples. With the excitation combination of 4/5 MHz, relatively constant values are set (Figure 26b). Again, the Σ_{AF} and Σ_{AH} values react like predicted.

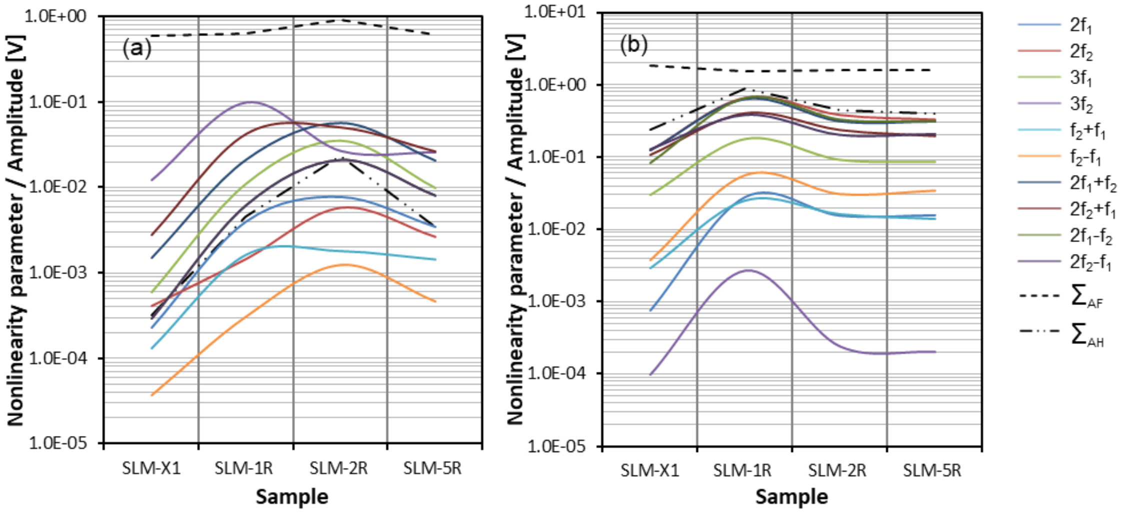

Figure 26. Nonlinearity parameter: (a) f_1 = 3 MHz, f_2 = 5 MHz, α = 90°; (b) f_1 = 4 MHz, f_2 = 5 MHz, α = 90°.

When comparing the linear parameters γ_{f1} and γ_{f2}, the behaviour is similar to the welded samples. The 4/5 MHz excitation combination is significantly more sensitive (Figure 27).

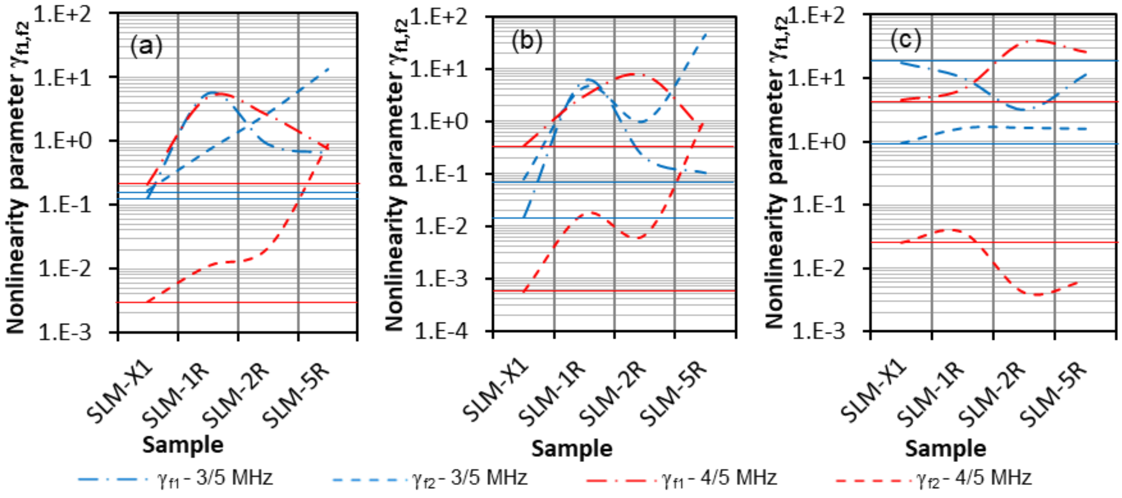

Figure 27. Comparison of γ_{f1} and γ_{f2} parameters: (a) α = 45°; (b) α = 60°; (c) α = 90°.

4.4. Turbine vane

A turbine vane made of Inconel 738 was also investigated. By structural-mechanical calculations, possible crack positions are known, typically in the middle of the trailing edge. The defect was introduced by erosion. It is 0.2 mm wide and 4 mm deep into the component through the cooling air outlet slots (Figure 28).

Figure 28. Vane sample (III.7) with eroded defect.

4.4.1. Results and discussion

The sensor arrangement is shown in Figures 29a, b. The results show that all the nonlinear parameters increase significantly. The parameter f_2+f_1 was detected only on the damaged sample Figure 29c).

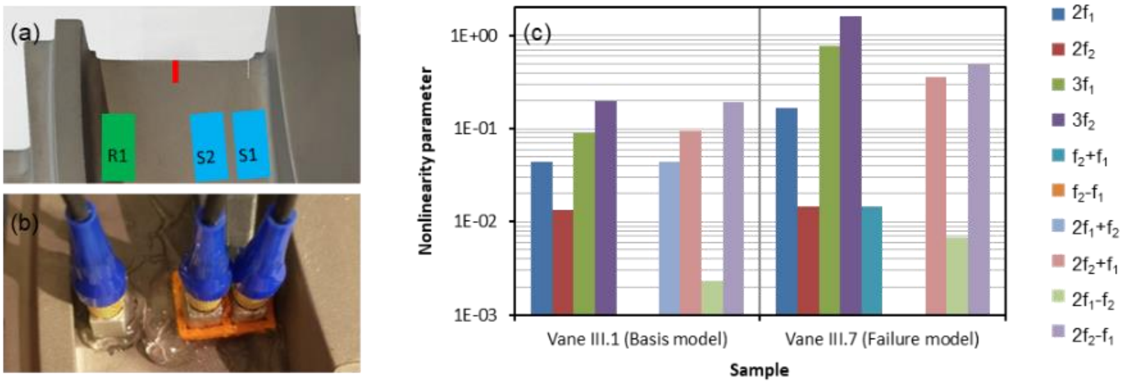

Figure 29. Nonlinearity parameter, parallel sensor orientation, f_1 = 4 MHz, f_2 = 5 MHz: (a) sensor orientation; (b) experimental setup; (c) comparison of nonlinearity parameter.

In the cross-shaped arrangement of the sensors (Figures 30a, b), the parameters $2f_1$, $2f_2$, $3f_2$, and $2f_2{-}f_1$ show increasing values for the damaged sample. The parameter $f_2{+}f_1$ appears only on the damaged sample (Figure 30c).

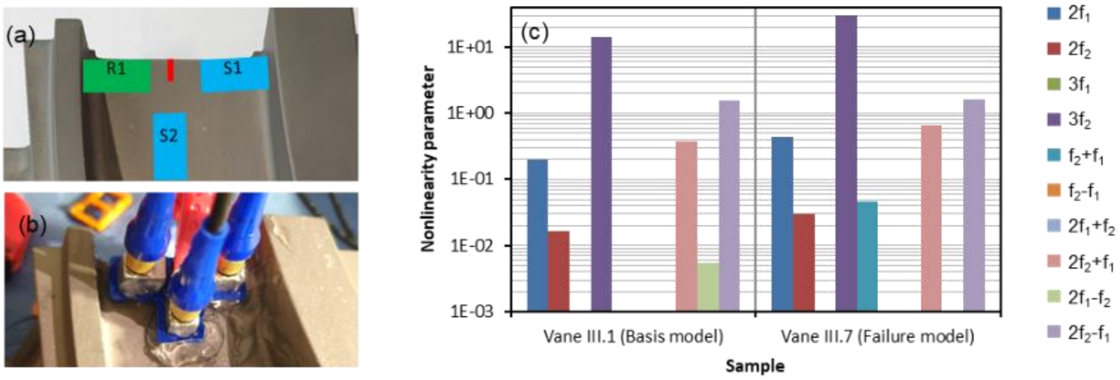

Figure 30. Nonlinearity parameter, 90° sensor orientation, f_1 = 4 MHz, f_2 = 5 MHz: (a) sensor orientation; (b) experimental setup; (c) comparison of nonlinearity parameter.

With opposite orientation of the sending and receiving sensors (Figures 31a, b), the parameters $2f_1$, $2f_2$, $3f_2$, and $2f_2{-}f_1$ show increasing values for the damaged sample (Figure 31c).

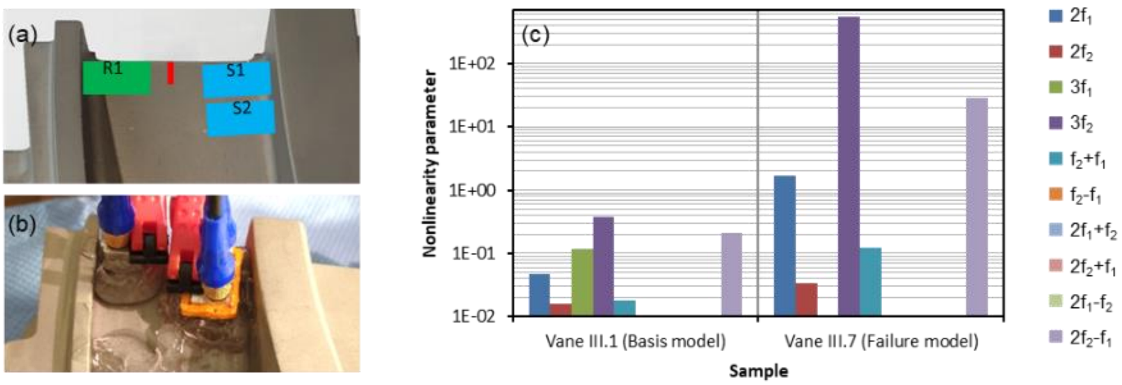

Figure 31. Nonlinearity parameter, opposite sensor orientation, f_1 = 4 MHz, f_2 = 5 MHz: (a) sensor orientation; (b) experimental setup; (c) comparison of nonlinearity parameter.

4.5. Turbine blade

Tests were also conducted on a turbine blade employed in operation conditions. The turbine blade (Figure 32) was used for several thousand operating hours in a 10-MW industrial gas turbine in the first blade stage and was positioned behind the combustion chamber and first vane stage. The turbine blades are regularly inspected using boroscopy to make small cracks or other damage visible. The turbine blade had a crack at the trailing edge between the cooling air outlet openings. The material was Inconel 625, and the blade was provided with a ceramic thermal barrier coating (TBC), which was slightly discoloured during operation. The blade B259T was operated under the same conditions but remained undamaged and therefore serves as a comparative basis for the following measurements.

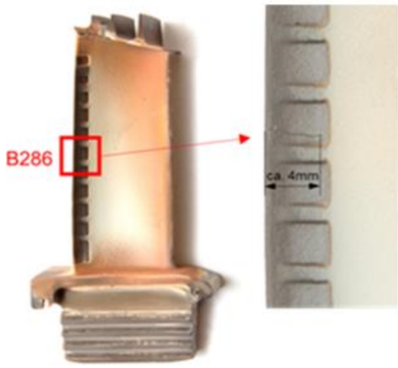

Figure 32. Turbine blade (B286) with a crack on the trailing edge.

4.5.1. Results and discussion

Figure 33 shows the nonlinear parameter measurements on the trailing edges of the turbine blades. The left sides of the figure illustrate the results of the undamaged blade (B259T). The sensors were positioned on the opposite side of the cooling air outlet slots, where a continuous surface is given.

In Figure 33a, an important indicator is that $2f_2$ occurs only in the damaged sample. The parameter values of $2f_2+f_1$ and $2f_2-f_1$ show a significant increase in the damaged sample.

At a sensor angle of α = 60° (shown in Figure 33b), the harmonic frequencies $2f_1-f_2$, $2f_2+f_1$, and $2f_1+f_2$ were regressed exclusively on the measurements on the damaged sample. With $2f_1$, $2f_2$, $3f_2$, and f_2+f_1, an increase of the parameters is measurable compared to the reference sample.

At an angle of α = 90° (Figure 33c), the frequency $f_2{-}f_1$ was not measured at both samples. Most other higher harmonic frequencies also indicate an increase in the parameter values. Those dependent on one frequency like $2f_1$, $3f_1$, and $3f_2$ but also the combination harmonics of two frequencies, $f_2 \pm f_1$, $2f_1 \pm f_2$, and $2f_2 \pm f_1$, show a clear increase in their parameter values.

All three combinations of angles were able to clearly identify the crack in the turbine blade. However, the sensor arrangement at 60° and 90° showed clearer changes in the nonlinear parameter values.

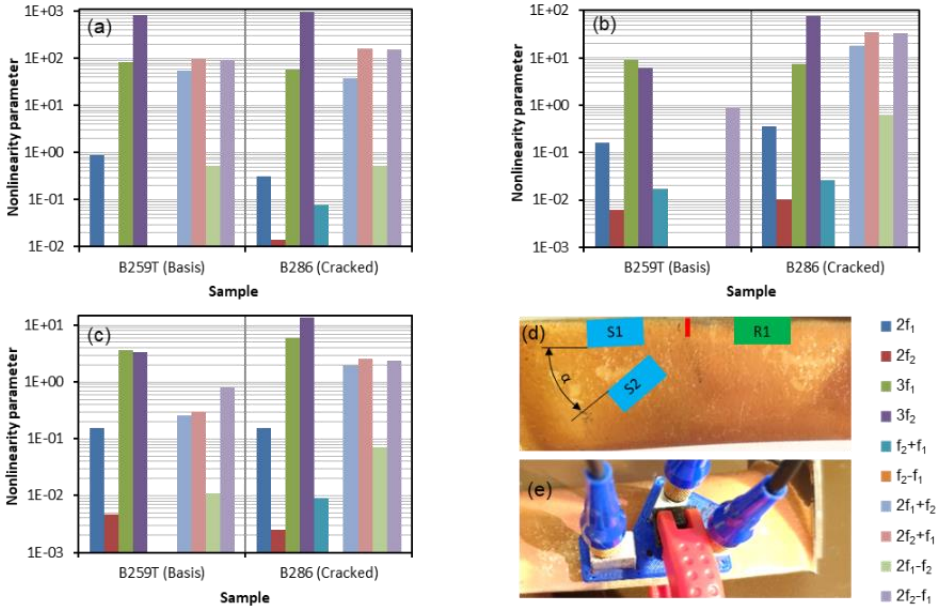

Figure 33. Nonlinearity parameter: (a) f_1 = 4 MHz, f_2 = 5 MHz, α = 45°; (b) f_1 = 4 MHz, f_2 = 5 MHz, α = 60°; (c) f_1 = 4 MHz, f_2 = 5 MHz, α = 90°; (d) sensor orientation; (e) experimental setup.

5. Conclusion

The aim of this study was the development of a frequency modulated nonlinear ultrasonic technique for the detection of cracks in turbine blades. New global nonlinearity parameters were developed to determine a correlation between the crack length and the measured nonlinear features. Their existence has been proven numerically and experimentally. A simple method for adding up the amplitude amounts of the fundamental amplitudes and harmonic amplitudes are used for the crack prediction. The behaviour of the fundamental frequencies is also a good indicator for crack detection and crack size estimation. Therefore, the linear parameters γ_{f1} and γ_{f2} have been proposed.

New sample types made of metal plates, produced with a welding process and SLM technology, were used. Different sensor angle combinations were compared, and in addition to the plate samples, tests were carried out with turbine guide vanes and rotor blades. The results show a clear trend of changing nonlinear parameters as a function of crack size and sensor angles. In all measurements, a dependence of the sensor position to the defect was observed.

It was shown that each crack behaves individually during the ultrasound measurements, since the highest nonlinearities were often found in small- and medium-sized defects. Nevertheless, it became clear that the interactions from the various harmonic frequencies also offer very good additions or alternatives to the already existing measurements and evaluation variants.

This study demonstrates an efficient way to determine the initial loss of structural integrity of these complex components.

Acknowledgement

Thanks to the MAN Energy Solutions SE for their support.

References

1. Li, Z.L.; Achenbach, J.D. Reflection and Transmission of Rayleigh Surface Waves by a Material Interphase. J. Appl. Mech. 1991, 58, 688.
2. Achenbach, J.D.; Lin, W.; Keer, L.M. Mathematical Modelling of Ultrasonic Wave Scattering by sub-Surface Cracks. Ultrasonics 1986, 24, 207–215.
3. Angel, Y.C.; Achenbach, J.D. Reflection and Transmission of Obliquely Incident Rayleigh Waves by a Surface-Breaking Crack. Acoust. Soc. Am. 1983, 74, S87–S87.
4. Hikata, A.; Chick, B.B.; Elbaum, C. Dislocation Contribution to the Second Harmonic Generation of Ultrasonic Waves. J. Appl. Phys. 1965, 36, 229–236.
5. Cantrell, J.H.; Yost, W.T. Nonlinear Ultrasonic Characterization of Fatigue Microstructures. Int. J. Fatigue 2001, 23, 487–490.
6. Mitra, M.; Gopalakrishnan, S. Guided Wave Based Structural Health Monitoring: A Review. Smart Mater. Struct. 2016, 25, 53001.
7. Cho, H.; Lissenden, C.J. Structural Health Monitoring of Fatigue Crack Growth in Plate Structures with Ultrasonic Guided Waves. Struct. Health Monit. 2012, 11, 393–404.
8. Chan, H.; Masserey, B.; Fromme, P. High Frequency Guided Ultrasonic Waves for Hidden Fatigue Crack Growth Monitoring in multi-Layer Model Aerospace Structures. Smart Mater. Struct. 2015, 24, 25037.
9. Masserey, B.; Fromme, P. Analysis of High Frequency Guided Wave Scattering at a Fastener Hole with a View to Fatigue Crack Detection. Ultrasonics 2017, 76, 78–86.
10. Masserey, B.; Fromme, P. Fatigue Crack Growth Monitoring Using High-Frequency Guided Waves. Struct. Health Monit. 2013, 12, 484–493.
11. Masserey, B.; Fromme, P. Noncontact monitoring of fatigue crack growth using high frequency guided waves. In Proceedings of SPIE 9061, Sensors and Smart Structures Technologies for Civil, Mechanical, and Aerospace Systems 2014,SPIE , Bellingham, WA, USA, 8 March 2014.

12. Broda, D.; Staszewski, W.J.; Martowicz, A.; Uhl, T.; Silberschmidt, V.V. Modelling of Nonlinear Crack—Wave Interactions for Damage Detection Based on Ultrasound—A Review. J. Sound Vib. 2014, 333, 1097–1118.
13. Guan, L.; Zou, M.; Wan, X.; Li, Y. Nonlinear Lamb Wave Micro-Crack Direction Identification in Plates with Mixed-Frequency Technique. Appl. Sci. 2020, 10, 2135.
14. Lim, H.J.; Sohn, H. Online Fatigue Crack Prognosis Using Nonlinear Ultrasonic Modulation. Struct. Health Monit. 2019, 18, 1889–1902.
15. Mihara, T.; Konishi, G.; Miura, Y.; Ishida, H. Accurate sizing of closed crack using nonlinear ultrasound of space with high voltage transformer pulser technique. In Proceedings of American Institute of Physics Conference, Baltimore, MD, USA, 21–26 July 2013; AIP Publishing LLC: Melville, NY, USA, 2014; pp. 727–732.
16. Moll, J.; Kexel, C.; Pötzsch, S.; Rennoch, M.; Herrmann, A.S. Temperature Affected Guided Wave Propagation in a Composite Plate Complementing the Open Guided Waves Platform. Sci. Data 2019, 6, 191.
17. Pan, Q.; Pan, R.; Shao, C.; Chang, M.; Xu, X. Research Review of Principles and Methods for Ultrasonic Measurement of Axial Stress in Bolts. Chin. J. Mech. Eng. 2020, 33, 1–16.
18. Jhang, K.-Y.; Kim, K.-C. Evaluation of Material Degradation Using Nonlinear Acoustic Effect. Ultrasonics 1999, 37, 39–44.
19. Frouin, J.; Sathish, S.; Matikas, T.E.; Na, J.K. Ultrasonic Linear and Nonlinear Behavior of Fatigued Ti–6Al–4V. J. Mater. Res. 1999, 14, 1295–1298.
20. Rothenfusser, M.; Mayr, M.; Baumann, J. Acoustic Nonlinearities in Adhesive Joints. Ultrasonics 2000, 38, 322–326.
21. Yost, W.T. Nonlinear ultrasonic pulsed measurements and applications to metal processing and fatigue. In Proceedings of the 27th annual review of progress in quantitative nondestructive evaluation, Ames, Iowa, USA, 16–20 July 2000; AIP: Melville, NY, USA, 2000; pp. 1268–1275.
22. Boccardi, S.; Callá, D.B.; Ciampa, F.; Meo, M. Nonlinear Elastic multi-Path Reciprocal Method for Damage Localisation in Composite Materials. Ultrasonics 2018, 82, 239–245.
23. Jeong, H.; Nahm, S.-H.; Jhang, K.-Y.; Nam, Y.-H. A Nondestructive Method for Estimation of the Fracture Toughness of CrMoV Rotor Steels Based on Ultrasonic Nonlinearity. Ultrasonics 2003, 41, 543–549.
24. Ostrovsky, L.A.; Johnson, P.A. Dynamic nonlinear elasticity in geomaterials. La Rivista del Nuovo Cimento 2001. 24, 1–46.
25. Straka, L.; Yagodzinskyy, Y.; Landa, M.; Hänninen, H. Detection of Structural Damage of Aluminum Alloy 6082 Using Elastic Wave Modulation Spectroscopy. NDT & E Int. 2008, 41, 554–563.
26. Malfense Fierro, G.P.; Meo, M. Residual Fatigue Life Estimation Using a Nonlinear Ultrasound Modulation Method. Smart Mater. Struct. 2015, 24, 25040.
27. Malfense Fierro, G.P.; Meo, M. Nonlinear Imaging (NIM) of Flaws in a Complex Composite Stiffened Panel Using a Constructive Nonlinear Array (CNA) Technique. Ultrasonics 2017, 74, 30–47.
28. Malfense Fierro, G.P. Development of Nonlinear Ultrasound Techniques for Multidisciplinary Engineering Applications. Ph.D. Thesis, University of Bath, Bath, UK, 2014.
29. Jingpin, J.; Xiangji, M.; Cunfu, H.; Bin, W. Nonlinear Lamb Wave-Mixing Technique for micro-Crack Detection in Plates. NDT & E Int. 2017, 85, 63–71.
30. Amura, M.; Meo, M.; Amerini, F. Baseline-free Estimation of Residual Fatigue Life Using a Third Order Acoustic Nonlinear Parameter. Acoust. Soc. Am. 2011, 130, 1829–1837.
31. TenCate, J.A.; van den Abeele, K.E.A.; Shankland, T.J.; Johnson, P.A. Laboratory Study of Linear and Nonlinear Elastic Pulse Propagation in Sandstone. J. Acoust. Soc. Am. 1996, 100, 1383–1391.
32. Bermes, C.; Kim, J.-Y.; Qu, J.; Jacobs, L.J. Nonlinear Lamb Waves for the Detection of Material Nonlinearity. Mech. Syst. Signal Process. 2008, 22, 638–646.

33. 3 Herrmann, J.; Kim, J.-Y.; Jacobs, L.J.; Qu, J.; Littles, J.W.; Savage, M.F. Assessment of Material Damage in a Nickel-Base Superalloy Using Nonlinear Rayleigh Surface Waves. J. Appl. Phys. 2006, 99, 124913.

34. Markovic, N.; Stojic, D.; Cvetkovic, R.; Radojicic, V.; Conic, S. Numerical Modeling of Ultrasonic Wave Propagation-by Using of Explicit FEM in ABAQUS. Facta Univ. Ser. Archit. Civ. Eng. 2018, 16, 135–147.

35. Schwarz, C.; Werner, E.; Dirschmid, H.J. 1D Wave Propagation in a Rod: Analytic Treatment for non-Trivial Boundary Conditions. Proc. Appl. Math. Mech. 2010, 10, 525–526.

36. Cui, Z.; Huang, Y. Discussion on Acoustic Databases in LS-DYNA. 2017. Available online: http://www.lstc.com/sites/default/files/marketing/new_features/12_Acoustic_Databases_ZheCui_2017_01.pdf (accessed on 8 March 2020).

37. Maraghechi, B.; Hasani, M.H.; Kolios, M.C.; Tavakkoli, J. Temperature Dependence of Acoustic Harmonics Generated by Nonlinear Ultrasound Wave Propagation in Water at Various Frequencies. J. Acoust. Soc. Am. 2016, 139, 2475.

38. Song, B.; Zhao, X.; Li, S.; Han, C.; Wei, Q.; Wen, S.; Liu, J.; Shi, Y. Differences in Microstructure and Properties between Selective Laser Melting and Traditional Manufacturing for Fabrication of Metal Parts: A Review. Front. Mech. Eng. 2015, 10, 111–125.

5 MULTI-FREQUENCY MODULATION

In the previous chapter, nonlinearity parameters up to the third order were analytically derived with dual-frequency ultrasound excitation and the advantages were experimentally demonstrated.

Overall, increasing the degree of nonlinearity is not advantageous, because the higher the order of nonlinearity, the lower the probability of receiving an evaluable signal [82, 114, 115]. However, it may be promising to increase the number of fundamental frequencies, which is the focus of this chapter. Therefore, the wave equation was analytically extended with quadruple wave excitation. When four different frequencies pass a material failure, this leads to 64 harmonic frequencies and sidebands as a result of the mutual interaction. The grouping concept was developed to use a large number of frequencies for failure detection. The fundamental frequencies are selected in such a way that several harmonic and sideband frequencies meet at a certain frequency. If, for example, the frequencies f_1 = 5 MHz and f_2 = 10 MHz are sent, then the harmonic frequency $3f_2$ and the sidebands $f_2 + f_1$ and $2f_2 - f_1$ will coincide at 15 MHz. This increased signal energy to a certain frequency also increases the sensitivity for detecting defects in materials. With four ultrasonic waves, different groups were formed, consisting of up to four fundamental frequencies, harmonic frequencies and sidebands. To evaluate the data reduced to one value, N_{index} was proposed, which represents the summation of the nonlinearity parameters. The study presented in this chapter is also intended to compare the various excitation techniques with one another. Thus, the following concepts were experimentally tested on identical samples and compared:

- Single-frequency excitation
- Dual-frequency excitation with constant frequencies
- Dual-frequency excitation with a linearly increasing frequency
- Four-frequency excitation with the grouping concept

Plate samples made of Inconel 718 were used for experimental evidence, which were welded together using a special microwelding process to generate failures of different lengths on the samples. In addition, the turbine blades of a gas turbine were examined, where cracks formed during its operation. Investigations showed that sending two frequencies has considerable advantages over single-frequency excitation. With four frequencies and the application of the grouping concept, very good results were obtained for the nonlinearity parameters as a function of the crack size.

The form 'Statement of Authorship' and the paper are provided on the following pages.

This declaration concerns the article entitled:			
Nonlinear ultrasound crack detection with multi-frequency excitation—a comparison			
Publication status			
Draft manuscript ☐ Submitted ☐ Accepted ☐ Published ☒			
Publication details (reference)			
Mevissen, F., & Meo, M. (2021). Nonlinear ultrasound crack detection with multi-frequency excitation—a comparison. *Sensors*, *21*(16), 5368. https://doi.org/10.3390/s21165368			
Candidate's contribution to the paper (detailed, and also given as a percentage)			
<u>Formulation of ideas:</u> 95% I came up with the idea of quadruple-frequency excitation and the grouping concept after my discussions with Professor Michele Meo.			
<u>Design of methodology:</u> 95% All the analytical work and development of the grouping concept were performed by me and checked by my supervisor.			
<u>Experimental work:</u> 95% I obtained the samples and performed all the experiments. Professor Michele Meo made suggestions to improve the conduction of the experiments.			
<u>Presentation of data in journal format:</u> 90% I processed the obtained data, created all the figures and chose the structure of the manuscript. Professor Michele Meo provided feedback on the draft and helped with the submission, review and publication processes.			
Statement from candidate			
This paper contains original research that I have conducted during the period of my higher degree of research candidature.			
Signed	[redacted]	**Date**	20/10/2022

Nonlinear ultrasound crack detection with multi-frequency excitation—a comparison

Frank Mevissen and Michele Meo

Department of Mechanical Engineering, University of Bath, Bath, BA2 7AY, UK

Abstract

Nonlinear ultrasound crack detection methods are used as modern, non-destructive testing tools for inspecting early damage in various materials. Nonlinear ultrasonic wave modulation, where typically two or more frequencies are excited, was demonstrated to be a robust method for failure indicators when using measured harmonics and modulated response frequencies. The aim of this study is to address the capability of multi-frequency wave excitation, where more than two excitation frequencies are used, for better damage identification when compared to single and double excitation frequencies without the calculation of dispersion curves. The excitation frequencies were chosen in such a way that harmonic and modulated response frequencies meet at a specific frequency to amplify signal energy. A new concept of nonlinearity parameter grouping with multi-frequency excitation was developed as an early failure parameter. An analytical solution of the one-dimensional wave equation was derived with four fundamental frequencies, and a total of 64 individual and 30 group nonlinearity parameters. Experimental validation of the approach was conducted on metal plates with different types of cracks and on turbine blades where cracks originated under service conditions. The results showed that the use of multi-frequency excitation offers advantages in detecting cracks.

1. Introduction

Linear ultrasound techniques are proven testing methods for inspecting components. The failure detection entails measuring changes in elastic properties such as the speed of sound, attenuation, transmission coefficient and reflection coefficient [1–3].

In 1964, Hikata et al. expanded this research and found that a sinusoidal ultrasonic wave distorts the fundamental frequency when it propagates in the presence of nonlinearities [4]. If an ultrasonic wave propagates into a solid body with the fundamental frequency and is disturbed during the propagation, harmonic frequencies are generated. When the amplitudes of these frequencies are measured and compared with the fundamental frequencies, these values represent an accurate indicator for detecting material changes [4]. When linear ultrasonic failure detection techniques reach their limits, nonlinear ultrasonic techniques revealed higher detection rates of incipient failures in materials [4, 5].

The comparison of the amplitudes is conducted using derived nonlinearity parameters. Jhang et al. studied the second harmonic parameter β to explain its dependence on the wave shift, which enabled drawing conclusions about the material to be examined [6]. This work was extended by Frouin et al. [7], Rothenfusser et al. [8] and Yost et al. [9], who showed the direct dependence of the amplitudes of the fundamental frequency as well as the frequency of the second harmonic. The analytical derivations were conducted by Jeong et al. [10], while Ostrovky et al. investigated the nonlinearity parameters for geomaterials [11]. To determine the residual fatigue life of a component, Malfense Fierro and Meo developed the nonlinearity parameters for two superimposed frequencies [12–14], which was further developed by Jinpin et al. [15]. The third-order nonlinearity parameter with one driving frequency was derived from Amura and Meo [16]. The nonlinearity parameters of the second and third harmonic frequencies are shown in Equation (1) for one excitation frequency, where A is the amplitude of the fundamental frequency, A_2 is the amplitude of the second harmonic frequency and A_3 is the amplitude of the third harmonic frequency:

$$\begin{aligned} \beta_{2f} &\propto \frac{A_2}{A^2}, \\ \gamma_{3f} &\propto \frac{A_3}{A^3}. \end{aligned} \tag{1}$$

The excitation with two different frequencies up to third-order nonlinearity was analytically derived and investigated [17]. A total of 12 derived nonlinearity parameters were successfully used to detect cracks in metal components and turbine blades (Equation (2)). The excitation with two different frequencies were defined with $u^{(1)} = A_1 sin\left[k_{f1}(x - ct)\right] + A_2 cos\left[k_{f2}(x - ct)\right]$, where A_1 and A_2 are the amplitudes and k_{f1} and k_{f2} are the wavenumbers of the fundamental frequencies f_1 and f_2. A_{f1+f2} are the amplitudes of the harmonic or modulated response frequencies:

$$
\begin{gathered}
\gamma_{f1} \propto \frac{A_{f1+f2}}{{A_1}^3 + A_1{A_2}^2}, \\
\gamma_{f2} \propto \frac{A_{f1+f2}}{{A_2}^3 + {A_1}^2 A_2}, \\
\beta_{2f1} \propto \frac{A_{f1+f2}}{{A_1}^2}, \\
\beta_{2f2} \propto \frac{A_{f1+f2}}{{A_2}^2}, \\
\gamma_{3f1} \propto \frac{A_{f1+f2}}{{A_1}^3}, \\
\gamma_{3f2} \propto \frac{A_{f1+f2}}{{A_2}^3}, \\
\beta_{f2\pm f1} \propto \frac{A_{f1+f2}}{A_1 A_2}, \\
\gamma_{2f1\pm f2} \propto \frac{A_{f1+f2}}{{A_1}^2 A_2}, \\
\gamma_{2f2\pm f1} \propto \frac{A_{f1+f2}}{A_1 {A_2}^2}.
\end{gathered} \tag{2}
$$

An overview of current research developments relating to nonlinear vibroacoustic modulation techniques is shown in [18]. Van Den Abeele et al. used two superimposed frequencies for excitation and examined the harmonics of both waves and their sideband frequencies to detect cracks [19]. They also developed a technique to investigate the influence of damaged materials on the amplitude-dependent resonance frequency shifts [20]. These methods are based on the nonlinear interactions of low-frequency and high-frequency waves. Straka et al. and Greenhall et al. worked on a nonlinear elastic wave modulation spectroscopy (NEWMS), where the effect of two superimposed waves was investigated, and low frequency and high frequency waves were combined to detect damage in components [21, 22]. Using time-reversal-based imaging methods, an application for non-destructive material testing (NDT) with two multi-frequency signals was developed [23]. A technique was presented where two signals are correlated to estimate the Time-of-Flight (ToF) for determining distance information [24]. Novak et al. developed a method to extract system reactions for the second and third harmonic frequencies with a nonlinear convolutional signal analysis [25]. Pfleiderer et al.

investigated the nonlinear response of subharmonics, ultra-subharmonics and ultra-frequency pairs for detecting defects in components [26]. Abraham et al. used nonlinear multi-frequency ultrasound measurement to characterise grain size fluctuations and distributions in metal samples [27]. Gao et al. developed a method for estimating corrosion size, position and depth in aircraft structures based on a local multi-frequency wavenumber estimation [28]. Malfense Fierro and Meo developed a phased array technique where three frequencies were used to identify cracks. The initiate signal f_2 is sent out to affect the dynamics of the crack topology. The subsequent transmitted pump signals f_1 and f_3 generate a modulation that can be used for crack detection, and it was demonstrated that using multiple frequency excitation improves crack detection capabilities [29].

Deng investigated shear horizontal (SH) mode propagation on solid plates, where two shear waves propagate vertically and parallel in the plate and intersect. If the phase velocity of the SH mode is equal to the longitudinal velocity of the plate material, this leads to a cumulative effect of the second harmonic excitation frequency [30, 31]. Pruell et al. showed that phase and group velocity matching can be used to generate acoustic nonlinearities to determine plasticity-driven fatigue damage [32, 33]. Approaches were developed where correction factors were integrated into the solution of the wave equation for other wave types [34, 35].

To show possibly occurring Lamb waves, Figure 1 reveals the dispersion diagram of the phase velocity for the material Inconel 718, which is examined in Section 4. Due to comparable behaviour, the group velocity was not shown in this context. The fundamental frequencies from 6 MHz to 10 MHz were used in parallel and represented by the S_1 mode according to [32]. The S_2 mode demonstrates the range of the second harmonic frequency (12 MHz to 20 MHz) and S_3 the third harmonic frequency range (18 MHz to 30 MHz). It becomes clear that phase synchronization with several excitation frequencies in this frequency range is not possible. The difference in phase velocities decreases only at higher frequencies, such in the third harmonic frequency range. The integration of the modulated response frequencies would make synchronisation highly complex.

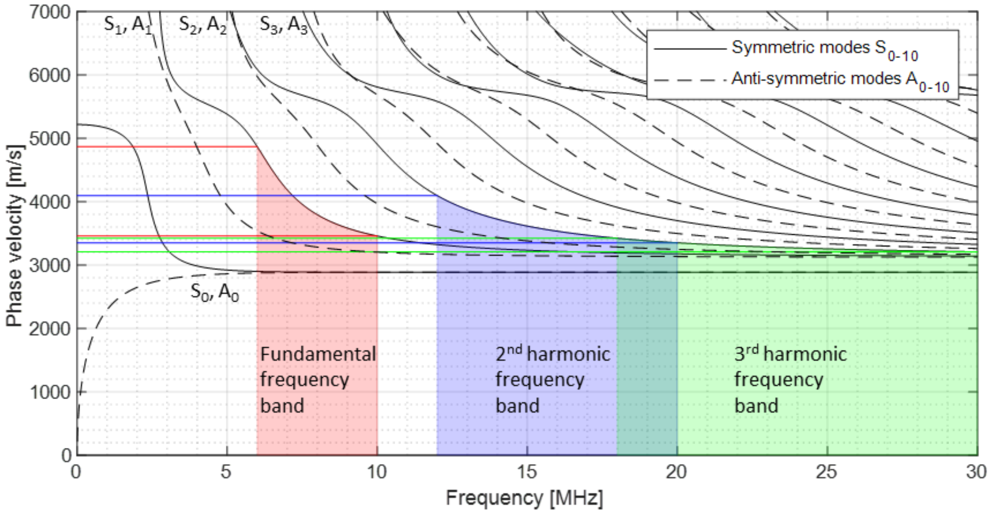

Figure 1. Dispersion curve – phase velocity.

In this paper the strength of the quasi-chaotic generation of harmonic and modulated response frequencies was clearly demonstrated where the dispersion curves are not considered.

Different excitation concepts were compared to detect cracks in metal plates and on turbine blades. For this purpose, excitations with up to four frequencies were examined. In the case of quadruple excitation, a new concept of nonlinearity grouping was developed analytically. The fundamental frequencies were defined in such a way that several harmonics and sideband frequencies meet at certain frequencies to improve crack detection and classification.

2. Multiple nonlinearity parameter

2.1. Analytical approach

To describe and evaluate the excitation with four frequencies, novel nonlinearity parameters up to the third order of nonlinearity were derived analytically in this section.

Figure 2 demonstrates this excitation with the one-dimensional model. In the area of the defect, nonlinearities are generated, and these signals are received at the other end.

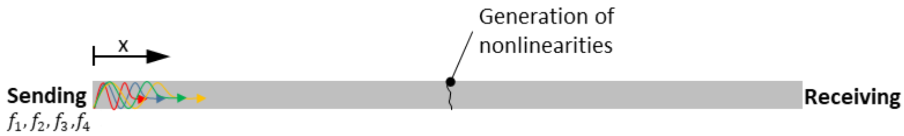

Figure 2. Model - multi-frequency excitation.

The one-dimensional wave equation was solved with four excitation frequencies. All harmonic frequencies and modulated response frequencies up to the third order were derived as well as the associated nonlinearity parameters, which include the amplitudes of the fundamental frequencies and the harmonic and sideband frequencies as variables. In the presence of nonlinearity, the stress σ is defined as:

$$\sigma = E\varepsilon + \frac{E\beta}{2}\varepsilon^2 + \frac{E\gamma}{6}\varepsilon^3, \tag{3}$$

where E is Young's modulus, ε is the strain, β is the second-order nonlinearity parameter and γ is the third-order nonlinearity parameter.

Equation (4) is the one-dimensional wave equation with the assumption that longitudinal waves propagate in a thin circular rod and the attenuation is neglected:

$$\rho \frac{\partial^2 u}{\partial t^2} = \frac{\partial \sigma}{\partial x}, \tag{4}$$

where ρ is the mass density and u represents the displacement. The wave speed is defined as $c = \sqrt{\frac{E}{\rho}}$ and the strain as $\varepsilon = \frac{\partial u}{\partial x}$. This is substituted into Equations (3) and (4) and leads to:

$$\underbrace{\frac{\partial^2 u}{\partial t^2} - c^2 \frac{\partial^2 u}{\partial x^2}}_{Linear\ part} = \underbrace{\underbrace{c^2 \beta \frac{\partial u}{\partial x}\frac{\partial^2 u}{\partial x^2}}_{2^{nd}\ order} + \underbrace{\frac{c^2\gamma}{2}\left(\frac{\partial u}{\partial x}\right)^2 \frac{\partial^2 u}{\partial x^2}}_{3^{rd}\ order}}_{Nonlinear\ part}. \tag{5}$$

Equation (5) is solved using the perturbation method; therefore, Equation (6) is used to find solutions for $u^{(2)}$ with the second-order parameter β and $u^{(3)}$ with the third-order parameter γ:

$$u = u^{(1)} + u^{(2)} + u^{(3)}. \tag{6}$$

According to Fourier, the assumption for $u^{(1)}$ for four excitation frequencies is:

$$\begin{gathered} u^{(1)} = A_1 sin\left[k_{f1}(x - ct)\right] + A_2 cos\left[k_{f2}(x - ct)\right] \\ +A_3 sin\left[k_{f3}(x - ct)\right] + A_4 cos\left[k_{f4}(x - ct)\right], \end{gathered} \tag{7}$$

where $A_{1,2,3,4}$ are the amplitudes and $k_{1,2,3,4}$ are the wavenumbers of the four fundamental frequencies. The detailed derivations are documented in Appendix A.

With an assumed constant wave propagation distance and wavenumber, the general expressions in Table 1 can be derived. The displacement u (Equations (A2) and (A5)) is interpreted as the accumulated amplitude of the harmonic frequency: $u(x)=A_{f1+f2+f3+f4}$.

Table 1. Nonlinearity parameter of quadruple-excitation.

Frequency	Nonlinearity parameter
f_n [1]	$\gamma_{fn} \propto \frac{A_{f1+f2+f3+f4}}{A_n{}^3 + A_n\left(\sum_{i=1}^{n-1} A_i{}^2 + \sum_{i=n+1}^{4} A_i{}^2\right)}$
$2f_n$ [1]	$\beta_{2fn} \propto \frac{A_{f1+f2+f3+f4}}{A_n{}^2}$
$3f_n$ [1]	$\beta_{3fn} \propto \frac{A_{f1+f2+f3+f4}}{A_n{}^3}$
$f_n \pm f_m$ [1,2]	$\beta_{fn\pm fm} \propto \frac{A_{f1+f2+f3+f4}}{A_n A_m}$
$2f_n \pm f_m$ [1,3]	$\gamma_{2fn\pm fm} \propto \frac{A_{f1+f2+f3+f4}}{A_n{}^2 A_m}$
$f_n + f_m \pm f_p$ [1,3]	$\gamma_{f_n+f_m\pm f_p} \propto \frac{A_{f1+f2+f3+f4}}{A_m A_n A_p}$

[1] $n, m, p \in \{1, 2, 3, 4\}$
[2] $n > m$
[3] $n \neq m \neq p$

The parameters β or γ were used depending on the degree of nonlinearity. In the following, δ is used overriding and independent of the degree of nonlinearity for all nonlinearity parameters. A comparison of the various nonlinearity parameters due to multi-frequency excitation is shown in Appendix B.

2.2. Group parameters

The choice of excitation frequencies is crucial to improving damage detection. The following criteria were defined for selecting the highest (f_4) and lowest frequency (f_1) in the multi-frequency analysis:

- No frequency overlap: $f_4 \neq \frac{f_1}{2}$
- No frequencies with theoretical zero values and negative values: $f_4 > \frac{f_1}{2}$
- Sensor bandwidth

With the defined criteria, the excitation frequencies f_1 = 6.8 MHz, f_2 = 7.3 MHz, f_3 = 10 MHz and f_4 = 12 MHz result in 64 individual harmonic and sideband frequencies. If the excitation frequency combination is chosen systematically (f_1 = 6 MHz, f_2 = 7.3 MHz, f_3 = 8.7 MHz and f_4 = 10 MHz), only 30 harmonic and sideband frequencies result. The signal energies of the various harmonic and sidebands add up at specific frequencies; therefore, the group parameters form a stronger indicator for the presence of nonlinearities. The nonlinearity parameters shown in Table 1 described individual values for each frequency. When different fundamental frequencies, harmonic frequencies and sidebands coincide on a frequency, these parameters are no longer valid. The nonlinearity information of one frequency must be summarised on one nonlinearity parameter. For this purpose, the solutions from $u^{(2)}$ (Equation (A2)) and $u^{(3)}$ (Equation (A5)) were re-examined for the grouped nonlinearity parameters. If, for example, the sideband frequencies f_3–f_1 and f_4–f_2 coincide at the frequency 2.6 MHz (Table 3), it can be assumed that the individually calculated nonlinearity parameters, δ, are identical at this point. The total displacement, according to Equations (A2) and (A5), is defined as: $u=u_{f3-f1}+u_{f4-f2}$, which is interpreted as the accumulated amplitude of the sideband frequency (2.6 MHz). Therefore, equations were solved for the new combined nonlinearity parameters. 30 new parameters were derived for this work, called group parameter δ_G. Table 2 to Table 5 illustrate the groups with corresponding frequencies, the harmonic and sideband designation and the new group nonlinearity parameters δ_G.

The derivation of this parameter is illustrated by Equation (8). For group 1, where only one harmonic or sideband per frequency were used, the parameters result from Equations (A2) and (A5). In group 2, two harmonics and sidebands always meet one frequency, which is described by the generalised shift of group 2 with u_{G2}. The amplitudes A_1 and A_2 reveal the summary of the solutions from Equations (A2) and (A5) which should be solved. The placeholder $\Gamma_{f/h/s}$ represents the combination of fundamental, harmonic and sideband frequencies:

$$
\begin{gathered}
u_{G2} = A_1 \tfrac{sin}{cos}\left[(\Gamma_{f/h/s_1})(x-ct)\right]x + A_2 \tfrac{sin}{cos}\left[(\Gamma_{f/h/s_2})(x-ct)\right]x, \\
u_{G3} = A_1 \frac{sin}{cos}\left[(\Gamma_{f/h/s_1})(x-ct)\right]x \\
+A_2 \tfrac{sin}{cos}\left[(\Gamma_{f/h/s_2})(x-ct)\right]x + A_3 \tfrac{sin}{cos}\left[(\Gamma_{f/h/s_3})(x-ct)\right]x, \\
u_{G4} = A_1 \tfrac{sin}{cos}\left[(\Gamma_{f/h/s_1})(x-ct)\right]x + A_2 \tfrac{sin}{cos}\left[(\Gamma_{f/h/s_2})(x-ct)\right]x \\
+A_3 \tfrac{sin}{cos}\left[(\Gamma_{f/h/s_3})(x-ct)\right]x + A_4 \tfrac{sin}{cos}\left[(\Gamma_{f/h/s_4})(x-ct)\right]x.
\end{gathered} \tag{8}
$$

This procedure was also used for the further displacement terms u_{G3} and u_{G4}.

Table 2. Nonlinearity parameter group 1, δ_{G1}.

Group	A_x	Frequency [MHz]	$\Gamma_{f/h/s_x}$	Nonlinearity parameter group δ_G
1	1	2	$2f_1–f_4$	$\delta_{G1}^{1} = \frac{A_{f1+f2+f3+f4}}{{A_1}^2 A_4}$
	1	4	$f_4–f_1$	$\delta_{G1}^{2} = \frac{A_{f1+f2+f3+f4}}{A_4 A_1}$
	1	12	$2f_1$	$\delta_{G1}^{3} = \frac{A_{f1+f2+f3+f4}}{{A_1}^2}$
	1	13.3	f_2+f_1	$\delta_{G1}^{4} = \frac{A_{f1+f2+f3+f4}}{A_2 A_1}$
	1	14	$2f_4–f_1$	$\delta_{G1}^{5} = \frac{A_{f1+f2+f3+f4}}{{A_4}^2 A_1}$
	1	18	$3f_1$	$\delta_{G1}^{6} = \frac{A_{f1+f2+f3+f4}}{{A_1}^3}$
	1	18.7	f_4+f_3	$\delta_{G1}^{7} = \frac{A_{f1+f2+f3+f4}}{A_4 A_3}$
	1	19.3	$2f_1+f_2$	$\delta_{G1}^{8} = \frac{A_{f1+f2+f3+f4}}{{A_1}^2 A_2}$
	1	20	$2f_4$	$\delta_{G1}^{9} = \frac{A_{f1+f2+f3+f4}}{{A_4}^2}$
	1	28.7	$2f_4+f_3$	$\delta_{G1}^{10} = \frac{A_{f1+f2+f3+f4}}{{A_4}^2 A_3}$
	1	30	$3f_4$	$\delta_{G1}^{11} = \frac{A_{f1+f2+f3+f4}}{{A_4}^3}$

Table 3. Nonlinearity parameter group 2, δ_{G2}.

Group	A_x	Frequency [MHz]	$\Gamma_{f/h/s_x}$	Nonlinearity parameter group δ_G
2	1 2	2.6	$f_3–f_1$ $f_4–f_2$	$\delta_{G2}^{1} = \frac{A_{f1+f2+f3+f4}}{A_3 A_1 + A_4 A_2}$
	1 2	3.3	$f_1+f_2–f_4$ $2f_1–f_3$	$\delta_{G2}^{2} = \frac{A_{f1+f2+f3+f4}}{A_1 A_2 A_4 + {A_1}^2 A_3}$
	1 2	12.6	$f_3+f_4-f_1$ $2f_4–f_2$	$\delta_{G2}^{3} = \frac{A_{f1+f2+f3+f4}}{A_3 A_4 A_1 + {A_4}^2 A_2}$
	1 2	14.7	$2f_2$ f_3+f_1	$\delta_{G2}^{4} = \frac{A_{f1+f2+f3+f4}}{{A_2}^2 + A_3 A_1}$
	1 2	16	f_4+f_1 f_3+f_2	$\delta_{G2}^{5} = \frac{A_{f1+f2+f3+f4}}{A_4 A_1 + A_3 A_2}$
	1 2	17.3	$2f_3$ f_4+f_2	$\delta_{G2}^{6} = \frac{A_{f1+f2+f3+f4}}{{A_3}^2 + A_4 A_2}$
	1 2	20.7	$2f_1+f_3$ $2f_2+f_1$	$\delta_{G2}^{7} = \frac{A_{f1+f2+f3+f4}}{{A_1}^2 A_3 + {A_2}^2 A_1}$
	1 2	27.3	$2f_3+f_4$ $2f_4+f_2$	$\delta_{G2}^{8} = \frac{A_{f1+f2+f3+f4}}{{A_3}^2 A_4 + {A_4}^2 A_2}$

Table 4. Nonlinearity parameter group 3, δ_{G3}.

Group	A_x	Frequency [MHz]	$\Gamma_{f/h/s_x}$	Nonlinearity parameter group δ_G
3	1 2 3	1.3	f_2-f_1 f_3-f_2 f_4-f_3	$\delta_{G3}^{1}=\frac{A_{f1+f2+f3+f4}}{A_2A_1+A_3A_2+A_4A_3}$
	1 2 3	6	f_1 $2f_2-f_3$ $f_2+f_3-f_4$	$\delta_{G3}^{2}=\frac{A_{f1+f2+f3+f4}}{{A_1}^3+A_1{A_2}^2+A_1{A_3}^2+A_1{A_4}^2+{A_2}^2A_3+A_2A_3A_4}$
	1 2 3	10	f_4 $2f_3-f_2$ $f_2+f_3-f_1$	$\delta_{G3}^{3}=\frac{A_{f1+f2+f3+f4}}{{A_4}^3+{A_1}^2A_4+{A_2}^2A_4+{A_3}^2A_4+{A_3}^2A_2+A_2A_3A_1}$
	1 2 3	22	$3f_2$ $2f_1+f_4$ $f_1+f_2+f_3$	$\delta_{G3}^{4}=\frac{A_{f1+f2+f3+f4}}{{A_2}^3+{A_1}^2A_4+A_1A_2A_3}$
	1 2 3	23.3	$2f_2+f_3$ $2f_3+f_1$ $f_1+f_2+f_4$	$\delta_{G3}^{5}=\frac{A_{f1+f2+f3+f4}}{{A_2}^2A_3+{A_3}^2A_1+A_1A_2A_4}$
	1 2 3	24.7	$2f_2+f_4$ $2f_3+f_2$ $f_1+f_3+f_4$	$\delta_{G3}^{6}=\frac{A_{f1+f2+f3+f4}}{{A_2}^2A_4+{A_3}^2A_2+A_1A_3A_4}$
	1 2 3	26	$3f_3$ $2f_4+f_1$ $f_2+f_3+f_4$	$\delta_{G3}^{7}=\frac{A_{f1+f2+f3+f4}}{{A_3}^3+{A_4}^2A_1+A_2A_3A_4}$

Table 5. Nonlinearity parameter group 4, δ_{G4}.

Group	A_x	Frequency [MHz]	$\Gamma_{f/h/s_x}$	Nonlinearity parameter group δ_G
4	1 2 3 4	4.6	$2f_2-f_4$ $f_1+f_2-f_3$ $f_1+f_3-f_4$ $2f_1-f_2$	$\delta_{G4}^{1}=\frac{A_{f1+f2+f3+f4}}{{A_2}^2A_4+A_1A_2A_3+A_1A_3A_4+{A_1}^2A_2}$
	1 2 3 4	7.3	$2f_3-f_4$ f_2 $f_1+f_3-f_2$ $f_1+f_4-f_3$	$\delta_{G4}^{2}=\frac{A_{f1+f2+f3+f4}}{{A_3}^2A_4+{A_2}^3+{A_1}^2A_2+A_2{A_3}^2+A_2{A_4}^2+A_1A_3A_2+A_1A_4A_3}$
	1 2 3 4	8.7	f_3 $2f_2-f_1$ $f_2+f_4-f_3$ $f_1+f_4-f_2$	$\delta_{G4}^{3}=\frac{A_{f1+f2+f3+f4}}{{A_3}^3+{A_1}^2A_3+{A_2}^2A_3+A_3{A_4}^2+{A_2}^2A_1+A_2A_4A_3+A_1A_4A_2}$
	1 2 3 4	11.3	$2f_3-f_1$ $f_2+f_4-f_1$ $f_3+f_4-f_2$ $2f_4-f_3$	$\delta_{G4}^{4}=\frac{A_{f1+f2+f3+f4}}{{A_3}^2A_1+A_2A_4A_1+A_3A_4A_2+{A_4}^2A_3}$

If several harmonics or sidebands meet on one frequency, it was expected that the signal energy increases at this point. This assumption was proved experimentally, and the groupings were conducted with two frequencies for comparison. In this case, the previously defined criteria for frequency combination selection do not apply. The frequencies f_1 = 5 MHz and f_2 = 10 MHz are selected for the experiments (Figure 3).

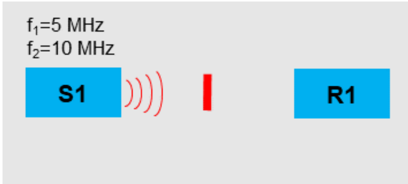

Figure 3. Sensor arrangement – evidence signal grouping.

Using the pulse generator Rigol DG1022Z, the sinus signals were sent to the sensor Olympus A5013. The same sensor was used on the receiving side. Table 6 illustrates the fundamentals, harmonics and sidebands with the corresponding frequencies and groupings. With this frequency combination, there are several harmonics and sidebands at the frequencies 5 MHz, 10 MHz, 15 MHz and 20 MHz.

Table 6. Signal grouping.

Group	$\Gamma_{f/h/s}$	Frequency [MHz]
—	$2f_1–f_2$	0
1	f_1	5
	$f_2–f_1$	5
2	f_2	10
	$2f_1$	10
3	$3f_1$	15
	f_2+f_1	15
	$2f_2–f_1$	15
4	$2f_2$	20
	$2f_1+f_2$	20
—	$2f_2+f_1$	25
—	$3f_2$	30

The first measurement was separately executed with one frequency f_1 and f_2. In the frequency spectrum, the amplitudes were measured at positions $f_{1/2}$, $2f_{1/2}$ and $3f_{1/2}$ (Figures 4a, b). The same experiments were repeated using two superimposing frequencies (f_1 and f_2) transmitted in parallel (Figure 4c). For this purpose, 100 signals were sent out, an average frequency spectrum was formed and the corresponding amplitudes were evaluated.

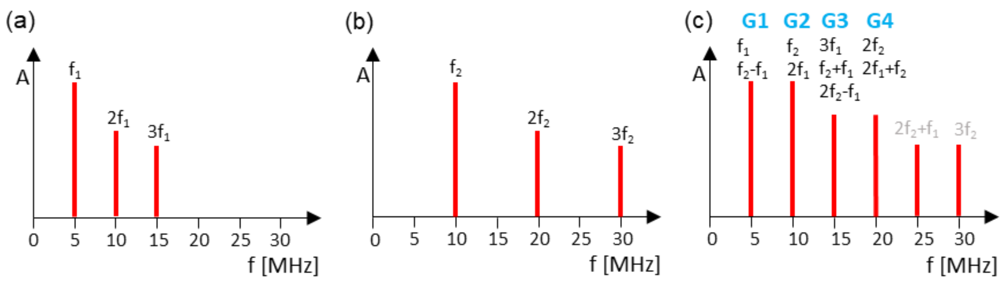

Figure 4. Grouping spectra: (a) f_1 = 5 MHz; (b) f_2 = 10 MHz; (c) f_1 = 5 MHz and f_2 = 10 MHz.

The signal energies were calculated from the measured amplitudes and shown as a comparison in Figure 5. The signal energy resulting from the excitation with one frequency is on the left side of the graphs (*1f*), while the energy from the two-frequency excitation is demonstrated on the right (*2f*). It is evident that more energy was transmitted in the multi-harmonic and sideband grouped signals (*2f*).

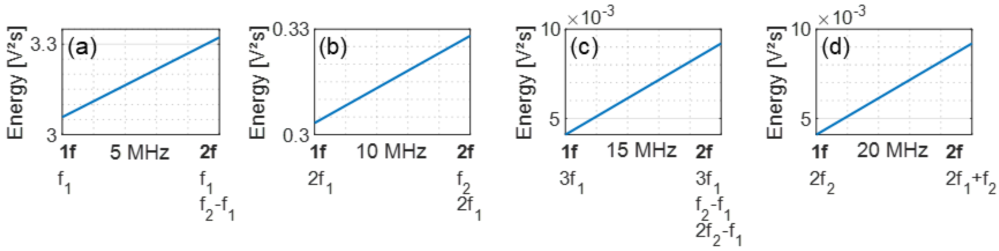

Figure 5. Energy comparison: (a) group 1 (5 MHz); (b) group 2 (10 MHz); (c) group 3 (15 MHz); (d) group 4 (20 MHz).

2.3. Evaluation parameter

The aim of this work is to demonstrate a practicable application of the multi-frequency excitation and compare the results with one, two and four excitation frequencies.

In other research, the total sums of the fundamental frequencies and those of the harmonic and sideband frequencies were compared for evaluation (Equation (9)) [17, 36]:

$$E = \int_{-\infty}^{\infty} |\hat{x}(f_n)|^2 df_n \propto \sum |A_F| + \sum |A_H| \propto \sum |E_F| + \sum |E_H|, \quad (9)$$

where E is the energy, $\hat{x}$ is the signal, A_F are the fundamental amplitudes, and A_H are the harmonic amplitudes, E_F is the signal energy of the fundamental frequencies and E_H is the energy of the harmonic signal. This approach may not be applicable with the four frequency excitation, however, because the grouping of the fundamental frequencies as well as the harmonic and sideband frequencies may overlap. Another possibility of evaluation with the same disadvantages is to use the acoustic moment concept, which is the integral of the power spectral density (PSD) function of a signal [37, 38].

In addition to the nonlinearity parameters, the comparison value N_{index} was introduced for this purpose. This is a summation of the parameter values δ (Equation (10)):

$$N_{index}^{(1f,2f,2f-swept,4f)} = \sum_{n=1}^{m} |\delta_n|, \quad (10)$$

where m is the total number of nonlinearity parameters of the individual measurements.

3. Proof of the use of the one-dimensional wave equation

The derived nonlinearity parameters are based on one-dimensional wave propagation, and it was examined whether this model can also be applied to multi-dimensional applications. A round bar made of the material 1.4571 with a diameter of 5 mm and length of 100 mm was used to simulate a one-dimensional model. To generate artificial contact nonlinearities, the sample was cut in the middle and glued back together. At an area of 1 mm wide, no glue was used so that the two halves had metallic contact. For the measurements, the Olympus sensor A109S were used to send the longitudinal waves into the sample via the front side and to receive them on the other side (Figure 6).

One frequency (6 MHz), two frequencies (6 and 10 MHz) and 4 frequencies (6, 7.3, 8.7 and 10 MHz) were sent according to the group derivation from Section 2.2. The signals were generated with Rigol DG1022Z pulse generators over two channels each and an input voltage of 150 V. The output signal was amplified with the Phoenix ISL 40 dB amplifier.

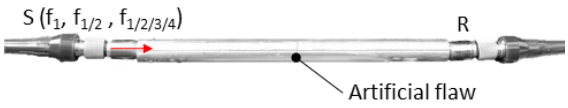

Figure 6. Experimental setup - longitudinal waves.

These tests were also conducted with a reference sample without damage for comparison. The nonlinearity parameters were calculated from these measurements, and the determined N_{index} values are shown in Figure 7a. To clarify the comparison of the excitation methods, the normalised view was also selected (Figure 7b). It becomes clear that the difference with the 4f excitation is stronger than with the 1f excitation.

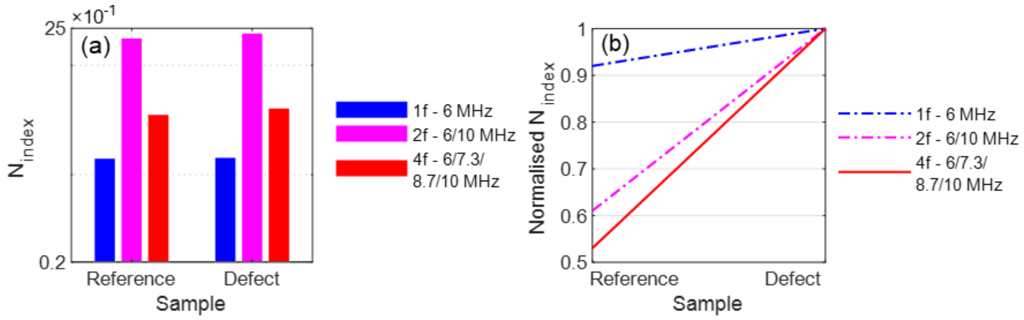

Figure 7. Evaluation: (a) N_{index}; (b) normalised N_{index}.

4. Experimental investigation – plate samples

In this section, the analytical derivations were proven experimentally and compared with the different excitation concepts.

4.1. Experimental setup

Identical test setups were installed for all experiments (Figure 8a), where two Rigol DG1022Z pulse generators were used for signal generation. Each device had two output channels to send the single or superimposed frequencies to the sending sensor. For synchronisation, both devices were connected to each other via the trigger inputs and outputs. The combined signals were amplified with the amplifier Falco WMA-300. The S1 sensor was the Olympus A5013. The same sensor was used to receive the signal (R1), which was amplified with the Phoenix ISL 40 dB amplifier and sent to the Picoscope 4424 oscilloscope. The post-processing was conducted from this position.

Figure 8b reveals the experimental setup. The sensors were held in an additively manufactured holder and always ensured precise alignment. Two clamps were used for a certain contact pressure, and standard contact gel was applied under the sensors for better contact.

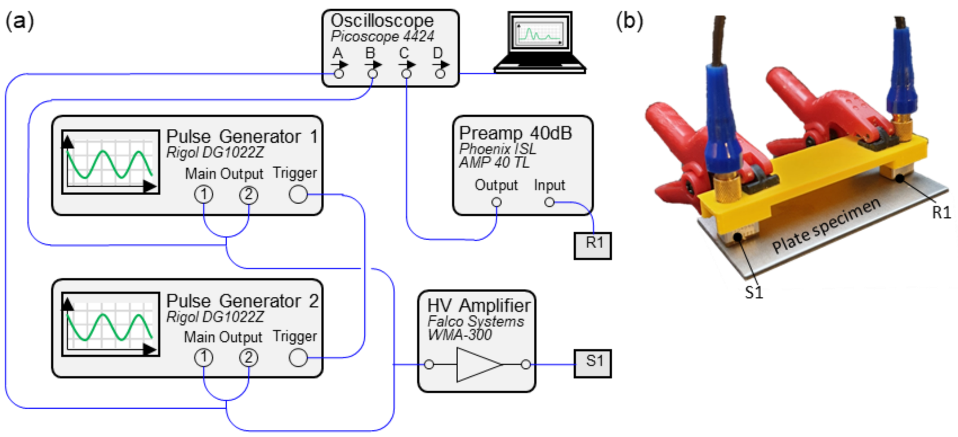

Figure 8. Experimental setup: (a) scheme; (b) sensor arrangement.

The samples used were Inconel 718 plates with the dimensions 2 mm × 70 mm × 30 mm, which consist of two plates connected using a special micro laser welding process. Samples with a defect width of 5, 2 and 1 mm were used and arranged centrally (Figure 9). Due to these artificial defects, contact nonlinearities were generated and evaluated, and reference samples without defects were available for comparison. Six variants of each sample were examined and the arithmetic mean values processed.

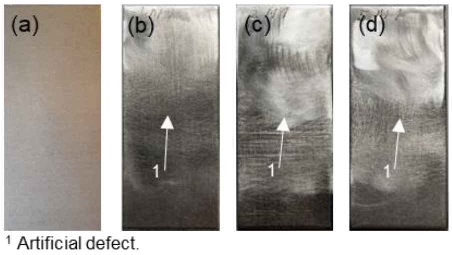

Figure 9. Specimen: (a) X1 - reference sample; (b) 1M - failure size: 1 mm; (c) 2M - failure size: 2 mm; (d) 5M - failure size: 5 mm.

4.2. One-frequency excitation

In this section, the excitation via single frequencies was examined. A 6 MHz frequency signal and a 10 MHz signal were separately sent to the samples (Figure 10).

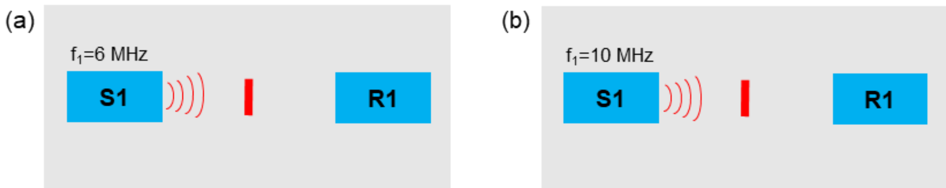

Figure 10. Excitation frequencies: (a) f_1 = 6 MHz; (b) f_1 = 10 MHz.

The second and third harmonic frequencies were considered accordingly. When 6 MHz is excited, the nonlinearity parameters of samples 1M and 2M increase significantly (Figure 11a). A form of saturation was observed as the values drop in the 5M sample. With the nonlinearity parameters of the third harmonic frequency, the value for the 1M sample decreases and then continuously increases for the other samples (2M and 5M). If the samples are sonicated with 10 MHz, a downward trend for both the second and third harmonic frequencies was given. Only the 5M sample demonstrated a significant increase in nonlinearities compared to the reference sample (Figure 11b).

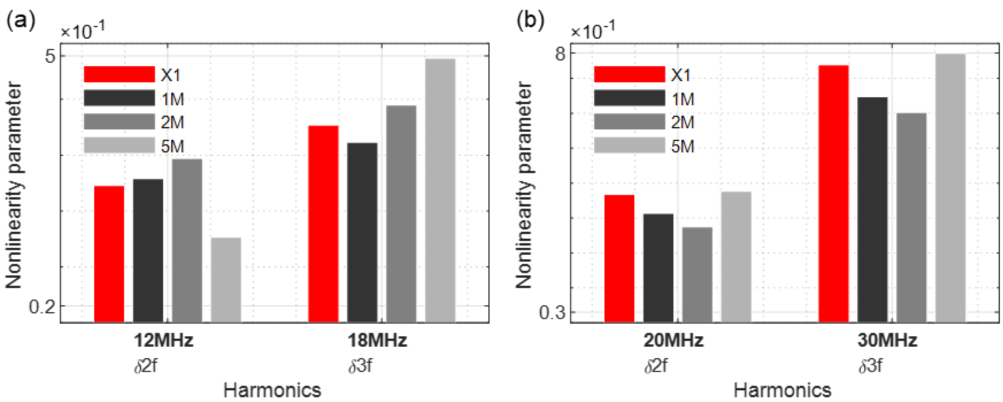

Figure 11. Nonlinearity parameter: (a) f_1 = 6 MHz; (b) f_1 = 10 MHz.

4.3. Two-frequency excitation

4.3.1. Constant frequencies

If two frequencies emitted in parallel are used, the evaluation becomes more complex since a total of 12 harmonic and sideband frequencies are formed which can be evaluated. This technique was successfully used and proven in [17]. A 6 MHz and 10 MHz signal were generated, superimposed and sent via sensor S1. If the waves overlap, harmonic frequencies and more complex modulated response frequencies were generated, which are evaluated in the following. To compensate the overlapping effects of alternating compressive and tensile stresses on the various sine waves, 100 signals were transmitted per experiment and the mean values of the amplitudes were evaluated.

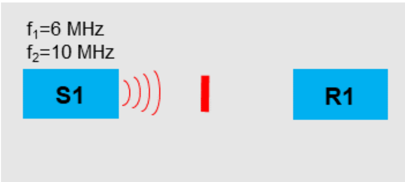

Figure 12. Excitation frequencies: $f_1 = 6$ MHz, $f_2 = 10$ MHz.

Figure 13 reveals the evaluation of the nonlinearity parameters, and all demonstrate a change compared to the reference sample. The parameter value $\delta 2f_2$ showed a clear pattern depending on the crack size. This phenomenon was moreover observed in [17, 36], where the largest nonlinearities were not generated for the largest crack. These are strongly dependent on the fundamental frequencies and illustrate significantly more influence with the 1M and 2M samples.

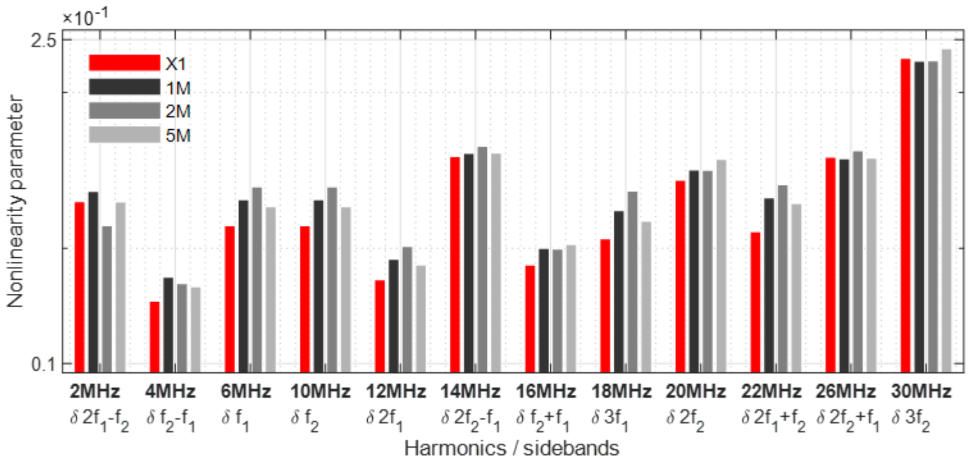

Figure 13. Nonlinearity parameter.

4.3.2. Linear increasing frequency

To investigate as many frequency combinations as possible, the concept of linearly increasing frequencies was also explored. A constant frequency of 10 MHz was transmitted via the sensor S1, and a 6 MHz signal was sent in parallel, which increases linearly to 10 MHz over a period of 60 seconds. The signals were received by sensor R1 (Figure 14), and 60 measurements per second were recorded.

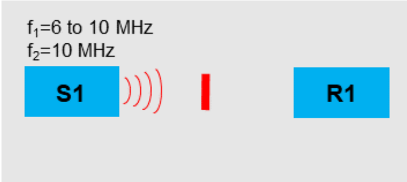

Figure 14. Excitation frequencies: f_1 = 6 to 10 MHz, f_2 = 10 MHz.

In Figure 15 to Figure 19, the nonlinearity parameters are shown for the individual harmonics and sidebands.

In Figure 15a, the x-axis illustrates the actual increasing frequency combination starting with 6/10 MHz up to 10/10 MHz. At the excitation frequencies of 8.4/10 MHz, the values of the 5M sample increase drastically. The values of the 1M sample are consistently higher than those of the 2M sample, while the reference values are always lower except for a peak at 7.4/10 MHz. With parameter $\delta 2f_2$ (Figure 15b), there were increased nonlinearities in the 5M sample at the frequency combinations 6.4/10 MHz, 9.25/10 MHz and 9.6/10 MHz; therefore, the 1M sample reveals smaller peaks at 6.4/10 MHz and 7.8/10 MHz.

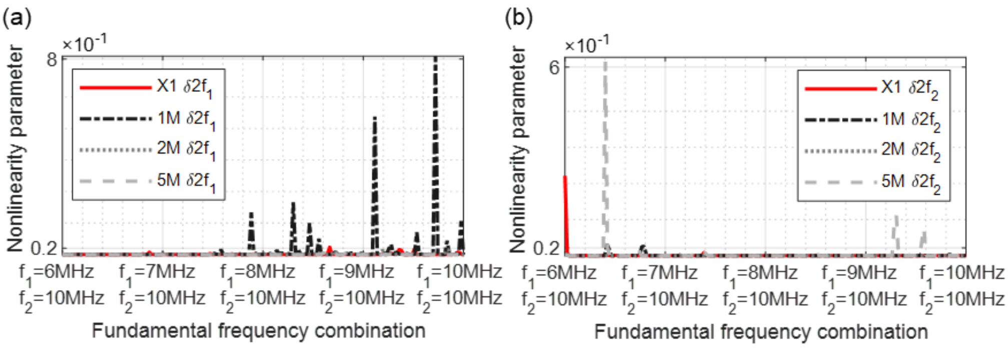

Figure 15. Nonlinearity parameter: (a) $\delta 2f_1$; (b) $\delta 2f_2$.

The third harmonic frequency of the sample 1M demonstrates several significant points at $\delta 3f1$ (Figure 16a). With $\delta 3f2$, increased material nonlinearities were detected in the reference sample at the start of the measurement. In the further course, several peaks of the 5M sample arise again (Figure 16b).

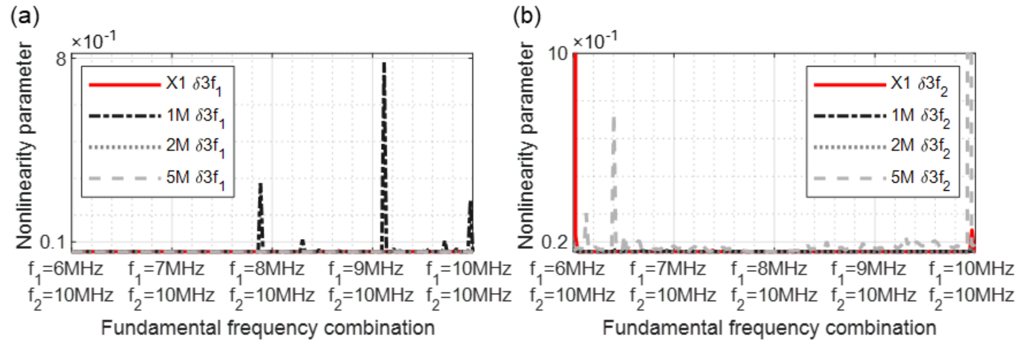

Figure 16. Nonlinearity parameter: (a) $\delta 3f_1$; (b) $\delta 3f_2$.

In Figure 17a, the strength of the dual frequency excitation with a modulated response parameter becomes clear. A comparison demonstrates that the $\delta f_2 – f_1$ values for the 1M sample as well as for the 2M and 5M samples reveal significant increases in nonlinearity. For the parameter $\delta f_2 + f_1$, all samples reveal peaks from different frequency excitation combinations (Figure 17b).

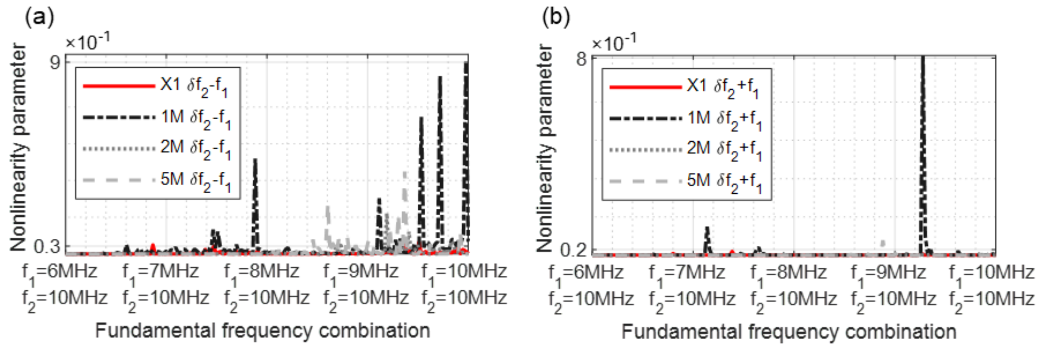

Figure 17. Nonlinearity parameter: (a) $\delta f_2 – f_1$; (b) $\delta f_2 + f_1$.

The parameter $\delta 2f_1 – f_2$ (Figure 18a) demonstrates a clear crack-predicting behaviour. All damaged samples reveal nonlinear features. The previously shown nonlinearity behaviour is continued in (Figure 18b), with clear nonlinear signature particularly in the frequency range 9/10 MHz to 10/10 MHz.

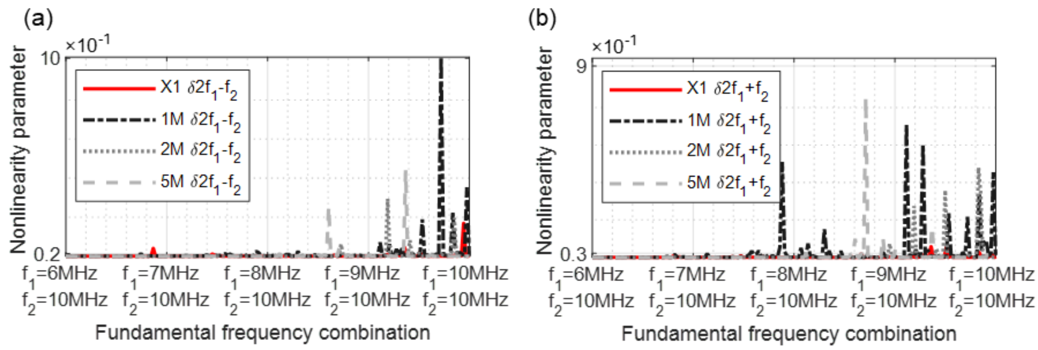

Figure 18. Nonlinearity parameter: (a) $\delta 2f_1 – f_2$; (b) $\delta 2f_1 + f_2$.

In Figure 19a, the sample 1M stands out again due to increased parameter values. In the higher frequency combination range, the damage of the samples 2M and 5M could be identified. Of all parameters, $2f_2+f_1$ (Figure 19(b)) best demonstrates the nonlinearity increases as a function of the crack size. Although higher values were required from the frequency combination 7/10 MHz, the clearest results are from 8.6/10 MHz to 10/10 MHz.

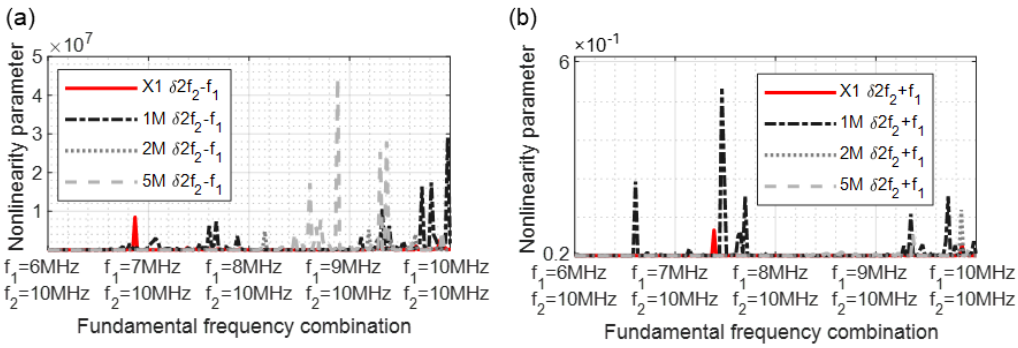

Figure 19. Nonlinearity parameter: (a) $\delta 2f_2\text{–}f_1$; (b) $\delta 2f_2+f_1$.

4.4. Four-frequency excitation

Four frequencies were sent into the sample with sensor S1 (Figure 20). The frequency selection should relate to the concept of frequency grouping (Section 2.2).

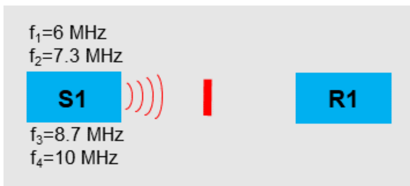

Figure 20. Excitation frequencies: f_1 = 6 MHz, f_2 = 7.3 MHz, f_3 = 8.7 MHz, f_4 = 10 MHz.

In Figure 21 to Figure 24, the nonlinearity parameters were shown separately with the different groupings. Figure 21 demonstrates all nonlinearity parameters for one frequency (Table 2). The parameter values of the damaged samples usually differ significantly from those of the reference sample. With the 5M sample, insufficient nonlinearities are generated to observe a clear change to the reference sample. For the parameters $\delta 2f_1$, δf_2+f_1, $\delta 2f_4\text{–}f_1$, $\delta 3f_1$, $\delta 2f_1+f_2$, $\delta 2f_4+f_3$ and $\delta 3f_4$, the values of the reference sample and the damaged 5M sample are on the same level. With this nonlinearity group, frequencies with a large bandwidth from 2 MHz to 30 MHz were considered.

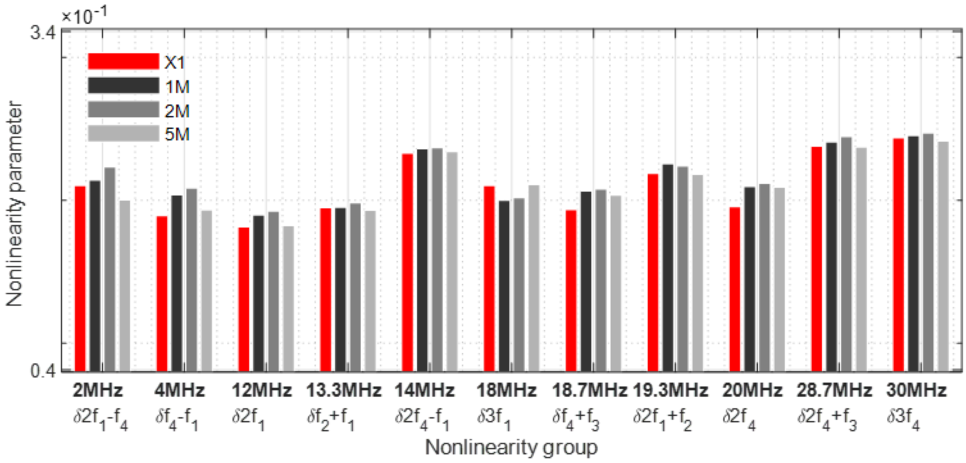

Figure 21. Nonlinearity parameter – δ_{G1}.

In the nonlinearity grouping with 2 frequencies (Table 3), eight parameters were evaluated (Figure 22), with a clear change to the reference sample. At 12.6 MHz ($\delta f_3+f_4–f_1/\delta 2f_4–f_2$), 14.7 MHz ($\delta 2f_2/\delta f_3+f_1$), 16 MHz ($\delta f_4+f_1/\delta f_3+f_2$), 17.3 MHz ($2f_3/\delta f_4+f_2$) and 20.7 MHz ($\delta 2f_1+f_3/\delta 2f_2+f_1$), there is an increase in the nonlinearity parameters as a function of the crack size. The bandwidth ranges from 2.6 MHz to 27.3 MHz.

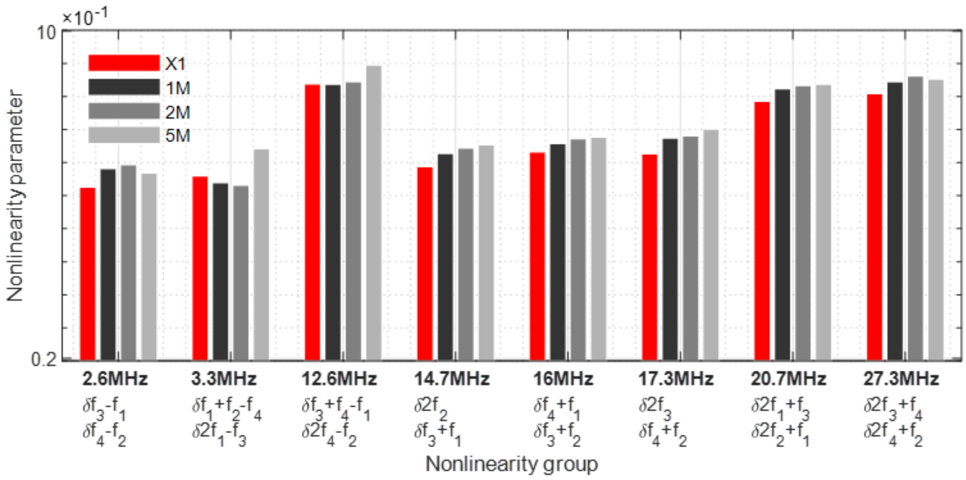

Figure 22. Nonlinearity parameter – δ_{G2}.

Figure 23 demonstrates the frequencies where three nonlinearity parameters meet (Table 4). This group consists of 7 frequencies covering a bandwidth from 1.3 MHz to 26 MHz. These results revealed the strength of the multiple harmonic and modulated response frequencies on one frequency. They reflect the size of the cracks in the samples, with exception of the higher frequencies (23.3 MHz, 24.7 MHz and 26 MHz). Contrary to group 1, an increase in the parameter values of the 5M sample is given; however, the values remain below the 1M and 2M samples.

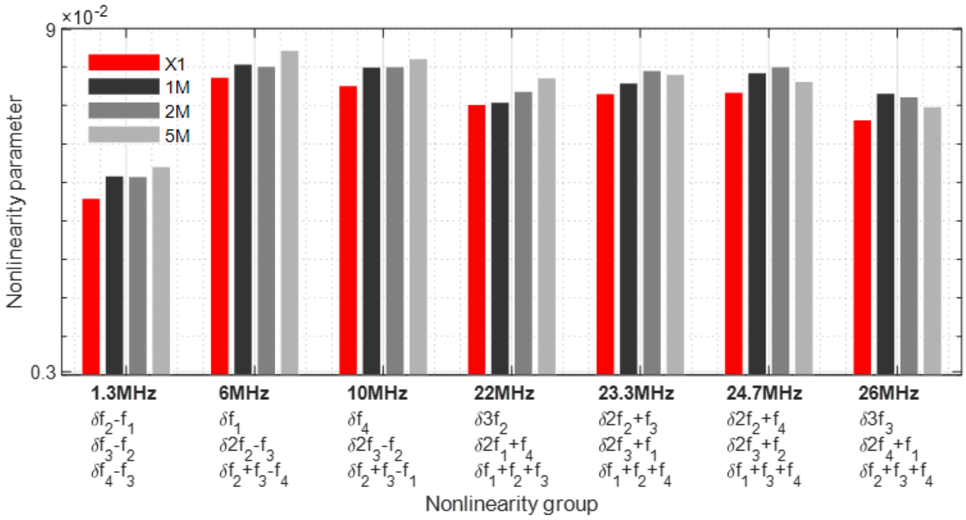

Figure 23. Nonlinearity parameter – δ_{G3}.

The group with four nonlinearity parameters per frequency is shown in Figure 24 (Table 5), which was revealed in a narrower frequency range from 4.6 MHz to 11.3 MHz. This illustrated that the energy of four fundamental, harmonic and sideband frequencies are combined at one frequency, which is why this group has the greatest influence in the evaluation. At 7.3 MHz and 8.7 MHz, two fundamental frequencies are included. At 4.6 MHz, the values of the 5M sample decrease. The other frequencies reveal the nonlinearity parameters as a function of the crack size.

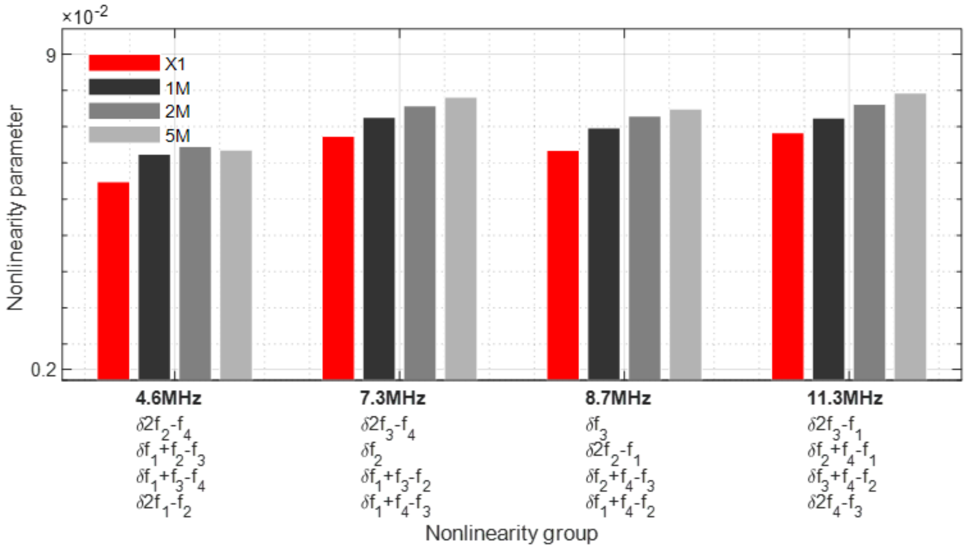

Figure 24. Nonlinearity parameter – δ_{G4}.

4.5. Results and discussion

The various excitation techniques are compared in this section. Therefore, Figure 25 illustrates all N_{index} values. Since the reference sample X1 represents the basis of comparison ($N_{index} = 0$), only the difference to these values were shown. If the values are higher than zero, the nonlinearities increase; if they are smaller, the nonlinearities decrease. The values drop sharply with single-frequency excitation at 10 MHz. Only the values of the 5M sample are in the positive range. The 6 MHz excitation provided better values, even if the values of the 1M sample are minimally below the value of the reference sample. The constant excitation with two frequencies reveals a clear increase in the values, which, however, decrease in the still-positive range for the 5M sample. The arithmetic mean of all measurement data was used to evaluate the swept values. The N_{index} of the 2M sample is on the same level as the reference sample. In this graphic, it was only possible to deliver a course as a function of the crack size with the quadruple-excitation.

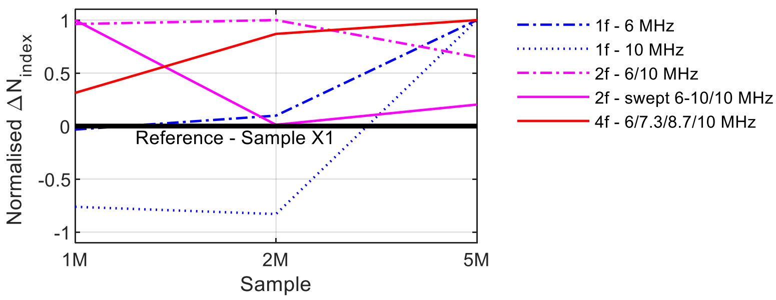

Figure 25. Comparison N_{index} values.

5. Experimental investigation - turbine blades

In the previous section, the various excitation philosophies were tested on metal plates with artificial defects. In this section, turbine blades with cracks on the trailing edges were examined using the different excitation concepts.

5.1. Experimental setup

Four Inconel 628 turbine blades from an industrial gas turbine were used for this study. Three blades had cracks on the trailing edges on different positions (Figure 26), while one blade was unused and undamaged and serves as a reference for comparison. These blades are cooled internally, with the cooling air directed into the blade root and exiting via various outlet slots at the trailing edge following the serpentine cooling.

Figure 26 illustrates the blades used with the crack position and Table 7 the corresponding crack lengths.

Figure 26. Damaged turbine blades.

Table 7. Overview - turbine blades.

Blade	Crack position [cooling air outlet chamber (Figure 26)]	Crack length [mm]
B292	—	—
B046	2	6.0
B254	3	6.8
B286	6	6.1

The experimental setup was implemented as described in Section 4. The emitting sensor S1 was positioned in the area of the inner shroud on a smooth area on the blade airfoil (Figure 27a). The receiving sensor R1 was located opposite, near the outer shroud. Using an additively manufactured sensor holder, the sensors are held in the same position during all tests, and an identical measuring distance was ensured (Figure 27b).

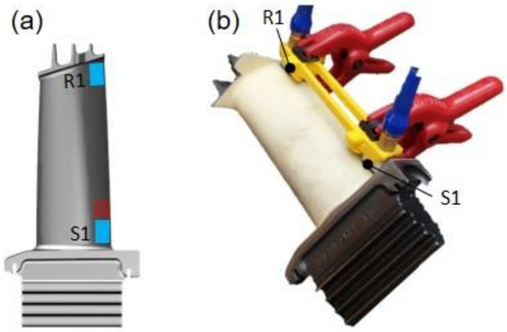

Figure 27. Measurements turbine blades: (a) sensor orientation; (b) experimental setup.

5.2. Measurements with results and discussion

Figure 28 revealed the excitation with a frequency of 6 MHz (Figure 28a) and 10 MHz (Figure 28b). When excited with 6 MHz, the second harmonic parameter δf_2 demonstrates a clear increase in nonlinearities; the 10 MHz excitation, however, hardly allows conclusions to be drawn about the damage.

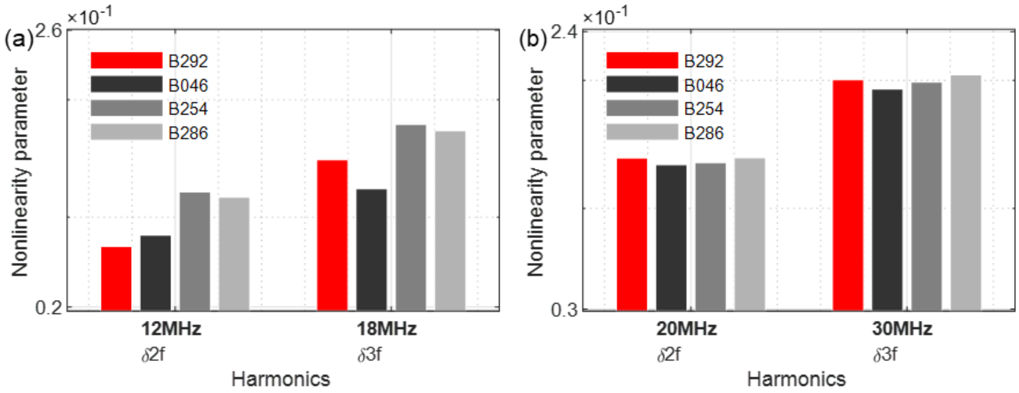

Figure 28. Nonlinearity parameter: (a) $f_1 = 6$ MHz; (b) $f_1 = 10$ MHz.

The dual frequency excitation with 6 MHz and 10 MHz clearly reveals increases in nonlinearity (Figure 29).

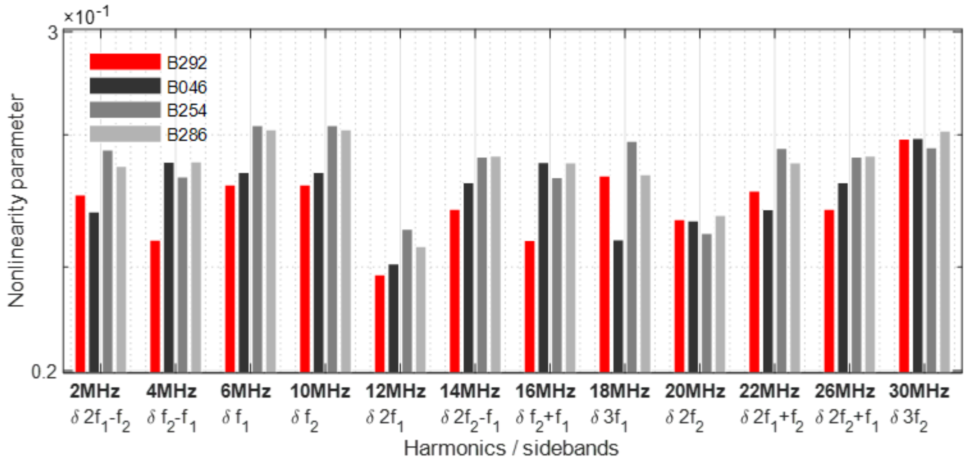

Figure 29. Nonlinearity parameter.

In Figure 30 and Figure 31, the most relevant results are demonstrated with swept signals. It is noticeable that the reference blades (B292) also have a higher degree of nonlinearity peaks (Figure 30a). Using an excitation frequency combination starting with 8.2/10 MHz, both the reference blade B292 and blade B286 show harmonics. Further significant increases in the nonlinearity parameters were measured for all damaged blades. As with the metal plate samples, the excitation frequency combinations from 8/10 MHz lead to considerable increases in the nonlinearity parameters. Blade B254 achieved the highest values for both $\delta 2f_1$ and parameter $\delta 3f_1$ (Figure 30b).

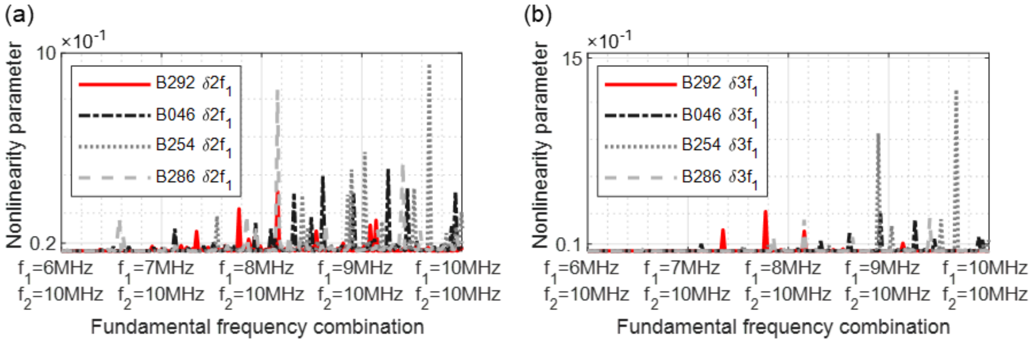

Figure 30. Nonlinearity parameter: (a) $\delta 2f_1$; (b) $\delta 3f_1$.

The results of two modulated response parameters ($\delta 2f_2 \pm f_1$) are illustrated in Figure 31. The blade B254 reveals the highest nonlinear values. The crack can also be diagnosed for blades B046 and B286 by the increased nonlinearity values.

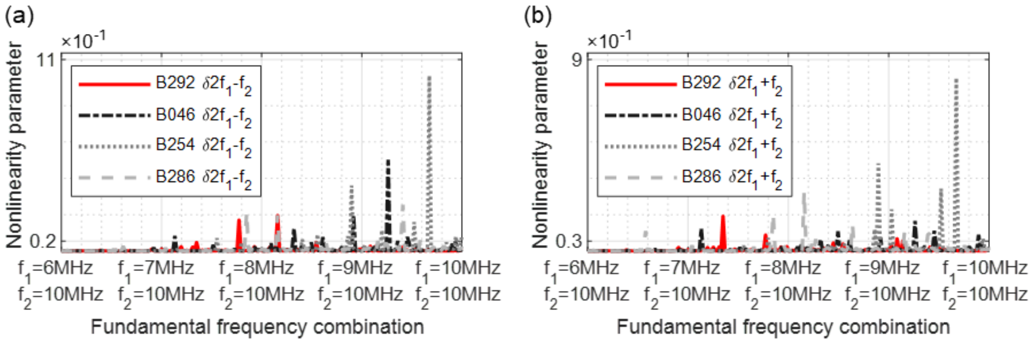

Figure 31. Nonlinearity parameter: (a) $\delta 2f_1$–f_2; (b) $\delta 2f_1+f_2$.

When evaluating the excitation with four frequencies, the procedure described in Section 2.2 was followed. The grouping of the nonlinearity parameters was used for crack detection. Figure 32 illustrates group 1, with one nonlinearity parameter per frequency. The parameters δf_4–f_1, $\delta 2f_4$–f_1, $\delta 3f_1$, δf_4+f_3, $\delta 2f_4$, $\delta 2f_4+f_3$ and $\delta 3f_4$ reveal a clear increase in the nonlinearity parameters and allow a positive crack prognosis.

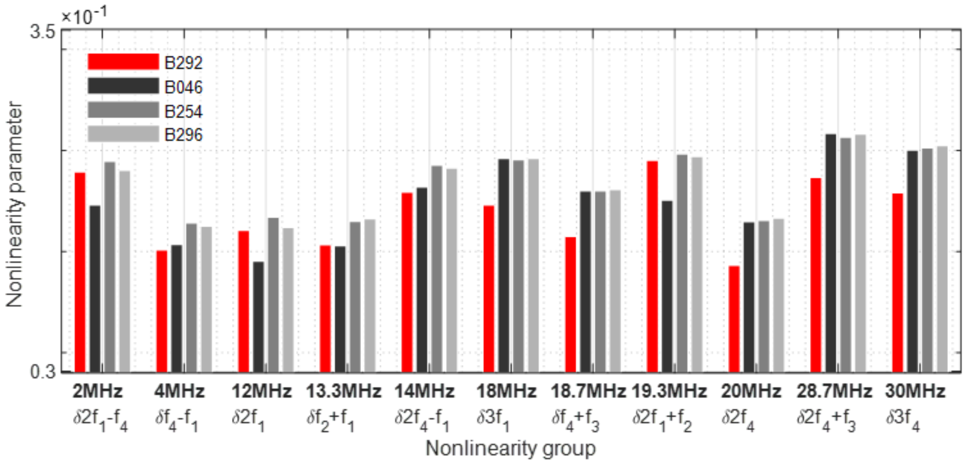

Figure 32. Nonlinearity parameter – δ_{G1}.

If two parameters decrease on one frequency (Figure 33), the results are strong, showing that detecting cracks was possible with this group evaluation alone.

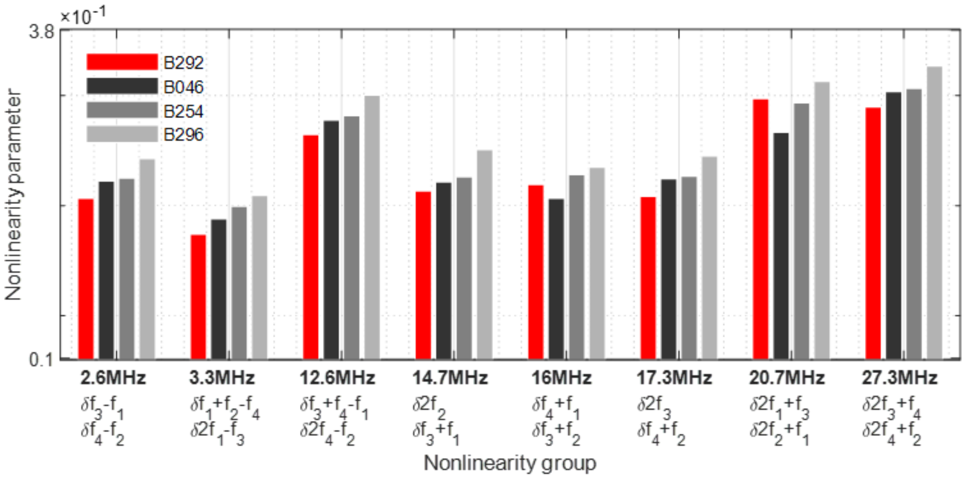

Figure 33. Nonlinearity parameter – δ_{G2}.

This behaviour continues and is also shown in the nonlinearity group 3 (Figure 34). Only $\delta 3f_2$ failed to clearly detect the crack on the blade B046.

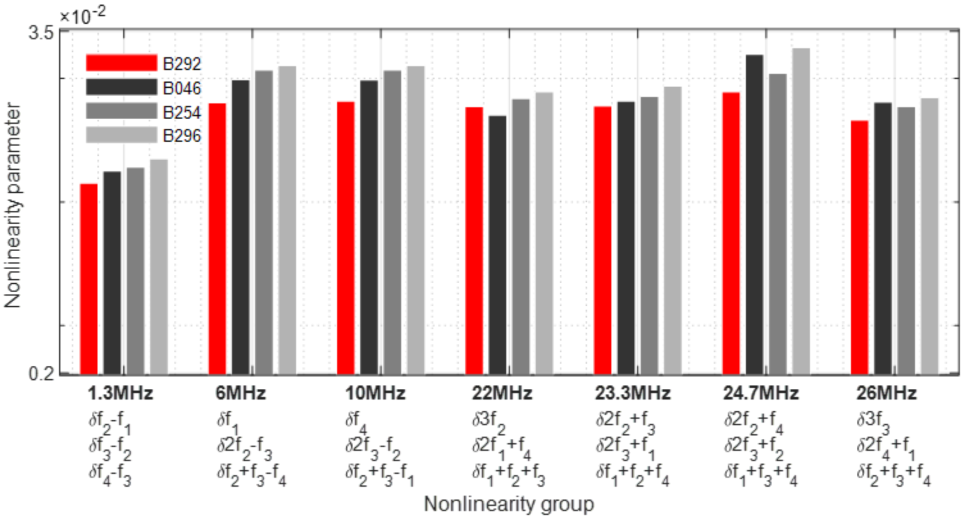

Figure 34. Nonlinearity parameter – δ_{G3}.

As in Section 4, the differences between the various parameter values have become smaller (Figure 35). Because the signal energies of four fundamental, harmonic and modulated response parameters each coincide on one frequency, this group approach provides the strongest informative value.

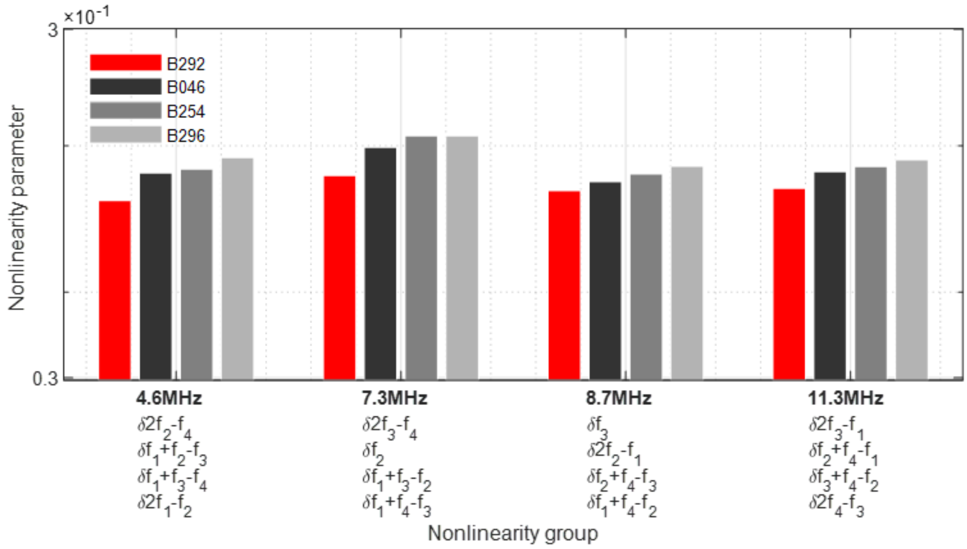

Figure 35. Nonlinearity parameter – δ_{G4}.

In Figure 36, the normalised N_{index} values for the different processes are used for evaluation again. If only one frequency is used for excitation, a crack forecast with these values is hardly possible; if two frequencies are used, both constant excitation and excitation by means of swept signals reveal a comparable, increasing behaviour; and with four frequency excitations, these values increase continuously.

In most of the measurements, the B254 blade revealed the highest values. Although this blade had the longest crack with a crack length of 6.8 mm, the high nonlinearities can have various causes. Compared to the plate metal samples, the position of the cracks on the blades is variable. The crack of the blades B046 is only 5 mm behind the sensors, and the distance increases accordingly up to blade B286. In addition, real cracks behave differently, and many factors can lead to an increase of nonlinearities. The decisive factor is whether the crack is closed or open, and it is furthermore crucial how the asperities of the crack topography are in contact and how much of them are in interaction [39, 40].

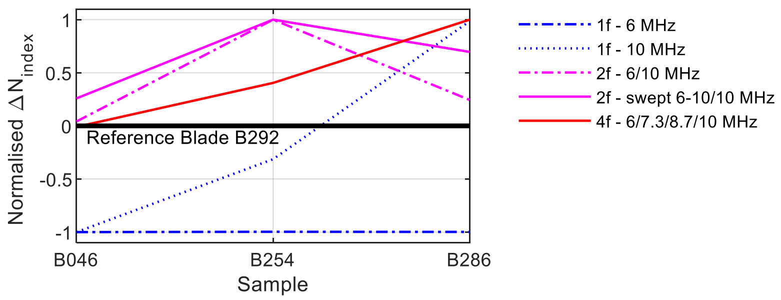

Figure 36. Comparison N_{index} values.

6. Conclusion

A comparison of various nonlinear ultrasonic wave modulation techniques was presented. The tests were conducted on metal plates, with artificially generated cracks and on turbine blades with real cracks.

When using one excitation frequency, the results for both the plate samples and turbine blades were not convincing and showed that selecting the appropriate fundamental frequency is crucial to the success of the measurement.

The parallel excitation with two frequencies provides a total of 12 nonlinearity parameters to evaluate the components, and the new N_{index} values was used as a comparison with the other excitation techniques. For the plate samples, some nonlinearity parameters revealed a clear increase depending on the crack size. With the two-frequency excitation with a linearly increasing signal, the informative value of the failures had not improved in comparison.

The four-frequency excitation was analytically solved using the extended one-dimensional wave equation. A total of 64 individual nonlinearity parameters were derived. Furthermore, the four fundamental frequencies were chosen so that as many different fundamental frequencies, harmonic frequencies and sidebands as possible meet at one frequency. The concept of grouping nonlinear parameters simplifies the evaluation with a total of 30 nonlinearity parameters, which facilitates identifying a defect in the material. This behaviour and advantages were proven experimentally. The N_{index} values of these measurements demonstrated behaviour as a function of the crack size. It was shown that, especially with the quasi-chaotic frequency evaluation, detecting the failure is possible without calculating dispersion curves.

The use of four fundamental frequencies offers clear advantages in detecting defects in materials by pairing with the frequency grouping method.

Appendix A

This section includes the further derivation for the solution of the one-dimensional wave equation with four excitation frequencies up to the third order of nonlinearity (Section 2.1).

Substituting Equation (7) in the right side of Equation (5) with the second-order nonlinearity parameter β and making further transformations with trigonometric formulas lead to:

$$\frac{\partial^2 u}{\partial t^2} - c^2 \frac{\partial^2 u}{\partial x^2} =$$

$$c^2\beta \begin{pmatrix} -\frac{1}{2}A_1^2k_{f1}^3\, s\, in\big[k_{f1}(x-ct)\big] \\ +\frac{1}{2}A_2^2k_{f2}^3\, s\, in\big[k_{f2}(x-ct)\big] \\ -\frac{1}{2}A_3^2k_{f3}^3\, s\, in\big[k_{f3}(x-ct)\big] \\ +\frac{1}{2}A_4^2k_{f4}^3\, s\, in\big[k_{f4}(x-ct)\big] \\ -\frac{1}{2}A_1A_2k_{f1}k_{f2}(k_{f2}-k_{f1})\, cos\big[(k_{f2}-k_{f1})(x-ct)\big] \\ -\frac{1}{2}A_1A_2k_{f1}k_{f2}(k_{f2}+k_{f1})\, cos\big[(k_{f2}+k_{f1})(x-ct)\big] \\ -\frac{1}{2}A_1A_3k_{f1}k_{f3}(k_{f3}-k_{f1})\, sin\big[(k_{f3}-k_{f1})(x-ct)\big] \\ -\frac{1}{2}A_1A_3k_{f1}k_{f3}(k_{f3}+k_{f1})\, sin\big[(k_{f3}+k_{f1})(x-ct)\big] \\ -\frac{1}{2}A_1A_4k_{f1}k_{f4}(k_{f4}-k_{f1})\, cos\big[(k_{f4}-k_{f1})(x-ct)\big] \\ -\frac{1}{2}A_1A_4k_{f1}k_{f4}(k_{f4}+k_{f1})\, cos\big[(k_{f4}-k_{f1})(x+ct)\big] \\ +\frac{1}{2}A_2A_3k_{f2}k_{f3}(k_{f3}-k_{f2})\, cos\big[(k_{f3}-k_{f2})(x-ct)\big] \\ -\frac{1}{2}A_2A_3k_{f2}k_{f3}(k_{f3}+k_{f2})\, cos\big[(k_{f3}+k_{f2})(x-ct)\big] \\ +\frac{1}{2}A_2A_4k_{f2}k_{f4}(k_{f4}-k_{f2})\, sin\big[(k_{f4}-k_{f2})(x-ct)\big] \\ +\frac{1}{2}A_2A_4k_{f2}k_{f4}(k_{f4}+k_{f2})\, sin\big[(k_{f4}+k_{f2})(x-ct)\big] \\ -\frac{1}{2}A_3A_4k_{f3}k_{f4}(k_{f4}-k_{f3})\, cos\big[(k_{f4}-k_{f3})(x-ct)\big] \\ -\frac{1}{2}A_3A_4k_{f3}k_{f4}(k_{f4}+k_{f3})\, cos\big[(k_{f4}+k_{f3})(x-ct)\big] \end{pmatrix}. \tag{A1}$$

Based on this expression and according to [17], the following solution results for $u^{(2)}$:

$$\begin{aligned} u^{(2)} = &-\frac{\beta A_1^2k_{f1}^2}{8} cos\big[2k_{f1}(x-ct)\big]\,x + \frac{\beta A_2^2k_{f2}^2}{8} cos\big[2k_{f2}(x-ct)\big]x \\ &-\frac{\beta A_3^2k_{f3}^2}{8} cos\big[2k_{f3}(x-ct)\big]\,x + \frac{\beta A_4^2k_{f4}^2}{8} cos\big[2k_{f4}(x-ct)\big]x \\ &+\frac{\beta A_1A_2k_{f1}k_{f2}}{4} sin\big[(k_{f2}-k_{f1})(x-ct)\big]\,x + \frac{\beta A_1A_2k_{f1}k_{f2}}{4} sin\big[(k_{f2}+k_{f1})(x-ct)\big]\,x \\ &+\frac{\beta A_1A_3k_{f1}k_{f3}}{4} \cos\big[(k_{f3}-k_{f1})(x-ct)\big]\,x - \frac{\beta A_1A_3k_{f1}k_{f3}}{4} \cos\big[(k_{f3}+k_{f1})(x-ct)\big]\,x \\ &-\frac{\beta A_1A_4k_{f1}k_{f4}}{4} \sin\big[(k_{f4}-k_{f1})(x-ct)\big]\,x - \frac{\beta A_1A_4k_{f1}k_{f4}}{4} \sin\big[(k_{f4}+k_{f1})(x-ct)\big]\,x \\ &-\frac{\beta A_2A_3k_{f2}k_{f3}}{4} \sin\big[(k_{f3}-k_{f2})(x-ct)\big]\,x + \frac{\beta A_2A_3k_{f2}k_{f3}}{4} \sin\big[(k_{f3}+k_{f2})(x-ct)\big]\,x \\ &-\frac{\beta A_2A_4k_{f2}k_{f4}}{4} \cos\big[(k_{f4}-k_{f2})(x-ct)\big]\,x + \frac{\beta A_2A_4k_{f2}k_{f4}}{4} \cos\big[(k_{f4}+k_{f2})(x-ct)\big]\,x \\ &+\frac{\beta A_3A_4k_{f3}k_{f4}}{4} \sin\big[(k_{f4}-k_{f3})(x-ct)\big]\,x + \frac{\beta A_3A_4k_{f3}k_{f4}}{4} \sin\big[(k_{f4}+k_{f3})(x-ct)\big]\,x. \end{aligned} \tag{A2}$$

The solution of Equation (5) should now be extended by the cubic nonlinearity parameter γ to obtain an encompassing description of the nonlinearity parameters. Substituting Equation (7) into the right side of Equation (5) in the third-order nonlinearity parameter γ gives:

$$\frac{\partial^2 u}{\partial t^2} - c^2 \frac{\partial^2 u}{\partial x^2} =$$

$$\frac{c^2\gamma}{2}\left[\begin{pmatrix} A_1 sin\left[k_{f1}(x-ct)\right] + A_2 cos\left[k_{f2}(x-ct)\right] + \\ A_3 sin\left[k_{f3}(x-ct)\right] + A_4 cos\left[k_{f4}(x-ct)\right] \end{pmatrix}^2 \right. \tag{A3}$$

$$\left.\begin{pmatrix} -A_1 {k_{f1}}^2 si\,n\left[k_{f1}(x-ct)\right] - A_2 {k_{f2}}^2 co\,s[k_2(x-ct)] \\ -A_3 {k_{f3}}^2 si\,n\left[k_{f3}(x-ct)\right] - A_4 {k_{f4}}^2 co\,s[k_4(x-ct)] \end{pmatrix}\right].$$

Transformation with binominal and trigonometric formulas leads to:

$$\frac{\partial^2 u}{\partial t^2} - c^2 \frac{\partial^2 u}{\partial x^2} =$$

$$\begin{aligned}
\frac{c^2\gamma}{2}\Big[&-\frac{1}{2}\left(A_1 {A_2}^2 {k_{f1}}^2 {k_{f2}}^2 + A_1 {A_4}^2 {k_{f1}}^2 {k_{f4}}^2 + A_1 {A_3}^2 {k_{f1}}^2 {k_{f3}}^2 + \frac{1}{2} {A_1}^3 {k_{f1}}^4\right) sin\left[k_{f1}(x-ct)\right] \\
&-\frac{1}{2}\left({A_1}^2 A_2 {k_{f1}}^2 {k_{f2}}^2 + A_2 {A_4}^2 {k_{f2}}^2 {k_{f4}}^2 + A_2 {A_3}^2 {k_{f2}}^2 {k_{f3}}^2 + \frac{1}{2} {A_2}^3 {k_{f2}}^4\right) sin\left[k_{f2}(x-ct)\right] \\
&-\frac{1}{2}\left({A_1}^2 A_3 {k_{f1}}^2 {k_{f3}}^2 + {A_2}^2 A_3 {k_{f2}}^2 {k_{f3}}^2 + A_3 {A_4}^2 {k_{f3}}^2 {k_{f4}}^2 + \frac{1}{2} {A_3}^3 {k_{f3}}^4\right) sin\left[k_{f3}(x-ct)\right] \\
&-\frac{1}{2}\left({A_1}^2 A_4 {k_{f1}}^2 {k_{f4}}^2 + {A_2}^2 A_4 {k_{f2}}^2 {k_{f4}}^2 + {A_3}^2 A_4 {k_{f3}}^2 {k_{f4}}^2 + \frac{1}{2} {A_4}^3 {k_{f4}}^4\right) sin\left[k_{f4}(x-ct)\right] \\
&-\tfrac{1}{4} {A_1}^3 {k_{f1}}^4 sin\left[3k_{f1}(x-ct)\right] + \tfrac{1}{4} {A_2}^3 {k_{f2}}^4 cos\left[3k_{f2}(x-ct)\right] \\
&-\tfrac{1}{4} {A_3}^3 {k_{f3}}^4 sin\left[3k_{f3}(x-ct)\right] + \tfrac{1}{4} {A_4}^3 {k_{f4}}^4 cos\left[3k_{f4}(x-ct)\right] \\
&-\tfrac{1}{2} {A_1}^2 A_2 ({k_{f1}}^3 k_{f2} + \tfrac{1}{2} {k_{f1}}^2 {k_{f2}}^2) cos\left[(2k_{f1}+k_{f2})(x-ct)\right] \\
&+\tfrac{1}{2} {A_1}^2 A_2 ({k_{f1}}^3 k_{f2} - \tfrac{1}{2} {k_{f1}}^2 {k_{f2}}^2) cos\left[(2k_{f1}-k_{f2})(x-ct)\right] \\
&-\tfrac{1}{2} {A_1}^2 A_3 (\tfrac{1}{2} {k_{f1}}^2 {k_{f3}}^2 + {k_{f1}}^3 k_{f3}) sin\left[(2k_{f1}+k_{f3})(x-ct)\right] \\
&+\tfrac{1}{2} {A_1}^2 A_3 (\tfrac{1}{2} {k_{f1}}^2 {k_{f3}}^2 - {k_{f1}}^3 k_{f3}) sin\left[(2k_{f1}-k_{f3})(x-ct)\right] \\
&-\tfrac{1}{2} {A_1}^2 A_4 ({k_{f1}}^3 k_{f4} + \tfrac{1}{2} {k_{f1}}^2 {k_{f4}}^2) cos\left[(2k_{f1}+k_{f4})(x-ct)\right] \\
&+\tfrac{1}{2} {A_1}^2 A_4 ({k_{f1}}^3 k_{f4} - \tfrac{1}{2} {k_{f1}}^2 {k_{f4}}^2) cos\left[(2k_{f1}-k_{f4})(x-ct)\right] \\
&+\tfrac{1}{2} A_1 {A_2}^2 (\tfrac{1}{2} {k_{f1}}^2 {k_{f2}}^2 + k_{f1} {k_{f2}}^3) sin\left[(2k_{f2}+k_{f1})(x-ct)\right] \\
&+\tfrac{1}{2} A_1 {A_2}^2 (k_{f1} {k_{f2}}^3 - \tfrac{1}{2} {k_{f1}}^2 {k_{f2}}^2) sin\left[(2k_{f2}-k_{f1})(x-ct)\right] \\
&+\tfrac{1}{2} {A_2}^2 A_3 ({k_{f2}}^3 k_{f3} + \tfrac{1}{2} {k_{f2}}^2 {k_{f3}}^2) sin\left[(2k_{f2}+k_{f3})(x-ct)\right] \\
&+\tfrac{1}{2} {A_2}^2 A_3 ({k_{f2}}^3 k_{f3} - \tfrac{1}{2} {k_{f2}}^2 {k_{f3}}^2) sin\left[(2k_{f2}-k_{f3})(x-ct)\right] \\
&+\tfrac{1}{4} {A_2}^2 A_4 {k_{f2}}^2 {k_{f4}}^2 cos\left[(2k_{f2}+k_{f4})(x-ct)\right] \\
&+\tfrac{1}{4} {A_2}^2 A_4 {k_{f2}}^2 {k_{f4}}^2 cos\left[(2k_{f2}-k_{f4})(x-ct)\right] \\
&-\tfrac{1}{2} A_1 {A_3}^2 (\tfrac{1}{2} {k_{f1}}^2 {k_{f3}}^2 + k_{f1} {k_{f3}}^3) sin\left[(2k_{f3}+k_{f1})(x-ct)\right] \\
&+\tfrac{1}{2} A_1 {A_3}^2 (\tfrac{1}{2} {k_{f1}}^2 {k_{f3}}^2 - k_{f1} {k_{f3}}^3) sin\left[(2k_{f3}-k_{f1})(x-ct)\right] \\
&-\tfrac{1}{2} A_1 {A_3}^2 (\tfrac{1}{2} {k_{f2}}^2 {k_{f3}}^2 + k_{f2} {k_{f3}}^3) cos\left[(2k_{f3}+k_{f2})(x-ct)\right]
\end{aligned} \tag{A4}$$

$$
\begin{aligned}
&+\tfrac{1}{2}A_2{A_3}^2(k_{f2}{k_{f3}}^3-\tfrac{1}{2}{k_{f2}}^2{k_{f3}}^2)cos\big[(2k_{f3}-k_{f2})(x-ct)\big]\\
&-\tfrac{1}{2}{A_3}^2A_4({k_{f3}}^3k_{f4}+\tfrac{1}{2}{k_{f3}}^2{k_{f4}}^2)cos\big[(2k_{f3}+k_{f4})(x-ct)\big]\\
&+\tfrac{1}{2}{A_3}^2A_4({k_{f3}}^3k_{f4}-\tfrac{1}{2}{k_{f3}}^2{k_{f4}}^2)cos\big[(2k_{f3}-k_{f4})(x-ct)\big]\\
&+\tfrac{1}{2}A_1{A_4}^2(\tfrac{1}{2}{k_{f1}}^2{k_{f4}}^2+k_{f1}{k_{f4}}^3)sin\big[(2k_{f4}+k_{f1})(x-ct)\big]\\
&+\tfrac{1}{2}A_1{A_4}^2(k_{f1}{k_{f4}}^3-\tfrac{1}{2}{k_{f1}}^2{k_{f4}}^2)sin\big[(2k_{f4}-k_{f1})(x-ct)\big]\\
&+\tfrac{1}{4}A_2{A_4}^2{k_{f2}}^2{k_{f4}}^2cos\big[(2k_{f4}+k_{f2})(x-ct)\big]\\
&+\tfrac{1}{4}A_2{A_4}^2{k_{f2}}^2{k_{f4}}^2cos\big[(2k_{f4}-k_{f2})(x-ct)\big]\\
&+\tfrac{1}{2}A_3{A_4}^2(\tfrac{1}{2}{k_{f3}}^2{k_{f4}}^2+k_{f3}{k_{f4}}^3)sin\big[(2k_{f4}+k_{f3})(x-ct)\big]\\
&+\tfrac{1}{2}A_3{A_4}^2(k_{f3}{k_{f4}}^3-\tfrac{1}{2}{k_{f3}}^2{k_{f4}}^2)sin\big[(2k_{f4}-k_{f3})(x-ct)\big]\\
&-\tfrac{1}{2}A_1A_2A_3({k_{f1}}^2k_{f2}k_{f3}+k_{f1}{k_{f2}}^2k_{f3}+k_{f1}k_{f2}{k_{f3}}^2)cos\big[(k_{f1}+k_{f2}+k_{f3})(x-ct)\big]\\
&-\tfrac{1}{2}A_1A_2A_3({k_{f1}}^2k_{f2}k_{f3}+k_{f1}{k_{f2}}^2k_{f3}-k_{f1}k_{f2}{k_{f3}}^2)cos\big[(k_{f1}+k_{f2}-k_{f3})(x-ct)\big]\\
&-\tfrac{1}{2}A_1A_3A_4({k_{f1}}^2k_{f3}k_{f4}+k_{f1}{k_{f3}}^2k_{f4}+k_{f1}k_{f3}{k_{f4}}^2)cos\big[(k_{f1}+k_{f3}+k_{f4})(x-ct)\big]\\
&+\tfrac{1}{2}A_1A_3A_4({k_{f1}}^2k_{f3}k_{f4}+k_{f1}{k_{f3}}^2k_{f4}-k_{f1}k_{f3}{k_{f4}}^2)cos\big[(k_{f1}+k_{f3}-k_{f4})(x-ct)\big]\\
&+\tfrac{1}{2}A_1A_2A_4({k_{f1}}^2k_{f2}k_{f4}+k_{f1}k_{f2}{k_{f4}}^2)sin\big[(k_{f1}+k_{f2}+k_{f4})(x-ct)\big]\\
&+\tfrac{1}{2}A_1A_2A_4({k_{f1}}^2k_{f2}k_{f4}-k_{f1}k_{f2}{k_{f4}}^2)sin\big[(k_{f1}+k_{f2}-k_{f4})(x-ct)\big]\\
&+\tfrac{1}{2}A_1A_2A_3({k_{f1}}^2k_{f2}k_{f3}-k_{f1}{k_{f2}}^2k_{f3}-k_{f1}k_{f2}{k_{f3}}^2)cos\big[(k_{f2}+k_{f3}-k_{f1})(x-ct)\big]\\
&+\tfrac{1}{2}A_1A_3A_4(k_{f1}{k_{f3}}^2k_{f4}-{k_{f1}}^2k_{f3}k_{f4}-k_{f1}k_{f2}{k_{f4}}^2)cos\big[(k_{f1}+k_{f4}-k_{f3})(x-ct)\big]\\
&+\tfrac{1}{2}A_1A_2A_4({k_{f1}}^2k_{f3}k_{f4}-k_{f1}{k_{f3}}^2k_{f4}-k_{f1}k_{f3}{k_{f4}}^2)cos\big[(k_{f3}+k_{f4}-k_{f1})(x-ct)\big]\\
&+\tfrac{1}{2}A_1A_2A_4(k_{f1}{k_{f2}}^2k_{f4}+k_{f1}k_{f2}{k_{f4}}^2)sin\big[(k_{f2}+k_{f4}-k_{f1})(x-ct)\big]\\
&+\tfrac{1}{2}A_1A_2A_3(k_{f1}k_{f2}{k_{f3}}^2-k_{f1}{k_{f2}}^2k_{f3}+{k_{f1}}^2k_{f2}k_{f3})cos\big[(k_{f1}+k_{f3}-k_{f2})(x-ct)\big]\\
&+\tfrac{1}{2}A_2A_3A_4({k_{f2}}^2k_{f3}k_{f4}-k_{f2}k_{f3}{k_{f4}}^2)sin\big[(k_{f2}+k_{f3}+k_{f4})(x-ct)\big]\\
&+\tfrac{1}{2}A_2A_3A_4({k_{f2}}^2k_{f3}k_{f4}-k_{f2}k_{f3}{k_{f4}}^2)sin\big[(k_{f2}+k_{f4}-k_{f3})(x-ct)\big]\\
&-\tfrac{1}{2}A_2A_3A_4({k_{f2}}^2k_{f3}k_{f4}+k_{f2}k_{f3}{k_{f4}}^2)sin\big[(k_{f2}+k_{f3}-k_{f4})(x-ct)\big]\\
&+\tfrac{1}{2}A_2A_3A_4({k_{f2}}^2k_{f3}k_{f4}+k_{f2}k_{f3}{k_{f4}}^2)sin\big[(k_{f3}+k_{f4}-k_{f2})(x-ct)\big]\\
&-\tfrac{1}{2}A_1A_2A_4(k_{f1}k_{f2}{k_{f4}}^2)sin\big[(k_{f1}+k_{f4}-k_{f2})(x-ct)\big]\Big].
\end{aligned}
\tag{A4 Cont.}
$$

Based on [17] , this results in the following solution:

$$
\begin{aligned}
u^{(3)}=&+\left(\frac{\gamma(A_1{A_2}^2k_{f1}{k_{f2}}^2+A_1{A_4}^2k_{f1}{k_{f4}}^2+A_1{A_3}^2k_{f1}{k_{f3}}^2+\frac{1}{2}{A_1}^3{k_{f1}}^4)}{8}\right)cos\big[k_{f1}(x-ct)\big]x\\
&-\left(\frac{\gamma({A_1}^2A_2{k_{f1}}^2k_{f2}+A_2{A_4}^2k_{f1}{k_{f4}}^2+A_2{A_3}^2k_{f2}{k_{f3}}^2+\frac{1}{2}{A_2}^3{k_{f2}}^4)}{8}\right)sin\big[k_{f2}(x-ct)\big]x\\
&+\left(\frac{\gamma({A_1}^2A_3{k_{f1}}^2k_{f3}+{A_2}^2A_3{k_{f2}}^2k_{f3}+A_3{A_4}^2k_{f3}{k_{f4}}^2+\frac{1}{2}{A_3}^3{k_{f3}}^4)}{8}\right)cos\big[k_{f3}(x-ct)\big]x
\end{aligned}
\tag{A5}
$$

$$-\left(\frac{\gamma(A_1{}^2A_4k_{f1}{}^2k_{f4}+A_2{}^2A_4k_{f2}{}^2k_{f4}+A_3{}^2A_4k_{f3}{}^2k_{f4}+\frac{1}{2}A_4{}^3k_{f4}{}^4)}{8}\right)sin\big[k_{f4}(x-ct)\big]x$$

$$+\frac{\gamma A_1{}^3k_{f1}{}^3}{48}cos\big[3k_{f1}(x-ct)\big]\,x+\frac{\gamma A_2{}^3k_{f2}{}^3}{48}sin\big[3k_{f2}(x-ct)\big]x$$

$$+\frac{\gamma A_3{}^3k_{f3}{}^3}{48}cos\big[3k_{f3}(x-ct)\big]\,x+\frac{\gamma A_4{}^3k_{f4}{}^3}{48}sin\big[3k_{f4}(x-ct)\big]x$$

$$-\left(\frac{\gamma A_1{}^2A_2(k_{f1}{}^3k_{f2}+\frac{1}{2}k_{f1}{}^2k_{f2}{}^2)}{8(2k_{f1}+k_{f2})}\right)sin\big[(2k_{f1}+k_{f2})(x-ct)\big]x$$

$$+\left(\frac{\gamma A_1{}^2A_2(k_{f1}{}^3k_{f2}-\frac{1}{2}k_{f1}{}^2k_{f2}{}^2)}{8(2k_{f1}-k_{f2})}\right)sin\big[(2k_{f1}-k_{f2})(x-ct)\big]x$$

$$+\left(\frac{\gamma A_1{}^2A_3(\frac{1}{2}k_{f1}{}^2k_{f3}{}^2+k_{f1}{}^3k_{f3})}{8(2k_{f1}+k_{f3})}\right)cos\big[(2k_{f1}+k_{f3})(x-ct)\big]x$$

$$+\left(\frac{\gamma A_1{}^2A_3(\frac{1}{2}k_{f1}{}^2k_{f3}{}^2-k_{f1}{}^3k_{f3})}{8(2k_{f1}-k_{f3})}\right)cos\big[(2k_{f1}-k_{f3})(x-ct)\big]x$$

$$-\left(\frac{\gamma A_1{}^2A_4(k_{f1}{}^3k_{f4}+\frac{1}{2}k_{f1}{}^2k_{f4}{}^2)}{8(2k_{f1}+k_{f4})}\right)sin\big[(2k_{f1}+k_{f4})(x-ct)\big]x$$

$$+\left(\frac{\gamma A_1{}^2A_4(k_{f1}{}^3k_{f4}-\frac{1}{2}k_{f1}{}^2k_{f4}{}^2)}{8(2k_{f1}-k_{f4})}\right)sin\big[(2k_{f1}-k_{f4})(x-ct)\big]x$$

$$-\left(\frac{\gamma A_1A_2{}^2(\frac{1}{2}k_{f1}{}^2k_{f2}{}^2+k_{f1}k_{f2}{}^3)}{8(2k_{f2}+k_{f1})}\right)cos\big[(2k_{f2}+k_{f1})(x-ct)\big]x$$

$$-\left(\frac{\gamma A_1A_2{}^2(\frac{1}{2}k_{f1}{}^2k_{f2}{}^2-k_{f1}k_{f2}{}^3)}{8(2k_{f2}-k_{f1})}\right)cos\big[(2k_{f2}-k_{f1})(x-ct)\big]x \qquad \text{(A5) Cont.}$$

$$-\left(\frac{\gamma A_2{}^2A_3(k_{f2}{}^3k_{f3}+\frac{1}{2}k_{f2}{}^2k_{f3}{}^2)}{8(2k_{f2}+k_{f3})}\right)cos\big[(2k_{f2}+k_{f3})(x-ct)\big]x$$

$$-\left(\frac{\gamma A_2{}^2A_3(k_{f2}{}^3k_{f3}-\frac{1}{2}k_{f2}{}^2k_{f3}{}^2)}{8(2k_{f2}-k_{f3})}\right)cos\big[(2k_{f2}-k_{f3})(x-ct)\big]x$$

$$+\frac{\gamma A_2{}^2A_4k_{f2}{}^2k_{f4}{}^2}{16(2k_{f2}+k_{f4})}sin\big[(2k_{f2}+k_{f4})(x-ct)\big]x+\frac{\gamma A_2{}^2A_4k_{f2}{}^2k_{f4}{}^2}{16(2k_{f2}-k_{f4})}sin\big[(2k_{f2}-k_{f4})(x-ct)\big]x$$

$$+\left(\frac{\gamma A_1A_3{}^2(\frac{1}{2}k_{f1}{}^2k_{f3}{}^2+k_{f1}k_{f3}{}^3)}{8(2k_{f3}+k_{f1})}\right)cos\big[(2k_{f3}+k_{f1})(x-ct)\big]x$$

$$+\left(\frac{\gamma A_1A_3{}^2(\frac{1}{2}k_{f1}{}^2k_{f3}{}^2-k_{f1}k_{f3}{}^3)}{8(2k_{f3}-k_{f1})}\right)cos\big[(2k_{f3}-k_{f1})(x-ct)\big]x$$

$$-\left(\frac{\gamma A_2A_3{}^2(\frac{1}{2}k_{f2}{}^2k_{f3}{}^2+k_{f2}k_{f3}{}^3)}{8(2k_{f3}+k_{f2})}\right)sin\big[(2k_{f3}+k_{f2})(x-ct)\big]x$$

$$+\left(\frac{\gamma A_2A_3{}^2(\frac{1}{2}k_{f2}{}^2k_{f3}{}^2-k_{f2}k_{f3}{}^3)}{8(2k_{f3}-k_{f2})}\right)sin\big[(2k_{f3}-k_{f2})(x-ct)\big]x$$

$$-\left(\frac{\gamma A_3{}^2A_4(k_{f3}{}^3k_{f4}+\frac{1}{2}k_{f3}{}^2k_{f4}{}^2)}{8(2k_{f3}+k_{f4})}\right)sin\big[(2k_{f3}+k_{f4})(x-ct)\big]x$$

$$+\left(\frac{\gamma A_3{}^2A_4(k_{f3}{}^3k_{f4}-\frac{1}{2}k_{f3}{}^2k_{f4}{}^2)}{8(2k_{f3}-k_{f4})}\right)sin\big[(2k_{f3}-k_{f4})(x-ct)\big]x$$

$$-\left(\frac{\gamma A_1 A_4{}^2(\frac{1}{2}k_{f1}{}^2k_{f4}{}^2+k_{f1}k_{f4}{}^3)}{8(2k_{f4}+k_{f1})}\right)cos\left[(2k_{f4}+k_{f1})(x-ct)\right]x$$

$$-\left(\frac{\gamma A_1 A_4{}^2(\frac{1}{2}k_{f1}{}^2k_{f4}{}^2-k_{f1}k_{f4}{}^3)}{8(2k_{f4}-k_{f1})}\right)cos\left[(2k_{f4}-k_{f1})(x-ct)\right]x$$

$$+\frac{\gamma A_2 A_4{}^2k_{f2}{}^2k_{f4}{}^2}{16(2k_{f4}+k_{f2})}sin\left[(2k_{f4}+k_{f2})(x-ct)\right]x+\frac{\gamma A_2 A_4{}^2k_{f2}{}^2k_{f4}{}^2}{16(2k_{f4}-k_{f2})}sin\left[(2k_{f4}-k_{f2})(x-ct)\right]x$$

$$-\left(\frac{\gamma A_3 A_4{}^2(\frac{1}{2}k_{f3}{}^2k_{f4}{}^2+k_{f3}k_{f4}{}^3)}{8(2k_{f4}+k_{f3})}\right)cos\left[(2k_{f4}+k_{f3})(x-ct)\right]x$$

$$-\left(\frac{\gamma A_3 A_4{}^2(k_{f3}k_{f4}{}^3-\frac{1}{2}k_{f3}{}^2k_{f4}{}^2)}{8(2k_{f4}-k_{f3})}\right)cos\left[(2k_{f4}-k_{f3})(x-ct)\right]x$$

$$-\left(\frac{\gamma A_1A_2A_3(k_{f1}{}^2k_{f2}k_{f3}+k_{f1}k_{f2}{}^2k_{f3}+k_{f1}k_{f2}k_{f3}{}^2)}{8(k_{f1}+k_{f2}+k_{f3})}\right)sin\left[(k_{f1}+k_{f2}+k_{f3})(x-ct)\right]x$$

$$-\left(\frac{\gamma A_1A_2A_3(k_{f1}{}^2k_{f2}k_{f3}+k_{f1}k_{f2}{}^2k_{f3}-k_{f1}k_{f2}k_{f3}{}^2)}{8(k_{f1}+k_{f2}-k_{f3})}\right)sin\left[(k_{f1}+k_{f2}-k_{f3})(x-ct)\right]x$$

$$-\left(\frac{\gamma A_1A_3A_4(k_{f1}{}^2k_{f3}k_{f4}+k_{f1}k_{f3}{}^2k_{f4}+k_{f1}k_{f3}k_{f4}{}^2)}{8(k_{f1}+k_{f3}+k_{f4})}\right)sin\left[(k_{f1}+k_{f3}+k_{f4})(x-ct)\right]x$$

$$+\left(\frac{\gamma A_1A_24(k_{f1}{}^2k_{f3}k_{f4}+k_{f1}k_{f3}{}^2k_{f4}-k_{f1}k_{f3}k_{f4}{}^2)}{8(k_{f1}+k_{f3}-k_{f4})}\right)sin\left[(k_{f1}+k_{f3}-k_{f4})(x-ct)\right]x$$

$$-\left(\frac{\gamma A_1A_2A_4(k_{f1}k_{f2}{}^2k_{f4}+k_{f1}k_{f2}k_{f4}{}^2)}{8(k_{f1}+k_{f2}+k_{f4})}\right)cos\left[(k_{f1}+k_{f2}+k_{f4})(x-ct)\right]x$$

$$-\left(\frac{\gamma A_1A_2A_4(k_{f1}k_{f2}{}^2k_{f4}-k_{f1}k_{f2}k_{f4}{}^2)}{8(k_{f1}+k_{f2}-k_{f4})}\right)cos\left[(k_{f1}+k_{f2}-k_{f4})(x-ct)\right]x \qquad \text{(A5) Cont.}$$

$$+\left(\frac{\gamma A_1A_2A_3(k_{f1}{}^2k_{f2}k_{f3}-k_{f1}k_{f2}{}^2k_{f3}-k_{f1}k_{f2}k_{f3}{}^2)}{8(k_{f2}+k_{f3}-k_{f1})}\right)sin\left[(k_{f2}+k_{f3}-k_{f1})(x-ct)\right]x$$

$$+\left(\frac{\gamma A_1A_2A_4(k_{f1}k_{f3}{}^2k_{f4}-k_{f1}{}^2k_{f3}k_{f4}-k_{f1}k_{f2}k_{f3}{}^2)}{8(k_{f1}+k_{f4}-k_{f3})}\right)sin\left[(k_{f1}+k_{f4}-k_{f3})(x-ct)\right]x$$

$$+\left(\frac{\gamma A_3A_4A_1(k_{f1}{}^2k_{f3}k_{f4}-k_{f1}k_{f3}{}^2k_{f4}-k_{f1}k_{f2}k_{f4}{}^2)}{8(k_{f3}+k_{f4}-k_{f1})}\right)sin\left[(k_{f3}+k_{f4}-k_{f1})(x-ct)\right]x$$

$$-\left(\frac{\gamma A_1A_2A_4(k_{f1}k_{f2}{}^2k_{f4}+k_{f1}k_{f2}k_{f4}{}^2)}{8(k_{f2}+k_{f4}-k_{f1})}\right)cos\left[(k_{f2}+k_{f4}-k_{f1})(x-ct)\right]x$$

$$+\left(\frac{\gamma A_1A_2A_3(k_{f1}k_{f3}k_{f3}{}^2-k_{f1}k_{f2}{}^2k_{f3}+k_{f1}{}^2k_{f2}k_{f3})}{8(k_{f1}+k_{f3}-k_{f2})}\right)sin\left[(k_{f1}+k_{f3}-k_{f2})(x-ct)\right]x$$

$$-\left(\frac{\gamma A_2A_3A_4(k_{f2}{}^2k_{f3}k_{f4}-k_{f2}k_{f3}k_{f4}{}^2)}{8(k_{f2}+k_{f3}+k_{f4})}\right)cos\left[(k_{f2}+k_{f3}+k_{f4})(x-ct)\right]x$$

$$-\left(\frac{\gamma A_2A_3A_4(k_{f2}{}^2k_{f3}k_{f4}-k_{f2}k_{f3}k_{f4}{}^2)}{8(k_{f2}+k_{f4}-k_{f3})}\right)cos\left[(k_{f2}+k_{f4}-k_{f3})(x-ct)\right]x$$

$$+\left(\frac{\gamma A_2A_3A_4(k_{f2}{}^2k_{f3}k_{f4}+k_{f2}k_{f3}k_{f4}{}^2)}{8(k_{f2}+k_{f3}-k_{f4})}\right)cos\left[(k_{f2}+k_{f3}-k_{f4})(x-ct)\right]x$$

$$-\left(\frac{\gamma A_2A_3A_4(k_{f2}{}^2k_{f3}k_{f4}+k_{f2}k_{f3}k_{f4}{}^2)}{8(k_{f3}+k_{f4}-k_{f2})}\right)cos\left[(k_{f3}+k_{f4}-k_{f2})(x-ct)\right]x$$

$$-\left(\frac{\gamma A_1A_2A_4k_{f1}k_{f2}k_{f4}{}^2)}{8(k_{f1}+k_{f4}-k_{f2})}\right)cos\left[(k_{f1}+k_{f4}-k_{f2})(x-ct)\right]x.$$

Appendix B

Table B1 summarises the derived nonlinearity parameters with an increasing number of fundamental frequencies. If only one frequency is used, the second and third harmonic frequencies are available for evaluation. With two fundamental frequencies, 12 nonlinearity parameters were derived, including the linear-dependent parameter δf_n, the harmonic parameters $\delta 2f_n$, $\delta 3f_n$ and the modulated response parameters $\delta f_n \pm f_m$ and $\delta 2f_n \pm f_m$. If four frequencies are transmitted in parallel, the number of harmonics and sidebands increases to a maximum of 64. New parameters of the type $\delta f_n + f_m \pm f_p$ were added.

The second harmonic parameters $\delta 2f_n$ and sideband $\delta f_n \pm f_m$ were derived from the second-order nonlinearity parameter β. All others have their origin in the third-order nonlinearity parameter, γ.

Table B1. Comparison – nonlinearity parameters.

One excitation frequency		**Two excitation frequencies**		**Four excitation frequencies**	
Harmonic/ sideband	Number of harmonics/ sidebands	Harmonic/ sideband	Number of harmonics/ sidebands	Harmonic/ sideband	Number of harmonics/ sidebands
—	—	f_n	2	f_n	4
$2f_n$	1	$2f_n$	2	$2f_n$	4
$3f_n$	1	$3f_n$	2	$3f_n$	4
—	—	$f_n \pm f_m$	2	$f_n \pm f_m$	12
—	—	$2f_n \pm f_m$	4	$2f_n \pm f_m$	24
—	—	—	—	$f_n + f_m \pm f_p$	16
	∑2		∑12		∑64

Acknowledgement

Thanks to the MAN Energy Solutions SE for their support.

References

1. Li, Z. L., & Achenbach, J. D. (1991). Reflection and Transmission of Rayleigh Surface Waves by a Material Interphase. *J. Appl. Mech., 58*(3), 688.

2. Achenbach, J. D., Lin, W., & Keer, L. M. (1986). Mathematical modelling of ultrasonic wave scattering by sub-surface cracks. *Ultrasonics, 24*(4), 207–215.

3. Angel, Y. C., & Achenbach, J. D. (1983). Reflection and transmission of obliquely incident Rayleigh waves by a surface-breaking crack. *Acoust. Soc. Am., 75*(2), 313-319.

4. Hikata, A., Chick, B. B., & Elbaum, C. (1965). Dislocation Contribution to the Second Harmonic Generation of Ultrasonic Waves. *J. Appl. Phys., 36*(1), 229–236.

5. Cantrell, J. H., & Yost, W. T. (2001). Nonlinear ultrasonic characterization of fatigue microstructures. *Int. J. Fatigue, 23*(SUPPL. 1), 487–490.

6. Jhang, K.-Y., & Kim, K.-C. (1999). Evaluation of material degradation using nonlinear acoustic effect. *Ultrasonics, 37*(1), 39–44.

7. Frouin, J., Sathish, S., Matikas, T. E., & Na, J. K. (1999). Ultrasonic Linear and Nonlinear Behaviour of Fatigued Ti–6Al–4V. *J. Mater. Res.*, *14*(04), 1295–1298.

8. Rothenfusser, M., Mayr, M., & Baumann, J. (2000). Acoustic nonlinearities in adhesive joints. *Ultrasonics*, *38*(1-8), 322–326.

9. Yost, W. T. (2000). Nonlinear ultrasonic pulsed measurements and applications to metal processing and fatigue. In *The 27th annual review of progress in quantitative nondestructive evaluation, Ames, Iowa (USA), 16-20 July 2000*. (pp. 1268–1275): AIP.

10. Jeong, H., Nahm, S.-H., Jhang, K.-Y., & Nam, Y.-H. (2003). A nondestructive method for estimation of the fracture toughness of CrMoV rotor steels based on ultrasonic nonlinearity. *Ultrasonics*, *41*(7), 543–549.

11. Ostrovsky, L. A., & Johnson, P. A. (2000). Dynamic nonlinear elasticity in geomaterials. *Riv. del Nuovo Cim.*, *24*(7), 1–46.

12. Malfense Fierro, G. P., & Meo, M. (2015). Residual fatigue life estimation using a nonlinear ultrasound modulation method. *Smart Mater. Struct.*, *24*(2), 25040.

13. Malfense Fierro, G. P., & Meo, M. (2017). Nonlinear imaging (NIM) of flaws in a complex composite stiffened panel using a constructive nonlinear array (CNA) technique. *Ultrasonics*, *74*, 30–47.

14. Malfense Fierro, G. P. (2014). *Development of Nonlinear Ultrasound Techniques for Multidisciplinary Engineering Applications*. Ph.D. Thesis. University of Bath, Bath, UK.

15. Jingpin, J., Xiangji, M., Cunfu, H., & Bin, W. (2017). Nonlinear Lamb wave-mixing technique for micro-crack detection in plates. *NDT E Int.*, *85*, 63–71.

16. Amura, M., Meo, M., & Amerini, F. (2011). Baseline-free estimation of residual fatigue life using a third order acoustic nonlinear parameter. *Acoust. Soc. Am.*, *130*(4), 1829–1837.

17. Mevissen, F., & Meo, M. (2020). A Nonlinear Ultrasonic Modulation Method for Crack Detection in Turbine Blades. *Aerospace*, *7*(6), 72.

18. Pieczonka, L., Klepka, A., Martowicz, A., & Staszewski, W. J. (2015). Nonlinear vibroacoustic wave modulations for structural damage detection: an overview. *Opt. Eng.*, *55*(1), 11005.

19. van den Abeele, K. E.-A., Johnson, P. A., & Sutin, A. (2000). Nonlinear Elastic Wave Spectroscopy (NEWS) Techniques to Discern Material Damage, Part I: Nonlinear Wave Modulation Spectroscopy (NWMS). *Research in Nondestructive Evaluation*, *12*(1), 17–30.

20. van den Abeele, K. E.-A., Carmeliet, J., Cate, J. A. ten, & Johnson, P. A. (2000). Nonlinear Elastic Wave Spectroscopy (NEWS) Techniques to Discern Material Damage, Part II: Single-Mode Nonlinear Resonance Acoustic Spectroscopy. *Research in Nondestructive Evaluation*, *12*(1), 31–42.

21. Straka, L., Yagodzinskyy, Y., Landa, M., & Hänninen, H. (2008). Detection of structural damage of aluminum alloy 6082 using elastic wave modulation spectroscopy. *NDT E Int.*, *41*(7), 554–563.

22. Greenhall, J., Grutzik, S., Graham, A., Sinha, D. N., & Pantea, C. (2020). Nonlinear acoustic crack detection in thermoelectric wafers. *Mech. Syst. Signal Process.*, *139*, 106598.

23. Fan, C., Yang, L., & Zhao, Y. (2020). Ultrasonic multi-frequency time-reversal-based imaging of extended targets. *NDT E Int.*, *113*, 102276.

24. Queirós, R., Corrêa Alegria, F., Silva Girão, P., & Cruz Serra, A. (2015). A multi-frequency method for ultrasonic ranging. *Ultrasonics*, *63*, 86–93.

25. Novak, A., Bentahar, M., Tournat, V., El Guerjouma, R., & Simon, L. (2012). Nonlinear acoustic characterization of micro-damaged materials through higher harmonic resonance analysis. *NDT & E International*, *45*(1), 1–8.

26. Pfleiderer, K., Aufrecht, J., Solodov, I., & Busse, G. (2004). Multi-frequency ultrasonic NDE for early defect recognition and imaging. *IEEE Ultrasonics Symposium*, *1*, 693–696.

27. Abraham, S. T., Shivaprasad, S., Sreevidya, N., Das, C. R., Albert, S. K., Venkatraman, B., et al. (2019). A Novel Multi-frequency Nonlinear Ultrasonic Approach for the Characterization of Annealed Polycrystalline Microstructure. *Metall. Mater. Trans. A*, *50*(12), 5567–5573.

28. Gao, T., Sun, H., Hong, Y., & Qing, X. (2020). Hidden corrosion detection using laser ultrasonic guided waves with multi-frequency local wavenumber estimation. *Ultrasonics, 108*, 106182.

29. Malfense Fierro, G. P., & Meo, M. (2020). Non-linear Phased Array Imaging of Flaws Using a Dual and Tri Frequency Modulation Technique. *Frontiers in Built Environment, 6*.

30. Deng, M. (1998). Cumulative second-harmonic generation accompanying nonlinear shear horizontal mode propagation in a solid plate. *J. Appl. Phys., 84*(7), 3500–3505.

31. Deng, M. (1999). Cumulative second-harmonic generation of Lamb-mode propagation in a solid plate. *Journal of Applied Physics, 85*(6), 3051–3058.

32. Pruell, C., Kim, J.-Y., Qu, J., & Jacobs, L. J. (2009). Evaluation of fatigue damage using nonlinear guided waves. *Smart Materials and Structures, 18*(3), 35003.

33. Pruell, C., Kim, J.-Y., Qu, J., & Jacobs, L. J. (2007). Evaluation of plasticity driven material damage using Lamb waves. *Appl. Phys. Lett., 91*(23).

34. Niethammer, M., Jacobs, L. J., Qu, J., & Jarzynski, J. (2001). Time-frequency representations of Lamb waves. *J. Acoust. Soc. Am., 109*(5), 1841–1847.

35. Herrmann, J., Kim, J.-Y., Jacobs, L. J., Qu, J., Littles, J. W., & Savage, M. F. (2006). Assessment of material damage in a nickel-base superalloy using nonlinear Rayleigh surface waves. *J. Appl. Phys., 99*(12), 124913.

36. Mevissen, F., & Meo, M. (2019). Detection of Cracks in Turbine Blades with Nonlinear Ultrasonic Frequency Modulation. In *IWSHM 2019, Stanford, USA, 10-12 September 2019*. (pp. 824–834): DEStech Publications.

37. Malfense Fierro, G. P., & Meo, M. (2018). IWSHM 2017: Structural health monitoring of the loosening in a multi-bolt structure using linear and modulated nonlinear ultrasound acoustic moments approach. *Structural Health Monitoring: An International Journal, 17*(6), 1349–1364.

38. Amerini, F., & Meo, M. (2011). Structural health monitoring of bolted joints using linear and nonlinear acoustic/ultrasound methods. *Structural Health Monitoring: An International Journal, 10*(6), 659–672.

39. Blanloeuil, P., Rose, L., Guinto, J. A., Veidt, M., & Wang, C. H. (2016). Closed crack imaging using time reversal method based on fundamental and second harmonic scattering. *Wave Motion, 66*, 156–176.

40. Ohara, Y., Mihara, T., Sasaki, R., Ogata, T., Yamamoto, S., Kishimoto, Y., et al. (2007). Imaging of closed cracks using nonlinear response of elastic waves at subharmonic frequency. *Appl. Phys. Lett., 90*(1), 11902.

6 Creep Detection and Metallurgical Evaluation

In the previous chapters, the importance of detecting cracks in gas turbine components at an early stage was emphasised. Creep is a failure mode that leads to plastic deformation and cracks and ultimately to component failure. This defect occurs particularly on turbine blades, as they are exposed to high centrifugal and gas forces in combination with high temperatures. In gas turbines, this failure is unavoidable but can be influenced by coatings, operating parameters and the choice of materials. Hastelloy X is a typical material used in the hot-gas area of gas turbines. This superalloy was examined in this chapter both metallurgically and by ultrasound to detect and evaluate creep damage.

Three samples with creep damage were available, which were mechanically loaded at different temperatures under laboratory conditions. One sample was broken, and another was welded to determine the influence of the load on the weld seam. During the metallurgical tests, pores and microcracks formed in the edge area of the samples. Energy-dispersive X-ray analysis showed that chromium diffused outwards in the edge area to oxidise. This chromium depletion in the edge area led to the formation of pores and microcracks at the grain boundaries of the material. Inside the component, however, molybdenum was mainly precipitated. To classify the creep damage, the sizes of the pores and microcracks were evaluated, along with the damage density and surface occupancy in the evaluated areas.

The samples were examined with ultrasonic dual-frequency excitation. With a special experimental setup, longitudinal waves were sent to the samples in a fixed grid to determine the area distribution of the nonlinearity parameters. The opposing behaviours of certain nonlinearity parameters were also highlighted. In comparison, the harmonic frequencies $2f_{1,2}$ and $3f_{1,2}$ revealed a high sensitivity to the damage size of the pores and the accumulating sidebands ($f_2 + f_1$, $2f_1 + f_2$ and $2f_2 + f_1$), hence showing a good agreement with the failure area and damage density.

Overall, the findings of this chapter help improve the understanding of the damage process of Hastelloy X during creep to increase the service life of components through appropriate measuring techniques. Moreover, the systematics of the ultrasonic measurement support the identification of creep damage and reveal the current creep phase by comparing the nonlinearity parameters.

The form 'Declaration of Authorship' and the paper can be found on the following pages.

This declaration concerns the article entitled:			
Creep detection of Hastelloy X material for gas turbine components with nonlinear ultrasonic frequency modulation			
Publication status			
Draft manuscript ☐ Submitted ☐ Accepted ☐ Published ☒			
Publication details (reference)			
Mevissen, F., & Meo, M. (2022). Creep detection of Hastelloy X material for gas turbine components with nonlinear ultrasonic frequency modulation. *Materials Characterization*, *191*, 112099. https://doi.org/10.1016/j.matchar.2022.112099			
Candidate's contribution to the paper (detailed, and also given as a percentage)			
Formulation of ideas: 100% The idea of metallurgically examining creep samples made of Hastelloy X and examining them with ultrasonic dual-frequency excitation was mine.			
Design of methodology: 100% I chose the test method for the creep tests. I also procured the creep samples, designed the measuring device and manufactured it.			
Experimental work: 95% MAN Energy Solutions prepared the metallurgical samples, and I evaluated the results. I also performed all the ultrasound tests and evaluated them using my own MATLAB code.			
Presentation of data in journal format: 90% I analysed the collected data, created all the figures and chose the manuscript structure. My co-author, Professor Michele Meo, provided feedback on the above and helped with the submission, review and publication processes.			
Statement from candidate			
This paper contains original research that I have conducted during the period of my higher degree of research candidature.			
Signed	[redacted]	**Date**	20/10/2022

Creep detection of Hastelloy X material for gas turbine components with nonlinear ultrasonic frequency modulation

Frank Mevissen and Michele Meo

Department of Mechanical Engineering, University of Bath, Bath, BA2 7AY, UK

Abstract

Creep damage is one of the main failure modes in hot-gas-leading components in gas turbines, which results from high temperatures along with mechanical loads. The aim of this study is to clarify the metallurgical creep behaviour of the Hastelloy X material and detect and evaluate creep damage at an early stage with a nonlinear ultrasonic modulation technique.

For this purpose, multiple samples were examined to demonstrate that pores and microcracks in grain boundaries spread from the outside to the inside. Inside the specimen, molybdenum was identified as the main precipitation element. In addition, the chromium diffusion in the outer areas led to the depletion of this element and favoured the formation of pores and microcracks.

Failures were proven with nonlinear dual-frequency ultrasound technology. Moreover, two different longitudinal waves were sent into the samples to use harmonic and modulated response frequencies for evaluation. As a result, harmonic frequencies offered a favourable prediction of pore sizes, whereas defined sideband frequencies reacted very sensitively to the damage density and area distribution of the failures.

This study offers a method for detecting creep damage with nonlinear ultrasound techniques at an early stage as well as for differentiating between pores, microcracks, dislocations and precipitation. Therefore, the design of future gas turbine components made of Hastelloy X can be adapted with regard to the shown metallurgical behaviour and damage signatures.

1. Introduction

In modern gas turbines, it is important for the turbine blades and other hot-gas-leading components to be able to withstand extreme loads. Such loads include not only high centrifugal and gas forces, but also high temperatures. Since these high-tech components are challenging to manufacture, the goal is to extend their lifetime as much as possible. To assess the mechanical integrity of these parts, appropriate test technologies are required for the various failure modes. As a result of the continuous mechanical load on gas turbines used for power generation, coupled with the high temperatures, creep and oxidation commonly occur as failure modes [1], which can even lead to component failure.

In general, creep damage begins after a component is exposed to a high mechanical load and temperature, resulting in elastic strain. This is then followed by the primary stage, at which the strain rate decreases to a constant creep rate. The secondary stage of creep is usually characterised by a slow but constant plastic flow of material. Then, during the tertiary stage, additional pores form and the strain further increases, ultimately leading to component failure [2].

To detect these failures at the earliest stage possible, various technological approaches have been developed. For example, in [3], Semenov et al. investigated the crack growth kinetics of fatigue, creep and thermal fatigue cracks in turbine blades. In addition, in [4], Chen et al. made a lifetime prediction of turbine blades under creep. Moreover, in [5], using the Larson–Miller parameter, Marahleh et al. investigated the possibility of a numerical assessment of the service life of turbine blades with creep load. In [6], Kim et al. estimated the material deterioration of high-temperature components. Maharaj et al. studied the finite element simulation of creep behaviour at the coupling of a turbine blade to a turbine disc in a fir-tree region [7]. Lui et al. investigated a turbine blade failure due to creep [8] and proposed a numerical approach for assessing the service life of turbine blades, which is based on the Lemaitre–Chaboche creep damage model. Shi et al. studied an experimental method for the determination of creep with low cycle fatigue [9]. Hyde et al. used finite element methods based on Norton's creep law to predict the creep life of pipes [10]. Finally, in a review study, Raj et al. described and evaluated existing material characterisation techniques [11].

Another promising area is the use of nonlinear ultrasound techniques. For example, Baby et al. used a second-order nonlinearity parameter to detect creep [12] and assess service life. They found that the nonlinearity parameter (β) increases until reaching a maximum value at creep fraction life of ~0.6 and then decreases again until the test component breaks. Balasubramaniam et al. described a new nonlinear ultrasound technique for characterising creep damage [13]. They assessed the nonlinear response of samples at much lower amplitudes than those used in previous studies on nonlinear material behaviour. They also successfully detected creep damage to welded steel pipes with nonlinear ultrasound using the second harmonic nonlinearity parameter [14]. However, in their case, the weld seam did not lead to an increase in nonlinearity. Kang et al. compared different studies on creep und mechanical plastic deformation with second- and third-order nonlinearity parameters [15]. In another study, Xiang et al. examined titanium alloys with nonlinear Lamb waves. Because of the dispersive behaviour of Lamb waves, they performed phase synchronisation in the dispersion diagram so that both the fundamental and the harmonic frequencies move with the same phase velocity. They found that the initial creep load increases the level of nonlinearity as a result of the precipitation and dislocation effect. Since these factors decrease with higher creep loads, resulting in the generation of additional voids, the level of nonlinearity decreases [16]. In another study, a new analytical model was presented, which combines the wave equation of nonlinear Lamb waves in a plate with a dislocation model [17, 18]. The study results showed that the precipitation–displacement interaction has the greatest influence on the change in the second-order nonlinearity during creep in materials. Valluri et al. described a technique for characterising creep damage using nonlinear ultrasound, wherein the third harmonic nonlinearity parameter is the most sensitive [19]. Other researchers have also highlighted that high operating temperatures lead to increased oxidation, which can cause material failure as a result of the reduced functional properties of oxides [1, 20–22].

In this study, a frequency modulation excitation concept is proposed to detect creep damage in gas turbine materials. Three different creep samples were examined, two of which were identically loaded. The only difference between these two samples is that one of them was welded at the middle. The third sample was loaded with a higher temperature but with a lower tensile force. To obtain a metallurgical classification, the damage size, damage density and area distribution of the pores were evaluated. The primary precipitation element was identified using the characteristic X-ray radiation of a scanning electron microscope. This technique is used for the detection of cracks [23, 24] and the determination of plastic deformation [25], two failure modes that also occur in the case of creep damage. Finally, the measured amplitudes and calculated nonlinearity parameters were compared with the metallurgical data.

2. Specimen

The creep samples were made of a material called Hastelloy X (DIN designations: No. 2.4665 and NiCr22Fe18Mo). This material is highly resistant to oxidation and is, therefore, often used in the hot-gas-leading parts of gas turbines. Its chemical composition is shown in Table 1.

Table 1. Nominal chemical composition [m%] of Hastelloy X [26].

Ni	Cr	Fe	Mo	Co	W	C	Mn	Si	B
47	22	18	9	1.5	0.6	0.1	1	1	0.008

The samples had dimensions of 2 × 30 × 150 mm. Figure 1a illustrates the unloaded reference sample from the same batch, which was used for comparison. All creep samples had measuring tips that were used for continuous strain measurement during the creep tests. Sample CR2-1 was broken after 3250 h and loaded with 70 MPa and 750 °C (Figure 1b), and a strain of 6.3% was achieved. Sample CR2-2 (Figure 1c) was loaded with identical parameters but was welded at the middle to assess the influence of the weld seam on the creep behaviour. Sample CR3 was loaded with 35 MPa and 800 °C for 5850 h (Figure 1d), and a strain of 1% was reached before the test was stopped.

Figure 1. Creep specimens: (a) CR1; (b) CR2-1; (c) CR2-2; (d) CR3.

Figure 2 shows that widely different strain values were measured for samples CR2-1 and CR2-2. In sample CR2-2, a slightly higher strain than that in sample CR2-1 was determined up to 580 h. However, after that, the values plateaued and sample CR2-1 showed a significantly greater strain, leading to the breaking of the sample at 3250 h. For the welded sample CR2-2, the tests were stopped after 3200 h when a strain of 2.5% was reached.

Sample CR3 was loaded with 800 °C and 35 MPa for 5900 h. When the strain reached 1%, the tests were also stopped.

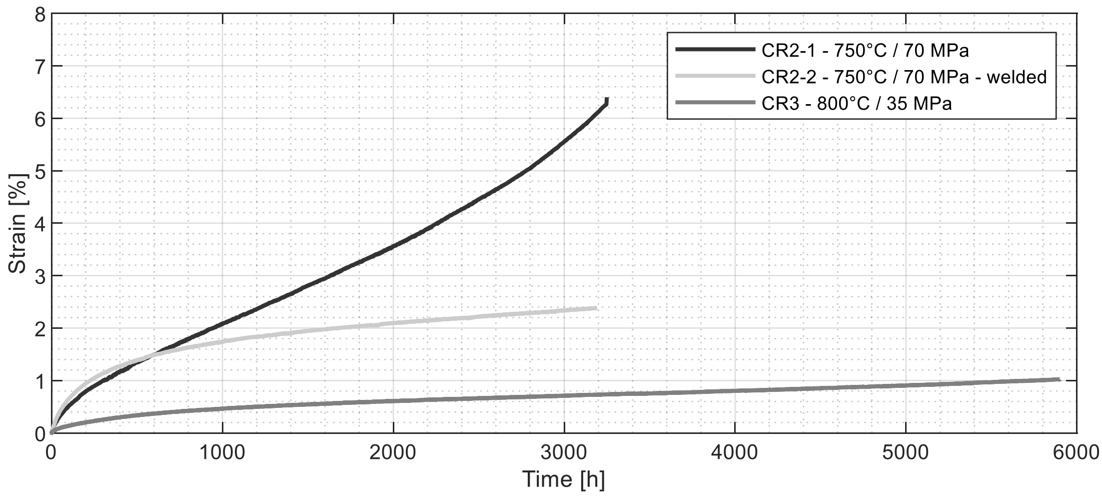

Figure 2. Strain–time diagram of creep samples.

Table 2 provides an overview of the samples used along with the test parameters and resulting strain values.

Table 2. Experimental parameters of the creep test.

Specimen	Temperature [°C]	Load [MPa]	Time [h]	Strain [%]
CR2-1	750	70	3250	6.3
CR2-2 (welded)	750	70	3200	2.5
CR3	800	35	5850	1.0

3. Metallurgical evaluations

To investigate the level of damage, the samples were metallurgically examined. First, to prepare for the metallurgical studies, the samples were ground to 0.5 mm. Then, one section plane was examined with the assumption that the statistical failure distribution of the entire plate samples with small wall thicknesses is comparable. These sample elements were then embedded in a plastic mould (Figure 3) to facilitate the following grinding and polishing work. To examine the cracks more closely, sample CR2-1 was divided into two parts (Figure 3b).

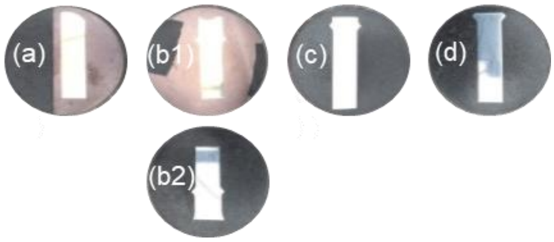

Figure 3. Sample preparation: (a) CR1; (b) CR2-1; (c) CR2-2; (d) CR3.

As outlined in Section 3.1, the samples were examined using a reflected light microscope (RLM). To make the grain structure visible, the samples were etched and then examined using a scanning electron microscope (SEM), as shown in Section 3.2. Finally, as shown in Section 3.3, the precipitation examinations were evaluated.

3.1. Reflected light microscopy

First, sample CR1 (reference sample) was investigated in different positions. The red dot shown in Figure 4 represents the position of an exemplary evaluation. From the figure, it can be seen that, apart from small carbide inclusions, no pores are visible.

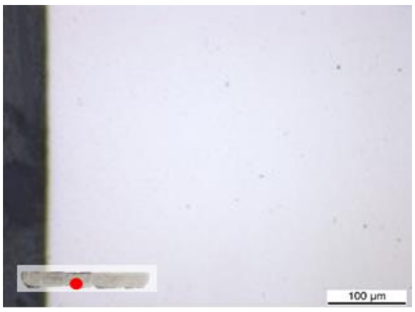

Figure 4. Reflected light microscopy of CR1.

As shown in Figure 5a, sample CR2-1 exhibited a crack area with enormous damage in the base material. Moreover, as shown in Figure 5b, approximately 5 mm away from the crack, a large number of pores and microcracks were detected. Figure 5c shows the area of the transition radius to the measuring tip. As shown in Figure 5d, the higher pore density was due to the influence of the breaking area. This influence then decreased (see Figure 5e and Figure 5f), and the damage was mainly revealed at the side areas.

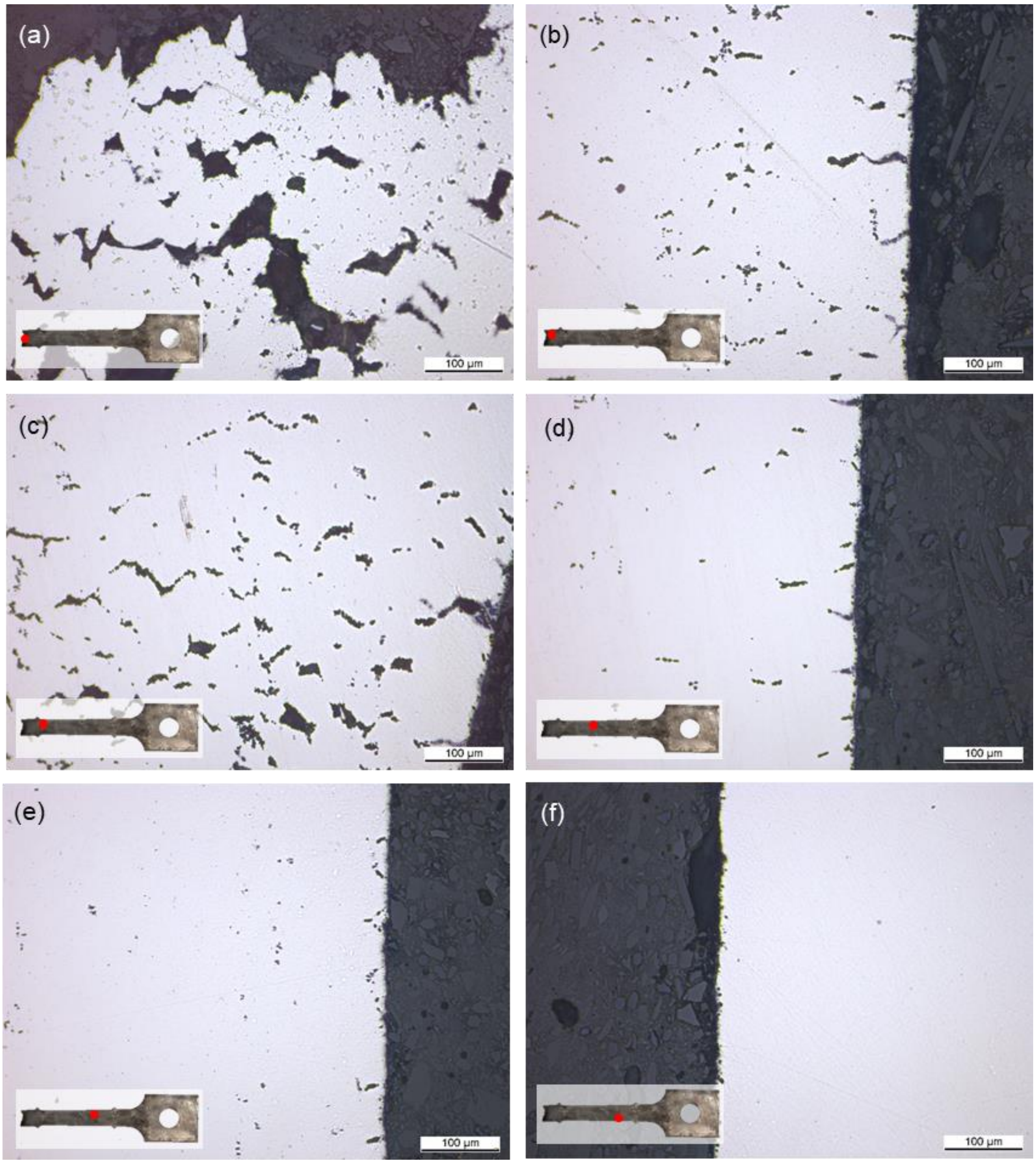

Figure 5. Reflected light microscopy of CR2-1.

Compared to the identically loaded sample CR2-1, stronger formation of microcracks was visible for sample CR2-2, with a length reaching up to 100 µm (Figure 6). However, no difference between the weld seam area and the rest of the material was determined. In [14], no influence of creep damage on weld seam was found either. The area of the transition radius showed pronounced microcracks (Figure 6d).

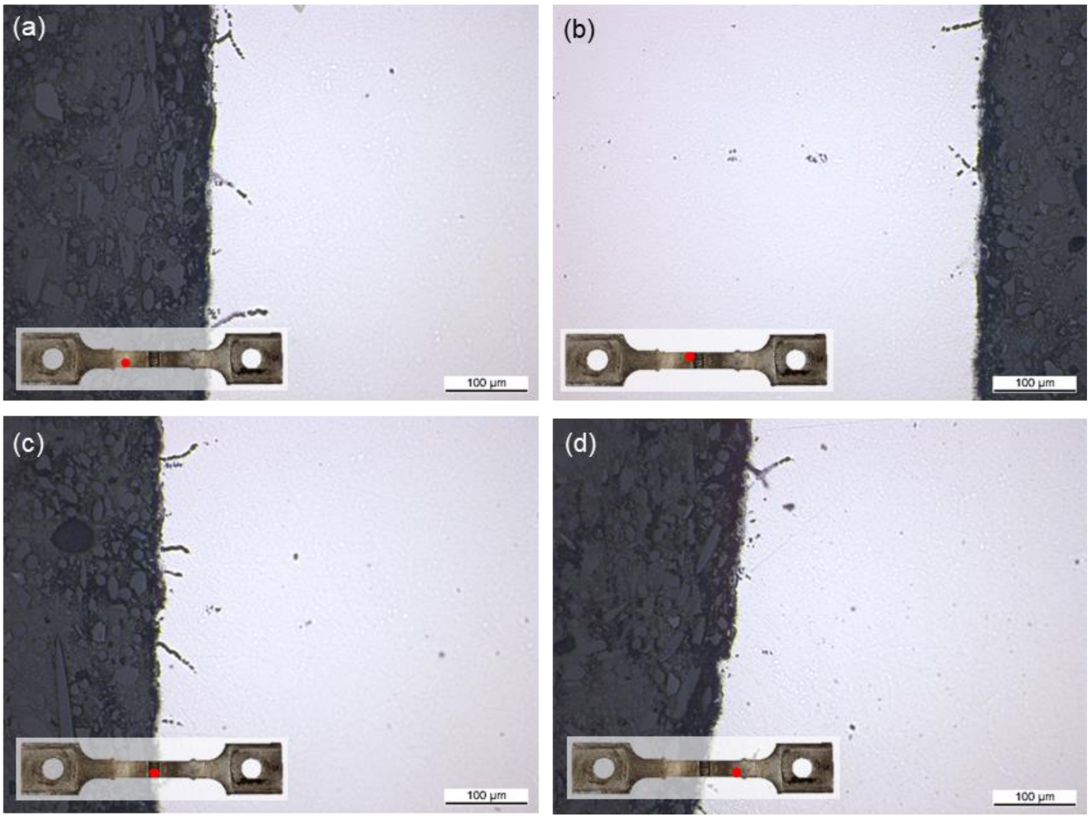

Figure 6. Reflected light microscopy of CR2-2.

Figure 7 shows the analysis results of creep damage in sample CR3. From the figure, it is clear that the damage progressed from the outside to the inside. Many small pores were visible in the edge area, which combined to form microcracks. In addition, a large concentration of imperfections were observed in the area of the transition radius (Figure 7d).

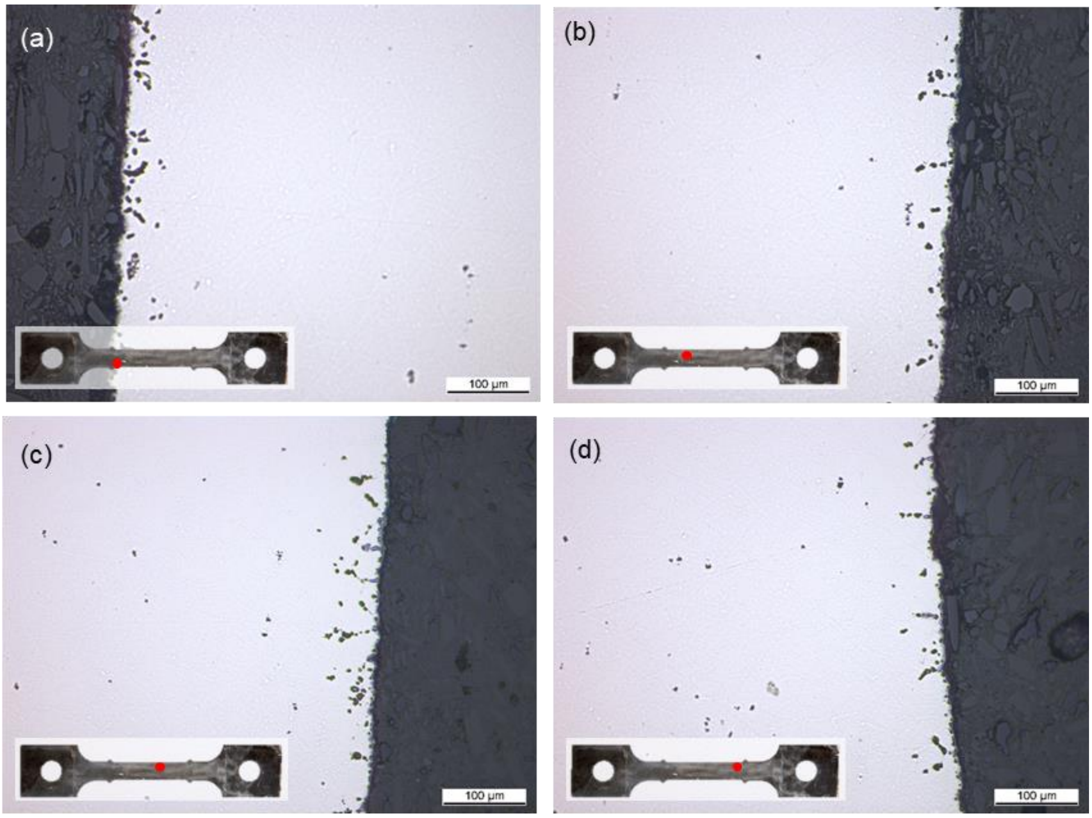

Figure 7. Reflected light microscopy of CR3.

The metallurgical results were evaluated in more detail using the image processing software Imagic IMS (Imagic Imaging Ltd., UK). The defect areas were statistically evaluated via colour mapping (Figure 8). Then, the damage sizes and the failure areas were evaluated.

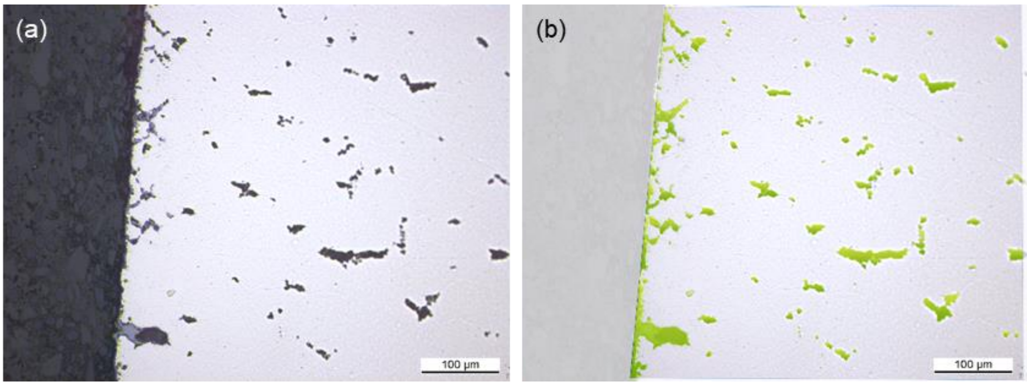

Figure 8. Surface evaluation: (a) original, (b) surface analysis.

Generally, the selection of areas to be evaluated is decisive for a meaningful evaluation. Therefore, the following evaluations were made:

- All evaluations between the measuring tips (A_{ALL}) (Figure 9a)
- Defined areas without the influence of breakage, weld seam and transition radius (A_{D}) (Figure 9b)
- Fillet radius areas (A_{FR}) (Figure 9c)

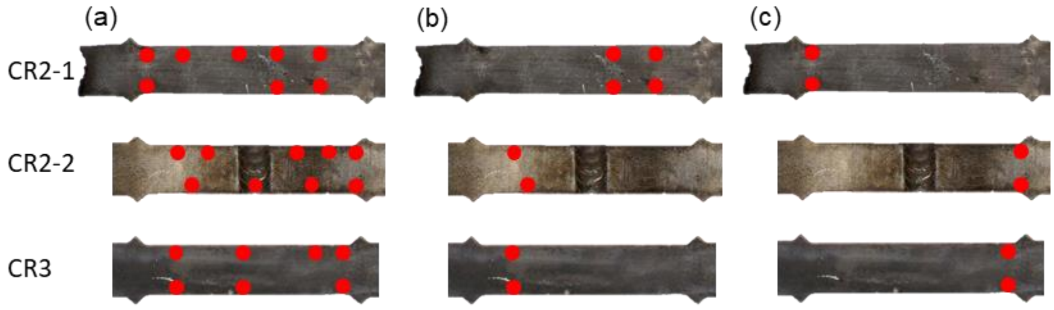

Figure 9. Evaluation areas: (a) A_{ALL}; (b) A_{D}; (c) A_{FR}.

From the images, the mean values of the damage sizes ($\bar{S}_d$) of individual samples were first determined (Figure 10a) and found to vary from 2.5 to 19.3 µm. In general, damage size is considered a good indicator for determining the current creep phase. Pores form first at the grain boundaries, which then combine to form microcracks and then progress to larger failures. With all values (A_{ALL}) considered, CR2-1 and CR2-2 show almost identical damage sizes, with the CR3 sample exhibiting the largest flaws. With the defined areas (A_{D}), the welded CR2-2 sample was found to have significantly larger pores than those of the broken CR2-1 sample. This was also demonstrated in the scanning electron microscopy images, wherein the pores in the edge area have already combined to form microcracks (Figure 6). Sample CR3 clearly showed the largest flaws, and sample CR2-1 had the largest damage in the transition radii.

Damage density (Figure 10b) describes the number of defects in an evaluated area and is calculated as $\rho_d = \frac{n_d}{A_0}$, where A_0 is the total evaluated area and n_d is the total number of damage points in the evaluation area. If several pores connect to form microcracks, this results in larger damage and a reduced damage density, hence further increasing the formation of pores in other positions. With all areas (A_{ALL}) and defined areas (A_{D}) considered, CR2-1 provided the highest density as a result of the influence of the break point of the sample. However, with only the transition radii considered, sample CR3 had the highest values.

In an area-based evaluation, the values are provided as percentages (Figure 10c). Sample CR2-1 exhibited peak values when all the values and the values at the transition radii were considered: $A_R = \frac{A_{\sum d} \cdot 100}{A_0}$, where $A_{\sum d}$ is the total area of damage. With the defined areas (A_D) considered, the values increased steadily from sample CR2-1 to sample CR3. This sample was loaded the longest, for a total of 5850 h.

When the damage density (ρ_d) and area proportion (A_R) reached a critical value, the remaining cross section became unable to withstand the load and the component failed.

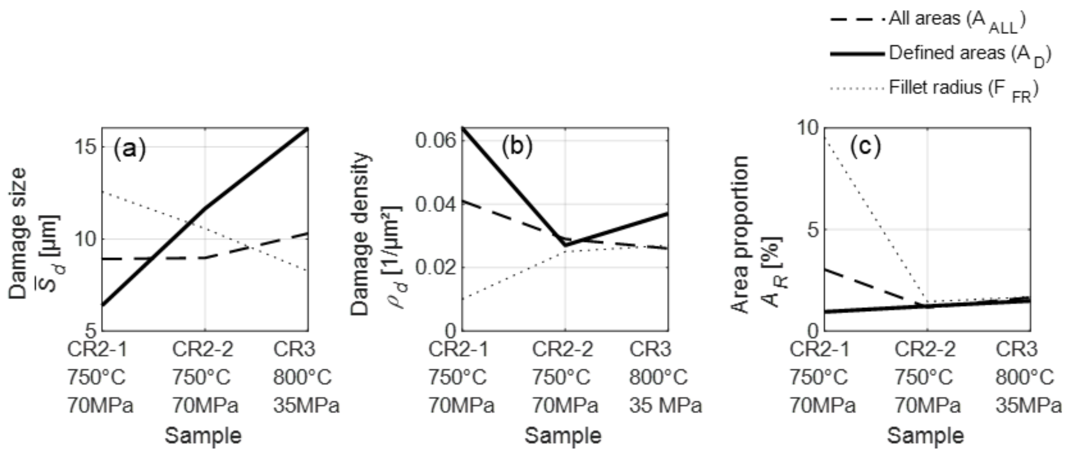

Figure 10. Metallurgical evaluation: (a) damage size; (b) damage density; (c) area proportion.

3.2. Scanning electron microscopy

To evaluate the influence of creep damage on the microstructure, the etched samples were examined using a scanning electron microscope (SEM). Figure 11 shows the reference sample with a clear austenitic crystalline structure with primary carbides, which formed during the solidification of the melt.

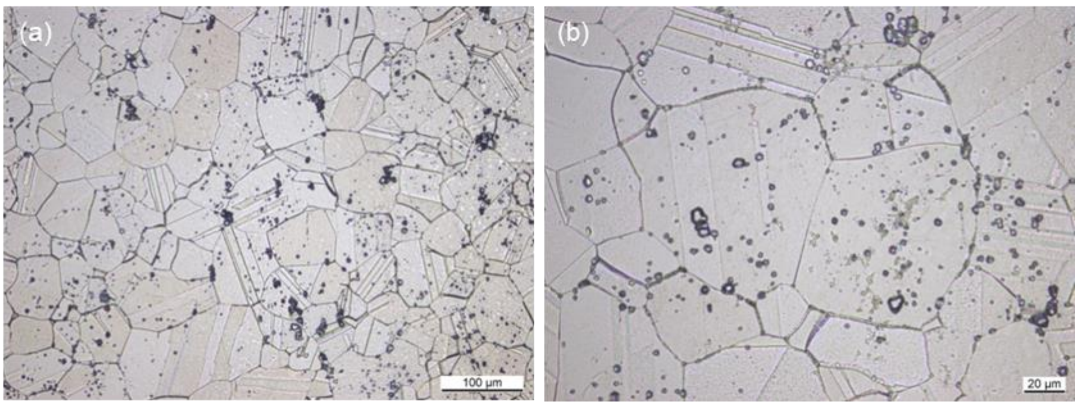

Figure 11. Scanning electron microscopy images of sample CR1.

Although sample CR2-1 (Figure 12) shows an austenitic structure, a high precipitation density can also be observed, with occasional pore formation at the grain boundaries.

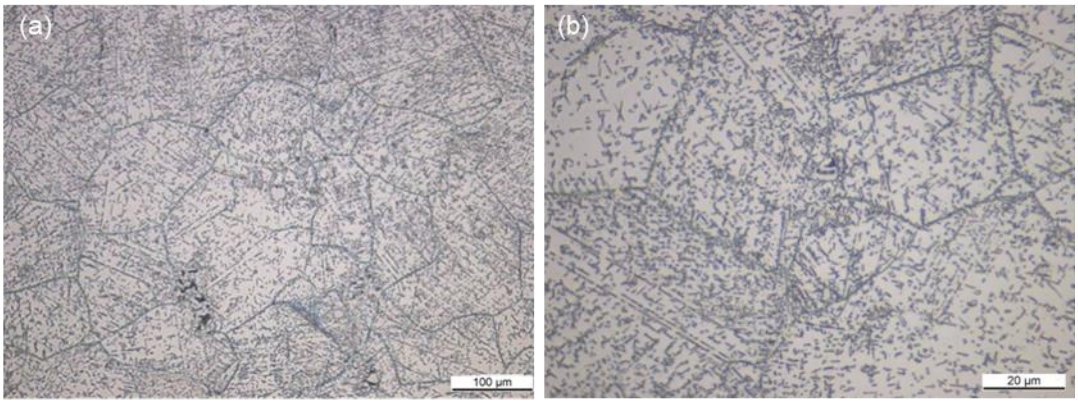

Figure 12. Scanning electron microscopy images of sample CR2-1.

In addition to an increased precipitation density, the welded CR2-2 sample was found to exhibit clear microcracks on the sides (Figure 13). The pores inside were hardly detectable, and there was no discernible difference in the welded area (Figure 13a).

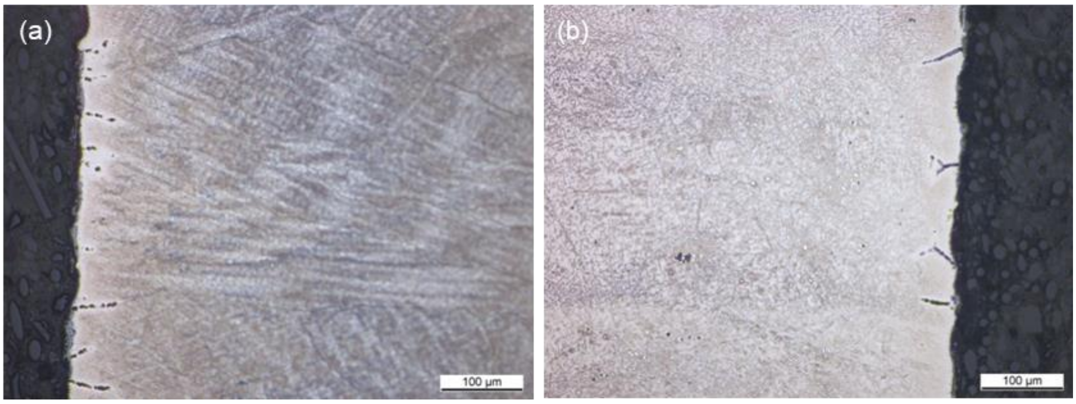

Figure 13. Scanning electron microscopy images of sample CR2-2.

Sample CR3 demonstrates how creep damage develops. In Figure 14a, an oxide layer can be observed on the outside, from which the creep damage progresses. Moreover, for this sample, pores form at the grain boundaries from the outside to the inside, which then combine to form microcracks at points with a high precipitation density.

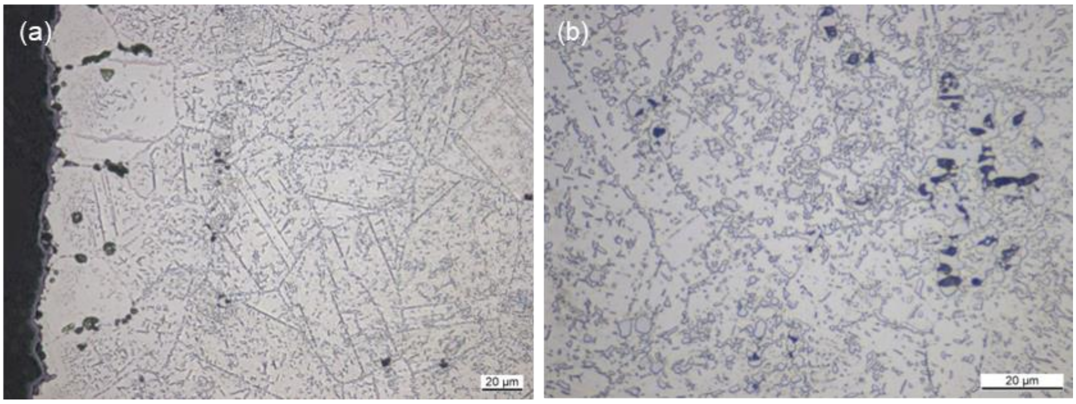

Figure 14. Scanning electron microscopy images of sample CR3.

3.3. Precipitation

With a scanning electron microscope, an increased precipitation density was detected in all creep samples. This section focusses on determining which elements are mainly involved in precipitation.

Characteristic X-ray radiation was used along with SEM and energy-dispersive X-ray (EDX) analysis to characterise element precipitation in creep samples. Figure 15 illustrates the mapping inside the specimen. Analysis showed that molybdenum was the primary precipitation element, and nickel the secondary precipitation element.

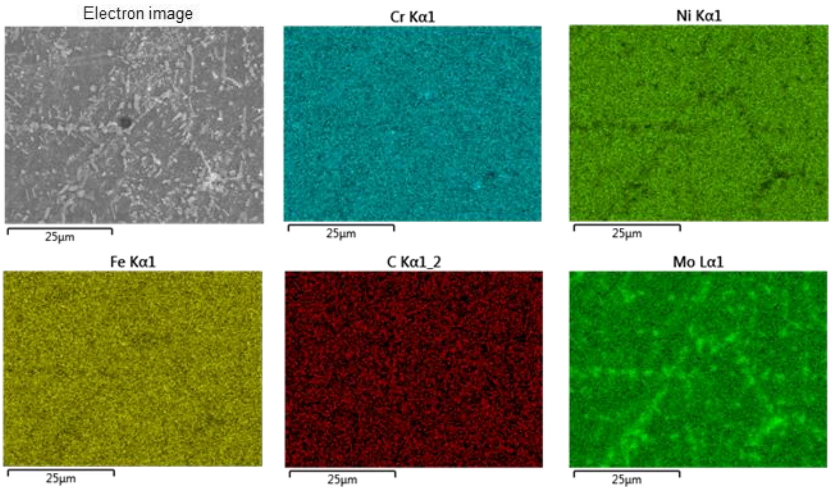

Figure 15. EDX mapping of the inner area.

Figure 16 shows the element mapping at the edge of a sample, where intergranular microcracks have already formed. It can be observed that chromium mainly diffused outwards into the edge area, where oxygen was also found to exhibit an increased concentration. Comparison of the chromium and oxygen mapping revealed the formation of chromium oxide in the edge area, which led to the depletion of chromium inside. In the case of nickel and iron, only a few dislocations formed in the outer oxide layer. However, molybdenum showed no dislocations in the edge area.

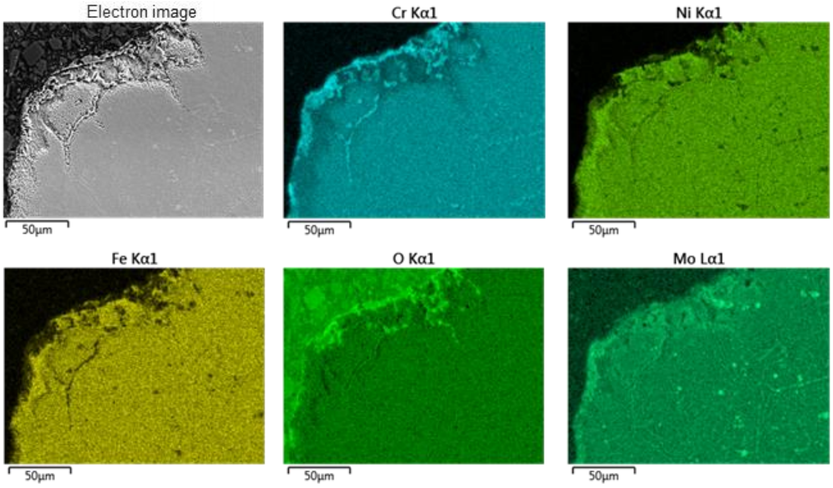

Figure 16. EDX mapping of the outer area (crack).

Because of the temperature load, the chromium particles diffused out of the mixed crystal as a result of their high affinity for oxygen, where they oxidised directly outside the material [22]. If no natural oxide is present on the surface, then the process of oxidation starts with the adsorption of oxygen on the surface, followed by the splitting of O_2 atoms into O atoms. Then, as the reaction proceeds, oxygen is dissolved in the metal and an oxide is formed.

Overall, since the carbides in the area near the edge are also dissolved, this leads to a certain degree of harmonisation. The reaction occurs at both the metal–oxide and the oxide–oxygen interfaces, forming several oxide layers [22]. Above 900 °C, the oxide layers evaporate over a long period of time. Therefore, the chromium oxide needs to be reproduced repeatedly from the metallic chromium present in the base material. Figure 17 shows a chromium(III) oxide layer (Cr_2O_3), which is very hard and brittle. The typical corundum crystalline structure consists of hexagonal lattices.

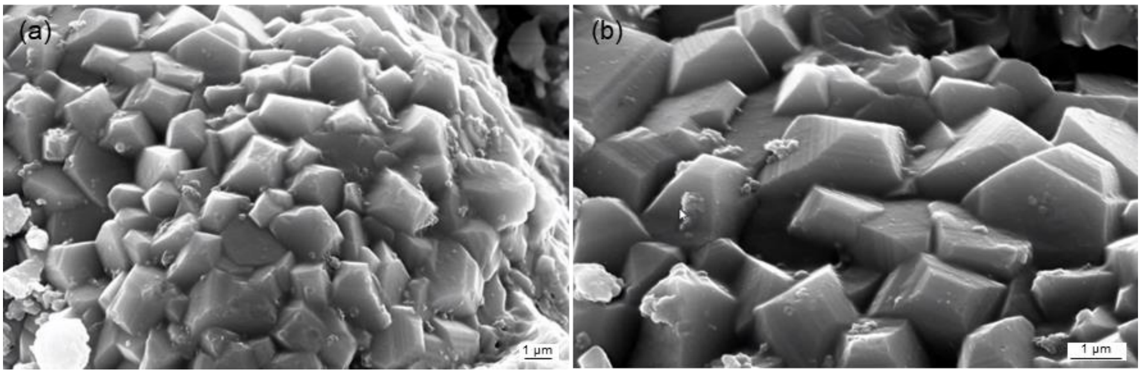

Figure 17. Chromium(III) oxide (Cr_2O_3): (a) overview; (b) crystal structure.

Figure 18a shows another representative sample in which a second layer of iron/nickel oxide has formed on the chromium oxide layer, represented as a red line in the EDX image (Figure 18b). However, the level of adhesion was found to be significantly lower than that of the chromium oxide layer.

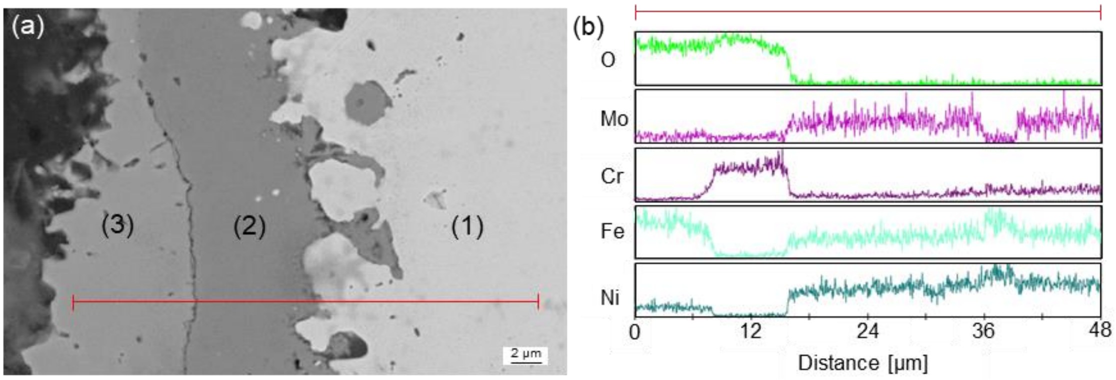

Figure 18. Oxide layer: (a) (1) base material, (2) chromium oxide and (3) iron/nickel oxide; (b) concentration profile, EDX analysis.

According to the level of damage, pores form at the grain boundaries of edge areas as a result of chromium diffusion. In this area, the concentration of the base material depletes in chromium over time. Therefore, its concentration falls below a critical level and internal oxidation and subsequent material failure occur [27]. It is also worth noting that creep damage favours the formation of intergranular pores and cracks, resulting in mixed damage from oxidation and creep.

4. Ultrasonic experiments

Before the samples were prepared for the metallurgical tests, they were examined with longitudinal ultrasound waves. Then, the measured amplitudes of the different frequencies were used to evaluate the measurement results. Generally, an introduced ultrasonic wave propagates in a body with a defined frequency. If this propagation is disturbed as a result of a failure, harmonic frequencies are produced [28–33]. The amplitudes of these harmonic frequencies are then measured and compared to those of the fundamental frequencies. Using two fundamental frequencies has been proven to be an indicator for the detection of material changes with a high resolution [23, 24]. Dual-frequency excitation not only delivers harmonic frequencies for each excitation frequency but also interdependent modulated response frequencies. The following expressions show the nonlinearity parameters used to evaluate the ultrasonic experiments in this study [23, 24]:

$$\begin{aligned}
\beta_{2f1} &\propto \frac{A_{f1+f2}}{{A_1}^2},\\
\beta_{2f2} &\propto \frac{A_{f1+f2}}{{A_2}^2},\\
\gamma_{3f1} &\propto \frac{A_{f1+f2}}{{A_1}^3},\\
\gamma_{3f2} &\propto \frac{A_{f1+f2}}{{A_2}^3},\\
\beta_{f2\pm f1} &\propto \frac{A_{f1+f2}}{A_1 A_2},\\
\gamma_{2f1\pm f2} &\propto \frac{A_{f1+f2}}{{A_1}^2 A_2},\\
\gamma_{2f2\pm f1} &\propto \frac{A_{f1+f2}}{A_1 {A_2}^2}.
\end{aligned} \tag{1}$$

The criteria for the selection of fundamental frequencies are as follows:

- No frequency overlap $\left(f2 \neq \frac{f1}{2}\right)$
- Positive frequency values $\left(f2 > \frac{f1}{2}\right)$
- Sensor bandwidth

Table 3 shows the frequencies evaluated with the chosen excitation frequencies (f_1 = 6 MHz, f_2 = 10 MHz) covering a harmonic and sideband frequency range from 2 to 30 MHz.

Table 3. Evaluated frequencies.

Fundamental/harmonic/ sideband	Frequency [MHz]
f_1	6
f_2	10
$2f_1$	12
$2f_2$	20
$3f_1$	18
$3f_2$	30
f_2+f_1	16
f_2-f_1	4
$2f_1+f_2$	22
$2f_1-f_2$	2
$2f_2+f_1$	26
$2f_2-f_1$	14

4.1. Experimental setup and procedure

In this study, a Rigol DG1022Z pulse generator was used to generate the frequencies. Two frequencies (i.e. f_1 = 6 MHz, f_2 = 10 MHz) were sent over two channels to a Falco WMA-300 amplifier and amplified with an output voltage of 150 V. The signals were sent to the sample by Sensor S, and the longitudinal waves were received on the other side with Sensor R and amplified with a Phoenix ISL 40 dB amplifier. Olympus V129-sm contact transducers were used for this application. The measurement data were then sent to an oscilloscope for further processing. A total of 100 pulses were sent, and their mean values were considered. This not only allowed avoiding wave reflections but also increased the probability of passing small flaws. The wave propagation due to the reduced wall thicknesses of the deformed components was examined without any influence [25]. In the additively manufactured specimen-clamping and positioning device shown in Figure 19b, the sample can be moved around two axes with a constant sensor position.

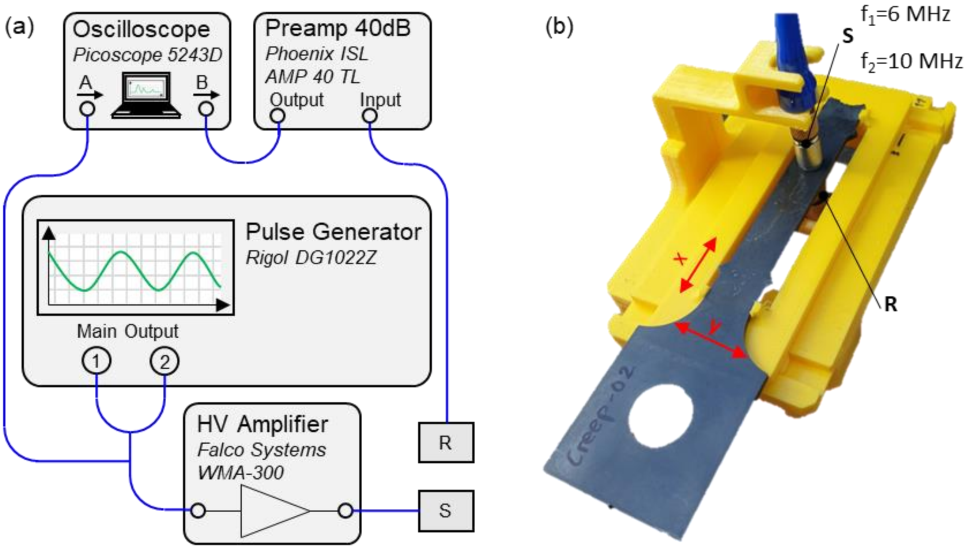

Figure 19. Experimental setup: (a) overview; (b) sensor attachment to a sample.

The area between the measuring tips was first examined (Figure 20), and then 3 × 21 measuring points were documented in the area between the strain measuring tips. Figure 20 shows the grid of the measuring points of the examined vertical rows (R1 to R3) and horizontal columns (C1 to C21).

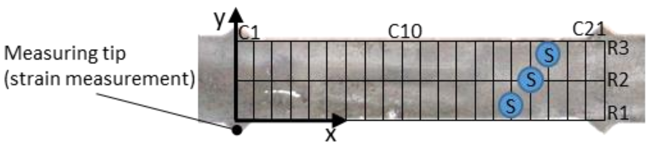

Figure 20. Experimental procedure.

4.2. Experimental results

The measurement results are shown in Figure 21–Figure 23 as calculated contour plots. The same legend scaling was used for all samples for the respective nonlinearity parameters.

Figures 21a, b illustrate the evaluations of the second harmonic frequencies ($2f_{1,2}$), revealing an increase in the nonlinearity parameters compared to the reference sample. Increased nonlinearities were also detected in the area of the fracture, which extended into the sample approximately 10 mm from the measuring tips. With the parameter of frequency $2f_1$, increased nonlinearities were also detected at the transition radii to the measuring tips. This evaluation revealed higher parameter values in the side areas along the *x*-axis compared to the middle. The third harmonic frequencies were also found to behave similarly (Figures 21c, d), and the creep damage was clearly observed. Moreover, the values in the middle area were slightly lower than on the sides.

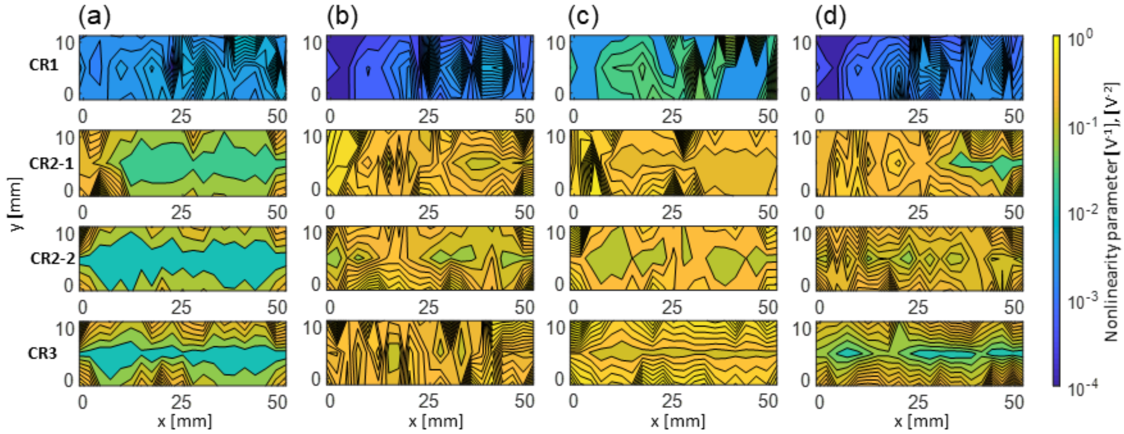

Figure 21. Nonlinearity parameters: (a) $2f_1$; (b) $2f_2$; (c) $3f_1$; (d) $3f_2$.

Overall, the first sideband frequencies ($f_2 \pm f_1$) exhibited partly opposite behaviour. In contrast to the f_2+f_1 frequency (Figure 22b), the middle range was smaller at the f_2-f_1 frequency (Figure 22a). The zone of influence of the fracture can be clearly observed in both figures.

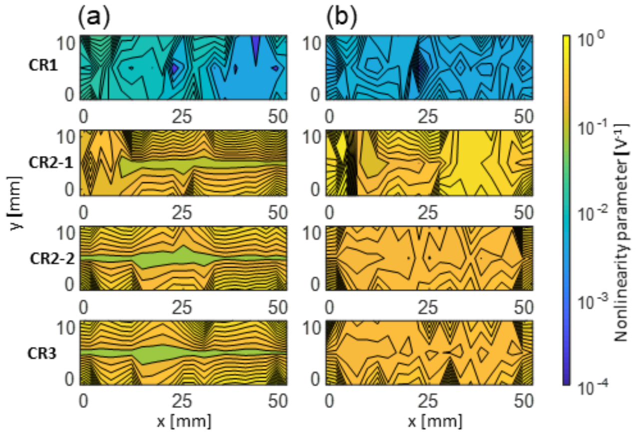

Figure 22. Nonlinearity parameters: (a) $f_2{-}f_1$; (b) $f_2{+}f_1$.

In general, the contour plot of the $2f_1{\pm}f_2$ frequency illustrates the different characteristics of the middle area (Figures 23a, b). Increased nonlinearities were also observed at the corners, especially for the $2f_1{-}f_2$ frequency.

Overall, the previously determined behaviour continued for the sideband frequency $2f_2{\pm}f_1$ (Figures 23c, d). Moreover, the middle ranges of the $2f_2{-}f_1$ frequency were clearly more pronounced than with $2f_2{+}f_1$, and the zone of influence of the crack was identified with the sidebands. The corner areas, where the transition radii to the measuring tips were positioned, also showed increased nonlinearity values.

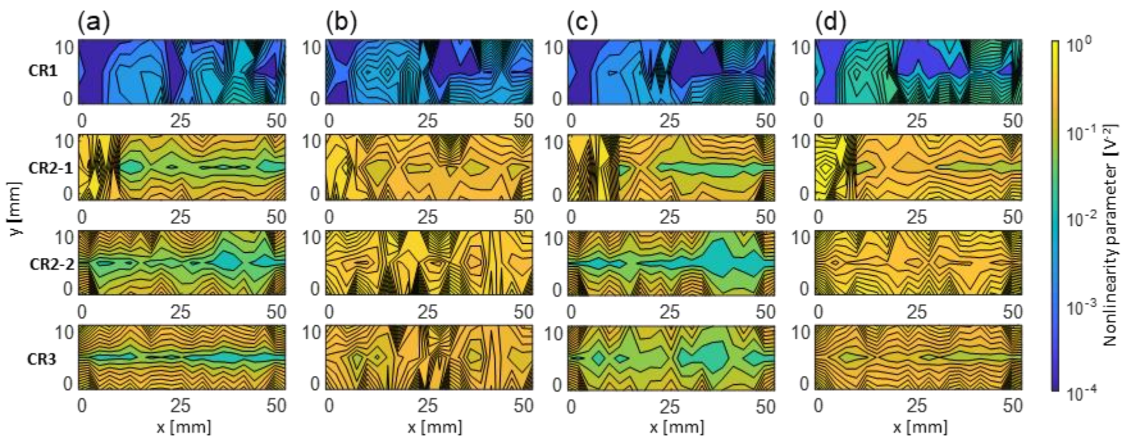

Figure 23. Nonlinearity parameters: (a) $2f_1{-}f_2$; (b) $2f_1{+}f_2$; (c) $2f_2{-}f_1$; (d) $2f_2{+}f_1$.

In summary, nonlinear ultrasound techniques with dual-frequency excitation were used to clearly identify the creep damage and crack zone in CR2-1. It was also observed that the $2f_1{-}f_2$ and $2f_2{-}f_1$ frequencies behave differently in the middle range compared to the $2f_1{+}f_2$ and $2f_2{+}f_1$ frequencies. In addition, increased nonlinearities were measured in the area of the transition radii. However, tests with removed oxide layers did not yield different results.

5. Results and discussion

In Section 3, we showed that the formation of pores begins at the outward grain boundaries, which then combine to form microcracks when the level of creep loading is increased. Although there were hardly any pores inside the material, the precipitation density was very pronounced. The ultrasonic measurements showed that pores and microcracks with sizes from 6.4 to 16 µm can be detected.

Moreover, the ultrasound test outlined in Section 3 revealed a difference in the measured data. Figure 24 shows a sectional image of a sample with metallurgical defects. The outer part is surrounded by oxide layers followed by pores and microcracks, and the inside part contains dislocations and precipitations. When measurements were performed in the middle (R2), the pores and microcracks on the top and bottom were found to lead to the formation of increased nonlinearities. In addition, measurements in the edge areas (R1 and R3) showed that the ultrasonic waves passed the pores and microcracks in the top, bottom and side areas. This difference is demonstrated in the contour plots in Section 4.2.

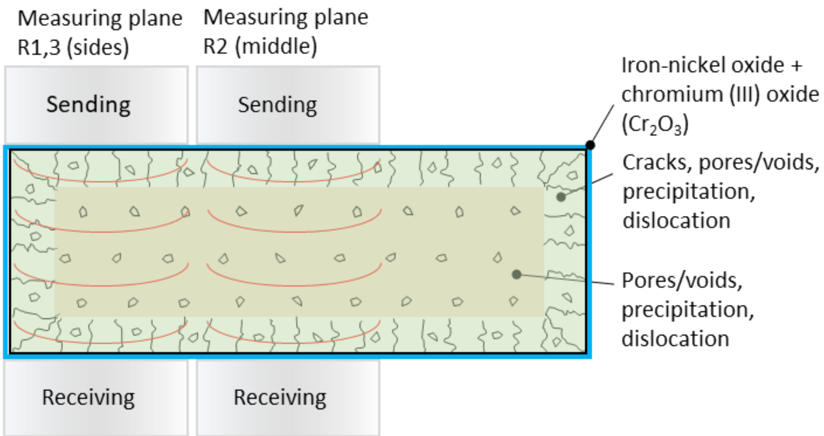

Figure 24. Sectional image of a sample undergoing an ultrasonic measurement.

A difference between the $2f_1-f_2$ and $2f_2-f_1$ nonlinearity parameters and the $2f_1+f_2$ and $2f_2+f_1$ nonlinearity parameters was also observed. This phenomenon has been demonstrated in material plasticity [25], in which the dislocation theory was combined with a one-dimensional wave equation with dual-frequency excitation. Table 4 shows the behaviour of the individual harmonic and modulated response frequencies, which have been analytically and experimentally proven.

Table 4. Dislocation behaviour [25].

Frequency	Behaviour nonlinearity parameter [1]
$2f_1$	−
$2f_2$	+
$3f_1$	−
$3f_2$	−
f_2-f_1	−
f_2+f_1	+
$2f_1-f_2$	−
$2f_1+f_2$	+
$2f_2-f_1$	−
$2f_2+f_1$	+

'+' means an increasing nonlinearity parameter with increasing plasticity.
'−' means a decreasing nonlinearity parameter with increasing plasticity.
[1] Measurement perpendicular to the surface and the tensile load vector.

Although the nonlinearities measured in [25] are considered evidence of dislocations in the material, the behaviour was not quite pronounced as in [25]. It was also found that the increased nonlinearities in the area of the transition radii are due to increased pore formation and microcracks.

Figure 25 shows a normalised comparison of nonlinearity parameters together with metallurgical data. For this study, A_{ALL}, A_D and A_{FR} were compared (Figure 9). For the sake of clarity, the harmonic nonlinearity parameters and sideband parameters were shown separately.

As shown in Figure 25a, sample CR2-1 had the greatest damage density and defect area, with the sideband frequencies showing a favourable match. In addition, sample CR3 exhibited the largest damage size, with the harmonic frequencies $2f_{1,2}$ and $3f_{1,2}$ reaching their peaks.

When A_D was considered (Figure 25b), the behaviour changed. For instance, CR2-1 had the largest damage density with the summing sidebands (i.e. f_2+f_1, $2f_1+f_2$ and $2f_2+f_1$), whereas CR3 had the largest area occupancy and damage size, with the harmonic frequencies $2f_{1,2}$ and $3f_{1,2}$ reaching their peaks.

During the radius evaluation (Figure 25c), sample CR2-1 was found to have the largest area occupancy as well as a relatively large damage density as a result of the influence of the fracture with the sideband frequencies f_2+f_1, $2f_1-f_2$ and $2f_2\pm f_1$. Moreover, sample CR3 was found to exhibit the largest damage size, which is also mirrored in the harmonic frequencies.

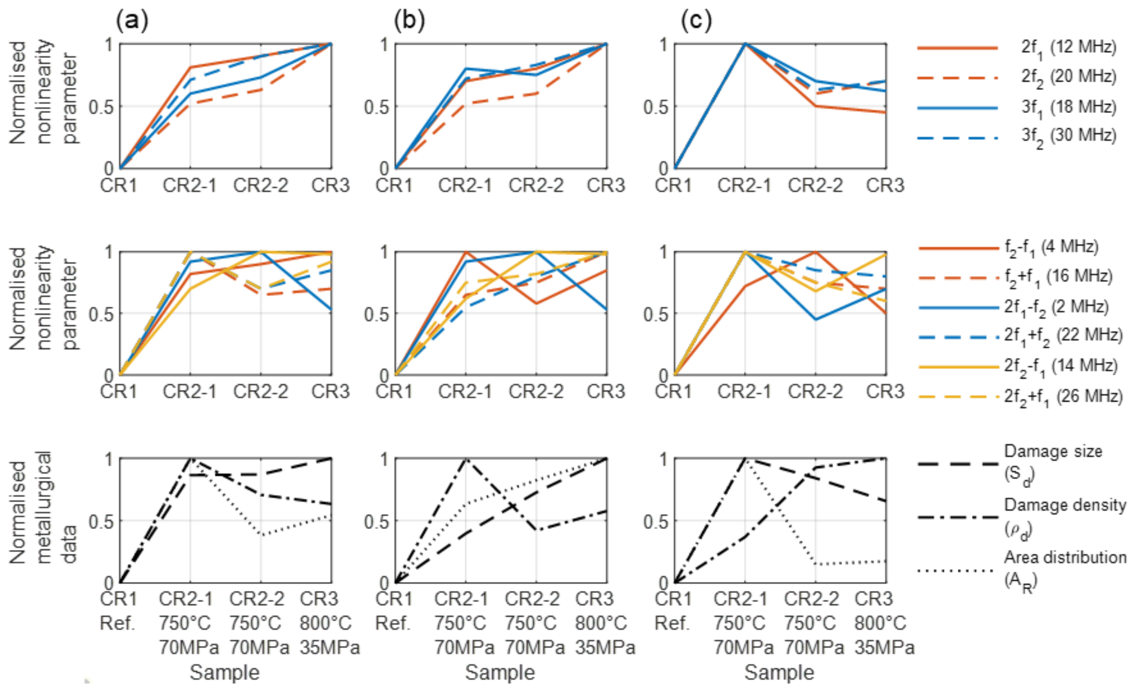

Figure 25. Comparison: (a) A_{ALL}; (b) A_D; (c) A_{FR}.

According to this evaluation, the harmonic frequencies $2f_{1,2}$ and $3f_{1,2}$ seem to be very sensitive to the size of the damage. With regard to the damage density and area, the summing sideband frequencies f_2+f_1, $2f_1+f_2$ and $2f_2+f_1$ showed very favourable matches, along with comparatively high frequencies (16, 22 and 26 MHz).

Generally, the different strain behaviour of sample CR2-1 and the welded CR2-2 sample can be explained by the high constriction in sample CR2-1 and thus the higher strain, which, however, was not constant over the entire measuring distance. In Figure 2, it can be seen that the sample started undergoing a strong strain from 343 h onwards.

It can be assumed that the relatively large damage sizes of samples CR2-2 and CR3 are due to the pores being already connected to form microcracks (Figure 6 and Figure 13).

The oxidation resistance of Hastelloy X can be improved by applying a protective layer using MCrAlY [22]. In addition, creep damage can only be improved by reducing the mechanical load or reducing the temperature load, such as via active cooling.

6. Conclusion

In this study, we used a nonlinear modulation ultrasound approach to detect and image creep and oxidation damage in various samples made of Hastelloy X. Metallurgical investigations showed that it is possible to prove that the temperature load causes chromium to diffuse outwards in the edge areas of the samples to oxidise on the outside. Favoured by the lack of chromium in the edge areas, pores form at the grain boundaries, which then combine to form microcracks.

It was also found that the harmonic frequencies $2f_{1,2}$ and $3f_{1,2}$ can serve as a useful parameter to accurately measure the damage sizes of failures. Moreover, the modulated response frequencies f_2+f_1, $2f_1+f_2$ and $2f_2+f_1$ were found to be in good agreement with the total surface area of the pores and damage density. The dislocation theory was used to explain dislocations and precipitations in the material, allowing clear differentiation between dislocations and microcracks.

SEM analysis revealed a high dislocation density. It was also found that the weld seam exhibits the same creep damage as that in the base material. Moreover, EDX analysis identified molybdenum as the main precipitation element inside the material. In addition, the chromium diffusion at the edge areas led to the depletion of the element and favoured the formation of pores and microcracks due to intergranular corrosion.

Overall, the investigations presented herein offer a better understanding of creep damage in a material when it is used in gas turbines and also help in the design of hot-gas-leading components. Nonlinear ultrasound technology has also been proven to be a powerful tool for detecting and classifying creep damage at an early stage as well as for differentiating between precipitation and microcracks.

Acknowledgement

Thanks to Wolfgang Bernauer, Dirk Formella and the MAN Energy Solutions SE for their support.

References

1. Mevissen, F., & Meo, M. (2019). A Review of NDT/Structural Health Monitoring Techniques for Hot Gas Components in Gas Turbines. *Sensors, 19*(3), 711.
2. Sahu, M. K., Swaminathan, J., Bandhoypadhyay, N. R., & Palit Sagar, S. (2018). Creep Damage Evaluation In P92 Steel Using Second Harmonic Of High Power Ultrasonic Signal. *Materials Today: Proceedings, 5*(2), 4467–4474.
3. Semenov, A. S., Semenov, S. G., & Getsov, L. B. (2015). Methods of Computational Determination of Growth Rates of Fatigue, Creep, and Thermal Fatigue Cracks in Poly- and Monocrystalline Blades of Gas Turbine Units. *Strength of Materials, 47*(2), 268–290.
4. Chen, L., Liu, Y., & Xie, L. (2007). Power-exponent function model for low-cycle fatigue life prediction and its applications – Part II: Life prediction of turbine blades under creep–fatigue interaction. *Int. J. Fatigue, 29*(1), 10–19.

5. Marahleh, G., Kheder, A., & Hamad, H. F. (2006). Creep life prediction of service-exposed turbine blades. *Mater. Sci. Eng. A*, *433*(1-2), 305–309.

6. Kim, H.-J. (2005). Assessment of creep life fraction for in-service high-temperature components. *Eng. Fail. Anal. C., 12*(4), 578–585.

7. Maharaj, C., Morris, A., & Dear, J. P. (2012). Modelling of creep in Inconel 706 turbine disc fir-tree. *Eng. Fail. Anal., 558*, 412–421.

8. Liu, D., Li, H., & Liu, Y. (2015). Numerical Simulation of Creep Damage and Life Prediction of Superalloy Turbine Blade. *Math. Probl. Eng., 2015*(1), 1–10.

9. Shi, D., Li, Z., Yang, X., & Wang, H. (2018). Accelerated LCF-creep experimental methodology for durability life evaluation of turbine blade. *Fatigue Fract. Eng. Mater. Struct., 41*(5), 1196–1207.

10. Hyde, T. H., Sun, W., & Becker, A. A. (2005). Use of life and strain fraction rules for creep life prediction of pressurized pipe components undergoing geometry change. *J. Strain Anal. Eng., 40*(4), 385–394.

11. Raj, B., Moorthy, V., Jayakumar, T., & Rao, K. B. S. (2003). Assessment of microstructures and mechanical behaviour of metallic materials through non-destructive characterisation. *Int. Mater. Rev., 48*(5), 273–325.

12. Baby, S., Nagaraja Kowmudi, B., Omprakash, C. M., Satyanarayana, D., Balasubramaniam, K., & Kumar, V. (2008). Creep damage assessment in titanium alloy using a nonlinear ultrasonic technique. *Scripta Materialia, 59*(8), 818–821.

13. Balasubramaniam, K., Valluri, J. S., & Prakash, R. V. (2011). Creep damage characterization using a low amplitude nonlinear ultrasonic technique. *Mater. Charact., 62*(3), 275–286.

14. Ehrlich, C., Kim, J.-Y., Jacobs, L. J., Qu, J., & Wall, J. (2012). Experimental characterization of creep damage in a welded steel pipe section using a nonlinear ultrasonic technique. In *Review of Progress in Quantitative Nondestructive Evaluation, USA, VT, Burlington, 17–22 July*. (pp. 292–298, AIP Conference Proceedings): AIP.

15. Kang, J. (2000). On the Detection of Creep Damage in a Directionally Solidified Nickel Base Superalloy Using Nonlinear Ultrasound. In *Quantitative Nondestructive Evaluation, USA, Wisconsin, 27 July-1 August 2000*. (pp. 1248–1255): AIP.

16. Xiang, Y.-X., Deng, M.-X., Xuan, F.-Z., Chen, H., & Chen, D.-Y. (2012). Creep Damage Evaluation of Titanium Alloy Using Nonlinear Ultrasonic Lamb Waves. *Chin. Phys. Lett., 29*(10), 106202.

17. Xiang, Y., Deng, M., & Xuan, F.-Z. (2014). Creep damage characterization using nonlinear ultrasonic guided wave method: A mesoscale model. *Int. J. Appl. Phys., 115*(4), 44914.

18. Xiang, Y., Zhu, W., Liu, C.-J., Xuan, F.-Z., Wang, Y.-N., & Kuang, W.-C. (2015). Creep degradation characterization of titanium alloy using nonlinear ultrasonic technique. *NDT E Int., 72*, 41–49.

19. Valluri, J. S., Balasubramaniam, K., & Prakash, R. V. (2010). Creep damage characterization using non-linear ultrasonic techniques. *Acta Materialia, 58*(6), 2079–2090.

20. Abdelrhman, A. M., Hee, L. M., Leong, M. S., & Al-Obaidi, S. (2015). Condition Monitoring of Blade in Turbomachinery: A Review. *Adv. Mech. Eng., 6*(4), 210717.

21. Burk, S. (2011). *Hochtemperaturoxidation Molybdän-basierter Legierungen unter Berücksichtigung von Einflüssen aus Umgebungsatmosphäre und legierungstechnischen Maßnahmen*. Ph.D. Thesis. University of Siegen, Siegen, Germany. (In German)

22. Obigodi-Ndjeng, G. (2011). *High Temperature Oxidation and Electrochemical Investigations on Nickel-base Alloys*. Ph.D. Thesis. University of Erlangen-Nürnberg, Erlangen, Germany.

23. Mevissen, F., & Meo, M. (2019). Detection of Cracks in Turbine Blades with Nonlinear Ultrasonic Frequency Modulation. In *IWSHM 2019, Stanford, USA, 10-12 September*. (Vol. 1, pp. 824–834): DEStech Publications.

24. Mevissen, F., & Meo, M. (2020). A Nonlinear Ultrasonic Modulation Method for Crack Detection in Turbine Blades. *Aerospace, 7*(6), 72.

25. Mevissen, F., & Meo, M (2022). Early stage plasticity detection in gas turbine components using a nonlinear ultrasound modulation technique. *Int. J. Solids Struct.* (Submitted).

26. Haynes International. HASTELLOY® X ALLOY. http://www.haynes.ch/doc/HASTELLOY_X.pdf. Accessed 21 April 2021.

27. Oberhauser, S. (2021). Hochtemperaturkorrosion und mögliche Abhilfemaßnahmen. https://www.wotechtechnicalmedia.de/womag/ausgabe/2017/03/18_oberhauser_korrosion_03j2017/ 18_oberhauser_korrosion_ 03j2017.php. Accessed 30 April 2021. (In German)

28. Hikata, A., Chick, B. B., & Elbaum, C. (1965). Dislocation Contribution to the Second Harmonic Generation of Ultrasonic Waves. *J. Appl. Phys., 36*(1), 229–236.

29. Amura, M., Meo, M., & Amerini, F. (2011). Baseline-free estimation of residual fatigue life using a third order acoustic nonlinear parameter. *Acoust. Soc. Am., 130*(4), 1829–1837.

30. Malfense Fierro, G. P., & Meo, M. (2015). Residual fatigue life estimation using a nonlinear ultrasound modulation method. *Smart Mater. Struct., 24*(2), 25040.

31. Yost, W. T. (2000). Nonlinear ultrasonic pulsed measurements and applications to metal processing and fatigue. In *The 27th annual review of progress in quantitative nondestructive evaluation, Ames, Iowa (USA), 16-20 July 2000*. (pp. 1268–1275): AIP.

32. Cantrell, J. H., & Yost, W. T. (2001). Nonlinear ultrasonic characterization of fatigue microstructures. *Int. J. Fatigue, 23*(SUPPL. 1), 487–490.

33. Cantrell, J. H. (2006). Quantitative Assessment of Fatigue Damage Accumulation in Wavy Slip Metals from Acoustic Harmonic Generation. *Philos. Mag., 86*(11).

7 Thermosonic Techniques for Crack Detection

In the previous chapters, creep damage (Chapter 6) and crack detection (Chapters 4 and 5) were examined using nonlinear ultrasound techniques. It was also pointed out that if the cracks are closed, then the nonlinear ultrasound techniques may fail because the waves may pass through the failure unhindered. In this regard, ultrasonically stimulated thermographic techniques showed promising results, in which the components were vibrated so that the cracked surfaces rub against each other. The resulting frictional heat was detected using a thermal imaging camera.

In this study, a piezo actuator was used to passively excite cracked turbine blades with a newly designed blade-clamping device. The actuator excited the turbine blades with frequencies (f_{ac}) ranging from 0 to 100 kHz to document the temperature increase with a thermal imaging camera. Thus, the temperature increase, $\Delta T = f(f_{ac})$, was evaluated for each blade. In the next step, frequencies with the highest increases in temperature were kept constant and the energy supply (P_{el}) to the actuator was gradually increased. The behaviour of the curves, $\Delta T = f(P_{el})$, was used to draw conclusions regarding the preloads or constraints in the crack area, which may indicate plastic deformation in the material around the crack area. In particular, the influence of preloads on the temperature increase due to friction was investigated with separate experiments. Moreover, a developed finite element model was used to simulate the vibration modes and calculate the temperature increase due to friction.

During the experiments, a previously unknown crack was detected under the TBC in a turbine blade, which underlines the strength of this process.

The form 'Statement of Authorship' and the paper are provided on the following pages.

This declaration concerns the article entitled:			
Ultrasonically stimulated thermography for crack detection of turbine blades			
Publication status			
Draft manuscript ☐ Submitted ☐ Accepted ☐ Published ☒			
Publication details (reference)			
Mevissen, F., & Meo, M. (2022). Ultrasonically stimulated thermography for crack detection of turbine blades. *Infrared Physics & Technology*, *122*, 104061. https://doi.org/10.1016/j.infrared.2022.104061			
Candidate's contribution to the paper (detailed, and also given as a percentage)			
Formulation of ideas: 80% The idea of using ultrasonically stimulated thermography with a piezo actuator as a source of excitation was my supervisor's, Professor Michele Meo. The idea of frequency-dependent temperature measurement with increasing electrical voltage with the same frequency was mine.			
Design of methodology: 90% I tested various piezo actuators in advance to determine the best one for this application. I also designed the blade holder device to attach the piezo actuator. In addition, I developed the finite element model with ANSYS Parametric Design Language (APDL) programming to simulate the frictional heat increase and discussed the results with Professor Michele Meo.			
Experimental work: 100% I performed and evaluated all the thermographic experiments.			
Presentation of data in journal format: 90% I analysed and processed all the collected data from the thermographic experiments. I also created all the figures and determined the layout of the manuscript. My co-author, Professor Michele Meo, provided feedback on the above and helped with the submission and review processes.			
Statement from candidate			
This paper contains original research that I have conducted during the period of my higher degree of research candidature.			
Signed	[redacted]	**Date**	20/10/2022

Ultrasonically stimulated thermography for crack detection of turbine blades

Frank Mevissen and Michele Meo

Department of Mechanical Engineering, University of Bath, Bath, BA2 7AY, UK

Abstract

The hot gas components in a gas turbine have to withstand extreme loads. As failure of turbine blades could have catastrophic consequences, the integrity of the entire engine must always be guaranteed, hence quick and reliable structural health monitoring (SHM) or nondestructive testing techniques (NDT) are essential.

In this work, an ultrasonic stimulated thermographic test system was developed to efficiently detect cracks in turbine blades. The used technique is based on the ultrasound excitation with a piezo actuator, where the contact surfaces of the crack are excited and generate frictional heat, which is captured by a thermal imaging camera. A method was developed, where the temperature increase is measured as a function of the electrical energy supply to the actuator. This allows understanding crack topology and the prediction of preloads in the crack. Numerical analysis were conducted for optimising the frequency to be excited for the type of damage experienced by the blade and for understanding the basic physics of the coupling between cracks configuration, local crack velocity and temperature increase. The procedure presented helps to efficiently detect cracks and to optimize the inspection cycles of these components.

1. Introduction

Different causes can lead to failure of components in a gas turbine [1]. Among various NDT methods for damage imaging, the vibro-stimulated thermography process has been developed in recent years to detect cracks quickly and efficiently. A component is vibrated so that the surfaces of the crack rub against each other and the generated frictional heat can be detected using a thermal imaging camera.

There are different possibilities how infrared thermography can be used for NDT [2–4]. Rahammer et al. conducted vibrothermal tests in composites using local defect resonance (LDR) technology [5] to investigate the changed resonance behaviour due to the changed stiffness in the area of the crack. Vibrothermography successfully demonstrated the viscoelastic temperature increase due to the delamination of composites [6, 7], while Solodov et al. utilised Chladni figures to demonstrate and visually illustrate resonance defects [8]. Gao et al. used statistical methods to detect cracks in turbine blades using sonic IR [9], and Obeidat et al. developed algorithms for post-processing to better extract damage [10–12]. The effect on the temperature of a closing crack was studied by Lu et al. [13], and the energy and heat index was developed for crack classification [14–16] based on the dissipated energy in the crack. Rothenfusser et al. examined the behaviour of open and closed cracks in turbine blades in an energy context [17]. Mendioroz et al. developed a technique to detect vertical cracks with a thermal imaging camera using ultrasound excitation [18]. Cracks in aluminium structures were successfully detected using sonic IR thermography and extended post-processing techniques to process the results [19]. Weekes et al. successfully detected cracks under a ceramic thermal barrier coating (TBC) used in many hot gas components in gas turbines [20], and Zang et al. developed finite element methods for verifying experiments using sonic IR on turbine blades with cracks [21, 22].

In the literature overview shown so far, single frequencies were used for excitation. Studies with multi-frequency excitations are presented in the following.

Zang et al. excited turbine blades using multiple frequencies to locate cracks with a thermal imaging camera [23, 24], and some studies used high-frequency loudspeakers as a source of excitation [25, 26]. Kang et al. increased the vibration amplitudes in the test component through an alternative constructive fastening solution for the ultrasonic horn and test component [27]. It was shown that different excitation frequencies offers advantages in crack detection. Holland successfully detected delamination under the TBC of turbine vanes with a broadband vibrothermography technique [28]. A frequency dependency of the heat generated at the flaws was shown.

Many technical possibilities can stimulate and vibrate the components, such as using sonotrodes [29–45], where 20 to 40 kHz signals are transmitted with high energy to the component to be measured. This creates a quasi-chaotic excitation, since single impulses are mainly transmitted and no periodic signals [18, 20, 34, 38, 43, 45–48]. A disadvantage is that damage to the contact surface of the sonotrode with the test component can occur [31, 33, 38, 44]. Typical piezoelectric sensors can also be used for excitation [49–51]. Dyrwal, Meo and Ciampa used air-coupled transducers (ACT) to excite turbine blades to detect cracks with thermography [52]. An advantage here is the contactless use of these transducers, but the whole system sensitively reacts to the position of the sensor and to smallest deviations of the focusing point.

The aim of this work was the development of an efficient detection and classification of cracks with an ultrasonic stimulated thermal wave imaging approach. In addition, a novel developed procedure was used to identify preloads in cracks. This is an important indicator of plastic deformations caused by one of the typical failure modes in turbine blades. A piezo actuator was used as a source of excitation in this study, which allowed exciting the test components with frequencies up to 100 kHz and detecting the generated frictional heat using a thermal imaging camera. The turbine blades were excited indirectly via a rigid holding device to prevent damage to the blades and the TBC. For this purpose, turbine blades were used with cracks located at different positions on the trailing edges. This cracks formed during operation in a gas turbine.

The temperature increase on the cracks was mapped as a function of the excitation frequencies. This was used to investigate the crack behaviour using varying actuator amplitudes with constant excitation frequencies. Finite element simulations were developed to study the behaviour of the crack and to optimise the experimental approaches. It was numerically demonstrated the importance of exciting the appropriate velocity component to generate frictional heat when the crack is open or closed. The generated heat was calculated numerically and compared with the experiments.

2. Specimen description

For the thermographic study, 12 turbine blades made from Inconel 628 of a 10 MW industrial gas turbine with cracks at the trailing edges were used. These blades are internally cooled. The cooling air is led into the blade via the blade root and exits after serpentine cooling via different exit slots at the trailing edge. Figure 1 shows the positions of the cracks on the trailing edges of the turbine blades for further evaluations. In Table 1, all blades were summarised with corresponding names, crack positions and the visible crack lengths.

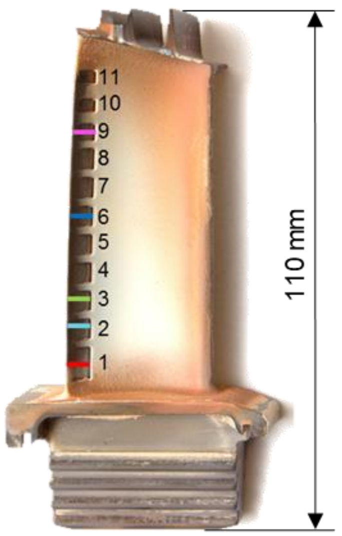

Figure 1. Cracked turbine blades.

Table 1. Investigated turbine blades – overview.

Blade name	Crack in cooling air chamber	Visible Crack length L [mm]
B327	1	1.6
B285	1	4.5
B100	2	5.4
B046	2	6
B189	2	6
B154	2	6.1
B221	2	6.6
B259	3	2.4
B115	3	5.8
B254	3	6.8
VKH1084	6	2.5
B286	6	6.1
B189	9	—

3. Experimental setup

A piezo actuator was used to vibrate the turbine blades. Typical applied strains are 0.1% to 0.15% of the actuator length. Piezo actuators behave like capacitive loads, which is why their charging and discharging currents increase with the working frequency. The preloaded actuator from Piezosystem Jena was used due to its robust design and low heat impact area. Table 2 summarises the properties.

Table 2. Properties – piezo actuator.

Type	Dimensions [mm]	Stiffness [N/µm]	Displacement [µm]	Mechanical resonance [kHz]	Blocking Force [N]
Piezosystem Jena PiSha 150/16/2	Ø25×29 Holder: Ø10×4	600	2	40	1000

The entire scheme of the experimental setup is shown in Figure 2a. The actuator was directly bolted to the mounting device of the turbine blade using internal thread (Figure 2b).

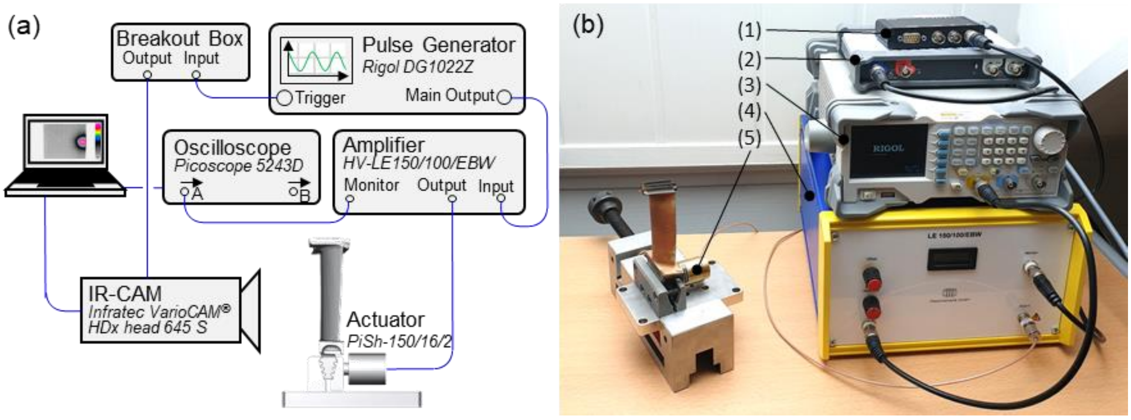

Figure 2. Experimental setup: (a) Scheme; (b) Components: (1) Breakout box, (2) Oscilloscope - Picoscope 5243D, (3) Puls generator - Rigol DG1022Z, (4) Amplifier - HV-LE150/100/EBW, (5) Piezo actuator - PiSha150/16/2.

A linearly rising sine wave signal generated by the Rigol DG1022Z pulse generator was used to excite the crack resonance frequencies. This signal is amplified by the device HV-LE150/100/EBW from Piezosystem Jena. The extended bandwidth of the amplifier introduces sufficient power over a large frequency range to the piezo actuator. As a control, the signal was transmitted via the monitor output to an oscilloscope and further evaluated using a computer. A breakout box was integrated via the trigger output to synchronise the frequency signal of the pulse generator with the recorded images of the thermal camera. For recording, the Infratec thermography system was used with the VarioCAM® HDx head research 645S camera, which is an uncooled micro bolometer camera with a detector format of 640 × 480 pixels and automatic focusing. The noise equivalent differential temperature (NETD) is up to 20 mK.

The device for blade mounting was clamped to achieve maximum system rigidity, and to avoid erroneous reflection measurements, a black paper box was placed over the specimen.

4. Thermographic spectra

To examine the investigations with increasing energy supply in the actuator, the frequencies leading to the highest temperature increase were first determined. For this purpose, the thermograms for all turbine blades were measured.

All measurements were performed in 5 kHz steps and synchronised with the highest accuracy. The frequency was linearly increased by 60 seconds for each excitation block, which guaranteed detecting small temperature increases. This was performed in the frequency range of 0 to 100 kHz.

Thermal energy is also transferred into the system through the piezo actuator's heat and can thereby influence the result of the thermal imaging camera measurement. An influence of the heating of the ambient air and convective transmission to the blades was not measured. The thermal power P_{th} generated in the actuator can be estimated as follows [53] (Equation (1)):

$$P_{th} \approx \frac{\pi}{2} tan(\delta) f C U^2, \quad (1)$$

where $tan(\delta)$ is the dielectric loss factor (ratio of effective to reactive power), f the working frequency, C the actuator capacitance and U the voltage difference between positive and negative peak voltage. Figure 6a shows the heat loss, P_{th}, as a function of the input voltage, U, for frequencies up to 100 kHz. The frequency influences the thermal output emitted, where the higher the actuator frequency, the greater the temperature increase.

Measurements from 0 to 100 kHz were performed to estimate the heat influence on the experimental setup (Figure 6b). Temperature profiles were measured at different positions and compared regarding the outer shell of the actuator (1), the contact surface for the washer (2), the holder (3), the inner shroud of the turbine blade (4) and two positions on the airfoil (5) and (6). The temperature significantly rises at the contact surface (2) with an excitation of 10 kHz, and a temperature increase of 4.2 K was measured at 30 kHz to 40 kHz.

This also affects the airfoil, where the temperature begins to rise continuously from an excitation of 20 kHz. The influence on two cooling air outlets on the airfoil were also evaluated. A maximum temperature increase of 1.19 K was measured at the position of the first cooling air chamber (5), further up on the ninth cooling air chamber (6) a maximum of 1.03 K.

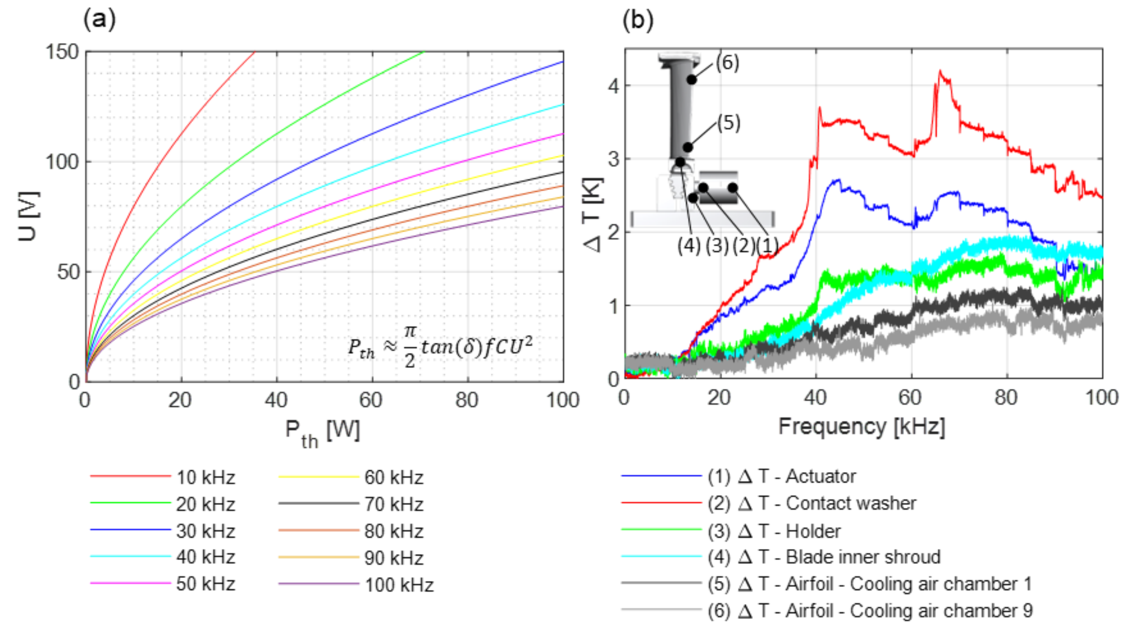

Figure 3. Temperature influence actuator: (a) theoretical heat loss actuator - $U\ f(P_{th})$; (b) experimentally determined heat transfer.

The theoretical calculations and experiments showed actuator influence on the heating of the turbine blade with a slow transfer of heat to the test object. Rapid heating in the crack area due to friction represents a clear difference detectable due to the higher temperatures.

Figure 4 shows the thermograms of the various turbine blades and cooling air openings. The designations C1, C2, C3, C6 and C9 in the figures describe the evaluated positions of the cracks on the turbine blades. The significant temperature increases occur primarily in the frequency range from 30 to 50 kHz for all measurements. As already shown in Figure 3b, the general temperature difference increases continuously. Nevertheless, the temperature peaks were clearly identified. With consideration of all blades, the arithmetic average temperature increase was 6.5 K. In the case of cracks in the sixth chamber, the frequencies also shift to higher values since a maximum temperature increase of 26 K was measured (Figure 4-C6(b)). These significant increases in temperature are certainly favoured by the rigid clamping and thus by the direct transmission of the actuator energy.

The crack in the ninth chamber (Figure 4-C9(a)) is noteworthy, as a crack in the second chamber was originally detected on blade B189, but a further crack was not detected using conventional inspection methods and only made visible by thermographic experiments. This crack was located under the TBC.

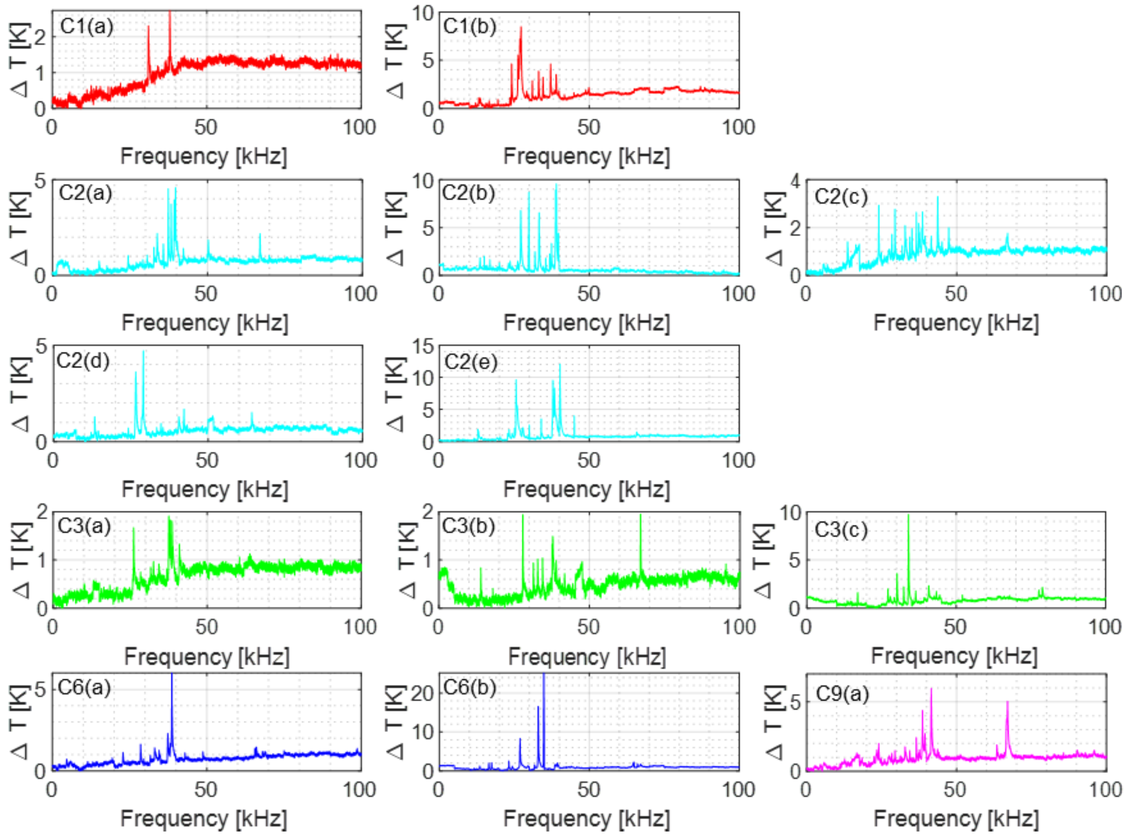

Figure 4. Thermograms: C1(a) B327; C1(b) B285; C2(a) B100; C2(b) B046; C2(c) B189; C2(d); C2(e) B221; C3(a) B259; C3(b) B115; C3 (c) B254; C6(a) VKH1084; C6(b) B286; C9(a) B189.

Some cracks also showed two positions of high heat generation. The point of maximum heat generation of all blades, L1 (Figure 5), is approximately 50% of the visual crack length, which proves that the cracks are wedge shaped and slightly open to the outside. This also means that there are plastic deformations in the areas of the cracks or erosion. Since there are mainly turbine blades with cracks in the second chamber, these were dominant for the evaluation. In addition, for blade B254 the heat generation point was located deep in the component (88% compared to the visual crack length, L).

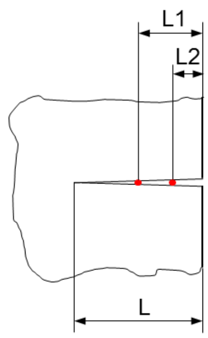

Figure 5. Positions heat generation.

Table 3 summarises the most important results of the experiments. The crack dimensions and positions (L1, L2) of the temperature generation are shown along with the highest temperature peaks with the corresponding frequencies. The number of measured peaks in the thermograms provides information about incorporating the thermographic measuring method.

Table 3. Results thermography turbine blades – summary.

Blade name	Crack chamber	Visible Crack length L [mm]	Position max. heat generation		Peak ΔT [K] [1]	Peak f [kHz] [1]	No. Peaks
			L1 [mm]	L2 [mm]			
B327	1	1.6	1.3	—	2.7	38.0	6
B285	1	4.5	3.6	2.3	8.48	27.25	22
B100	2	5.4	2.5	1.1	4.6	39.7	18
B046	2	6	1.9	—	9.6	39.0	16
B189	2	6	3.2	—	3.3	43.7	19
B154	2	6.1	4.7	1.0	4.7	29.0	11
B221	2	6.6	3.5	2.2	12.1	40.3	13
B259	3	2.4	1.1	—	1.9	37.5	11
B115	3	5.8		—	2.0	67.0	11
B254	3	6.8	6.6	2.2	9.7	34.0	14
B286	6	6.1	2.7	0.9	25.2	34.8	14
VKH1084	6	2.5	0.9	—	6.0	38.7	18
B189	9	—	2.2	1.4	5.93	41.56	16

[1] Refers to max. heat generation point L1.

The frequencies determined from the maximum temperature peaks serve as the basis for the investigations in the next section.

5. Temperature behaviour with increasing energy supply

In the previous section, the frequency was gradually increased and relevant crack resonance frequencies determined using thermography. Next, the frequencies with the highest temperature increase were kept constant for the individual blades while the energy supply to the actuator (amplitude) was gradually increased. The electrical power is defined as [53] (Equation (2)):

$$P_{el} = \frac{1}{2} C U^2 f. \tag{2}$$

Figure 6 show the temperature behaviour with slowly rising electrical energy in the piezo actuator. The frequencies with the highest temperature increase (Table 3) were selected for the individual blades and kept constant for the studies. After each measuring point, the actuator was switched off for electrical voltage readjustment. The actuator was activated for 2 seconds at each measuring point. This concept also works with frequencies with a lower temperature increase, but the frequencies with the peak temperatures offer the best possible response to even small actuator excitations.

The power display on the abscissa was shown in a standardised manner (P_{norm}) since the induced power in the actuator fluctuates depending on the excitation frequency.

The closer the friction point is to the trailing edges of the blades, the higher the relative sliding speeds and thus also the temperature. Uncertainties occur such as residual internal stresses or constraints due to the crack topography. The curves are characterised by different curve gradients. If the curve gradient is negative, saturation occurs and the temperature increase is limited, which could indicate closed cracks. With positive gradients, the temperature continues to rise and it is assumed that the crack has minimal inner constraints.

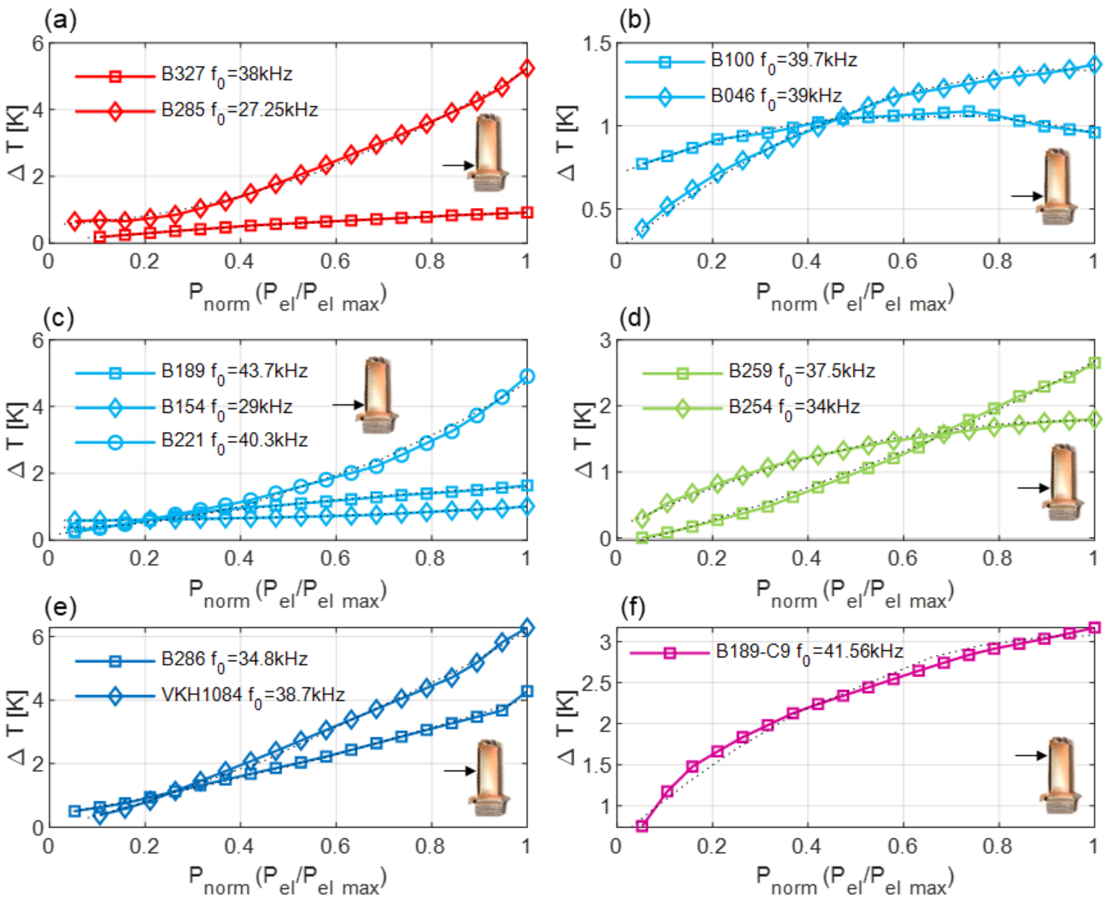

Figure 6. Heating behaviour: (a) chamber 1; (b, c) chamber 2; (d) chamber 3; (e) chamber 6; (f) chamber 9.

A quadratic fitting curve was used through the measuring points on all measurements (dotted line). It can be observed that there is a direct connection to the kinetic energy ($E_{kin} = \frac{1}{2}m\vec{v}_{sl}^2$) since the measured temperature is proportional to the relative sliding velocity ($\Delta T \propto \vec{v}_{sl}$). If excitation occurs in the resonance area of the crack, a significant part of the energy induced in the actuator was converted into crack vibration.

6. Preload

Different behaviour of the cracks were determined, where constraints from preload forces were assumed. Therefore, the influence of preloads on the cracks was examined more closely. Figure 7 shows an experimental setup to demonstrate a preload's influence on thermographic examinations. A metallic body is clamped in the test setup and was painted matte black to avoid reflections. Using additive manufacturing, a device was constructed to guide a cylindrical pin, which should lead to a heat increase on the friction surface of the device. To measure the temperatures with changed preloads, the cylinder pin is preloaded with a compression spring and grub screw. The influence of the screwed-in threaded pin on the inertia of the vibrating system is estimated to be negligible. Six different load positions were examined (0.14 N to 0.98 N).

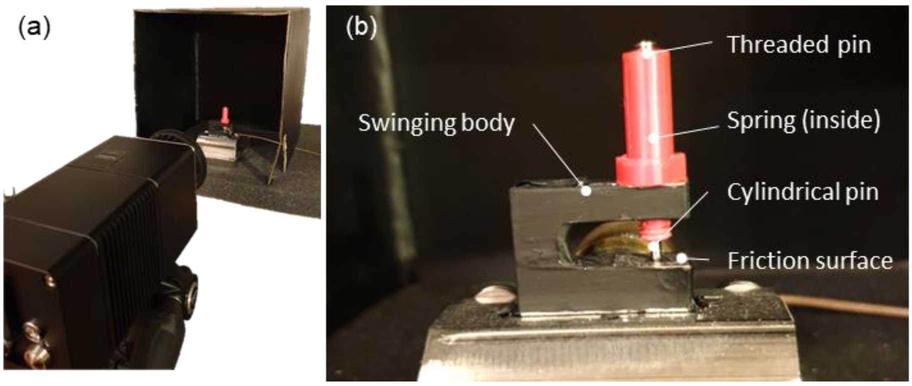

Figure 7. Influence preload: (a) experimental setup - overview; (b) experimental setup - components.

Figure 8 shows the result, where the input energy, P_{el}, was illustrated standardised. With small contact forces, a convex course appears, which becomes concave with higher forces. Quadratic behaviour occurs, as demonstrated in the other experiments. The numerical evidence and comparison are shown in Section 7.3.

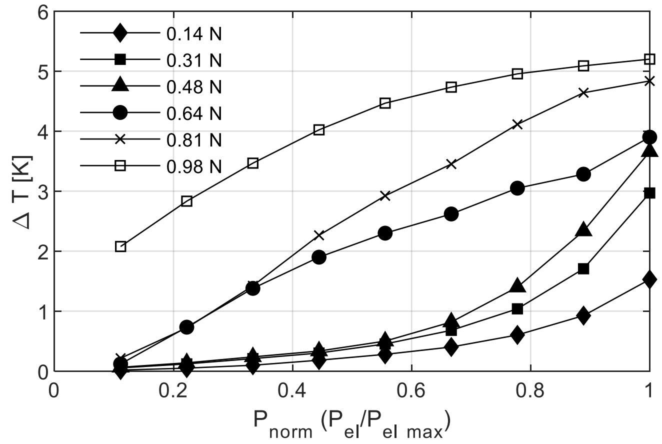

Figure 8. Experimental evidence influence preload.

7. FEM simulations

Cracks react differently to different excitation frequencies or excited wave modes. Using the finite element method (FEM), the excitation frequency could be optimised to achieve the highest temperature increase at crack locations. The different velocity vectors in the crack area were calculated and compared with the simulated temperature increases due to friction. Figure 8 experimentally showed a preload's influence on the thermographic results, which were numerically evaluated and compared.

7.1. FEM model

The blade model was geometrically simplified for the numerical thermographic simulations. To avoid influencing the thermal flow and stiffness, the FEM model's internal cooling channels were modelled. The lower surface was fixed, and the periodic excitation, equivalent to the experiments, occurs over the root area of the blade (Figure 9). This excitation is transferred to the crack model and vibrates this region. A sufficiently small time increment must be selected to correctly represent the temperature increase ($6e^{-5}$ s). With the Ansys calculation program, the 'CoupledFields' extension is required to calculate temperature increases due to friction. The thermo-mechanical contact condition was programmed via the Ansys Parametric Design Language (APDL). The crack was simulated using a frictional contact algorithm, and an initial force of 10 N was applied whereby the contact areas were lightly pressed together.

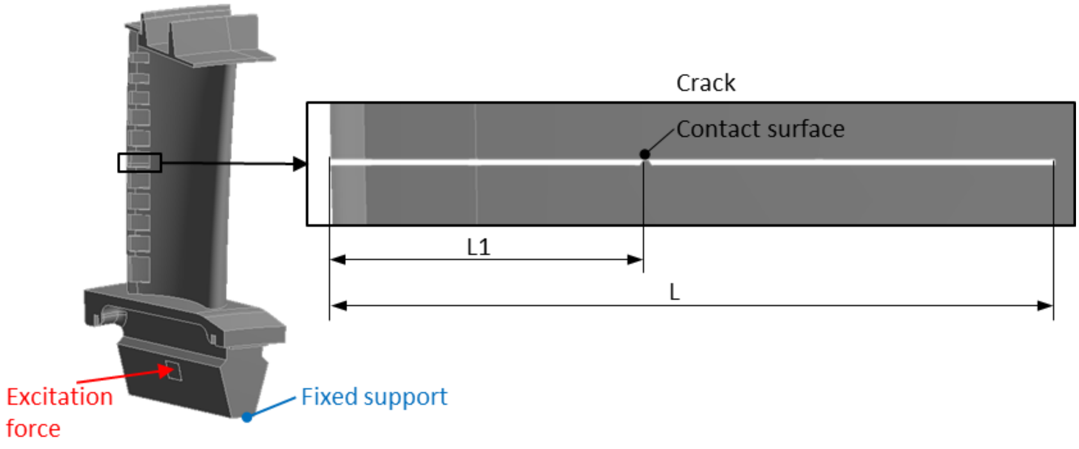

Figure 9. Thermographic FEM model.

The crack was modelled over the visual crack length, L, and the heat generation point, L1, where the temperature-increase evaluation was conducted. The surfaces to the right and left of the heat generation zone move freely and cannot overlap during vibration.

The damping of the entire system significantly influences the measured results. Many factors have influence which cannot be mapped with FEM due to the chosen system boundary. The ground below the measuring device also affects the damping. One method is to experimentally determine the attenuation for the numerical simulations. The Rayleigh damping $\boldsymbol{C} = \alpha_{D1}\boldsymbol{M} + \alpha_{D2}\boldsymbol{K}$ is used for this purpose, where α_{D1} is the proportionality constant of the mass matrix and α_{D2} the proportionality constant of the stiffness matrix. High-frequency vibrations are damped by the factor α_{D2} and low-frequency vibrations by the factor α_{D1}. If the damping ratios of two different vibrations are known (λ_{Di}), these factors can be calculated with Equation (3):

$$\alpha_{D1} = \frac{2\omega_1\omega_2}{\omega_2^2-\omega_1^2}(\lambda_{D1}\omega_2 - \lambda_{D2}\omega_{D1}),$$
$$\alpha_{D2} = \frac{2(\lambda_{D2}\omega_2-\lambda_{D1}\omega_1)}{\omega_2^2-\omega_1^2}. \quad (3)$$

The experiment was positioned on the same ground as those in the previous section. The blade was manually excited and the vibration measured using a portable laser vibrometer (Polytec Laser PDV 100). These experiments were repeated with different samples. The decay coefficient, δ, is determined by the logarithmic decrement with the measured values $\delta_i = \frac{1}{n} ln \frac{x_D(t)}{x_D(t+nT_D)}$, where n is the number of measured oscillations, t is the time, T_D are the periods and x_D are the vibration amplitudes of the decaying vibration. The value i describes the respective evaluated frequency. The damping ratio $\zeta_i = \frac{1}{\sqrt{1+(\frac{2\pi}{\delta_i})^2}}$ was then determined. The λ_D values are the values of ζ, which are given as percentages, which were used to calculate the damping factors of α_{D1} and α_{D2} for the FEM calculation (Table 4).

Table 4. Experimental determined damping values.

f_1 [Hz]	δ_1 [s^{-1}]	ζ_1 [%]	f_2 [Hz]	δ_2 [s^{-1}]	ζ_2 [%]	α_{D1}	α_{D2}
3263	7,1	0,035	6707	11,53	0,027	11,74	6,2e^{-9}

7.2. Crack dynamics

In this section, the different crack modes are shown, the velocity vectors are computed and the reaction forces of the cracks' contact surfaces are demonstrated for comparison.

If a component with an outwardly open crack is set in oscillation, different vibration modes result depending on the resonance frequency at the crack region (Figure 10). The local resonance crack modes can be exploited to generate a high temperature gradient.

The behaviour of the rubbing mode in y-direction can be compared to that of a mass-swinging pendulum (Figure 10a), where due to laws of energy conservation, the kinetic energy is equal to the potential energy. In the maximum deflection at point P1, the oscillation speed and thus also the kinetic energy are zero and the potential energy in this case is the strain energy with the maximum value $E_{pot} = E_{strain} = \frac{1}{2}VE\varepsilon^2$. When swinging back to point P2, the strain energy is zero and the kinetic energy also reaches its maximum by the maximum swinging speed $E_{kin,y} = \frac{1}{2}m\dot{y}^2$ in the y-direction. The sliding velocity at the contact point of the crack thus leads to an increase in temperature, which is important for thermographic measurements.

Figure 10b shows the shear vibration mode, where the energy behaviour is identical to the previous mode. This means that at P2 the kinetic energy reaches its maximum value ($E_{kin,x} = \frac{1}{2}m\dot{x}^2$), whereas in P1 the strain energy is maximum and the kinetic energy is zero.

The clapping mode, shown in Figure 10c, allows the crack surfaces to clap onto each other, where the maximum speed is reached before the cracks' surfaces meet ($E_{kin,z} = \frac{1}{2}m\dot{z}^2$). Real systems always involve a combination of all three modes.

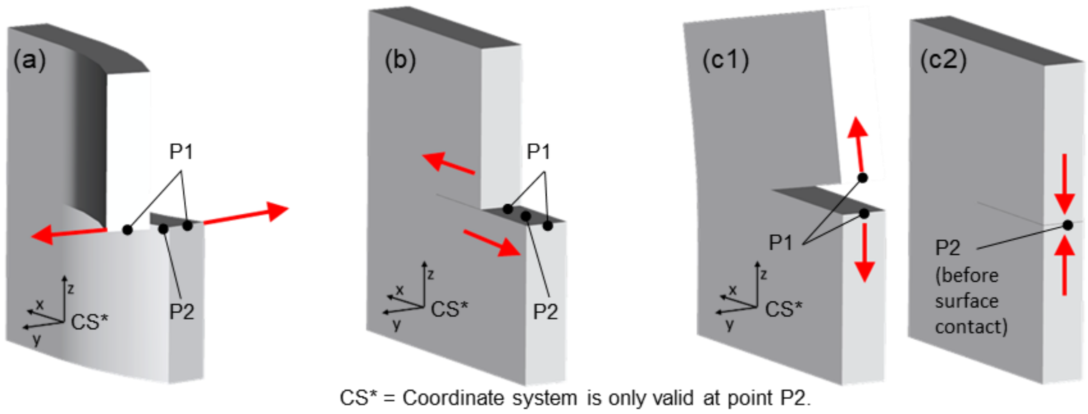

Figure 10. Crack modes: (a) rubbing mode y-direction; (b) rubbing mode x-direction; (c) clapping mode z-direction.

The FEM investigations were conducted similarly to the experiments in the frequency range from 0 to 100 kHz (Section 4). The simulation results showed the behaviour of the various vibrating crack modes (Figure 10). Figure 11a and Figure 11b show the velocity vectors and relative temperature increase due to friction for the exemplary B286 blade. The two temperature peaks (Figure 11c) occur at the points where the lateral velocity vectors have a maximum and the relative displacement creates a surface pressure at the crack location (Figure 11b). It was shown that the rubbing mode in y-direction (Figure 10a) causes a large increase in measured temperatures.

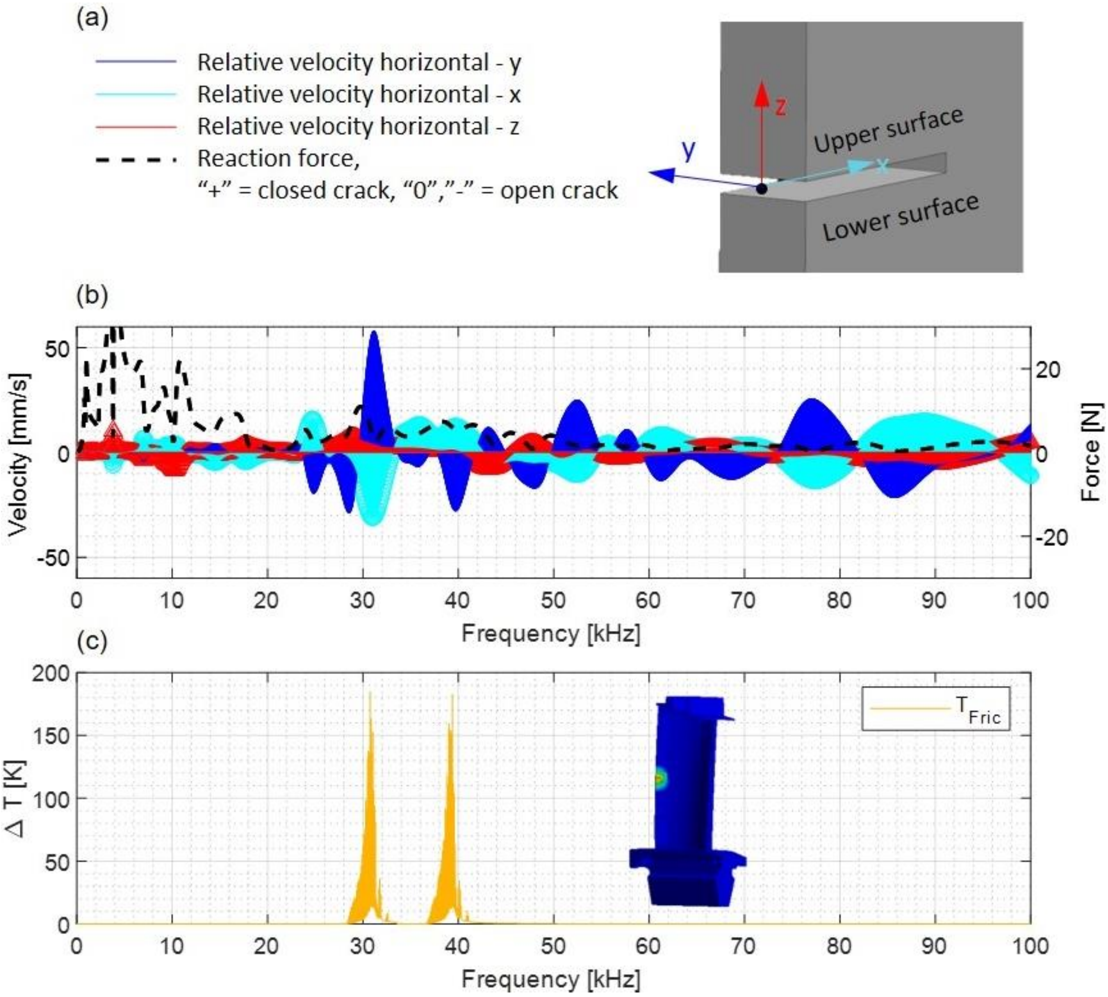

Figure 11. Results FEA: (a) legend; (b) crack velocity vectors and reaction forces; (c) frictional temperature.

7.3. Influence preload

A preload's influence on a crack during the thermographic experiments was examined for blade model shown in the previous section. The highest relative sliding velocity was determined at a frequency of 31.1 kHz (Figure 11b). Figure 12 shows the maximum temperature increase of the friction surface for the various contact loads from 10 N to 200 N. The preload was integrated into the surface normal of the upper contact surface of the model. The periodic sinusoidal excitation with a maximum amplitude of 1000 N was introduced into the test object to simulate the functionality of the piezo actuator.

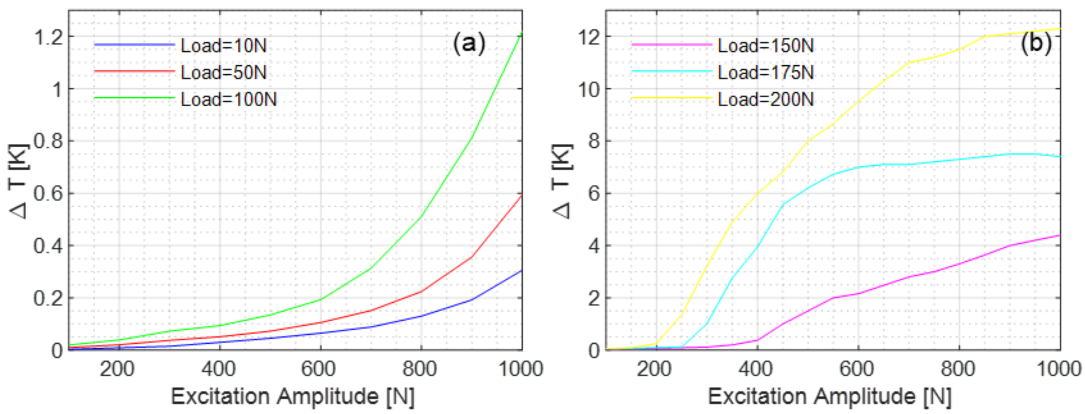

Figure 12. Study preload: (a) load = 10 N to 100 N; (b) load = 150 N to 200 N.

Figure 12a showed quadratic behaviour of the curves at forces from 10 N to 100 N, where if the load increases, the curve progressively reverses and becomes concave (Figure 12b). This confirms the previous assumption that the concave course of the curve evidences the presence of constraints due to vertical loads.

Figure 13 shows the qualitative comparison of the experimental data (Figure 8) and numerically determined data (Figure 12) for sequentially increased loads denoted by the increasing number of '+' signs.

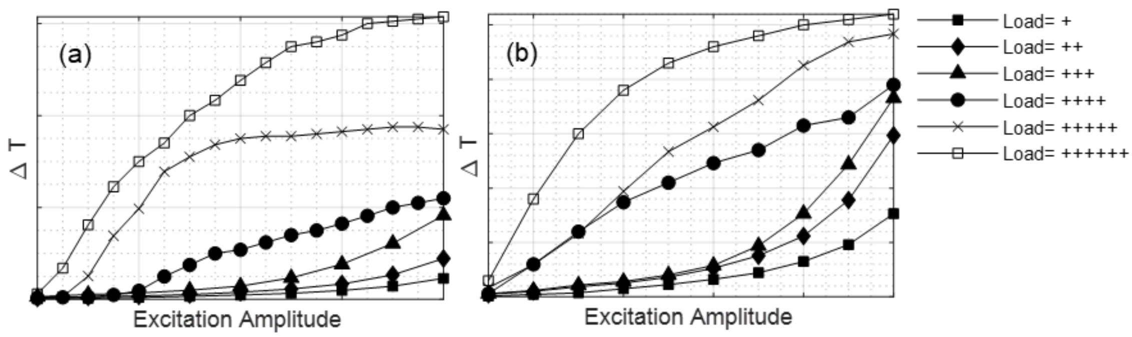

Figure 13. Comparison normalised preload study: (a) numerical analysis; (b) experimental results.

The verification of experiments and numerical calculations allow statements about possible preloads in cracks.

8. Conclusion

This paper proposes an ultrasonic stimulated thermal wave imaging system for crack detection in turbine blades. The presented method allows determining the presence of preloads on the crack surface as well as local plastic deformation. It was shown that the temperature increase as a function of the introduced actuator energy changes from concave to convex with higher preloads in the crack areas. This was demonstrated by the development of finite element models able to reproduce results.

Turbine blades with real cracks on the trailing edges and in unknown locations under the ceramic TBC were investigated. The experimental results supported by finite element modelling results showed that the acquired thermograms provide crack detection and allow to provide information about the crack characteristic.

The presented procedure enables quick and accurate nondestructive investigation of turbine blades or other hot gas-leading components of gas turbines, leading to significant cost saving and safer operations.

Acknowledgement

The authors kindly acknowledge the financial support provided by the European Commission through the project TurboSens, grant agreement no. EFRE-0801016. In addition, thanks to the MAN Energy Solutions SE for their support.

References

1. Mevissen, F., & Meo, M. (2019). A Review of NDT/Structural Health Monitoring Techniques for Hot Gas Components in Gas Turbines. *Sensors, 19*(3), 711.
2. Maldague, X. P. (1993). *Nondestructive Evaluation of Materials by Infrared Thermography*. (1st edn). London: Springer London.
3. Ibarra-Castanedo, C., Tarpani, J. R., & Maldague, X. P. V. (2013). Nondestructive testing with thermography. *Eur. J. Phys., 34*(6), S91-S109.
4. Ciampa, F., Mahmoodi, P., Pinto, F., & Meo, M. (2018). Recent Advances in Active Infrared Thermography for Non-Destructive Testing of Aerospace Components. *Sensors, 18*(2), 609.
5. Rahammer, M., Solodov, I., Bisle, W., Scherling, D., & Kreutzbruck, M. (2016). Thermosonic Testing with Phase Matched Guided Wave Excitation. *J. Nondestruct. Eval., 35*(3), 154.
6. Renshaw, J., Chen, J. C., Holland, S. D., & Bruce Thompson, R. (2011). The sources of heat generation in vibrothermography. *NDT E Int., 44*(8), 736–739.
7. Renshaw, J., Holland, S. D., & Barnard, D. J. (2009). Viscous material-filled synthetic defects for vibrothermography. *NDT E Int., 42*(8), 753–756.
8. Solodov, I., Derusova, D., & Rahammer, M. (2015). Thermosonic Chladni figures for defect-selective imaging. *Ultrasonics, 60*, 1–5.
9. Gao, C., Mayton, D., Meeker, W. Q., Thompson, D. O., & Chimenti, D. E. (2007). Detecting cracks in fan blades using sonic IR. In *Review of Progress in Quantitative Nondestructive Evaluation: 34th Annual Review of Progress in Quantitative Nondestructive Evaluation, Golden, Colorado, USA, 22–27 July 2007*. (pp. 1708–1715): AIP.
10. Obeidat, O., Yu, Q., & Han, X. (2016). Developing Algorithms to Improve Defect Extraction and Suppressing Undesired Heat Patterns in Sonic IR Images. *Sensing and Imaging, 17*(1), 2418.
11. Obeidat, O., Yu, Q., & Han, X. Develop algorithms to improve detectability of defects in Sonic IR imaging NDE. In *Review of Progress in Quantitative Nondestructive Evaluation*. (p. 100009).

12. Obeidat, O., Yu, Q., & Han, X. Further development of image processing algorithms to improve detectability of defects in Sonic IR NDE. In *43rd annual Review of Progress in Quantitative Nondestructive Evaluation*. (Vol. 36, p. 100007).

13. Lu, J., Han, X., Newaz, G., Favro, L. D., & Thomas, R. L. (2007). Study of the effect of crack closure in Sonic Infrared Imaging. *Nondestruct. Test. Evaluation, 22*(2-3), 127–135.

14. Morbidini, M. (2007). *A comparison of the vibration-modulation and thermosonic*. Ph.D Thesis. Imperial College London, London, UK.

15. Morbidini, M., & Cawley, P. (2008). The Reliable Implementation of Thermosonics NDT. In *17th World Conference on Nondestructive Testing, Shanghai, China, 25-28 October 2008*. (1st ed., 536, Vol. 975): AIP Conference Proceedings.

16. Morbidini, M., & Cawley, P. (2009). The detectability of cracks using sonic IR. *J. Appl. Phys., 105*(9), 93530.

17. Rothenfusser, M. (2004). Acoustic Thermography: Vibrational Modes of Cracks and the Mechanism of Heat Generation. In *Review of Progress in Quantitative Nondestructive Evaluation, Golden, Colorado, USA, 25-30 July 2004*. (pp. 624–631): AIP.

18. Mendioroz, A., Celorrio, R., & Salazar, A. (2017). Ultrasound excited thermography: an efficient tool for the characterization of vertical cracks. *Meas. Sci. Technol., 28*(11), 112001.

19. Guo, X., & Vavilov, V. (2013). Crack detection in aluminum parts by using ultrasound-excited infrared thermography. *Infrared Phys. Technol., 61*, 149–156.

20. Weekes, B., Cawley, P., Almond, D. P., Thompson, D. O., & Chimenti, D. E. The Effects of Crack Opening and Coatings on the Detection Capability of Thermosonics. In *Review of Progress in Quantitative Nondestructive Evaluation*. (30ab, pp. 399–406).

21. Zhang, D., Han, X., Newaz, G., Favro, L. D., & Thomas, R. L. (2013). Improvements on FEA with a two-step simulation of experimental procedures in turbine blade crack detection in sonic IR NDE. *AIP Conference Proceedings, 1511*, 518.

22. Zhang, D., Han, X., Newaz, G., Favro, L. D., & Thomas, R. L. (2012). Modeling turbine blade crack detection in sonic IR imaging with a method of creating flat crack surface in finite element analysis. *AIP Conference Proceedings, 1430*, 527.

23. Zhang, D., Han, X., & Newaz, G. Sonic IR crack detection of aircraft turbine engine blades with multi-frequency ultrasound excitations. In *Review of Progress in Quantitative Nondestructive Evaluation*. (pp. 1644–1651).

24. Zhang, D. (2014). *Study of Chaotic Ultrasound and Frequency Sweep Excitations in Sonic IR NDE Technology*. Ph.D. Thesis. Wayne State University, Detroit, MI, USA.

25. Zalameda, J. N., Winfree, W. P., Yost, W. T., Thompson, D. O., & Chimenti, D. E. (2007). Air coupled acoustic thermography (acat) inspection technique. In *Review of Progress in Quantitative Nondestructive Evaluation, Golden, Colorado, USA, 22–27 July 2007*. (pp. 467–474): AIP.

26. Solodov, I., Rahammer, M., Gulnizkij, N., & Kreutzbruck, M. (2016). Noncontact Sonic NDE and Defect Imaging Via Local Defect Resonance. *J. Nondestruct. Eval., 35*(3), 1–8.

27. Kang, B., Cawley, P., Thompson, D. O., & Chimenti, D. E. (2007). Multi-Mode Excitation System for Thermosonic Testing of Turbine Blades. In *Review of progress in quantitative Nondestructive Evaluation, Golden, Colorado, USA, 22–27 July 2007*. (pp. 520–527): AIP.

28. Holland, S. D. (2007). First Measurements from a New Broadband Vibrothermography Measurement System. In *Review of Progress in Quantitative Nondestructive Evaluation, Portland, Oregon, USA, 30 July–4 August 2007*. (pp. 478–483): AIP.

29. Pieczonka, L., Aymerich, F., Brozek, G., Szwedo, M., Staszewski, W. J., & Uhl, T. (2013). Modelling and numerical simulations of vibrothermography for impact damage detection in composites structures. *Struct. Control Health Monit., 20*(4), 626–638.

30. Polimeno, U., Almond, D. P., Weekes, B., & Chen, E. (2014). A compact thermosonic inspection system for the inspection of composites. *Composites Part B: Engineering, 59*, 67–73.

31. Homma, C. (2000). Study of the Heat Generation Mechanism in Acoustic Thermography. In *Quantitative Nondestructive Evaluation, Brunswick, Maine, USA, 31 July-5 August 2000*. (pp. 566–573): AIP.

32. Chen, J. C., Kephart, J., Lick, K., & Riddell, W. T. (2007). Crack growth induced by sonic IR inspection. *Nondestruct. Test. Evaluation, 22*(2-3), 83–92.

33. Feng, F., Zhang, C., Min, Q., Zhu, J., Wang, W., & Chao, X. (2017). Heating characterization of the thickness-through fatigue crack in metal plate using sonic IR imaging. *NDT E Int., 87*, 38–43.

34. Han, X., Favro, L. D., & Thomas, R. L. (2011). Sonic IR Imaging of delaminations and disbonds in composites. *J. Phys. D Appl. Phys., 44*(3), 34013.

35. Han, X., & Song, Y. Study the effect of engagement force of ultrasound transducer on crack detectability in sonic IR imaging. In *Review of progess in quantitative Nondestructive Evaluation*. (Vol. 32, pp. 532–538).

36. Lick, K. E., Wong, C. H., & Chen, J. C. (2000). Determination of the Minimum Energy Required for Sonic-IR Detection. In *Review of progress in quantitative Nondestructive Evaluation, Portland, Oregon, USA, 30 July-4 August 2000*. (pp. 515–522): AIP.

37. Riddell, W. T., Chen, J. C., & Wong, C.-H. (2013). Effect of Fatigue Precracking on Crack Engagement during Sonic IR Testing. *Research in Nondestructive Evaluation, 24*(1), 18–34.

38. Zhang, C., Feng, F., Min, Q., & Zhu, J. (2015). Effect of engagement force on vibration characteristics and frictional heating in sonic IR imaging. *NDT E Int., 76*, 52–60.

39. Zhang, D., Han, X., & Newaz, G. (2014). Sonic IR crack detection of aircraft turbine engine blades with multi-frequency ultrasound excitations. *AIP Conference Proceedings, 1581*, 1644.

40. Chaki, S., Marical, P., Panier, S., Bourse, G., & Mouftiez, A. (2011). Interfacial defects detection in plasma-sprayed ceramic coating components using two stimulated infrared thermography techniques. *NDT E Int., 44*(6), 519–522.

41. Malfense Fierro, G. P., Ginzburg, D., Ciampa, F., & Meo, M. (2017). Imaging of Barely Visible Impact Damage on a Complex Composite Stiffened Panel Using a Nonlinear Ultrasound Stimulated Thermography Approach. *J. Nondestruct. Eval., 36*(4), 249.

42. Han, X. (2003). Frequency dependence of the thermosonic effect. *Review of Scientific Instruments, 74*(1), 414–416.

43. Han, X., Zeng, Z., Li, W., Islam, M. S., Lu, J., Loggins, V., et al. (2004). Acoustic chaos for enhanced detectability of cracks by sonic infrared imaging. *J. Appl. Phys., 95*(7), 3792–3797.

44. Barden, T. J., Almond, D. P., Pickering, S. G., Morbidini, M., & Cawley, P. (2007). Detection of impact damage in CFRP composites by thermosonics. *Nondestruct. Test. Evaluation, 22*(2-3), 71–82.

45. Kang B.B., Cho Y.H.,Baeg N.U., Na H.S. (2011). Characteristics of the Vibration Generated by Different Excitation Methods During Thermosonic Non-destructive Testing. In *9th world congress railway research 2011, Lille, France, 22-26 May*.

46. Han, X. (2004). Importance of Acoustic Chaos in Sonic IR Imaging NDE. In *Quantivative Nondestructive Evaluation*. (Vol. 700, pp. 496–500): AIP.

47. Riahi, M., Dehestani, P., & Valipour, A. (2016). Using finite element to estimate vibration energy loss by cracks in thermosonic phenomenon under chaotic and non-chaotic vibrations. *J. Vib. Control, 22*(2), 457–467.

48. Abu-Nabah, B. A., & Al-Said, S. A. M. (2018). Sonic IR crack size estimation using 2D heat diffusion model with arbitrary heat source function along the crack. *Quant. Infrared Thermogr. J., 1*, 1–20.

49. Derusova, D. A., Vavilov, V. P., & Pawar, S. S. (2015). Evaluation of equivalent defect heat generation in carbon epoxy composite under powerful ultrasonic stimulation by using infrared thermography. *IOP Conf. Ser: Mater. Sci. Eng., 81*, 12084.

50. Parvasi, S. M., Xu, C., Kong, Q., & Song, G. (2016). Detection of multiple thin surface cracks using vibrothermography with low-power piezoceramic-based ultrasonic actuator—a numerical study with experimental verification. *Smart Mater. Struct., 25*(5), 55042.

51. Favro, L. D., Thomas, R. L., Han, X., Ouyang, Z., Newaz, G., & Gentile, D. (2001). Sonic infrared imaging of fatigue cracks. *Int. J. Fatigue*, *23*, 471–476.

52. Dyrwal, A., Meo, M., & Ciampa, F. (2018). Nonlinear air-coupled thermosonics for fatigue micro-damage detection and localisation. *NDT E Int.*, *97*(3), 59–67.

53. Piezosytem Jena. Piezoline. https://www.piezosystem.de/fileadmin/redakteure/bilder/Sonstige/Piezofibel/Piezoline-piezosystem-jena.pdf. Accessed 27 October 2018.

8 CONCLUSIONS AND RECOMMENDATIONS FOR FUTURE WORK

The aim of this research work is to develop new techniques for the early and sensitive detection of failures in gas turbine components with a high degree of accuracy. This chapter summarises the findings on nonlinear ultrasound and vibrothermographic techniques.

8.1 Nonlinear Ultrasound

This chapter highlights the techniques developed for damage detection in materials with novel nonlinear frequency modulation methods. According to the literature, using frequency modulation offers advantages in the detection of defects in materials (Chapter 2.2.2). So far, the nonlinearity parameters of the second-harmonic ($2f$) and third-harmonic ($3f$) frequencies were used for evaluation, along with sums and differential sidebands ($f_2 \pm f_1$) for frequency modulation. However, an analytical holistic view of frequency modulation with two transmitted frequencies up to the third order of nonlinearity was missing. Therefore, the nonlinearity parameters of the frequencies $f_{1,2}$, $2f_{1,2}$, $3f_{1,2}$, $f_2 \pm f_1$, $2f_1 \pm f_2$ and $2f_2 \pm f_1$ were analytically derived together. These frequencies were clearly detectable in the frequency spectrum during the experiments. The wave propagation and generation of the derived nonlinearities were also verified in the numerical simulations. A total of 12 nonlinearity parameters were used to detect cracks, allowing the prediction of the sizes of the defects. Overall, the work presented in Chapter 4 forms the basis for further consideration of nonlinear phenomena and their use in identifying defects in materials.

Frequency modulation was found to have clear advantages compared to single-frequency excitation, whereby the question was whether a further increase in the number of fundamental frequencies can bring about some advantages. Therefore, the analytical model discussed above was extended to four sent frequencies and resulted in 64 fundamental, harmonic and modulated response frequencies (Table 1), and their existence was proven experimentally (Chapter 5).

Table 1. Nonlinearity parameters of quadruple excitation.

Frequencies					
Fundamental frequencies	2nd harmonic frequencies	3rd harmonic frequencies	2f sidebands	2nd harmonic sidebands	3f sidebands
f_n [1]	$2f_n$ [1]	$3f_n$ [1]	$f_n \pm f_m$ [1,2]	$2f_n \pm f_m$ [1,3]	$f_n + f_m \pm f_p$ [1,3]

[1] $n, m, p \in \{1, 2, 3, 4\}$.
[2] $n > m$.
[3] $n \neq m \neq p$.

If the fundamental frequencies are systematically defined in advance, then several harmonic and sideband frequencies will superimpose at certain frequencies. For this purpose, groups were used, which consist of up to four fundamental frequencies, harmonic frequencies and sidebands. Because of the increased signal energy introduced at these particular frequencies, it was possible to predict cracks and estimate their sizes. The proposed technique, called the grouping technique, was compared to other excitation methods in this study. Excitation was performed with one fundamental frequency, with two fundamental frequencies (constant and linearly increasing) and with four fundamental frequencies. Two-frequency excitation already demonstrated clear advantages over waves with only one fundamental frequency. With quadruple excitation combined with the grouping concept, precise predictions regarding crack sizes were possible.

Crack detection was successfully resolved in Chapters 4 and 5. However, if a crack has already formed, then there is a high risk that component breakage will endanger the operation of the entire gas turbine. In many cases, a crack is signalled by the initiation of plastic deformation, which may be due to TMF, LCF or FOD. The topic of plastic deformation also includes component damage due to creep, which was discussed in detail in Chapter 6. Creep samples made of Hastelloy X material were investigated, which is often used in the hot-gas area of gas turbines because of its advantageous physical properties. The samples were subjected to high temperatures and mechanical loads for 3200 to 5850 hours. One sample was welded to draw conclusions regarding the creep behaviour of the weld seam. During the metallurgical examinations of the samples, there was already increased pore formation, starting from the edge area of the samples, which continued to decrease towards the inside. The weld seam, however, demonstrated no difference compared to the rest of the material. Pore formation was evaluated precisely, and parameters such as the damage sizes, damage densities and the occupied damage area were evaluated. Scanning electron microscopy was used to clearly identify the creep damage, and EDX analysis was used to determine the precipitation elements, which showed that molybdenum was mainly precipitated inside the component. A different picture, however, emerged in the edge area, because this is where chromium was primarily precipitated. The chromium particles diffused into the outside area, where they oxidised to form a Cr_2O_3 layer when combined with oxygen. A further layer of iron-nickel oxide was also detected on the chromium oxide layer. This chromium diffusion led to its depletion in the edge area, hence supporting the formation of intergranular pores and microcracks. Given the promising results obtained in Chapters 4, ultrasonic dual frequencies were sent to the samples using identical technology. Creep samples were examined in an area grid, and the known nonlinearity parameters were evaluated. In comparison to the reference sample, the creep damage and the increased pore concentration were clearly detectable. Compared to the metallurgical results, the harmonic frequencies showed an increased sensitivity to the damage sizes of the pores and the summing sidebands ($f_2 + f_1$, $2f_1 + f_2$ and $2f_2 + f_1$) showed a good agreement with the damage density. Overall, the knowledge gained in this study can help better understand the behaviour of materials and increase their service life by using appropriate measurements for components and modifying their design, such as by applying a protective coating.

8.2 Vibrothermography

To detect closed cracks, turbine blades were examined using ultrasonically stimulated thermography (Chapter 7). Cracks were found to form on the trailing edges of the turbine blades in various positions during the operation of the gas turbines. To avoid the known disadvantages of direct excitation on the components and the difficult transfer of energy with contactless excitation techniques, a sample holder with passive excitation was designed. Excitation was then performed using a piezo actuator, which was screwed directly onto the sample holder. On this device, the turbine blades were clamped with the blade roots, similar to the installation of a turbine disc in gas turbines. As a result, the coating on the blade airfoil was protected during the measurements. In the first step, the blades were excited with the actuator from 0 to 100 kHz. The temperature increases of the individual blades were then determined as a function of the excitation frequency. Moreover, a previously unknown crack was detected, which was below the TBC in the base material. Frequencies with the highest increases in temperature were kept constant in the next step, and the voltage supply to the actuator was slowly increased. This allowed evaluations with the measured temperature increase as a function of the electrical energy input into the actuator. The course of the curves showed whether the cracks were closed or whether they were prevented from vibrating by internal constraints, such as preloads. Therefore, a squared curve behaviour and, thus, a comparison to the kinetic energy of the vibration of the crack were discussed. Moreover, the behaviour of possible preloads in the crack was investigated with a new experimental setup. It was thus possible to demonstrate that the curve progression, $\Delta T = f(P_{el})$, changes from convex to concave with increased preloads in the crack area. Different vibration modes (rubbing, clapping) were examined in a newly developed finite element model. The simulated temperature increase confirmed the preload theory in the crack area.

8.3 Summary of Contributions

The major contributions of this research work are summarised below.

Nonlinear ultrasound:

- The first holistic derivation of frequency modulation from two fundamental frequencies up to the third order of nonlinearity
- An analytical derivation of quadruple excitation and the development of the grouping concept for the efficient detection of cracks

- A new metallurgical understanding of the creep behaviour of the Hastelloy X material with different precipitated elements, depending on the evaluated position on the sample
- A clear identification of creep damage by means of ultrasound, with conclusions regarding the metallurgical outcomes

Ultrasonically stimulated thermography:

- The design of a new component-friendly sample holder with passive actuator excitation
- The measurement of temperature increase as a function of the frequency and energy input into the actuator to identify cracks
- A proof of preloads between the crack surfaces with the curve behaviour, $\Delta T = f(P_{el})$, allowing new conclusions regarding the possible plastic deformation in the crack area
- The development of a finite element model for the simulation and verification of temperature increases in the crack area

8.4 Future Work

Overall, the studies presented herein on the detection of creep and cracks on turbine blades show promising results. Nonetheless, these proposed techniques should be examined more closely to reach a better understanding of their capabilities and limitations.

The failure detection technologies presented in Chapter 3 offer many promising possibilities for modern NDT&E and SHM systems. For example, tip timing techniques have been used successfully for many years in gas turbines for failure identification. Moreover, continuously monitoring the temperature of highly stressed components is very promising. The decisive factor here is the further development of smaller, more cost-effective sensors that can be used in-situ in the hot-gas area of gas turbines.

Most of the ultrasound techniques were presented as NDT&E variants. The algorithms developed for failure identification in this work can also be used as an SHM system for component monitoring while the gas turbines are in operation. Moreover, additive manufacturing processes allow equipping even complex-shaped components, such as turbine blades, with appropriate sensors. Contactless sensors, such as ACTs, have also been found to have favourable potential in this application. The greatest challenge here is to develop reliable and inexpensive piezo elements for use in the high temperature range. Promising research was presented in the overview of the literature in Chapter 2. In this work, algorithms for failure detection were derived, which can also be applied on a larger scale to machine learning algorithms to derive lifetime conclusions regarding certain gas turbine components.

The algorithms developed for crack detection using nonlinear frequency modulation were derived in Chapters 4 and 5 and verified numerically and experimentally. In general, it can be useful to extend these studies and test the algorithms on samples with various crack sizes to obtain a more precise understanding of the accuracy of the measurements. Investigation of microcracks with different sizes with the corresponding damage tolerance can also lead to new insights.

In Chapters 4 and 5, the algorithms were primarily examined on specimens with artificial defects and on turbine blades with trailing edge cracks. However, it can also be useful to investigate this on other turbine blade variants with defects at different positions. Besides turbine blades, this method can be adapted to and tested on other hot-gas-leading components of gas turbines.

Overall, the behaviour of creep in materials is very complex and is still not fully understood. The samples examined in this work were loaded in the laboratory with a high technical effort. This can be compared to the samples used in a gas turbine, since the atmosphere is aggressive because of the hot gas flow behind the combustion chambers.

In the case of ultrasonically stimulated thermography, the experimental setup can be further automated for planned commercial use. However, it is worth noting that the generation of frictional heat through crack excitation is still not entirely clear. For a more precise simulation, the finite element model can be improved with a more detailed crack design.

Overall, the CAN technology presented in Chapter 2.2.1 can be extended with the experimental setup shown in Chapter 7. The piezo actuator demonstrably set the crack to vibrate, whereby the crack dynamics can be examined using nonlinear ultrasound instead of a thermal imaging camera.

9 REFERENCES

1. Jansohn, P. (2013). *Modern gas turbine systems: High efficiency, low emission, fuel flexible power generation*. (Woodhead Publishing series in energy, no. 20). Cambridge, UK: Woodhead Publishing.

2. Pallos, K. J. (2001). *GER-3957B - Gas Turbine Repair Technology.* Atlanta, GA, USA: GE Energy Services Technology.

3. Meher-Homji, C. B. (1995). Blading Vibration and Failures in Gas Turbines: Part A — Blading Dynamics and the Operating Environment. In *ASME 1995 International Gas Turbine 1995, Houston, TX, USA, 5 June 1995*. (Vol. 4, p. V004T11A014). New York, NY, USA: American Society of Mechanical Engineers.

4. Jaw, L. C., Wu, D. N., & Bryg, D. J. (2001). Tracking and Control of Gas Turbine Engine Component Damage/Life. In *RTO AVT Symposium, Manchester, UK, 8-11 October 2001*. (RTO-MP-079(I)).

5. Geisheimer, J. L., Kwapisz, D., Holst, T., & Hafner, M. (2013). Blade Tip Clearance Sensors for Use in Engine Health Monitoring Applications. *SAE Int. J. Aerosp., 6*(2), 417–423.

6. Lemieux, D. H. (2003). On-Line Thermal Barrier Coating Monitoring for Real-Time Failure Protection and Life Maximization. Orlando, FL, USA: Siemens Westinghouse Power Corporation.

7. Bison, P. G., Cernuschi, F., & Grinzato, E. (2006). Ageing evaluation of thermal barrier coating: Comparison between pulsed thermography and thermal wave interferometry. *Quant. Infrared Thermogr. J., 3*(2), 169–181.

8. Bison, P., Cernuschi, F., & Grinzato, E. (2008). In-depth and In-plane Thermal Diffusivity Measurements of Thermal Barrier Coatings by IR Camera: Evaluation of Ageing. *Int. J. Thermophys., 29*(6), 2149–2161.

9. Sun, J. G., & Tao, N. (2016). Thermal property measurement for thermal barrier coatings using pulsed thermal imaging – multilayer analysis method, *1706*, 100004.

10. Kimura, M., Ando, A., Maurya, D., & Priya, S. (2017). *Advanced Piezoelectric Materials: Chapter 2 - Lead Zirconate Titanate-Based Piezoceramics*: Woodhead Publishing.

11. Amini, M. H., Sinclair, A. N., & Coyle, T. W. (2015). High Temperature Ultrasonic Transducer for Real-time Inspection. *Phys. Procedia, 70*, 343–347.

12. Kažys, R., Voleišis, A., & Voleišienė, B. (2008). High temperature ultrasonic transducers. *Ultragarsas, 63*(2), 7–17.

13. Searfass, C. T., & Tittmann, B. R. (2010). High temperature ultrasonic transducer up to 1000 °C using lithium niobate single crystal. *Appl. Phys. Lett., 97*(23), 232901.

14. Zhang, C., Feng, F., Min, Q., & Zhu, J. (2015). Effect of engagement force on vibration characteristics and frictional heating in sonic IR imaging. *NDT E Int., 76*, 52–60.

15. Homma, C. (2000). Study of the Heat Generation Mechanism in Acoustic Thermography. In *Quantitative Nondestructive Evaluation, Brunswick, Maine, USA, 31 July-5 August 2000*. (pp. 566–573): AIP.

16. Feng, F., Zhang, C., Min, Q., Zhu, J., Wang, W., & Chao, X. (2017). Heating characterization of the thickness-through fatigue crack in metal plate using sonic IR imaging. *NDT E Int., 87*, 38–43.

17. Barden, T. J., Almond, D. P., Pickering, S. G., Morbidini, M., & Cawley, P. (2007). Detection of impact damage in CFRP composites by thermosonics. *Nondestruct. Test. Evaluation, 22*(2-3), 71–82.

18. Dyrwal, A., Meo, M., & Ciampa, F. (2018). Nonlinear air-coupled thermosonics for fatigue micro-damage detection and localisation. *NDT E Int., 97*(3), 59–67.19.

19. Achenbach, J. D., Lin, W., & Keer, L. M. (1986). Mathematical modelling of ultrasonic wave scattering by sub-surface cracks. *Ultrasonics, 24*(4), 207–215.

20. Angel, Y. C., & Achenbach, J. D. (1983). Reflection and transmission of obliquely incident Rayleigh waves by a surface-breaking crack. *Acoust. Soc. Am., 75*(2), 313-319.

21. Krautkramer, H., Schlengermann, U., Niklas, L., Bobbin, J., Zenzinger, B., Krautkramer, J., et al. (2013). *Ultrasonic Testing of Materials*: Springer.

22. Li, Z. L., & Achenbach, J. D. (1991). Reflection and Transmission of Rayleigh Surface Waves by a Material Interphase. *J. Appl. Mech., 58*(3), 688.

23. Jhang, K.-Y. (2009). Nonlinear ultrasonic techniques for nondestructive assessment of micro damage in material: A review. *Int. J. Precis. Eng. Manuf., 10*(1), 123–135.

24. Felice, M. V., & Fan, Z. (2018). Sizing of flaws using ultrasonic bulk wave testing: A review. *Ultrasonics, 88*, 26–42.

25. Blitz, J. (1996). *Ultrasonic methods of non-destructive testing.* London: Chapman & Hall.

26. Ensminger, D. (2012). *Ultrasonics: Fundamentals, Technologies, and Applications*. (3rd edn). Boca Raton, USA: CRC Press.

27. Cho, H., & Lissenden, C. J. (2012). Structural health monitoring of fatigue crack growth in plate structures with ultrasonic guided waves. *Struct. Health Monit., 11*(4), 393–404.

28. Chan, H., Masserey, B., & Fromme, P. (2015). High frequency guided ultrasonic waves for hidden fatigue crack growth monitoring in multi-layer model aerospace structures. *Smart Mater. Struct., 24*(2), 25037.

29. Masserey, B., & Fromme, P. (2017). Analysis of high frequency guided wave scattering at a fastener hole with a view to fatigue crack detection. *Ultrasonics, 76*, 78–86.

30. Masserey, B., & Fromme, P. (2015). In-situ monitoring of fatigue crack growth using high frequency guided waves. *NDT E Int., 71*, 1–7.

31. Masserey, B., & Fromme, P. Noncontact monitoring of fatigue crack growth using high frequency guided waves. In *SPIE 9061, Sensors and Smart Structures Technologies for Civil, Mechanical, and Aerospace Systems 2014.* San Diego, California, USA.

32. Masserey, B., & Fromme, P. (2013). Fatigue crack growth monitoring using high-frequency guided waves. *Struct. Health Monit., 12*(5-6), 484–493.

33. Mitra, M., & Gopalakrishnan, S. (2016). Guided wave based structural health monitoring: A review. *Smart Mater. Struct., 25*(5), 53001.

34. Vanlanduit, S., Guillaume, P., & van der Linden, G. (2003). On-line monitoring of fatigue cracks using ultrasonic surface waves. *NDT E Int., 36*(8), 601–607.

35. Mukhopadhyay, S. C. (2011). *New Developments and Applications in Sensing Technology*. (1st edn, Vol. 83). Berlin / Heidelberg, Germany: Springer.

36. Masserey, B., Aebi, L., & Mazza, E. (2006). Ultrasonic surface crack characterization on complex geometries using surface waves. *Ultrasonics*, *44 (Suppl. 1)*, e957–e961.

37. Lin, B., Zhang, L., Dorantes, D., Li, Y., Fu, X., & Hu, X. (2011). Numerical simulation of surface acoustic wave and detection of surface crack in steel. *Trans. Tianjin Univ., 17*(4), 254–258.

38. Cheeke, J. D. N. (2002). *Fundamentals and applications of ultrasonic waves*. (CRC series in pure and applied physics). Boca Raton, FL, USA: CRC Press.

39. Giurgiutiu, V. (2014). *Structural health monitoring with piezoelectric wafer active sensors.* Oxford, UK: Elsevier Academic Press.

40. Willberg, C., Duczek, S., Vivar-Perez, J. M., & Ahmad, Z. A. B. (2015). Simulation Methods for Guided Wave-Based Structural Health Monitoring: A Review. *Appl. Mech. Rev.*, *67*(1), 10803.

41. Rokicki, E., Przysowa, R., Kotkowski, J., & Majewski, P. (2021). High Temperature Magnetic Sensors for the Hot Section of Aeroengines. *Aerospace, 8*(9), 261.

42. Bose, S. (2007). *High temperature coatings.* Amsterdam, Boston: Amsterdam; Boston: Elsevier.

43. Bürgel, R., Jürgen Maier, H., & Niendorf, T. (2011). *Handbuch Hochtemperatur- Werkstofftechnik.* Wiesbaden: Vieweg+Teubner. (In German)

44. Chen, X., He, M. Y., Spitsberg, I., Fleck, N. A., Hutchinson, J. W., & Evans, A. G. (2004). Mechanisms governing the high temperature erosion of thermal barrier coatings. *Wear*, *256*(7-8), 735–746.

45. Gallardo, J., Rodríguez, J., & Herrera, E. (2002). Failure of gas turbine blades. *Wear, 252*(3), 264–268.

46. Jackson, R. D. (2009). *The effect of bond coat oxidation on the microstructure and endurance of two thermal barrier coating systems*. Ph.D. Thesis. University of Birmingham, Birmingham, UK.

47. Padture, N. P., Gell, M., & Jordan, E. H. (2002). Thermal Barrier Coatings for Gas-Turbine Engine Applications. *Science*, *296*(5566), 280–284.

48. Fukuchi, T., Fuse, N., Okada, M., Ozeki, T., Fujii, T., Mizuno, M., et al. (2014). Topcoat Thickness Measurement of Thermal Barrier Coating of Gas Turbine Blade Using Terahertz Wave. *Electrical Engineering in Japan, 189*(1), 1–8.

49. Kirschner, M., Wobst, T., Rittmeister, B., & Mundt, C. (2015). Erosion Testing of Thermal Barrier Coatings in a High Enthalpy Wind Tunnel. *J. Eng. Gas Turbines Power, 137*(3), 32101.

50. Morinaga, M., & Takahashi, T. (2001). Development of Non-destructive Inspection Method for the Performance of Thermal Barrier Coating. *Ann. N. Y. Acad. Sci., 934*(1), 489–496.

51. Swar, R., Hamed, A., Shin, D., Woggon, N., & Miller, R. (2012). Deterioration of Thermal Barrier Coated Turbine Blades by Erosion. *Int. J. Rotating Mach., 2012*(2012).

52. Wellman, R. G., & Nicholls, J. R. (2007). A review of the erosion of thermal barrier coatings. *J. Phys. D: Appl. Phys., 40*(16), R293-R305.

53. Xiao, Y. Q., Yang, L., Zhou, Y. C., Wei, Y. G., & Wang, N. G. (2017). Dominant parameters affecting the reliability of TBCs on a gas turbine blade during erosion by a particle-laden hot gas stream. *Wear, 390-391*, 166–175.

54. Wellman, R. G., Nicholls, J. R., & Murphy, K. (2009). Effect of microstructure and temperature on the erosion rates and mechanisms of modified EB PVD TBCs. *Wear, 267*(11), 1927–1934.

55. Yang, L., Zhou, Y. C., & Lu, C. (2011). Damage evolution and rupture time prediction in thermal barrier coatings subjected to cyclic heating and cooling: An acoustic emission method. *Acta Materialia, 59*(17), 6519–6529.

56. Zhang, W.-W., Li, G.-R., Zhang, Q., & Yang, G.-J. (2017). Comprehensive damage evaluation of localized spallation of thermal barrier coatings. *J. Adv. Ceram., 6*(3), 230–239.

57. Harrold, R. T., & Sanjana, Z. N. (1987). Non-Destructive Evaluation of the Curing of Resin and Prepreg Using an Acoustic Waveguide Sensor: Digital Repository @ Iowa State University.

58. Harrold, R. T., & Sanjana, Z. N. (2006). *Monitoring thermal barrier coating deterioration via acoustic response to gas flow, pressure and impact*. (U.S. Patent 7062971B2).

59. Willsch, M., Bosselmann, T., & Theune, N. M. (2004). New approaches for the monitoring of gas turbine blades and vanes. *SENSORS, 2004 IEEE, 1*, 20–23.

60. Atkinson, D., & Hayward, G. (2001). The generation and detection of longitudinal guided waves in thin fibers using a conical transformer. *IEEE Trans. Ultrason. Ferroelectr. Freq. Control, 48*(4), 1046–1053.

61. Harrold, R. T., & Sanjana, Z. N. (2002). *Acoustic waveguide sensing the condition of components within gas turbines*. (U.S. Patent 6487909B2).

62. Cegla, F. B. (2008). Energy concentration at the center of large aspect ratio rectangular waveguides at high frequencies. *J. Acoust. Soc. Am., 123*(6), 4218–4226.

63. Jarvis, A. J. C., Cegla, F. B., Thompson, D. O., & Chimenti, D. E. (2011). Defect Monitoring at Elevated Temperatures (>500 °C) Using an Array of Ultrasonic Waveguides. In *Review of progress in Quantitative Nondestructive Evaluation: Volume 30A; Volume 30B, San Diego, California, USA, 18–23 July 2010*. (pp. 1679–1686, AIP Conference Proceedings): AIP.

64. Sheen, S. H., Chien, H. T., Wang, K., Lawrence, W. P., & Engel, D. (2010). *Linear-array ultrasonic waveguide transducer for under sodium viewing: ANL--GenIV--178*: Nuclear Engineering Division.

65. Chong Ma, Zheng Du, Yina Guo, Shaohui Ni, & Xin Zhao (2010). Ultrasonic Waveguides Detection-based approach to locate defect on workpiece. *2010 Chinese Control and Decision Conference*, 757-761.

66. Zhou, Z., Zhang, K., Zhou, J., Sun, G., & Wang, J. (2015). Application of laser ultrasonic technique for non-contact detection of structural surface-breaking cracks. *Opt. Laser Technol., 73*, 173–178.

67. Arias, I. (2003). *Modeling of the Detection of Surface-Breaking Cracks by Laser Ultrasonics*. Ph.D. Thesis, Northwestern University, Evanston, IL, USA.

68. Liu, P., Nazirah, A. W., & Sohn, H. (2016). Numerical simulation of damage detection using laser-generated ultrasound. *Ultrasonics, 69*, 248–258.

69. An, Y.-K., Kwon, Y., & Sohn, H. (2013). Noncontact laser ultrasonic crack detection for plates with additional structural complexities. *Struct. Health Monit., 12*(5-6), 522–538.

70. Pei, C., Demachi, K., Zhu, H., Fukuchi, T., Koyama, K., & Uesaka, M. (2012). Inspection of cracks using laser-induced ultrasound with shadow method: Modeling and validation. *Optics & Laser Technology, 44*(4), 860–865.

71. Edwards, R. S., Dixon, S., & Jian, X. (2006). Depth gauging of defects using low frequency wideband Rayleigh waves. *Ultrasonics, 44*(1), 93–98.

72. Jian, X., Dixon, S., Guo, N., & Edwards, R. (2007). Rayleigh wave interaction with surface-breaking cracks. *J. Appl. Phys., 101*(6), 64906.

73. Jian, X., Dixon, S., Guo, N., Edwards, R. S., & Potter, M. (2006). Pulsed Rayleigh wave scattered at a surface crack. *Ultrasonics, 44 (Suppl. 1)*, e1131-e1344.

74. Dixon, S., Burrows, S. E., Dutton, B., & Fan, Y. (2011). Detection of cracks in metal sheets using pulsed laser generated ultrasound and EMAT detection. *Ultrasonics, 51*(1), 7–16.

75. Cantrell, J. H. (1994). Crystalline structure and symmetry dependence of acoustic nonlinearity parameters. *J. Appl. Phys., 76*(6), 3372–3380.

76. Cantrell, J. H. (2009). Nonlinear dislocation dynamics at ultrasonic frequencies. *J. Appl. Phys., 105*(4), 43520.

77. Hikata, A., Chick, B. B., & Elbaum, C. (1965). Dislocation Contribution to the Second Harmonic Generation of Ultrasonic Waves. *J. Appl. Phys., 36*(1), 229–236.

78. Xiang, Y., Zhu, W., Liu, C.-J., Xuan, F.-Z., Wang, Y.-N., & Kuang, W.-C. (2015). Creep degradation characterization of titanium alloy using nonlinear ultrasonic technique. *NDT E Int., 72*, 41–49.

79. Malfense Fierro, G. P., & Meo, M. (2015). Residual fatigue life estimation using a nonlinear ultrasound modulation method. *Smart Mater. Struct.*, *24*(2), 25040.

80. Amura, M., Meo, M., & Amerini, F. (2011). Baseline-free estimation of residual fatigue life using a third order acoustic nonlinear parameter. *Acoust. Soc. Am.*, *130*(4), 1829–1837.

81. Cantrell, J. H., & Yost, W. T. (2001). Nonlinear ultrasonic characterization of fatigue microstructures. *Int. J. Fatigue*, *23*(SUPPL. 1), 487–490.

82. Broda, D., Staszewski, W. J., Martowicz, A., Uhl, T., & Silberschmidt, V. V. (2014). Modelling of nonlinear crack–wave interactions for damage detection based on ultrasound—A review. *J. Sound Vib.*, *333*(4), 1097–1118.

83. Dutta, D., Sohn, H., Harries, K. A., & Rizzo, P. (2009). A Nonlinear Acoustic Technique for Crack Detection in Metallic Structures. *Struct. Health Monit.*, *8*(3), 251–262.

84. Hu, H. F., Staszewski, W. J., Hu, N. Q., Jenal, R. B., & Qin, G. J. (2010). Crack detection using nonlinear acoustics and piezoceramic transducers—instantaneous amplitude and frequency analysis. *Smart Mater. Struct.*, *19*(6), 65017.

85. Ohara, Y., Takahashi, K., Murai, S., & Yamanaka, K. (2013). High-selectivity imaging of closed cracks using elastic waves with thermal stress induced by global preheating and local cooling. *Appl. Phys. Lett.*, *103*(3), 31917.

86. Solodov, I., Krohn, N., & Busse, G. (2002). CAN: an example of nonclassical acoustic nonlinearity in solids. *Ultrasonics*, *40*(1-8), 621–625.

87. Ohara, Y., Mihara, T., Sasaki, R., Ogata, T., Yamamoto, S., Kishimoto, Y., et al. (2007). Imaging of closed cracks using nonlinear response of elastic waves at subharmonic frequency. *Appl. Phys. Lett.*, *90*(1), 11902.

88. Solodov, I., Wackerl, J., Pfleiderer, K., & Busse, G. (2004). Nonlinear self-modulation and subharmonic acoustic spectroscopyfor damage detection and location. *Appl. Phys. Lett.*, *84*(26), 5386–5388.

89. Moussatov, A., Gusev, V., & Castagnède, B. (2003). Self-induced hysteresis for nonlinear acoustic waves in cracked material. *Phys. Rev. Lett.*, *90*(12), 124301.

90. Yamanaka, K., Mihara, T., & Tsuji, T. (2004). Evaluation of Closed Cracks by Model Analysis of Subharmonic Ultrasound. *Jpn. J. Appl. Phys.*, *43*(5B), 3082–3087.

91. Yamanaka, K., Ogiso, H., & Kolosov, O. (1994). Analysis of Subsurface Imaging and Effect of Contact Elasticity in the Ultrasonic Force Microscope. *Jpn. J. Appl. Phys.*, *33*(Part 1, No. 5B), 3197–3203.

92. Yamanaka, K., Ogiso, H., & Kolosov, O. (1994). Ultrasonic force microscopy for nanometer resolution subsurface imaging. *Appl. Phys. Lett.*, *64*(2), 178–180.

93. Blanloeuil, P., Rose, L., Guinto, J. A., Veidt, M., & Wang, C. H. (2016). Closed crack imaging using time reversal method based on fundamental and second harmonic scattering. *Wave Motion*, *66*, 156–176.

94. Baltazar, A., Rokhlin, S. I., & Pecorari, C. (2002). On the relationship between ultrasonic and micromechanical properties of contacting rough surfaces. *J. Mech. Phys. Solids*, *50*(7), 1397–1416.

95. Biwa, S., Nakajima, S., & Ohno, N. (2004). On the Acoustic Nonlinearity of Solid-Solid Contact With Pressure-Dependent Interface Stiffness. *J. Appl. Mech.*, *71*(4).

96. Buck, O., Morris, W. L., & Richardson, J. M. (1978). Acoustic harmonic generation at unbonded interfaces and fatigue cracks. *Appl. Phys. Lett.*, *33*(5), 371–373.

97. Chen, J., Jiang, W., & Shui, Y. (2001). Observation of nonlinear acoustic effects at isotropic solid–solid interfaces. *J. Acoust. Soc. Am.*, *109*(2), 501–507.

98. Hirose, S., & Achenbach, J. D. (1993). Higher harmonics in the far field due to dynamic crack-face contacting. *J. Acoust. Soc. Am.*, *93*(1), 142–147.

99. Kim, J.-Y., Baltazar, A., Hu, J. W., & Rokhlin, S. I. (2006). Hysteretic linear and nonlinear acoustic responses from pressed interfaces. *Int. J. Solids Struct.*, *43*(21), 6436–6452.

100. Pecorari, C. (2003). Nonlinear interaction of plane ultrasonic waves with an interface between rough surfaces in contact. *J. Acoust. Soc. Am.*, *113*(6), 3065.

101. Nazarov, V. E., & Sutin, A. M. (1997). Nonlinear elastic constants of solids with cracks. *J. Acoust. Soc. Am.*, *102*(6), 3349–3354.

102. Jinno, K., Sugawara, A., Ohara, Y., & Yamanaka, K. (2014). Analysis on Nonlinear Ultrasonic Images of Vertical Closed Cracks by Damped Double Node Model. *Mater. Trans.*, *55*(7), 1017–1023.

103. Sarens, B., Verstraeten, B., Glorieux, C., Kalogiannakis, G., & van Hemelrijck, D. (2010). Investigation of contact acoustic nonlinearity in delaminations by shearographic imaging, laser doppler vibrometric scanning and finite difference modeling. *Ultrasonics, Ferroelectrics and Frequency Control, IEEE Transactions on*, *57*(6).

104. Sato, M. (2007). Comparing three methods of free boundary implementation for analyzing elastodynamics using the finite-difference time-domain formulation. *Acoust. Sci. Technol.*, *28*(1), 49–52.

105. Yamanaka, K., Ohara, Y., Oguma, M., & Shintaku, Y. (2011). Two-Dimensional Analyses of Subharmonic Generation at Closed Cracks in Nonlinear Ultrasonics. *Appl. Phys. Express*, *4*(7), 76601.

106. Ohara, Y., Potter, J., Haupert, S., Nakajima, H., Tsuji, T., & Mihara, T. (2018). Multi-mode nonlinear ultrasonic phased array for closed crack imaging. In *21st International Symposium on Nonlinear Acoustics, Santa Fe, New Mexico, USA, July 9–13, 2018, 50th Anniversary*. (p. 55001, Proceedings of Meetings on Acoustics): Acoustical Society of America.

107. Jhang, K.-Y., & Kim, K.-C. (1999). Evaluation of material degradation using nonlinear acoustic effect. *Ultrasonics*, *37*(1), 39–44.

108. Frouin, J., Sathish, S., Matikas, T. E., & Na, J. K. (1999). Ultrasonic Linear and Nonlinear Behavior of Fatigued Ti–6Al–4V. *J. Mater. Res.*, *14*(04), 1295–1298.

109. Rothenfusser, M., Mayr, M., & Baumann, J. (2000). Acoustic nonlinearities in adhesive joints. *Ultrasonics*, *38*(1-8), 322–326.

110. Yost, W. T. (2000). Nonlinear ultrasonic pulsed measurements and applications to metal processing and fatigue. In *The 27th annual review of progress in quantitative nondestructive evaluation, Ames, Iowa (USA), 16-20 July 2000*. (pp. 1268–1275): AIP.

111. Pieczonka, L., Klepka, A., Martowicz, A., & Staszewski, W. J. (2015). Nonlinear vibroacoustic wave modulations for structural damage detection: an overview. *Opt. Eng.*, *55*(1), 11005.

112. Jingpin, J., Junjun, S., Guanghai, L., Bin, W., & Cunfu, H. (2015). Evaluation of the intergranular corrosion in austenitic stainless steel using parallel wave mixing method. *NDT E Int.*, *69*, 1–8.

113. Ostrovsky, L. A., & Johnson, P. A. (2000). Dynamic nonlinear elasticity in geomaterials. *Riv. del Nuovo Cim.*, *24*(7), 1–46.

114. Liu, M., Tang, G., Jacobs, L. J., & Qu, J. (2012). Measuring acoustic nonlinearity parameter using parallel wave mixing. *J. Appl. Phys.*, *112*(2), 24908.

115. van den Abeele, K. (2007). Multi-mode nonlinear resonance ultrasound spectroscopy for defect imaging: an analytical approach for the one-dimensional case. *J. Acoust. Soc. Am.*, *122*(1), 73–90.

116. Malfense Fierro, G. P., & Meo, M. (2017). Nonlinear imaging (NIM) of flaws in a complex composite stiffened panel using a constructive nonlinear array (CNA) technique. *Ultrasonics*, *74*, 30–47.

117. Malfense Fierro, G. P. (2014). *Development of Nonlinear Ultrasound Techniques for Multidisciplinary Engineering Applications*. Ph.D. Thesis. University of Bath, Bath, UK.

118. Fan, C., Yang, L., & Zhao, Y. (2020). Ultrasonic multi-frequency time-reversal-based imaging of extended targets. *NDT E Int.*, *113*, 102276.

119. Queirós, R., Corrêa Alegria, F., Silva Girão, P., & Cruz Serra, A. (2015). A multi-frequency method for ultrasonic ranging. *Ultrasonics*, *63*, 86–93.

120. van den Abeele, K. E.-A., Johnson, P. A., & Sutin, A. (2000). Nonlinear Elastic Wave Spectroscopy (NEWS) Techniques to Discern Material Damage, Part I: Nonlinear Wave Modulation Spectroscopy (NWMS). *Research in Nondestructive Evaluation, 12*(1), 17–30.

121. van den Abeele, K. E.-A., Carmeliet, J., Cate, J. A. ten, & Johnson, P. A. (2000). Nonlinear Elastic Wave Spectroscopy (NEWS) Techniques to Discern Material Damage, Part II: Single-Mode Nonlinear Resonance Acoustic Spectroscopy. *Research in Nondestructive Evaluation, 12*(1), 31–42.

122. Straka, L., Yagodzinskyy, Y., Landa, M., & Hänninen, H. (2008). Detection of structural damage of aluminum alloy 6082 using elastic wave modulation spectroscopy. *NDT E Int., 41*(7), 554–563.

123. Greenhall, J., Grutzik, S., Graham, A., Sinha, D. N., & Pantea, C. (2020). Nonlinear acoustic crack detection in thermoelectric wafers. *Mech. Syst. Signal Process., 139*, 106598.

124. Pfleiderer, K., Aufrecht, J., Solodov, I., & Busse, G. (2004). Multi-frequency ultrasonic NDE for early defect recognition and imaging. *IEEE Ultrasonics Symposium, 1*, 693–696.

125. Abraham, S. T., Shivaprasad, S., Sreevidya, N., Das, C. R., Albert, S. K., Venkatraman, B., et al. (2019). A Novel Multi-frequency Nonlinear Ultrasonic Approach for the Characterization of Annealed Polycrystalline Microstructure. *Metall. Mater. Trans. A, 50*(12), 5567–5573.

126. Gao, T., Sun, H., Hong, Y., & Qing, X. (2020). Hidden corrosion detection using laser ultrasonic guided waves with multi-frequency local wavenumber estimation. *Ultrasonics, 108*, 106182.

127. Malfense Fierro, G. P., & Meo, M. (2020). Non-linear Phased Array Imaging of Flaws Using a Dual and Tri Frequency Modulation Technique. *Frontiers in Built Environment, 6*.

128. Yang, Y., Ng, C.-T., & Kotousov, A. (2019). Second-order harmonic generation of Lamb wave in prestressed plates. *J. Sound Vib., 460*, 114903.

129. Eaves, A., Smith, A., Waterhouse, W., & Sansome, D. (1975). Review of the application of ultrasonic vibrations to deforming metals. *Ultrasonics, 13*(4), 162–170.

130. Hong, M., Su, Z., Wang, Q., Cheng, L., & Qing, X. (2014). Modeling nonlinearities of ultrasonic waves for fatigue damage characterization: theory, simulation, and experimental validation. *Ultrasonics, 54*(3), 770–778.

131. Jhang, K. Y. (2000). Applications of nonlinear ultrasonics to the NDE of material degradation. *IEEE transactions on ultrasonics, ferroelectrics, and frequency control, 47*(3), 540–548.

132. Daud, Y., Lucas, M., & Huang, Z. (2006). Superimposed ultrasonic oscillations in compression tests of aluminium. *Ultrasonics, 186*(1-3), 179-190.

133. Ashida, Y., & Aoyama, H. (2007). Press forming using ultrasonic vibration. *J. Mater. Process. Technol., 187-188*, 118–122.

134. Kirchner, H., Kromp, W., Prinz, F., & Trimmel, P. (1985). Plastic deformation under simultaneous cyclic and unidirectional loading at low and ultrasonic frequencies. *Mater. Sci. Eng. C, 68*(2), 197–206.

135. Rao, V. J., Kannan, E., Prakash, R. V., & Balasubramaniam, K. (2009). Observation of two stage dislocation dynamics from nonlinear ultrasonic response during the plastic deformation of AA7175-T7351 aluminum alloy. *Mater. Sci. Eng., 512*(1-2), 92–99.

136. Oruganti, R. K., Sivaramanivas, R., Karthik, T. N., Kommareddy, V., Ramadurai, B., Ganesan, B., et al. (2007). Quantification of fatigue damage accumulation using non-linear ultrasound measurements. *Int. J. Fatigue, 29*(9-11), 2032–2039.

137. Oruganti, R. K., Sivaramanivas, R., Karthik, T., Kommareddy, V., Ramadurai, B., Ganesan, B., et al. (2007). Quantification of fatigue damage accumulation using non-linear ultrasound measurements. *Int. J. Fatigue, 29*(9), 2032–2039.

138. Kim, C.-S., & Jhang, K.-Y. (2012). Fatigue-Induced Micro-damage Characterization of Austenitic Stainless Steel 316 Using Innovative Nonlinear Acoustics. *Chin. Phys. Lett., 29*(6), 60702.

139. Yao, Z., Kim, G.-Y., Faidley, L., Zou, Q., Mei, D., & Chen, Z. (2012). Effects of superimposed high-frequency vibration on deformation of aluminum in micro/meso-scale upsetting. *J. Mater. Process. Technol., 212*(3), 640–646.

140. Yao, Z., Kim, G.-Y., Wang, Z., Faidley, L., Zou, Q., Mei, D., et al. (2012). Acoustic softening and residual hardening in aluminum: Modeling and experiments. *Int. J. Plast., 39*, 75–87.

141. Estrin, Y. (1998). Dislocation theory based constitutive modelling: foundations and applications. *J. Mater. Process. Technol., 80-81*, 33–39.

142. Pruell, C., Kim, J.-Y., Qu, J., & Jacobs, L. J. (2009). A nonlinear-guided wave technique for evaluating plasticity-driven material damage in a metal plate. *NDT Int., 42*(3), 199–203.

143. Deng, M., & Pei, J. (2007). Assessment of accumulated fatigue damage in solid plates using nonlinear Lamb wave approach. *Appl. Phys. Lett., 90*(12), 121902.

144. Pruell, C., Kim, J.-Y., Qu, J., & Jacobs, L. J. (2007). Evaluation of plasticity driven material damage using Lamb waves. *Appl. Phys. Lett., 91*(23).

145. Xiang, Y., Deng, M., Xuan, F.-Z., & Liu, C.-J. (2011). Cumulative second-harmonic analysis of ultrasonic Lamb waves for ageing behavior study of modified-HP austenite steel. *Ultrasonics, 51*(8), 974–981.

146. Walker, S. V., Kim, J.-Y., Qu, J., & Jacobs, L. J. (2012). Fatigue damage evaluation in A36 steel using nonlinear Rayleigh surface waves. *NDT E Int., 48*, 10–15.

147. Jaya Rao, V. V. S., Kannan, E., Prakash, R. V., & Balasubramaniam, K. (2008). Fatigue damage characterization using surface acoustic wave nonlinearity in aluminum alloy AA7175-T7351. *J. Appl. Phys., 104*(12), 123508.

148. Dutta, R. K., Petrov, R. H., Delhez, R., Hermans, M., Richardson, I. M., & Böttger, A. J. (2013). The effect of tensile deformation by in situ ultrasonic treatment on the microstructure of low-carbon steel. *Acta Materialia, 61*(5), 1592–1602.

149. Frank, F. C., & Read, W. T. (1950). Multiplication Processes for Slow Moving Dislocations. *Phys. Rev., 79*(4), 722–723.

150. Hikata, A., & Elbaum, C. (1966). Generation of Ultrasonic Second and Third Harmonics Due to Dislocations. I. *APS, 144*(2), 469–477.

151. Apple, T. M., Cantrell, J. H., Amaro, C. M., Mayer, C. R., Yost, W. T., Agnew, S. R., et al. (2013). Acoustic harmonic generation from fatigue-generated dislocation substructures in copper single crystals. *Philosophical Magazine, 93*(21), 2802–2825.

152. Xiang, Y., Deng, M., Liu, C.-J., & Xuan, F.-Z. (2015). Contribution of mixed dislocations to the acoustic nonlinearity in plastically deformed materials. *J. Appl. Phys., 117*(21), 214903.

153. Gao, X., & Qu, J. (2018). Acoustic nonlinearity parameter induced by extended dislocations. *J. Appl. Phys., 124*(12), 125102.

154. Zhang, J., & Xuan, F.-Z. (2014). A general model for dislocation contribution to acoustic nonlinearity. *EPL (Europhysics Letters), 105*(5), 54005.

155. Zhang, J., Xuan, F.-Z., & Xiang, Y. (2013). Dislocation characterization in cold rolled stainless steel using nonlinear ultrasonic techniques: A comprehensive model. *EPL (Europhysics Letters), 103*(6), 68003.

156. Zhu, W., Deng, M., Xiang, Y., Xuan, F.-Z., Liu, C., & Wang, Y.-N. (2016). Modeling of ultrasonic nonlinearities for dislocation evolution in plastically deformed materials: Simulation and experimental validation. *Ultrasonics, 68*, 134–141.

157. Cash, W. D., & Cai, W. (2011). Dislocation contribution to acoustic nonlinearity: The effect of orientation-dependent line energy. *J. Appl. Phys., 109*(1), 14915.

158. Cash, W. D., & Cai, W. (2012). Contribution of dislocation dipole structures to the acoustic nonlinearity. *J. Appl. Phys., 111*(7), 74906.

159. Sahu, M. K., Swaminathan, J., Bandhoypadhyay, N. R., & Palit Sagar, S. (2018). Creep Damage Evaluation In P92 Steel Using Second Harmonic Of High Power Ultrasonic Signal. *Materials Today: Proceedings, 5*(2), 4467–4474.

160. Semenov, A. S., Semenov, S. G., & Getsov, L. B. (2015). Methods of Computational Determination of Growth Rates of Fatigue, Creep, and Thermal Fatigue Cracks in Poly- and Monocrystalline Blades of Gas Turbine Units. *Strength of Materials, 47*(2), 268–290.

161. Chen, L., Liu, Y., & Xie, L. (2007). Power-exponent function model for low-cycle fatigue life prediction and its applications – Part II: Life prediction of turbine blades under creep–fatigue interaction. *Int. J. Fatigue, 29*(1), 10–19.

162. Kim, H.-J. (2005). Assessment of creep life fraction for in-service high-temperature components. *Eng. Fail. Anal. C., 12*(4), 578–585.

163. Hyde, T. H., Sun, W., & Becker, A. A. (2005). Use of life and strain fraction rules for creep life prediction of pressurized pipe components undergoing geometry change. *J. Strain Anal. Eng., 40*(4), 385–394.

164. Raj, B., Moorthy, V., Jayakumar, T., & Rao, K. B. S. (2003). Assessment of microstructures and mechanical behaviour of metallic materials through non-destructive characterisation. *Int. Mater. Rev., 48*(5), 273–325.

165. Shi, D., Li, Z., Yang, X., & Wang, H. (2018). Accelerated LCF-creep experimental methodology for durability life evaluation of turbine blade. *Fatigue Fract. Eng. Mater. Struct., 41*(5), 1196–1207.

166. Marahleh, G., Kheder, A., & Hamad, H. F. (2006). Creep life prediction of service-exposed turbine blades. *Mater. Sci. Eng. A, 433*(1-2), 305–309.

167. Liu, D., Li, H., & Liu, Y. (2015). Numerical Simulation of Creep Damage and Life Prediction of Superalloy Turbine Blade. *Math. Probl. Eng., 2015*(1), 1–10.

168. Maharaj, C., Morris, A., & Dear, J. P. (2012). Modelling of creep in Inconel 706 turbine disc fir-tree. *Eng. Fail. Anal., 558*, 412–421.

169. Baby, S., Nagaraja Kowmudi, B., Omprakash, C. M., Satyanarayana, D., Balasubramaniam, K., & Kumar, V. (2008). Creep damage assessment in titanium alloy using a nonlinear ultrasonic technique. *Scripta Materialia, 59*(8), 818–821.

170. Balasubramaniam, K., Valluri, J. S., & Prakash, R. V. (2011). Creep damage characterization using a low amplitude nonlinear ultrasonic technique. *Mater. Charact., 62*(3), 275–286.

171. Ehrlich, C., Kim, J.-Y., Jacobs, L. J., Qu, J., & Wall, J. (2012). Experimental characterization of creep damage in a welded steel pipe section using a nonlinear ultrasonic technique. In *Review of Progress in Quantitative Nondestructive Evaluation, USA, VT, Burlington, 17–22 July*. (pp. 292–298, AIP Conference Proceedings): AIP.

172. Kang, J. (2000). On the Detection of Creep Damage in a Directionally Solidified Nickel Base Superalloy Using Nonlinear Ultrasound. In *Quantitative Nondestructive Evaluation, USA, Wisconsin, 27 July-1 August 2000*. (pp. 1248–1255): AIP.

173. Valluri, J. S., Balasubramaniam, K., & Prakash, R. V. (2010). Creep damage characterization using non-linear ultrasonic techniques. *Acta Materialia, 58*(6), 2079–2090.

174. Xiang, Y.-X., Deng, M.-X., Xuan, F.-Z., Chen, H., & Chen, D.-Y. (2012). Creep Damage Evaluation of Titanium Alloy Using Nonlinear Ultrasonic Lamb Waves. *Chin. Phys. Lett., 29*(10), 106202.

175. Xiang, Y., Deng, M., & Xuan, F.-Z. (2014). Creep damage characterization using nonlinear ultrasonic guided wave method: A mesoscale model. *Int. J. Appl. Phys., 115*(4), 44914.

176. Abdelrhman, A. M., Hee, L. M., Leong, M. S., & Al-Obaidi, S. (2015). Condition Monitoring of Blade in Turbomachinery: A Review. *Adv. Mech. Eng., 6*(4), 210717.

177. Burk, S. (2011). *Hochtemperaturoxidation Molybdän-basierter Legierungen unter Berücksichtigung von Einflüssen aus Umgebungsatmosphäre und legierungstechnischen Maßnahmen*. Ph.D. Thesis. University of Siegen, Siegen, Germany. (In German)

178. Obigodi-Ndjeng, G. (2011). *High Temperature Oxidation and Electrochemical Investigations on Nickel-base Alloys*. Ph.D. Thesis. University of Erlangen-Nürnberg, Erlangen, Germany.

179. Ciampa, F., Mahmoodi, P., Pinto, F., & Meo, M. (2018). Recent Advances in Active Infrared Thermography for Non-Destructive Testing of Aerospace Components. *Sensors, 18*(2), 609.

180. Renshaw, J., Chen, J. C., Holland, S. D., & Bruce Thompson, R. (2011). The sources of heat generation in vibrothermography. *NDT E Int., 44*(8), 736–739.

181. Renshaw, J., Holland, S. D., & Barnard, D. J. (2009). Viscous material-filled synthetic defects for vibrothermography. *NDT E Int., 42*(8), 753–756.

182. Gao, C., Mayton, D., Meeker, W. Q., Thompson, D. O., & Chimenti, D. E. (2007). Detecting cracks in fan blades using sonic IR. In *Review of Progress in Quantitative Nondestructive Evaluation: 34th Annual Review of Progress in Quantitative Nondestructive Evaluation, Golden, Colorado, USA, 22–27 July 2007*. (pp. 1708–1715): AIP.

183. Obeidat, O., Yu, Q., & Han, X. (2016). Developing Algorithms to Improve Defect Extraction and Suppressing Undesired Heat Patterns in Sonic IR Images. *Sensing and Imaging, 17*(1), 2418.

184. Obeidat, O., Yu, Q., & Han, X. Develop algorithms to improve detectability of defects in Sonic IR imaging NDE. In *Review of Progress in Quantitative Nondestructive Evaluation*. (p. 100009).

185. Obeidat, O., Yu, Q., & Han, X. Further development of image processing algorithms to improve detectability of defects in Sonic IR NDE. In *43rd annual Review of Progress in Quantitative Nondestructive Evaluation*. (Vol. 36, p. 100007).

186. Guo, X., & Vavilov, V. (2013). Crack detection in aluminum parts by using ultrasound-excited infrared thermography. *Infrared Phys. Technol., 61*, 149–156.

187. Lu, J., Han, X., Newaz, G., Favro, L. D., & Thomas, R. L. (2007). Study of the effect of crack closure in Sonic Infrared Imaging. *Nondestruct. Test. Evaluation, 22*(2-3), 127–135.

188. Rothenfusser, M. (2004). Acoustic Thermography: Vibrational Modes of Cracks and the Mechanism of Heat Generation. In *Review of Progress in Quantitative Nondestructive Evaluation, Golden, Colorado (USA), 25-30 July 2004*. (pp. 624–631): AIP.

189. Morbidini, M. (2007). *A comparison of the vibration-modulation and thermosonic*. Ph.D Thesis. Imperial College London, London, UK.

190. Morbidini, M., & Cawley, P. (2008). The Reliable Implementation of Thermosonics NDT. In *17th World Conference on Nondestructive Testing, Shanghai, China, 25-28 October 2008*. (1st ed., 536, Vol. 975): AIP Conference Proceedings.

191. Morbidini, M., & Cawley, P. (2009). The detectability of cracks using sonic IR. *J. Appl. Phys., 105*(9), 93530.

192. Mendioroz, A., Celorrio, R., & Salazar, A. (2017). Ultrasound excited thermography: an efficient tool for the characterization of vertical cracks. *Meas. Sci. Technol., 28*(11), 112001.

193. Holland, S. D. (2007). First Measurements from a New Broadband Vibrothermography Measurement System. In *Review of Progress in Quantitative Nondestructive Evaluation, Portland, Oregon, USA, 30 July-4 August 2007*. (pp. 478–483): AIP.

194. Zhang, D., Han, X., & Newaz, G. Sonic IR crack detection of aircraft turbine engine blades with multi-frequency ultrasound excitations. In *Review of Progress in Quantitative Nondestructive Evaluation*. (pp. 1644–1651).

195. Zhang, D. (2014). *Study of Chaotic Ultrasound and Frequency Sweep Excitations in Sonic IR NDE Technology*. Ph.D. Thesis. Wayne State University, Detroit, MI, USA.

196. Kang, B., Cawley, P., Thompson, D. O., & Chimenti, D. E. (2007). Multi-Mode Excitation System for Thermosonic Testing of Turbine Blades. In *Review of progress in quantitative Nondestructive Evaluation, Golden, Colorado, USA, 22–27 July 2007*. (pp. 520–527): AIP.

197. Weekes, B., Cawley, P., Almond, D. P., Thompson, D. O., & Chimenti, D. E. The Effects of Crack Opening and Coatings on the Detection Capability of Thermosonics. In *Review of Progress in Quantitative Nondestructive Evaluation*. (30ab, pp. 399–406).

198. Han, X., Favro, L. D., & Thomas, R. L. (2011). Sonic IR Imaging of delaminations and disbonds in composites. *J. Phys. D Appl. Phys., 44*(3), 34013.

199. Han, X., Zeng, Z., Li, W., Islam, M. S., Lu, J., Loggins, V., et al. (2004). Acoustic chaos for enhanced detectability of cracks by sonic infrared imaging. *J. Appl. Phys., 95*(7), 3792–3797.

200. Kang B.B., Cho Y.H.,Baeg N.U., Na H.S. (2011). Characteristics of the Vibration Generated by Different Excitation Methods During Thermosonic Non-destructive Testing. In *9th world congress railway research 2011, Lille, France, 22-26 May.*

201. Han, X. (2004). Importance of Acoustic Chaos in Sonic IR Imaging NDE. In *Quantivative Nondestructive Evaluation*. (Vol. 700, pp. 496–500): AIP.

202. Riahi, M., Dehestani, P., & Valipour, A. (2016). Using finite element to estimate vibration energy loss by cracks in thermosonic phenomenon under chaotic and non-chaotic vibrations. *J. Vib. Control, 22*(2), 457–467.

203. Abu-Nabah, B. A., & Al-Said, S. A. M. (2018). Sonic IR crack size estimation using 2D heat diffusion model with arbitrary heat source function along the crack. *Quant. Infrared Thermogr. J., 1*, 1–20.

204. Derusova, D. A., Vavilov, V. P., & Pawar, S. S. (2015). Evaluation of equivalent defect heat generation in carbon epoxy composite under powerful ultrasonic stimulation by using infrared thermography. *IOP Conf. Ser: Mater. Sci. Eng., 81*, 12084.

205. Parvasi, S. M., Xu, C., Kong, Q., & Song, G. (2016). Detection of multiple thin surface cracks using vibrothermography with low-power piezoceramic-based ultrasonic actuator—a numerical study with experimental verification. *Smart Mater. Struct., 25*(5), 55042.

206. Favro, L. D., Thomas, R. L., Han, X., Ouyang, Z., Newaz, G., & Gentile, D. (2001). Sonic infrared imaging of fatigue cracks. *Int. J. Fatigue, 23*, 471–476.

207. Zalameda, J. N., Winfree, W. P., Yost, W. T., Thompson, D. O., & Chimenti, D. E. (2007). Air coupled acoustic thermography (acat) inspection technique. In *Review of Progress in Quantitative Nondestructive Evaluation, Golden, Colorado, USA, 22–27 July 2007*. (pp. 467–474): AIP.

208. Solodov, I., Rahammer, M., Gulnizkij, N., & Kreutzbruck, M. (2016). Noncontact Sonic NDE and Defect Imaging Via Local Defect Resonance. *J. Nondestruct. Eval., 35*(3), 1–8.

209. Rahammer, M., Solodov, I., Bisle, W., Scherling, D., & Kreutzbruck, M. (2016). Thermosonic Testing with Phase Matched Guided Wave Excitation. *J. Nondestruct. Eval., 35*(3), 154.

210. Adebahr, W., Solodov, I., Rahammer, M., Gulnizkij, N., & Kreutzbruck, M. (2016). Local defect resonance for sensitive non-destructive testing. In *42nd Annual Review of Progress in Quantitative Nondestructive Evaluation: Incorporating the 6th European-American Workshop on Reliability of NDE, Minneapolis, Minnesota, USA, 26–31 July*. (p. 50005, AIP Conference Proceedings): AIP Publishing LLC.

211. Angelis, G. de, Meo, M., Almond, D. P., Pickering, S. G., & Angioni, S. L. (2012). A new technique to detect defect size and depth in composite structures using digital shearography and unconstrained optimization. *NDT E Int., 45*(1), 91–96.

212. Ciampa, F., Scarselli, G., & Meo, M. (2017). On the generation of nonlinear damage resonance intermodulation for elastic wave spectroscopy, *141*(4), 2364.

213. Solodov, I. (2014). Resonant Acoustic Nonlinearity of Defects for Highly-Efficient Nonlinear NDE. *J. Nondestruct. Eval., 33*(2), 252–262.

214. Scarselli, G., Ciampa, F., Nicassio, F., & Meo, M. (2017). Non-linear methods based on ultrasonic waves to analyse disbonds in single lap joints. *Proceedings of the Institution of Mechanical Engineers, Part C: J. Mech. Eng. Sci., 231*(16), 3066–3076.

215. Solodov, I., Bai, J., Bekgulyan, S., & Busse, G. (2011). A local defect resonance to enhance acoustic wave-defect interaction in ultrasonic nondestructive evaluation. *Appl. Phys. Lett., 99*(21), 211911.

216. Solodov, I., Bai, J., & Busse, G. (2013). Resonant ultrasound spectroscopy of defects: Case study of flat-bottomed holes. *J. Appl. Phys., 113*(22), 223512.

217. Solodov, I., & Busse, G. (2013). Resonance ultrasonic thermography: Highly efficient contact and air-coupled remote modes. *Appl. Phys. Lett., 102*(6), 61905.

218. Solodov, I., Rahammer, M., Derusova, D., & Busse, G. (2015). Highly-efficient and noncontact vibro-thermography via local defect resonance. *Quant. Infrared Thermogr. J., 12*(1), 98–111.